Why do decays decay? Transport and recombination dynamics of solar cells revealed via time resolved photoluminescence imaging: application to hybrid perovskites

Guillaume Vidon

Guillaume Vidon. Why do decays decay? Transport and recombination dynamics of solar cells revealed via time resolved photoluminescence imaging: application to hybrid perovskites. Condensed Matter [cond-mat]. Institut Polytechnique de Paris, 2022. English. NNT : . tel-03947293

HAL Id: tel-03947293
https://hal.science/tel-03947293v1

INSTITUT
POLYTECHNIQUE
DE PARIS

NNT : 2022IPPAX082

Thèse de doctorat

ÉCOLE
POLYTECHNIQUE

IP PARIS

Why do decays decay? Transport and recombination dynamics of solar cells revealed via time resolved photoluminescence imaging: application to hybrid perovskites.

Thèse de doctorat de l'Institut Polytechnique de Paris
préparée à l'IPVF

École doctorale n°626 École doctorale de l'Institut Polytechnique de Paris (EDIPP)
Spécialité de doctorat : Physique de la matière condensée

Thèse présentée et soutenue à Palaiseau, le 10/10/2022, par

GUILLAUME VIDON

Composition du Jury :

Jacques Peretti Directeur de recherche, CNRS (PMC)	Président
Maria Chamarro Professeur, Sorbonne Université (INSP)	Rapporteur
Damien Garrot Maître de conférences, Université Versailles Saint Quentin-en-Yvelines (GEMaC)	Rapporteur
Thomas Kirchartz Professor, Forschungszentrum Jülich, Universität Duisburg-Essen	Examinateur
Laurent Lombez Chargé de recherche, CNRS (LPCNO)	Examinateur
Jean-François Guillemoles Directeur de recherche, CNRS (UMR IPVF)	Directeur de thèse
Daniel Suchet Maître de conférences, École polytechnique (UMR IPVF)	Invité (co-encadrant)
Jean-Baptiste Puel Ingénieur-Chercheur EDF R&D (IPVF)	Invité (co-encadrant)

Remerciements

First I start with ”instutitional” acknowledgement. I had the chance to observe many different perovskite compositions from different groups internationally, including IPVF's baseline, Giulia Grancini's group, and Sandy Sanchez' group. I am thank-full to our scientific collaborators. I also thank the jury members to have taken time to discuss my work.

Il est venu pour moi le temps de dire merci en Français. Alors allons-y !

Merci Jean-Baptiste tout d'abord. Tu as été mon maître de stage puis de thèse et tu as toujours fait preuve de patience avec moi qui en manque un petit peu. Tu es resté positif quand j'étais négatif. Tu m'as toujours poussé à prendre du recul. J'ai toujours admiré ta calme mais résolue volonté de comprendre. Merci aussi pour les discussions sur les voyages, sur les idées écolos – je ne révélerai à personne que tu fais partie d'extinction rébellion, ne t'inquiète pas.

Merci Daniel (Suchet). Tu as été mon professeur si on peut dire. C'est toi qui m'as permis de donner des tutorats. Je crois que j'ai toujours admiré ta clarté et ta volonté d'expliquer. J'ai essayé tant que j'ai pu de m'en inspirer. Toi aussi tu as toujours su être positif quand j'étais renfrogné. Merci pour les discussions sur l'énergie/le futur et pour tout cet élan de vulgarisation. Tu m'as appris qu'être un scientifique c'est avant tout être un citoyen engagé.

Merci Jean-François. Tu as été mon directeur de thèse et fournisseur officiel d'idées. Jean-François j'ai toujours été admiratif et quelque peu jaloux de ta capacité à tout comprendre d'un coup. Je me rappelle qu'un jour quand j'étais encore en stage j'avais trouvé très sympathique de ta part de venir spontanément me voir pour me demander des nouvelles et discuter physique une heure avec moi. Tu n'as pas toujours le temps mais quand tu l'as, tu le prends et je te remercie pour ça.

Merci Stefania. Tu n'es pas sur liste officielle des encadrants de ma thèse mais tu mériterais d'y être. Tu as pris ta part de ma formation scientifique et tu t'es intéressée à mes recherches à un moment où j'avais l'impression d'être seul. Ton regard plus tourné vers les publications et les résultats m'a permis d'évoluer et de donner une autre dimension à mes travaux. Pour tout ça je te remercie.

Pour mes donc 4 superviseur/superviseuse j'ai prévu une remise de prix. Non Daniel ce ne sont malheureusement pas des Dundees Award mais presque. Je vous remets à tous les quatre le prix 2022 de l'encadrement de thèse. Félicitations. Mais j'ai aussi eu d'autres inspirations scientifiques :

- Expérimentales d'abord : merci Daniel Ory d'avoir consenti après une longue cour de ma part à me laisser faire des expériences. Merci de m'avoir formé d'abord peut être à contre cœur mais aujourd'hui je crois pour notre plaisir à tous les deux. Merci !

- Expérimentales toujours : merci Marie de m'avoir également formé – j'ai bien aimé travailler avec toi. Malgré nos caractères très différents je crois qu'on formait une bonne team et je crois que la TR-FLIM a trouvé qu'on était de bons parents. Merci !

- Chimiques ensuite (rassurez vous je n'ai rien fait moi-même de ce côté-là) : merci Davide Ceratti de toutes nos discussions passionnantes sur les pérovskites. Tu m'as transmis un petit peu de ta vision de ce magnifique système physicochimique que sont les pérovskites. Tu m'as aussi fait cultiver mon côté scientifique fou – mais pas que puisque tu m'as toujours aussi donné des conseils pour mon avenir. Merci !

Merci à toutes celles et tous ceux qui ont directement ou indirectement permis mes travaux :

- l'IPVF,
- les équipes support (RH, gestion, QHSE et exploitation Julie notamment),
- Le programme II pour avoir fourni plein d'échantillons – notamment Armelle pour la fabrication et Jean pour les discussions (scientifiques... ou ... non)
- L'équipe carac pour l'aide expérimentale (dont Baptiste que je n'ai pas encore cité, Alexandra Géraud, Nao)

Merci à tous mes co-auteurs et à tous ceux avec qui j'ai eu la chance de travailler. Je pense à Philip que je n'ai pas encore cité mais aussi à Pia – aux équipes de l'ILV qui ont abîmé ces perovskites avec des rayons X. Les équipes italiennes et Suisse avec qui j'ai pu travailler. Venons-en maintenant aux remerciements moins directement liés au travail.

Merci aux doctorants/post docs de la communauté IPVF en général pour pleins de moments de fun. Je pense aux anciens (Olivier, Minjin, Margaux, Sophie, Emilie, Anatole, Arpit). Merci aux doctorants actuels aussi :

- Alexandre Py, mon Wurfel buddy. Je suis très fier d'avoir co-fondé avec toi le Wurfel Klub. Mais pas que, d'avoir pu faire mes travaux de thèse à tes côtés !
- Bérengère et Salim les semi/complet C2niens mais aussi les semi/complets parisiens toujours partant pour une soirée
- Elisa pour m'avoir fait découvrir une partie de la culture du Mexique
- Marie encore une fois – et j'en profite pour qu'on se rappelle tous ensemble ce week end sympa après l'école d'hiver des Houches au ski chez toi !
- Thomas (Vezin) bien sûr que j'ai eu le plaisir d'avoir en collègue après celui de l'avoir en très bon ami. Partenaire scientifique de toujours (cf le PSC sur Tesla – spéciale dédicace à Martin au passage) et pourquoi pas partenaire scientifique pour toujours ?
- Arthur, Davide Regaldo, et tous les autres !

Je voudrais aussi remercier les gens avec qui j'ai fait des projets à côtés mais très importants à mes yeux :

- L'ImproveForce (et notamment Caterin)
- Gurleen pour cette intervention que nous avons co-organisée sur le Creative Thinking
- L'atelier FAQ-PV avec Stéphane et plein d'autres que j'ai déjà cité. Je suis très content d'avoir pu y participer car je crois que c'est un travail citoyen essentiel.

J'aimerais remercier le groupe des collègues de bureau proche spatialement et émotionnellement aussi – qui forme ce qu'on pourrait appeler "les vieux de l'IRDEP". L'IRDEP est un peu à l'IPVF ce ue le franc est à l'euro. Je pense bien sûr Valérie et Sophie et à nos mille discussions depuis ces trois ans. On a bien ri et on continuera ! Merci aussi à Thomas Vincent petit nouveau (depuis quand même des années) du bureau ! Je pense aussi aux squatteurs usuels – mangeurs de bonbons que sont Nathanaëlle et Damien.

Mais je n'ai pas fait que passer ma vie au travail et j'ai aussi puiser de l'inspiration auprès de mes amis de lycées et de prépa et d'école qui sont venus aujourd'hui. Je les remercie pour tout le fun qu'on a pu avoir ensemble !

Je remercie également mes trois principaux et principales colocs : Eric Antoine et Charlotte. Merci de ne pas avoir mangé ce que j'avais acheté pour le pot en avance. Merc à Antoine pour les trophées et félicitations pour le rendu de ton manuscrit. Je m'arrête là pour ne pas vriller trop mais je n'en pense pas moins. *A very convenient move.*

Merci aussi à ma famille et tout particulièrement à mes parents à qui je dois ma curiosité scientifique.

Enfin merci à Capucine.

Bonne lecture !

Acronyms

ADU	Analog Digital Unit (counts).
CTL	Charge transport layer.
CW	Continuous Wave.
GW	gate-width.
HI	Hyper-Spectral Imager.
IRF	instrument response function.
LGA	Large Gate Acquisition.
PL	Photo-luminescence.
PVK	Perovskite.
QFLS	Quasi Fermi Level Splitting.
ROI	Region of interest.
SIMPLED	SIMulated Photo-Luminescence Element Decomposition.
SNR	Signal over Noise Ratio.
SRH	Shocley-Read-Hall recombination.
SRV	Surface recombination velocity.
TR-FLIM	Time resolved fluorescence imaging.
TR-PL	Time resolved photo luminescence.
XPS	X-Ray Photo electron Spectroscopy.

Contents

Chapter 1

Introduction

> Sapience nentre point en ame malivole, et science sans conscience nest que ruyne de lame.
> *Wisdom entereth not into a malicious mind, and that knowledge without conscience is but the ruin of the soul*
>
> *Pantagruel*
> *François Rabelais, 1530*

Table of contents

1.1 What are solar cells and why do they matter today?

1.1.1 Why they matter today.

The scientific method is but a procedure that could be applied to *any* goal. But true scientists, on the other hand, "should focus their research for the good of mankind and for expanding the frontiers of scientific knowledge" according to the European Charter for Researchers.

Today, one of the main challenges for humanity is to reduce the global green-house gases emissions in order to lower the intensity of climate change which might have unprecedented consequences at the scale of mankind.

Every human activity transforms energy, from the movement of the body that turns chemical energy into heat and mechanical energy, to the use of electrical machines turning electric potential energy into motion. To sustain our current way of life, we have to find sources of energy. Sources of energy means matter or radiation that are not in equilibrium with their environment. Most of them are directly or indirectly coming from the sun (except for nuclear energy): oil, gas, coal and biomass come from photosynthesis, wind from temperature gradients in the atmosphere. The principle of solar panels is to harvest the flux of solar radiation and turn it directly into electrical potential energy.

Most of the reactions used today to convert energy emit green-house gases such as CO_2 or CH_4: the result is an increase of the greenhouse effect that causes, among others, an increase of the average temperature of the Earth. Reducing this carbon footprint is of tremendous importance. The intergovernmental panel on climate change (IPCC) intensely studies the effects and possible mitigation of the greenhouse gases emission. In one of their last report in April 2022 [IPCC 2022], they display Figure 1.1 that we reproduce here for convenience. These bars represent how much greenhouse gases humanity could spare each year by 2030 and *at what cost*. Solar energy is the second line (in terms of order) but the first in terms of potential with an approximate reduction of 4.5 $GtCO_2$-eq.year^{-1}, which represent a bit less than 10% of the total green house gas emission of 2019 at 59 $GtCO_2$-eq.year^{-1}. The color of the bar correspond to the cost: blue is low cost, while red is high cost. We observe that solar energy also presents the highest low cost potential of reduction for the year 2030.

The solar panels that will hopefully achieve this reduction by 2030 are not the ones subject to research today but

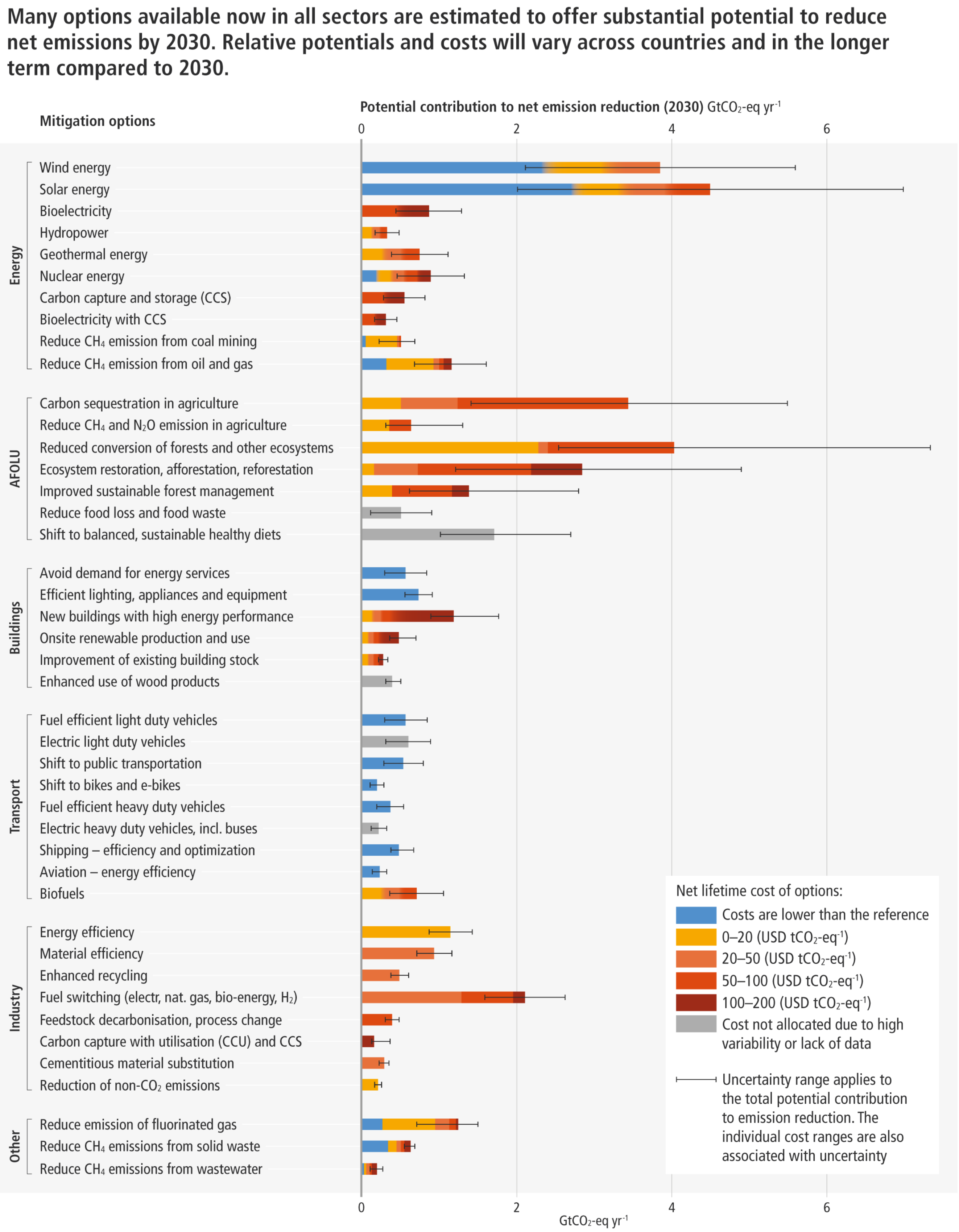

Many options available now in all sectors are estimated to offer substantial potential to reduce net emissions by 2030. Relative potentials and costs will vary across countries and in the longer term compared to 2030.

Figure 1.1: *Overview of mitigation options and their estimated ranges of costs and potentials in 2030. Reproduced from [IPCC 2022].*

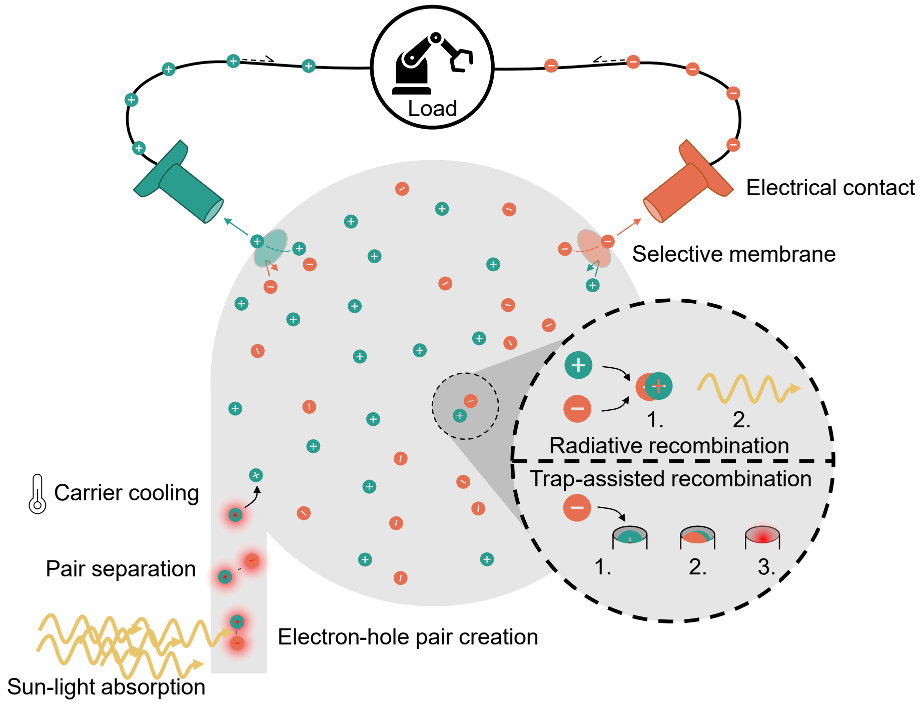

Figure 1.2: *Working principle of a solar cell. The main generation of excited carriers, recombination and extraction paths are displayed. Red gradients represent heat transferred to the lattice.*

the ones that were developed some years ago. The results achieved today come from the combination in the past of intense fundamental and industrial research. So why should we still research today on this? Two reasons appear: (i) to increase the total value of this bar; (ii) to increase the low cost (blue) share of the bar. Our work is among the fundamental research of today and aims at giving tools to characterize the future solar cells. To introduce how this work is integrated in the research effort to achieve these goals, we will first briefly discuss what a solar cell is, what limits its efficiency and with what kind of materials they are fabricated.

1.1.2 What is a solar cell?

A solar cell is a device able to convert radiation energy from the Sun into electrical energy. The working principles of such devices is illustrated in Figure 1.2. To obtain a solar cell, one requires some characteristics [Wurfel 2005]:

- First a material that absorbs sun light and transforms the incoming photons into electron-hole pairs. This is the absorption process.
- Second, transport of the carriers (electrons and holes)

to the electrodes is required;

- Last, membranes are needed, one letting electron flow out and one letting holes flow out, all the while blocking the other type of carriers. This is the extraction process.

There exist processes competing with extraction: namely **recombination**. This term designates the re-association of an electron and of a hole that therefore do not reach the membranes and do not participate to deliver energy to the load. The recombination process can happen via the emission of photons: this is a inevitable according to Kirchhoff's law of radiation. However, for most using cases this loss is negligible. Recombination may also happen via so called "defects" or "traps" in the material that are energy states where that favor the reunion of electrons and holes. This recombination channel is among the main loss mechanism for real devices compared to the maximal thermodynamic efficiency (see below).

A lot of possible designs are used to obtain these functionalities, and it is not the subject of the present study to describe all of them. The main type of materials used for as absorber are semiconductors. Most **semiconductors** are crystals, ie periodic arrays of atoms or molecules. In isolated atoms, the energy levels of electrons are discretized into orbital energies. If two atoms are put close one to the other, the energy levels accessible hybridize, ie a slightly higher and a slightly lower energy level result, see Figure 1.3. This effect comes from the coupling of energy states when atoms are close one to the other. The same principle applies to crystals where the closeness and number of atoms in the lattice leads to so many energy levels that they virtually become continuous. However, there may still exist gaps in the possible accessible energies. Semiconductors are the class of crystals for which the last occupied energy states of the electrons are close to a gap (called "the" bandgap) and for which the bandgap energy height E_g is of the order of 1 eV. The bandgap energy is therefore a characteristic of the spatial arrangements of the atoms/molecules inside the crystal and changes according to the inter-atomic distance.

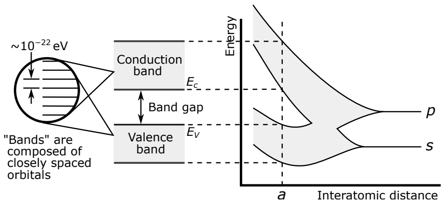

Figure 1.3: *Principle of band the apparition of band structures in solids. Reproduced from Wikipedia with CC-1 licence.*

What are the characteristics of a solar cell ?

The main characteristic of a solar cell is the I-V curve from which one can measure the power conversion efficiency, see Figure 1.4. From the I-V curve one can measure:

- The current density at short circuit, j_{sc} representative of the absorption and collection of the cell: better absorptance should produce higher j_{sc}.

- The voltage for which no current flows out of the device, named the open-circuit voltage V_{oc}
- The maximum power point (V_{MPP},J_{MPP}) for which the output power is maximal. This allows to define the power conversion efficiency PCE comparing the output power per unit surface to the incident power per unit surface coming from the Sun.
- The fill-factor, corresponding to the ratio of the maximum output power with the product $V_{oc}J_{sc}$.

We can make the following observation to obtain a good solar cell:

- absorption needs to be maximal
- the lifetime of carriers before recombination should also exceed the time it takes to extract them from the device
- the membranes should be as selective as possible

In the process of improving these three functions, (absorption, transport, extraction) one needs to probe specific figures of merit: the lifetime of carriers τ, the mobilities of the carriers inside the absorber $\mu_{e,h}$, the absorption coefficient α. An improvement of all of these parameters will lead to an improvement in power conversion efficiencies, but to what extent is subject to precise studies, for instance in [Kaienburg *et al.* 2020, Kirchartz and Rau 2018]. Let us just state that improving solar cells power conversion efficiency requires the measurement of the recombination and transport properties of the absorber and/or the cell.

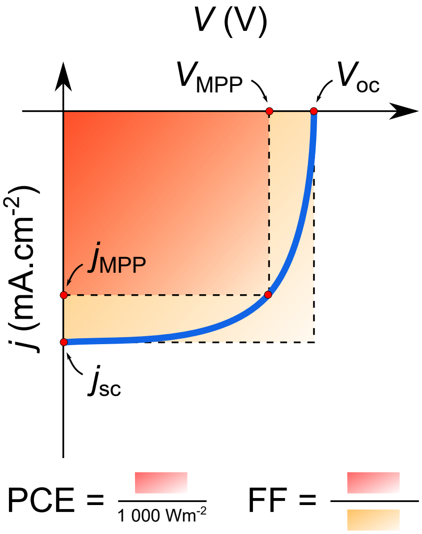

Figure 1.4: *Scheme of the definition of the electrical characteristics of the cell from its I-V curve in blue.*

What limits the PCE of solar cells?

For a precise description of the loss mechanisms, we refer to [Guillemoles *et al.* 2019]. The power conversion efficiency is limited for the "single-absorber-cold-carriers" design at around 30% depending on the bandgap energy of the material used for its realization. The model describing this limit is the Shockley Quiesser model, [Shockley and Queisser 1961]. The main loss mechanism is the thermalization of carriers or the non absorption of carriers, depicted in Figure 1.5. . This model does not take into account another source of loss : defects. The recombination is only radiative in the Shockley-Queisser model. Therefore, for real devices, the challenge is to have the lowest possible defect density in order to reach the maximal power conversion efficiency.

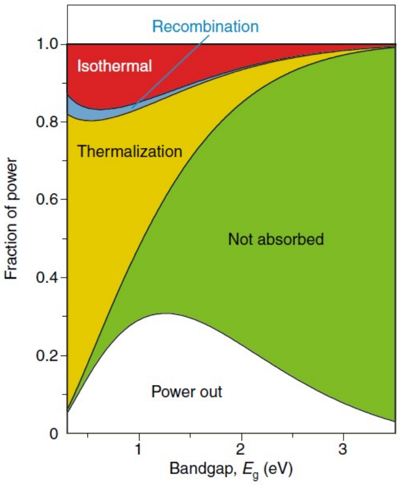

Figure 1.5: *Fraction of lost and output power as a function of bandgap in the Shockley Queisser model. Reproduced from [Guillemoles et al. 2019]*

With what type of material will we build solar cells tomorrow?

As evidenced in the very first section of this introduction, we need to increase the amount of energy converted from a given unit of surface. But as we briefly introduced: thermodynamics prevent us from converting approximately more than 30% of the incoming radiation in the simplest design possible. Today Silicon solar cells produced in the lab are close to the limit with PCE around 27% [NREL]. To push the limit further, one needs to change the design of solar cells.

To do so, one approach is the multi-junction approach. It consists in stacking solar cells: this technology is called tandem when there are two absorbers stacked one upon the other. This approach can combine two different absorbers with different bandgaps in order to absorb different parts of the spectrum. It is the current goal of IPVF but also of many research group in the world today to combine the very efficient and mature technology of Silicon solar cells to the emerging and promising technology of perovskite solar cells.

1.2 What are perovskite semiconductors?

Over the last decade, lead-halide perovskites solar cells have proved to be a serious candidate for reaching large scale photovoltaic (PV) solar energy conversion. They are a family of materials that crystallize in the perovskite structure ABX_3, with A a cation (such as Cesium), B a metal (such as Lead), and X an anion (such as Iodine), see Figure 1.6 where we indicate the usual species involved to form such material.

The first introduction of these materials as solar cells dates back to 2009 with the article of Miyasaka [Kojima *et al.* 2009], where they showed a 4%-efficiency solar cell based on methylammonium ($CH_3NH_3PbI_3^+$) lead halide perovskite or ($MAPbI_3$). Since then, many advances allowed for a variety of materials sharing the same structure to be developed. Today the record efficiency of single junction perovskite solar cell is at 25.6% [Jeong *et al.* 2021, NREL] for a formamidinium ($CH(NH_2)_2^+$) lead triiodide ($FAPbI_3$) absorber in the α phase.

Perovskite materials are not fabricated necessarily in a pure phase, meaning that the sites A, B and X are not necessarily occupied by only one species in the entire sample. Instead, the composition may alternate to have a propor-

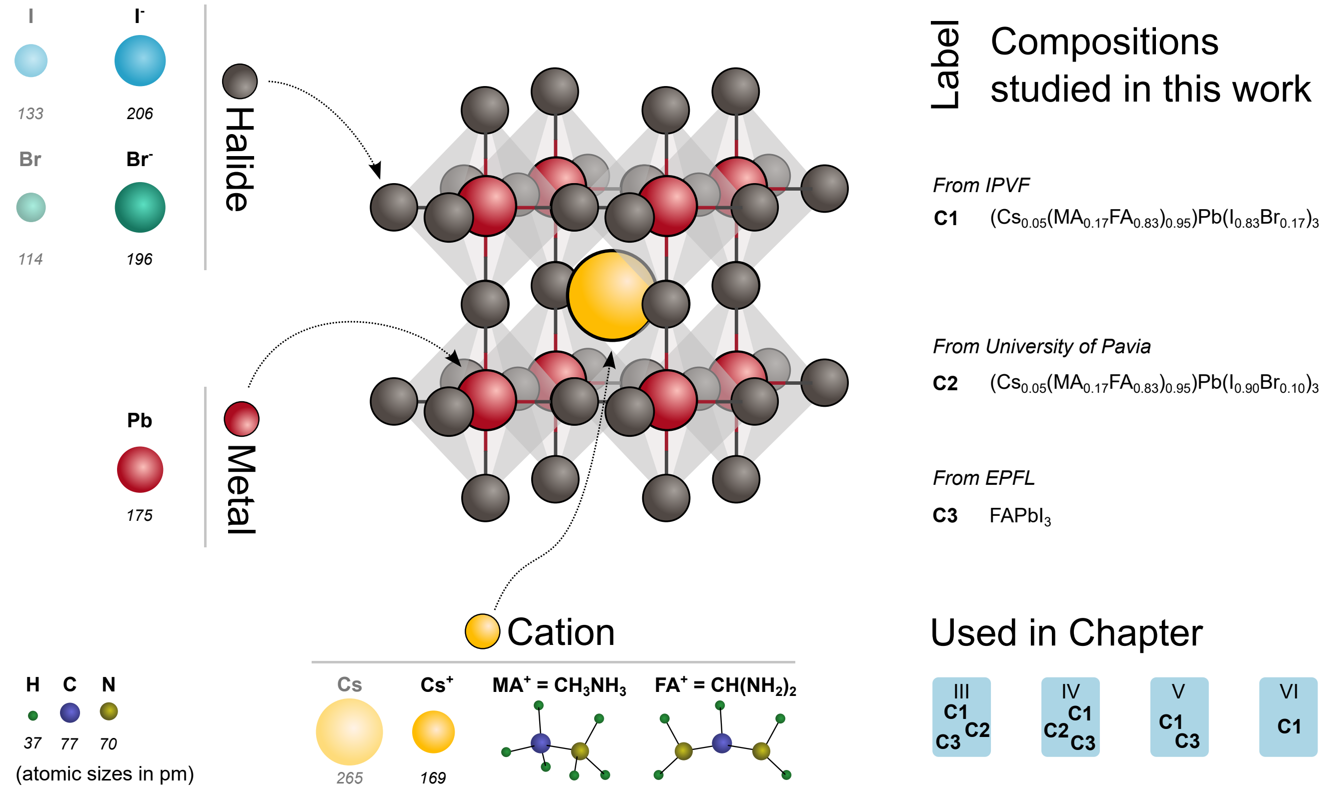

Figure 1.6: *Description of some of the elements forming the perovskite structure. The shaded atoms are the sizes of the atoms, while the ions or cations are in full color. The compositions used in this manuscript are depicted on the right, and we map them to the chapters they ares used in. Inspired from [Tennyson* et al. *2019].*

tion of unit cells with Br for some or I for others as the X position. They are also distinguished into two main categories: organic and inorganic ones, depending on whether they contain carbon, but again mixtures are possible like in the organic-inorganic class. One of the main features of perovskite materials is the ability to tune their bandgap by changing the "BX_3" atomic distribution [McMeekin *et al.* 2016]. For instance from $MAPbI_3$ with a bandgap of 1.53 eV to $MAPbBr_3$ with a bandgap of 2.3 eV, all compositions of the type $MAPb(I_{1-x}Br_x)_3$ give a continuum of accessible bandgaps, see Figure 1.7. [Hoke *et al.* 2014]

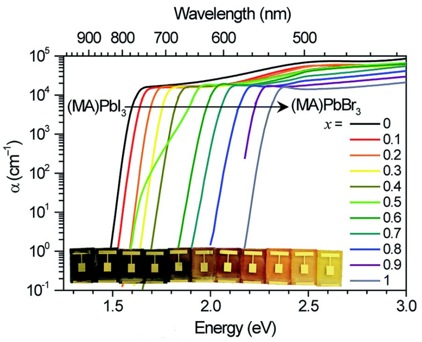

Figure 1.7: *Absorption coefficient measured for different compositions of the* $MAPb(I_{1-x}Br_x)_3$ *structure. Reproduced from [Hoke* et al. *2014]*

These materials hold a potential for large scale application because they are very easily produced. Contrary to Silicon based solar cells that require high purity materials, or III-V based technologies using high end technology such as Molecular Beam Epitaxy, perovskite materials can be made on a chemist' bench. Depositing them on surfaces via slot die coating or screen printing them is possible [Rong *et al.* 2018]. They also have potential to be the top cell of a tandem solar cell composed of a silicon based cell topped by a second cell made of perovskite: recently such a tandem cell reached 29.15% efficiency with a good stability over time [Al-Ashouri *et al.* 2020] and researcher from EPFL announced that they reached 31.25% for textured silicon-perovskite tandem (1 cm^2).

1.2.1 Properties

As explained in the previous section, a solar cell's efficiency is governed by its absorption, transport properties, carrier lifetime, and selectivity of the extracting layers [Rau and Kirchartz 2019].

Lead-halide perovskite absorbers show excellent absorption properties see Figure 1.4 for instance. The literature is quite rich and coherent on the high quality absorption of the perovskite layers [Sarritzu *et al.* 2018].

In comparison, the question of the transport properties of lead-halide perovskite is more debated today. The measurement of the carrier mobility (or diffusion coefficient) yields a wide range of values, even for a similar composition, when prepared by different labs [Herz 2017]. The role of photon-recycling in explaining the large diffusion length is a question today [Bercegol *et al.* 2019]. It was shown in our team that transport from the top to the bottom of the films after a photo-excitation close to the surface takes a few tens of nanoseconds [Bercegol *et al.* 2018]. Therefore, the role of diffusion needs to be thoroughly considered.

Defects and doping of perovskite layers are still under scrutiny today [Jin *et al.* 2020, Kiligaridis *et al.* 2021, Kumar *et al.* 2020, Motti *et al.* 2019]. A first question is: why are there so few photo-active defects in these very unpure layers and what are their nature? Indeed, the layers are mostly deposited from chemical solutions which are not nearly as pure as a silicon ingot. Perovskite layers seem to be "defect tolerant". In [Musiienko *et al.* 2021], at least 5 different defect states are found for the $MAPbI_3$ crystal and their energies in the bandgap are determined. Both shallow and deep defects are observed. What's more, when defects are characterized by observing the subbandgap absorption of the films, it is shown that iodide rich perovskite have the lowest static Urbach energy component among semiconductors [Kumar *et al.* 2020, Kaiser *et al.* 2021, Ledinsky *et al.* 2019, Ledinsky *et al.* 2020]. Moreover, the distinction between bulk and non bulk defects is still unclear today [Kumar *et al.* 2020]. Another key question is the difficulty to extrinsically dope the perovskite layer [Nayak *et al.* 2018].

The shallow defect could act as *de facto* dopants of the perovskite layers. Some studies suggested that the material perovskite are deposited on can affect their doping nature (from n-type to p-type) [Schulz *et al.* 2015]. Therefore the nature and opto-electronic impact of the defects in lead-halide perovskite layers is still a question today.

Selectivity at interfaces for perovskite layers is also under debate [Schulz *et al.* 2019, Wang *et al.* 2019c]. The optimal design for the interfaces band alignment in a full device is still questioned. The exact nature of the chemical and electronic interaction is also debated. The passivation strategies at interfaces are numerous: with the help of 2d perovskite layers [Cacovich *et al.* 2022b], self-assembled monolayer deposition, or with oxide layer encapsulation.

But lead halide perovskite also show specific behavior due to their physico/chemical nature. First they show a soft lattice structure [Rakita *et al.* 2015]. Second, perovskite layers are quite reactive with water, atmosphere elements and sunlight making their long term stability a key question today [Cacovich *et al.* 2020]. Moreover, self repair of the crystal after having reacted with light was evidenced [Ceratti *et al.* 2018]. Ion motion inside the lattice is also one of the unusual properties of lead halide perovskites [García-Batlle *et al.* 2021, Senocrate *et al.* 2018, Bertoluzzi *et al.* 2018]

1.2.2 Challenges

The upscale of the perovskite high performances to large areas remains an intense research focus today and is a key to the effective industrialization of such devices. Another key needed to unlock the full potential of perovskite solar cells is stability over time by encapsulation, to prevent reaction with the ambient and with the environment [Cacovich *et al.* 2020, Wang *et al.* 2019a]. These two key challenges are not within the scope of this manuscript. However, the techniques developed during this thesis, as well as the advanced modeling and characterization could be applied both to large scale devices and to ageing study.

In this thesis we studied the question of defects, transport and interfaces in lead-halide perovskite. The questions we tried to answer are linked to the spatial in-homogeneities of such defects, transport and interface properties. We used time resolved photo-luminescence imaging as a tool to obtain insight on these spatial distribution. To do so, we developed specific methods and tools. Before explaining the importance of photo-luminescence for characterization, we will briefly describe the main samples used throughout this manuscript.

1.2.3 The IPVF baseline

At IPVF, a structure of reference for the perovskite solar cell is defined, it is called "the baseline". The baseline is currently composed of ($Cs_{0.05}(MA_{0.17}FA_{0.83})_{0.95}Pb(Br_{0.17}I_{0.83})_3$) deposited with an excess of PbI_2. It has a bandgap of order of 1.6eV, compatible with high efficiency solar cells: the Shockley-Queisser limit is ≥30% for that bandgap [Shockley and Queisser 1961].

The basic structure of cells is described in Figure 1.8 with a layer of spin-coated perovskite deposited on a stack of FTO, TiO_2 mesoporous and compact. The TiO_2 acts as the membrane letting only (in theory) electrons pass to the conducting FTO, see Figure 1.2. On top of the perovskite is deposited a layer of Spiro-OMetad, acting as the hole selective membrane. The typical power conversion efficiencies obtained are in the range of 20%.

Figure 1.8: *Baseline IPVF solar cell architecture.*

1.2.4 The samples studied in this work

During this work, we had the chance to participate to two international collaborations. One with the group of Giulia Grancini at University of Pavia in Italy, the other with the group of Sándy Sanchez at Ecole polytechnique fédérale de Lausanne (EPFL) in Switzerland. Therefore, in this manuscript we use samples with mainly three different origins, as sketched in Figure 1.6:

1. Samples from IPVF are triple cation ($Cs_{0.05}(MA_{0.17}FA_{0.83})_{0.95}Pb(Br_{0.17}I_{0.83})_3$). Thin films on glass, half cells and full cells were studied, as precised in the corresponding section of the manuscript. See Appendix C.1 for more details.

2. Samples from a collaboration with Pavia University are triple cation ($Cs_{0.05}(MA_{0.17}FA_{0.83})_{0.95}Pb(Br_{0.10}I_{0.90})_3$). Some of the samples were "passivated" with the adjonction of phenylethylammonium (PEAI) doped with Fluorine or Chlorine. This collaboration with Giulia Grancini, Matteo Degani, Laxman Gouda and Yana Vaynzof. This collaboration lead to the following publication [Cacovich *et al.* 2022b] See Appendix C.2 for more details.

3. Samples from EPFL are $FAPbI_3$. The samples were flash annealed at different heating rates to study the

film's nucleation. They are from the group of Sandy Sánchez and Michael Graetzel. This collaboration lead to the following publication [Sánchez *et al.* 2022]. See Appendix C.3 for more details.

In Figure 1.6 we display in which chapter the samples are used.

1.3 Why does luminescence matter for solar cells?

As we saw, there are a number of questions on defects, transport and interfaces for lead-halide based devices. Luminescence is most indicated to study perovskite devices given their high absorption —and emission —of light. It allows to quantify key parameters that govern the solar cell efficiency: decay times, and transport properties. Moreover, the luminescence technique is contact-less: it can be used on all steps of the fabrication of the solar cell, before adding any electrical contact for instance. This allows to gain information on the physics happening at the different interfaces.

1.3.1 The importance of luminescence analysis for solar cells

Luminescence is the study of a material's **emitted** light. One could be puzzled at the fact that one studies the emitted light of a solar cell, which is supposed to be a good *absorber* and not *emitter* of light. The fundamental justification of using the emitted light as a tool to inspect absorbing materials is Kirchhoff'law of radiation. It states, in a simple form, that: at thermal equilibrium with a source, the absorptance and emittance of a body per angle and photon energy are equal [Wurfel 2005].

At equilibrium all absorbing materials are therefore emitting light when placed in contact with a radiative source at the same temperature. Now, questions can be asked on the use of this principle out of equilibrium, say when displaying a piece of absorbing material around 300K to a light source around 5800K such as the Sun's surface. One of the main assumptions is that the rate *constants* of equilibrium stay similar out of equilibrium (but not the rates themselves) [Wurfel 2005].

1.3.2 Types of luminescence

Many experiments use luminescence to probe properties of the absorbers. In most of them, an excess of carriers in the bands is obtained leading to an increase in luminescence from equilibrium. In **cathodo-luminescence** [Bidaud 2021], an incoming beam of electrons interacts with the material to create the extra carriers. In **electro-luminescence** [Ory *et al.* 2021], carriers are injected via the contacts, and in **photo-luminescence** they are promoted via the absorption of an incoming light flux. Virtually all of these techniques can be used in pulsed mode: in this case, the excitation is pulsed and the luminescence decay hence following is probed. In the rest, we will focus on **time-resolved photo-luminescence** (TR-PL).

1.3.3 Time-resolved photo-luminescence interpretation

The time-resolved photo-luminescence experiments consist in sending a light pulse to the sample and probing the luminescence intensity coming from the sample as a function of time. Using time-resolved measurement is a way of accessing different decay times of carriers inside the absorber. This method is common and was extensively used to study semiconductors, see the 1992 review by Ahrenkiel [Ahrenkiel 1992]. For most materials and laser powers, the luminescence decay shows a mono-exponential behavior allowing to fit one effective lifetime parameter quite precisely.

In the case of lead halide perovskites, the decay is usually not mono-exponential and therefore the question is asked: what information can one obtain from the TR-PL decay?

In the literature, two main methods are used to interpret TR-PL: one is based on phenomenological fitting of the decays, the other on the drift-diffusion model.

In the first case, fitting functions such as mono-exponential, bi-exponential [Son *et al.* 2016], stretched exponential [DeQuilettes *et al.* 2015, Yamada *et al.* 2017, Wang *et al.* 2019a], tri-exponential [Zhang *et al.* 2014] are arbitrarily chosen. The fit with these functions is often very close to the observed signal, but the fitted time constants and parameters need themselves to be interpreted. Indeed, if one fits two decay times τ_1 and τ_2 onto a decay: what do they mean? What can we conclude by comparing the τ_1s for different samples? The phenomenological methods have the great force to be easy to implement and fast to apply to experimental data, but the parameters given as an output are not easily interpreted.

Instead, the second method relies on the well known microscopic drift-diffusion model to describe the dynamics of carriers transport and recombination [Ahrenkiel and Lundstrom 1993, Baloch *et al.* 2018, Kirchartz *et al.* 2020, Maiberg and Scheer 2014, Trimpl *et al.* 2020, Bercegol *et al.* 2020]. The advantage of this model is its agility to be adapted to many situations: one can plug and play with different recombination models, include doping, include other moving species; for instance to investigate in-depth diffusion [Bercegol *et al.* 2018, Baloch *et al.* 2018] or photon recycling [Bercegol *et al.* 2019, Sridharan *et al.* 2021]. However, this interpretation method has multiple drawbacks. The first one is that the model contains a high number of parameters: this can lead to over fitting (can all the parameters be fitted on one curve?) and correlation in the fitted parameters (are the fitted parameters independent one from the other?). Moreover, the execution times can become very long rendering the analysis of images challenging.

All these interpretation methods are used on unique decays, or say tens of decays. But what can one say about a million decays? This is exactly the problem we face with time-resolved photo-luminescence imaging.

1.3.4 Time-resolved photo-luminescence imaging

With a time-resolved camera, one can obtain images at all times of the output PL decay, as sketched in Figure 1.9. Another option to obtain images is to scan the sample in the x-y plane and record one TR-PL decay for each position. In most research groups using this characterization method, scanning is performed and only a few groups use a TR-FLIM (Time resolved fluorescence imaging) camera.

In Figure 1.9 (a) we show our experimental setup that will be described precisely in the Methods Chapter 2. Its main components are: a pulsed light source, an objective lens and the TR-FLIM camera that is linked to a computer (not shown). The sample's emission follows the laser pulse as sketched in Figure 1.9 (c). Different regions can emit at different wavelengths and with different decays, as evidenced by the Region Of Interest (ROI) selection in Figure 1.9 (b). The result of the TR-FLIM acquisition is a ”data cube” composed of a stack of N images for N instants of time before and after the laser pulse as hit the sample. The TR-FLIM is not spectrally resolved, therefore as discussed below, we use bandpass filters to select the range of wavelengths that we want to observe.

Imaging time resolved photo-luminescence has a lot of potential as characterization tool for research and industrial ap-

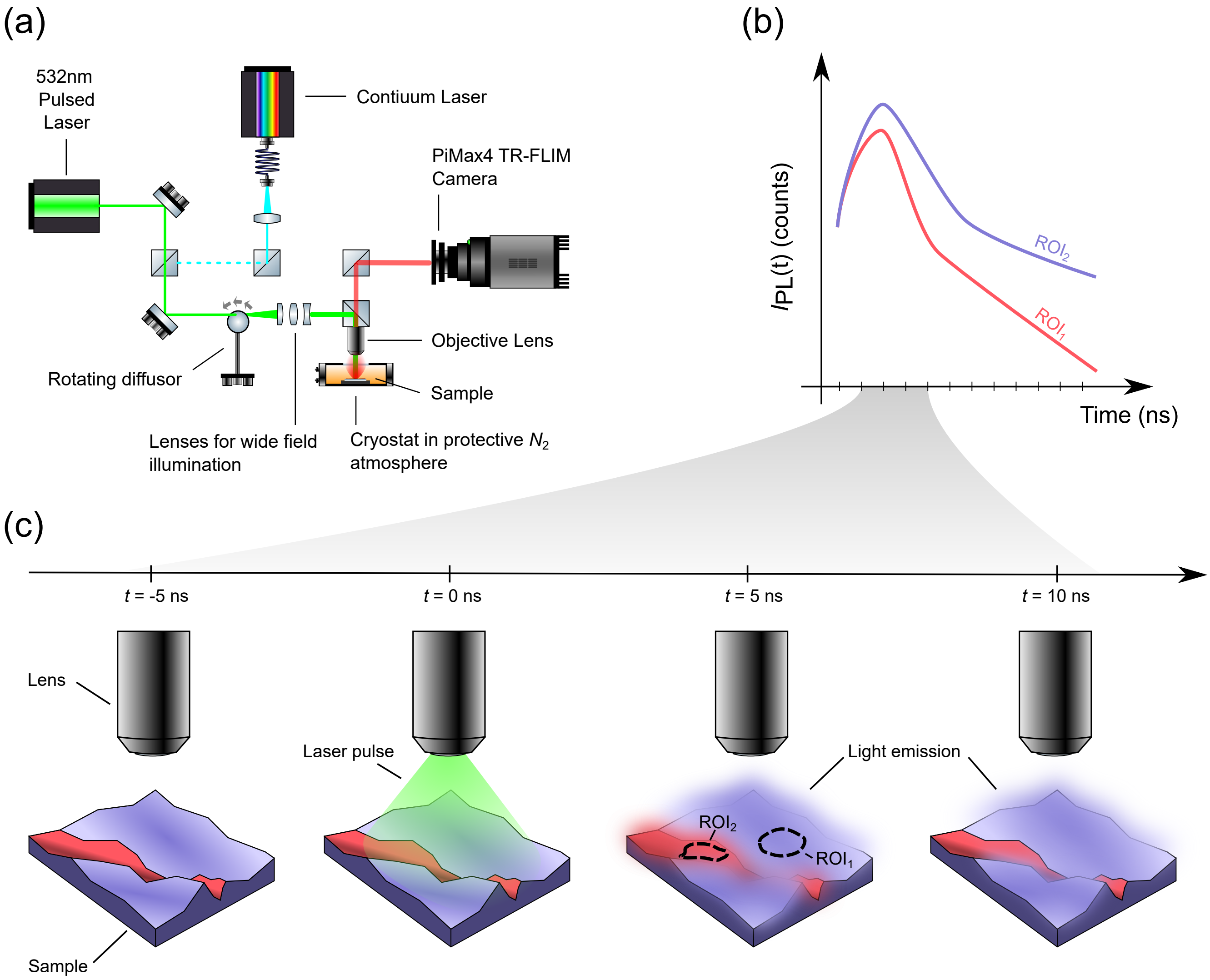

Figure 1.9: *TR-FLIM setup and principle. (a) Scheme of the experimental setup with the optical path displayed. (b) Scheme of the obtained average decays over two fictional regions of interest. (c) Scheme of a fictional sample (in fake colors) subject to the time resolved experiment.*

plication. If interpreted correctly, it provides images of the sample inhomogeneities without needing any electrical contact. But what type of inhomogeneity? This question is at the heart of the present work. Indeed, as we will evidence, comparing two decays (of two different pixels for instance) does not give instantaneous information on the state of non radiative recombination at these two locations. For instance the two regions might have different thicknesses, which, all things being equal, would lead to different decays. The ratio of surface to volume defects might also be different which complicates statements such as "region (x,y) has more recombination than region (x',y')". To our opinion, time resolved photo-luminescence imaging is a wonderful technique but the interpretation of the signal requires work. This manuscript hopefully contains some answers and details on exactly *what* work and *what conclusions* it can lead to.

1.4 This work

1.4.1 Main questions

In this work, our main focus was on the measurement and interpretation of time resolved photo-luminescence imaging on perovskite devices. Hence the provocative title of this thesis: **"Why does the decay decay?"**. It is not a metaphysical "why?", tackling the general notion of decay —or its parent notion of time, see [Henri Bergson 1889]. The question "why?" is intended here as "what causes the decay?" and from there "what type of information does the decay hold?". Our main task has been to develop methods to answer key questions on the most intriguing materials for PV today: perovskite absorbers and with the tools at our disposal, mainly the time resolved photo-luminescence imaging setup. Key questions we wanted to find answers to are:

- **Question 0.** Transport modifies the carriers distribution. How exactly does transport affect the decay compared to recombination?
- **Question 1.** How many defects are there in a given perovskite layer, what is their nature, and how are they spatially distributed across the sample?
- **Question 2.** How are the defects distributed in the thickness of the perovskite layer: are they more surface or bulk defects?
- **Question 3.** How doped are the perovskite layers and how are the dopant distributed on the samples?
- **Question 4.** Is charge extraction homogeneous on a full device sample? If not what are the spatial inhomogeneities of extraction?

All these question are intrinsically linked with *imaging*. Imaging represents a challenge because of the size of the datasets acquired, but also an opportunity today with the immense research effort towards tackling large datasets in the computer science community. For instance we participated in a collaboration with INRIA and the team of Jean-Christophe

Pesquet (see [Marnissi *et al.* 2017] for an example of their research on regularization functions for imaging applications). Therefore, we oriented our research towards imaging applications.

To answer these questions, we used sample obtained with two other collaborations, as mentioned above: one with Giulia Grancini (University of Pavia) and one with Sandy Sánchez (EPFL).

1.4.2 Main results and outline

In the following we will give the state of our research in answering the previously stated questions.

- **Chapter 2** gives the Methods and Models already known in the literature and relevant to this manuscript. We present the drift diffusion model and some defect models. We explain the modeling methods and codes developed to reach better simulation and better experimentation. We also present the extensive work of characterization of the TR-FLIM camera that lead to: (i) a precise understanding of its noise, (ii) a temporal super-resolution method and (iii) to its absolute calibration.

- **Chapter 3**'s main focus is on the phenomenological interpretation of TR-FLIM datacube: we show methods to answer **Question 0 and 1** above. We introduce a contribution plot for the decay (SIMPLED) that attributes the decay to its causes. We then discuss the notion of "lifetime" and show that it is ill defined. We discuss the comparison between images of decay time obtained in the time resolved experiment and images of Quasi Fermi Level Splitting obtained in the continuous wave experiment. We perform this analysis on the exact same position and show a clear correlation that is compatible with a simple model. This technique could lead to the measurement of the intrinsic carrier density n_i. We apply phenomenological interpretation to two datasets: (i) a series of triple cation devices from Pavia University with an cation that acts as a an homogeneous passivating layer, and (ii) the study of $FAPbI_3$ inhomogeneous layers from EPFL for which we discuss that thickness differences alone cannot explain the difference of observed decay time.

- **Chapter 4** is dedicated to giving more precise answers to **Question 1** and **Question 3** by studying the impact of the laser fluence on the observed decay. First we show that most of the perovskite layers we measured exhibit decays compatible with the drift-diffusion model. This allows to extract parameters via drift-diffusion fitting on decays averaged spatially. Then, we introduce a new method we developed based on the drift-diffusion model approximated *at short time*, that is usable on imaging datasets. We describe how the model is obtained, and show the application to the study of the triple cation baseline of IPVF. We obtain (i) a *non-radiative recombination map* that we assume is mainly surface recombination and (ii) a measure of the external radiative recombination coefficient of the layer. Finally, we investigate *doping* of the perovskite layers by showing the scaling of the initial absolute PL intensity at the beginning of the decay as a function of fluence. We evidence that the observed perovskite layers show low doping ($\leq 1 \times 10^{15}\,\mathrm{cm}^{-3}$). We apply this method locally on the imaging datasets and evidence spatial inhomogeneity of the dopant for the $\mathrm{FAPbI_3}$ samples, while most of the triple cation perovskite samples are homogeneous.

- **Chapter 5** is entirely devoted to **Question 2**; How are the defects distributed spatially? We discuss the interest of answering this question and then describe two methods to answer it. One was developed by us, and is also based on the observation of short-time dynamics, the other was adapted by us from the literature. We first show the application of our method on a "non-imaged" dataset. Then, we apply both methods to the study of defects resulting from X-Ray exposure of triple cation perovskite thin films during the XPS analysis. Both methods are applied locally and give the same interpretation: X-Rays induced bulk defects rather than surface defects.

- **Chapter 6** is a prospective chapter tackling the interpretation of decays on half-cells and full-cells, ie **Question 4**. This chapter does not give a definitive answer as on *how* to obtain images of extraction parameters from TR-FLIM acquisitions but rather gives clues on *where* to look. We show three approaches: one is based on a step by step observation of the cell's construction (from the thin film, to the half cells to the full cell). We evidence that extraction parameters are expected to play a role at low fluence, but that this fluence regime is exactly the one where defects/dopants of the perovskite also alter the recombination dynamics. The second approach consists in studying decays as a function of the applied bias. We show that, as expected in the literature, decays are modified after the application of a bias, but that this effect changes at the scale of the minute, presumably due to ion motion. The experimental procedure we use could be developed and might be a way to image ion motion. Finally we briefly discuss the approach of sending pulses of bias to study the samples.

Chapter 2

Methods and tools

This work relies on theoretical, experimental and numerical tools that are described in this chapter. The aim is to present the tools, their opportunities and their limits. Pre-existing tools will be briefly introduced but we will focus on new tools developed over the course of this work. As this thesis is in the branch of characterization and modeling, some of our *results* are *themselves* techniques and tools. For instance we developed a new way to perform decay time imaging (shown in Chapter 3) or a new interpretation model for the initial derivative of the decays (shown in Chapter 4). These methods and tools are part of the *results* chapters of this thesis.

The **theoretical models** we used are firstly described. They mainly concern luminescence and transport of semiconductors: the generalized Planck's law and the drift-diffusion model. We mention their main hypothesis and origin as well as example use cases. Their limits are also briefly discussed. These models are the first corner stone of this work.

The second corner stone of our work is the **experimental setup**. We will show how we unlocked three major experimental tools. One is the super-resolved temporal acquisition which allows to observe short timescales with a high temporal precision. The second is the absolute calibration of the camera which allows to put on a unique scale of intensity *any* acquisition obtained with *any* set of parameters. The last one is a statistical description of the noise of the camera: this allows to predict the signal over noise ratio only by observing the average signal. This work was new to the lab and allowed us to develop long-time acquisitions as well as new decay-time-imaging techniques.

The last cornerstone are **numerical techniques**. We made numerous use of the extraordinary abilities that computing machine bring to the world. Among the new tools we developed during this work are: a **data-observation software** to check the acquired experimental data *live* in the lab

; a suite of **automation software** for the experiments that allowed for new types of experiments to be conducted; a suite of **simulation and fitting** code based on the drift diffusion model.

Table of contents

2.1 Theoretical models

In this subsection, we introduce the main models use to describe the luminescence of the semiconductors under study during this thesis.

2.1.1 Semiconductors and light

A quantum interaction is possible between the crystalline lattice of semiconductors and photons. Actually one needs to distinguish the *external photoelectric effect* —described theoretically by Einstein in 1905 with the definition of Planck's quantum of energy, where a photon extracts one electron out of the sample, and the*photovoltaic effect* where electrons are not ejected out of the material. Photons with high enough energy may excite electrons from a low energy state to a high energy state —provided it exists and is empty. The reverse process is also possible: a high energy electron may release its excess energy under the form of a photon. This process is called *spontaneous emission*. Stimulated emission was also predicted by Einstein. **Absorption and emission of light by semiconductors are the main physical processes used in this thesis.**

In the dark and at thermal equilibrium, the states occupied by the electrons follow a Fermi-Dirac distribution:

$$f(\epsilon) = \frac{1}{\exp\left(\frac{\epsilon-\mu}{kT}\right)+1} \tag{2.1}$$

with:

$f(\epsilon)$ = The occupation factor for states of energy ϵ
μ = The Fermi Level (eV)
k = Boltzmann constant (J.K^{-1})
T = Temperature of the equilibrium (K)

The Fermi level at equilibrium describes the chemical potential of electrons in the device. By definition, **at equilibrium the Fermi level is the same for electrons and holes everywhere in the device**. However, in a complex device where many materials may be put in contact, the difference between the Fermi Level and the conduction band edge $\mu - E_c$ may have very different local values.

Planck's law of radiation in the continuous regime

Let us consider a piece of semiconductor subject to sunlight —ie a continuous (temporally) and spectrally-large source of photons. Some of the incoming photons have high enough energy to be absorbed by the semiconductor: those with an energy higher than the bandgap of the semiconductor. An absorbed photon excites one electron-hole pair. For perovskite materials, this electron-hole pair will quickly dissociate [Miyata *et al.* 2015] at room temperature, leading to a free electron and a free hole in their respective bands. The excess energy of these particles will be transferred to the lattice via phonons, heating up the sample. Quickly (on a time scale of typically less than 100 ps) a population of holes and a population of electrons in quasi equilibrium with the lattice are formed [Guillemoles *et al.* 2019]. It is a *quasi*-equilibrium because electrons and holes are not at equilibrium one with the other. However, each of the population can be described by a temperature and by a *quasi* Fermi-Level energy following a Fermi-Dirac distribution in energy. We note μ_e and μ_h these quasi-Fermi levels.

In this case, the difference of chemical potential between these two population is noted $\Delta\mu = \mu_e - \mu_h$ and called Quasi Fermi Level Splitting or QFLS. We introduce the density of

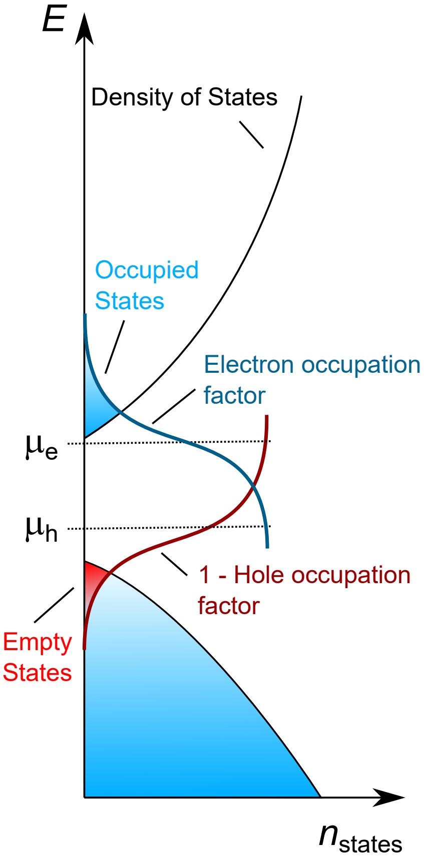

Figure 2.1: *Definition of the quasi Fermi Levels out of thermal equilibrium.*

electrons $n_e(z,t)$ and of holes $n_h(z,t)$ with z representing spatial dimensions (possibly only one) and t time. We have the following relation between the densities and the QFLS:

$$n_e(z,t) \times n_h(z,t) = n_i^2 \exp\left(\frac{\Delta\mu(z,t)}{kT}\right) \tag{2.2}$$

Therefore the QFLS represents the product of the densities of excited electrons and holes, **the QFLS is a measure of carrier density**. For reasons that are well above the scope of this work, the QFLS $\Delta\mu$, is also the **maximal work** that could be extracted out of one electron and one hole of a photovoltaic cell built upon this semiconductor as absorber. The maximal voltage possible observed at the electrodes would be $\Delta\mu/q$. The QFLS may be measured by means of photoluminescence —even without electrodes on the absorber, as explained in the next paragraph.

The radiation of a black body with excited electrons described by a Fermi distribution follows Planck's law of radiation—where the two main ingredients are the photon density of states and the Fermi thermal distribution of electrons. A semiconductor is not a black body, but rather a gray-body that does not absorb all incoming light. Würfel showed [Würfel *et al.* 1995] that the emission of such semiconductor follows a law close to Planck's law, that he called "the generalized Planck's law". Two more ingredients are needed: the energy-dependant-absorptivity of the material $A(E)$ and the quasi Fermi level splitting $\Delta\mu$. The crystal will emit luminescence according to the *generalized* Planck's law of radiation.

Statement 2.1.1. Generalized Planck's law. The number of emitted photons within energy E and $E + dE$, per second, by a surface dS in the direction Ω with an angle θ up to the normal of the surface and within the solid angle $d\Omega$ is:

$$\phi(E,\Omega) = \frac{A(E,\Omega)}{\pi^3\hbar^3c^2} \times \frac{E^2}{\exp\left(\frac{E-\Delta\mu}{kT}\right) - 1} \times \cos\theta d\Omega dE dS \tag{2.3}$$

with

$A(E,\Omega)$ = The absorptivity of the material. Without unit and between 0 and 1. Strongly depends on the bandgap energy E_g.
$\hbar$ = Reduced Planck's constant
c = Vacuum velocity of light
$\Delta\mu$ = Quasi-Fermi Level Splitting (QFLS) $\Delta\mu = \mu_e - \mu_h$ in (eV)

Usually we are in the case where $\Delta\mu \gg kT$. In this case one can approximate the generalized Planck's law of radiation by : [Wurfel 2005]

$$\phi(E,\Omega) \approx \exp\left(\frac{\Delta\mu}{kT}\right)\frac{A(E,\Omega)}{\pi^3\hbar^3c^2} \times \frac{E^2}{\exp\left(\frac{E}{kT}\right)} \times \cos\theta d\Omega dE dS \tag{2.4}$$

The number of photons emitted, ie the number of radiative recombination, therefore scales proportionally to $\exp\left(\frac{\Delta\mu}{kT}\right)$. We see that the higher the QFLS is, the more intense the luminescence is as well. This means that in the continuous quasi equilibrium regime:

$$\underbrace{R_{\text{rad}}(z,t)}_{\substack{\text{Number of radiative recombination}\\ \text{recombination events per s per cm}^3}} \propto n_e(z,t)n_h(z,t) \tag{2.5}$$

This proportionality will be at the heart of our model for the photo-luminescence. It can also be understood from a probabilistic point of view: to have a photon emission process one needs to have a electron in the conduction band and a empty state in the valence band ie a hole. Therefore the probability of emission in a small volume dV located at position z will be proportional to the product of the probability of having $n_e(z)dV$ electrons and $n_h(z)dV$ holes in this small volume.

We therefore sketched the models describing the following:

Statement 2.1.2. Kirchhoff's law of radiation A semiconductor that absorbs photons emits photons. The emitted photons bring the signature of their emission context: their energy distribution informs on the bandgap E_g of the material while their number is proportional to the exponential of the Quasi Fermi Level Splitting (QFLS) $\Delta\mu$ over kT, that is a proxy for the product of the densities of electrons and holes inside the material.

In this work, we use the output photons to indirectly measure the densities of carrier inside the devices under study. But let's consider that we measure a *low* QFLS that corresponds to *low* carrier densities: how can we know if it is due to poor absorption or to non radiative recombination via defects? This is where the time-dependent pulsed experiment comes useful.

2.1.2 The drift-diffusion model

Let us now consider the following problem: one sends a light pulse onto the semiconductor under study. What will be the spatio-temporal response of the carrier densities? And what will the temporal response of the emitted photo-luminescence be? Can we effectively distinguish poor absorption from high defect density?

Hypothesis leading to the drift-diffusion model

The drift-diffusion model may be obtained from Boltzmann transport equations by considering electrons and holes as gases of particles subject to forces (Electrical field), to random motion (Diffusion) as well as to generation and recombination. The drift diffusion equation is an example of convection-diffusion equations. The drift-diffusion equation describes both the transport and the recombination of carriers. It links the time derivative of the free electrons and holes densities n_e and n_h in a small volume dV to the possible input and output currents in and out of this small volume, as well as the recombination and generation of charges that could occur. It is compatible with the consideration of a conservation law for charge carriers considered as localized free particles in a gas rather than delocalized plane waves in a complex energetic landscape.

We will consider the spatial variations mainly in the thickness of the layer, ie along z, see Figure 2.2. A reason for this is that the application we will make of the drift-diffusion model will not require lateral considerations: either because we will average the signal spatially or because the scale of the pixels in the observed is much greater than the diffusion length of the samples under study.

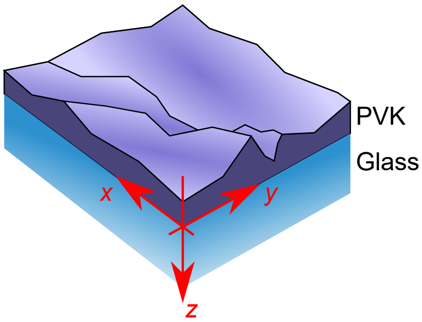

Figure 2.2: *Definition of the axis.*

The model

We consider that the carrier densities are such that they have some value in the dark $n_{0,e}$ and $n_{0,h}$. Due to the laser pulse, they will have an extra density $\Delta n_e(z,t)$ so that

$$n_e(z,t) = n_{0,e}(z) + \Delta n_e(z,t) \tag{2.6}$$

And a similar expression for holes.

Statement 2.1.3. The drift diffusion equations for electrons and holes may be written in this form (written here for electrons):

$$\underbrace{\frac{\partial \Delta n_e}{\partial t}(z,t)}_{\substack{\text{Local}\\\text{variation of density}}} + \underbrace{\vec{\nabla}.\vec{j_e}(z,t)}_{\substack{\text{Balance of currents}\\\text{in and out}}} = \underbrace{G_e(z,t) - R_e(z,t)}_{\substack{\text{Balance of } \textit{generation}\\\text{and } \textit{recombination}}} \tag{2.7}$$

with

Δn_e = the excess carrier density in $/\mathrm{cm}^3$
$\vec{\nabla}$ = the divergence operator in cm^{-1}
$.$ = the scalar product
$\vec{j_e}$ = the local current of electrons in $/\mathrm{cm}^2/\mathrm{s}$
R_e = local recombination rate in $/\mathrm{cm}^3/\mathrm{s}$
G_e = local generation rate in $/\mathrm{cm}^3/\mathrm{s}$

This equation is a partial differential equation that requires correct boundary conditions for Δn_e and or its derivatives at the edges of the spatio-temporal domain. We will give examples of these below. If we model how the currents, recombination and generation functions depend on Δn_e and on extra parameters, we may then solve the drift-diffusion Equation (2.7). But in general, solving the drift-diffusion analytically is impossible due to the non linearity of the radiative recombination term in Δn_e in Equation (2.5).

Currents

The main considered currents are Diffusion and Drift, that correspond to the two aspects behind the electrochemical potential $\eta_e = \mu_e - q\phi$ and $\eta_h = \mu_h + q\phi$ with q the (positive) elemental charge. This reasoning follows the thorough explanation given in Würfel's book [Wurfel 2005]. In general the currents are expressed as:

$$\underbrace{\vec{j_e}(z,t)}_{\substack{\text{Particle current}\\ \text{in } cm^{-2}s^{-1}}} = -D_e\vec{\nabla}n_e(z,t) - b_e n_e(z,t)\vec{E}(z,t) \tag{2.8}$$

with

j_e = the particle current of electrons in $cm^{-2}s^{-1}$
D_e = the diffusion coefficient of electrons in cm^2s^{-1}
b_e = the mobility of electrons in $cm^2s^{-1}V^{-1}$
$\vec{E}$ = the local electric field Vcm^{-1}

For holes, the equation is (notice the plus sign):

$$\vec{j_h}(z,t) = -D_h\vec{\nabla}n_h(z,t) + b_h n_h(z,t)\vec{E}(z,t) \tag{2.9}$$

The physical interpretation is the following : all particles will flee zones that are too crowded (diffusion via Fick's law) and particle will separate under the effect of an applied electric field. Moreover, this charge separation can screen the applied electric field.

Radiative Recombination

Recombination is the process by which an excited electron falls back into the valence band, and thus annihilates a hole.

For a perfect material, crossing the bandgap is only allowed via radiative recombination, ie emission of a photon of energy higher than the bandbap —with a distribution of probability given by the generalized Planck's law. One radiative recombination requires one hole and one electron. As discussed above, the internal radiative recombination rate is therefore:

$$R_{\text{rad}}(z,t) = k_2 n_e(z,t) n_h(z,t) \approx k_2 \Delta n_e(z,t) \Delta n_h(z,t) \quad (2.10)$$

With k_2 the radiative recombination coefficient in $cm^3 s^{-1}$. The approximation is valid when $\Delta n \gg n_0$. Let us state that if the material is doped, say n-doped, then $n_{0,e} = N_D$ the donor density, and the approximation fails for most excitation intensities.

From the definition of the internal radiative recombination rate, we can define the external PL intensity received by the detector at time t as (see Figure 2.3):

$$I_{\text{PL}}(t) = A \times \int_0^L \Delta n^2(z', t)\, dz' \quad (2.11)$$

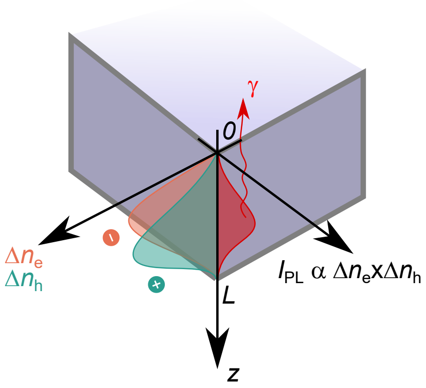

Figure 2.3: *Scheme of the definition of PL intensity from the carrier densities in thickness.*

with A being a proportionality factor that describes the precise losses and geometry of the measurement setup, and z the position in thickness. Here, we neglected self-absorption by the layer.

Non-Radiative Recombination

Materials are far from perfect and there may exist available states inside the bandgap called trap states. Such recombination via traps, are called Shockley-Read-Hall (SRH) recombination [Shockley and Read 1952, Hall 1952]. We will recall here the main notations of this model. We will also sketch the arguments of why one does not need to model the time dependence of the defect occupation factor.

If we consider a trap with energy E_t, density N_t occupation factor $f_e(t) \in [0,1]$ for electrons in this defect. The density of electrons in the defect at any time is $f_e N_t$. From consideration at thermal equilibrium, one can show that the rates of transition from the defects to the bands are (see Figure 2.4):

$$\begin{cases} j_{CB\to t} = & \sigma_e v_{\text{th}} \times \underbrace{N_t\left(1-f_e\right)}_{\text{Empty defects}} \times \underbrace{n_e}_{\text{Init. State}} \\ j_{t\to CB} = & \sigma_e v_{\text{th}} \times \underbrace{e^{-\frac{E_c-E_t}{\text{kT}}}}_{\text{Energy price}} \times \underbrace{N_c}_{\substack{\text{Empty states}\\ \text{in CB}}} \times \underbrace{N_t f_e}_{\text{Init. State}} \\ j^h_{t\to VB} = & \sigma_h v^h_{\text{th}} \times \underbrace{e^{-\frac{E_t-E_v}{\text{kT}}}}_{\text{Energy price}} \times \underbrace{N_v}_{\substack{\text{Empty states}\\ \text{in VB}}} \times \underbrace{N_t\left(1-f_e\right)}_{\text{Init. State}} \\ j^h_{VB\to t} = & \sigma_h v^h_{\text{th}} \times \underbrace{N_t f_e}_{\substack{\text{Defects without}\\ \text{holes}}} \times \underbrace{n_h}_{\text{Init. State}} \end{cases} \tag{2.12}$$

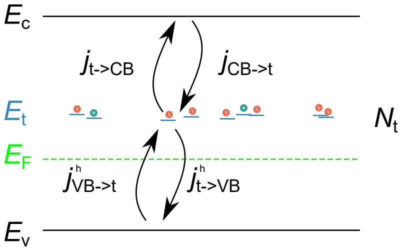

Figure 2.4: *Definition of the recombination currents in the band diagram.*

with

$j_{CB\to t}$ = the particle transfer of electrons from the conduction band to the defect in $cm^{-3}s^{-1}$
$j_{t\to CB}$ = the particle transfer of electrons from the conduction band to the defect in $cm^{-3}s^{-1}$
$j^h_{VB\to t}$ = the particle transfer of holes from the valence band to the defect in $cm^{-3}s^{-1}$
$j^h_{t\to VB}$ = the particle transfer of holes from the valence band to the defect in $cm^{-3}s^{-1}$
$\sigma_{e,h}$ = capture cross sections of the defect for electrons or holes in cm^2
v_{th} = thermal velocity of electrons or holes in $cm.s^{-1}$
N_t = the density of defects in cm^{-3}

These equation are under the hypothesis that the occupation factor of electrons in the conduction band and of holes in the valence band are $\ll 1$, which is verified as long as their quasi Fermi Levels μ_e and μ_h are away from their band edges of more than a few kT. To simplify the discussion, here we do not consider spatial variations (or consider only local transitions). In this case, one needs to solve the coupled equations:

$$\begin{cases} \dfrac{dn_e}{\text{dt}} = & j_{t\to CB} - j_{CB\to t} \\ N_t\dfrac{df_e}{\text{dt}} = & \left(j_{CB\to t} - j_{t\to CB}\right) - \left(j_{VB\to t} - j_{t\to VB}\right) \\ \dfrac{dn_h}{\text{dt}} = & j_{t\to VB} - j_{VB\to t} \end{cases} \tag{2.13}$$

We solve this system numerically in the Appendix D and prove the following:

Statement 2.1.4. For most deep energy of the defects, more than a few kT away from both bands, the occupation factor for the traps quickly (<100ps) reaches a quasi equilibrium value. This justifies a simplification of the equations and the elimination of the time dependence of f_e. In this case, just after laser absorption:

$$f_e^a \approx \frac{1}{1 + \frac{\sigma_h v_{\text{th}}^h}{\sigma_e v_{\text{th}}^e} \times \frac{n_h^0}{n_e^0}} \tag{2.14}$$

The rate equations simplify greatly and only the defect acts as a recombination center that attracts electrons and holes with the following rates:

$$\frac{dn_e}{\text{dt}} \approx -\frac{\frac{n_h^0}{n_e^0}}{\frac{1}{N_t \sigma_h v_{\text{th}}^h} + \frac{1}{N_t \sigma_e v_{\text{th}}^e} \times \frac{n_h^0}{n_e^0}} n_e \tag{2.15}$$

$$\frac{dn_h}{\text{dt}} \approx -\frac{1}{\frac{1}{N_t \sigma_h v_{\text{th}}^h} + \frac{1}{N_t \sigma_e v_{\text{th}}^e} \times \frac{n_h^0}{n_e^0}} n_h \tag{2.16}$$

with

$\sigma_{e,h}$ = capture cross sections of the defect for electrons or holes in cm^2
$v_{\text{th}}^{e,h}$ = thermal velocity of electrons or holes in $cm.s^{-1}$
N_t = the density of defects in cm^{-3}
$n_{e,h}^0$ = the density of electrons and holes just after absorption of the laser pulse in cm^{-3}

These rates may be further simplified by assuming high enough excitation intensity so that $n_h^0/n_e^0 = 1$.

Therefore, the impact of defects may be modeled in the simplified manner:

Statement 2.1.5. Simplified version of **transient** trap assisted recombination via a deep defect (SRH). In the high excitation case, both electron and holes decay with the same rate defined by:

$$\frac{dn_{e,h}}{\text{dt}} \approx -\underbrace{\frac{1}{\tau_h + \tau_e}}_{\equiv k_1} + n_{e,h} \tag{2.17}$$

with:

$$(\tau_{e,h})^{-1} = \underbrace{N_t}_{\substack{\text{Defect}\\\text{density}}} \times \underbrace{\sigma_{e,h}}_{\substack{\text{Capture}\\\text{cross sections}}} \times \underbrace{v_{\text{th}}^{e,h}}_{\substack{\text{Thermal}\\\text{velocity}}} \tag{2.18}$$

k_1 as the unit of an inverse of time

This approximation, obtain in the transient regime is close to what is obtained in the continuous regime [Wurfel 2005]:

Statement 2.1.6. Recombination via a defect (SRH) in the **continuous** regime. Both electron and holes decay with the same rate defined by:

$$\frac{dn_{e,h}}{\text{dt}} \approx -\frac{n_e n_h - n_i^2}{\tau_h\left(n_e + N_c e^{-(E_c-E_t)/kT}\right) + \tau_e\left(n_h + N_v e^{-(E_t-E_c)/kT}\right)} \tag{2.19}$$

with:

$$(\tau_{e,h})^{-1} = \underbrace{N_t}_{\substack{\text{Defect}\\\text{density}}} \times \underbrace{\sigma_{e,h}}_{\substack{\text{Capture}\\\text{cross sections}}} \times \underbrace{v_{\text{th}}^{e,h}}_{\substack{\text{Thermal}\\\text{velocity}}} \tag{2.20}$$

k_1 as the unit of an inverse of time

Auger recombination was not considered as it is relevant only at very high carrier densities $> 10^{17}\text{cm}^{-3}$, at least for MAPbI_3 perovskites [Handa *et al.* 2017], and was not found necessary in the present study.

Generation

Generation of free charges is the concept of excitation of electrons as an effect of photon absorption as described above. Two main concepts need to be taken into account: the spatial dependence of absorption following an exponentially decreasing behavior in thickness according to Beer-Lambert's law, see Figure 2.5, and the temporal aspect of generation.

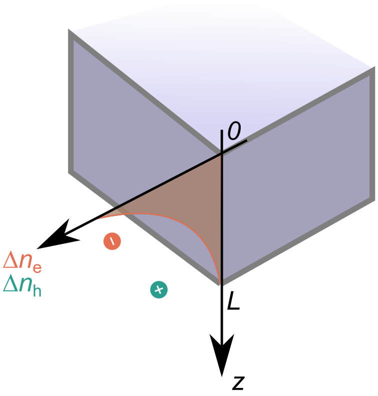

Figure 2.5: *Illustration of the Beer-Lambert initial condition.*

Statement 2.1.7. Taking the generation into account. The simplest model of photons absorption in the thickness of the material is the following:

$$g_{\text{spat}}(z) = n_\gamma \alpha(\lambda) \exp\left(-\alpha(\lambda) z\right) \tag{2.21}$$

with

$g_{\text{spat}}(z)$ = the spatial component of generation in cm^{-3}
n_γ = the fluence of the laser, in $ph.cm^{-2}$.pulse^{-1}
λ = the wavelength of the laser
$\alpha(\lambda)$ = the absorption coefficient of the material at the laser wavelength in cm^{-1}.
z = the spatial variable in cm

Two choices exist to take the temporal aspect of generation into account:

1. Use $g_{\text{spat}}(z)$ as an initial condition for $\Delta n_{e,h}(z, t = 0)$ and set $G_{e,h}(z,t) = 0$ for all time and space in Equation (2.7);

2. Use the following temporal-Gaussian-shape for the generation:

   $$G_{e,h}(z,t) = \frac{1}{\sqrt{2\pi}\sigma} e^{-\frac{(t-t_0)^2}{2\sigma^2}} \times n_\gamma \alpha(\lambda) e^{-\alpha(\lambda) z} \tag{2.22}$$

   with

   σ = temporal (half-)duration of the laser in s
   t_0 = temporal delay of the laser pulse in s

The two options were studied in [Maiberg and Scheer 2014] and appear to give very similar results. Depending on simulation numerical issues, option 2 is sometimes preferable as it lets the system of equations "slowly" adapt to the excitation. In Chapter 4, the first option is used to derive more easily the scaling law for the short-time scaling.

More complex optical models could be considered by including spatial reflections and interferences but this was not explored in this work.

The Poisson equation

When charges are separated due to applied electric fields or differences in diffusion velocities, electrons and holes attract each other. This attraction translates in an effective electric field —that screens the applied one when applicable. This is described by the Poisson equation.

$$\boldsymbol{\Delta}\phi = -\frac{q\left(\Delta n_h - \Delta n_e\right)}{\epsilon\epsilon_0} \tag{2.23}$$

with:

$\boldsymbol{\Delta}$ = the Laplace operator
ϕ = the electrical potential in Volts such that the electric field is $\vec{E} = -\vec{\nabla}\phi$
q = the (positive) elemental charge
ϵ = the relative permittivity of the semiconductor
ϵ_0 = the vacuum permittivity

One subtlety is that in the time dependent regime one might need to include the potential vector $\vec{A}$ to the description by choosing a gauge. This is not the case in our Matlab simulation. Nevertheless, we principally worked under the simplifying hypothesis $\Delta n_e(z,t) = \Delta n_h(z,t)$ under which the Poisson equation does not need to be taken into account.

Another subtlety is in the case of charged trap states in the conduction band. In this case the total charge needs to be modified in Equation (2.23) to include the defect charges.

Boundary conditions

To solve the drift-diffusion Equation (2.7), one needs to define the boundary conditions for the carrier densities $\Delta n_{e,h}(\Omega, t)$ where Ω represents the boundary of the domain. Recombination processes at the interfaces have been proved to critically affect the performance of devices [Haddad *et al.* 2020, Głowienka *et al.* 2020]. One way to model the recombination at the interface is to use the surface recombination concept:

$$\underbrace{j_{e,h}(z=0,t)}_{\substack{\text{Current flowing}\\ \text{out at top inter.}}} = S^{e,h}_{\text{top}} \Delta n_{e,h}(z=0,t) \tag{2.24}$$

where $S^{e,h}_{\text{top}}$ are the top surface recombination velocity, it has the unit of $cm.s^{-1}$. It represents recombination via traps at the interface.

In terms of defect density and capture cross section, how does this model with S_{top} compare with the model defects present in a density $N_{\text{def.}}$? This question is tackled in more details in Chapter 5. The result is that one needs to define a thickness z_s to link the two descriptions. In this case one obtains the following:

$$S_{\text{top}} \approx z_s \sigma_e v^e_{\text{th}} N_{\text{def.}}(z=0) \tag{2.25}$$

Top surface recombination velocities have the following orders of magnitude. For un-passivated inorganic semiconductors such as GaAs or Si, surface recombination velocities are of the order of $10^5 - 10^6$ cm/s [Yang *et al.* 2017, Yang *et al.* 2015, Taheri *et al.* 2021], while passivated surfaces may reach low values in the range of 10 - 10^2 cm/s [Yang *et al.* 2017, Zhao *et al.* 2014]. For perovskite films, even un-passivated, we [Cacovich *et al.* 2020, Vidon *et al.* 2021] and others [Yang *et al.* 2017, Jariwala *et al.* 2021] have found surface recombination velocities of the order of 10^3 cm/s.

For the bottom surface recombination, the equation is the following:

$$\underbrace{j_{e,h}(z=L,t)}_{\substack{\text{Current flowing}\\ \text{in at bot. inter.}}} = -S^{e,h}_{\text{bot}} \Delta n_{e,h}(z=L,t) \tag{2.26}$$

The minus sign comes from the definition of the current being positive is charge flow along the z axis. For perovskite based material deposited on glass, it was shown that the bottom surface recombination velocity is quite low ([Staub *et al.* 2016], <10 cm/s for the MAPI/Glass interface).

Photon recycling

Photon recycling and re-absorption play an important role in perovskite absorbers and should thus be considered in the modeling of their transport properties [Brenes *et al.* 2019, Pazos-Outón *et al.* 2016]. At least two models exist for photon recycling. One consists in reducing the amount of radiative recombination to take into account photons that are re-absorbed. The other consists in using an effective drift-diffusion equation for the photons in the material, coupled to the drift-diffusion equation for the charges.

In the first model, it was shown that photon recycling affects the apparent radiative recombination coefficient of perovskite thin films [Crothers *et al.* 2017]. Following [Richter *et al.* 2016], we can model photon recycling and re-absorption by introducing a factor applied to the internal radiative recombination coefficient, namely $k_2 = p_{esc} k_2^{int}$, with $p_{esc} < 1$ being the probability of escape for a photon, and k_2^{int} the internal radiative recombination coefficient.

In the second model, introduced by Ansari-Rad and Bisquert in [Ansari-Rad and Bisquert 2018] an effective drift-diffusion equation for the photons is introduced. We used their model to estimate the impact of photon recycling on our time resolved measurement on thin films and concluded that it plays very little role given that the absorption coefficient of the perovskite around the emission energy of E_g is small compared to the inverse thickness of the films $\alpha(E_g) \ll 1/L$.

Our base model

Taking into account all of the aforementioned models, we propose our base model:

Statement 2.1.8. Simplest drift-diffusion model. We use the following assumptions:

1. For all positions and time $\Delta n_e(z,t) = \Delta n_h(z,t)$.
2. We neglect electric field effects

Then we solve:

$$\frac{\partial \Delta n}{\partial t} - D\frac{\partial^2 \Delta n}{\partial z^2} = -k_1 \Delta n - k_2 \Delta n^2 \tag{2.27}$$

The initial condition is the following:

$$\Delta n(z, t=0) = n_\gamma \alpha(\lambda) \exp\left(-\alpha(\lambda) z\right) \tag{2.28}$$

The boundary conditions are the following:

$$D\frac{\partial n}{\partial z}(z=0,t) = S_{\text{top}} \Delta n(z=0,t) \tag{2.29}$$

$$D\frac{\partial n}{\partial z}(z=L,t) = -S_{\text{bot}} \Delta n(z=L,t) \tag{2.30}$$

Our observable is $I_{\text{PL}}(t)$ that we compute as:

$$I_{\text{PL}}(t) = A \times \int_0^L \Delta n^2(z',t)\, dz' \tag{2.31}$$

The input parameters of the model are:

D = The ambipolar diffusion coefficient in cm^2s^{-1}
k_1 = The non radiative bulk recombination coefficient in s^{-1}
k_2 = The radiative bulk recombination coefficient in cm^3s^{-1}
n_γ = The laser pulse fluence in phcm^{-2}
$\alpha(\lambda)$ = The sample's absorption coefficient at the laser wavelength λ in cm^{-1}
S_{top} = The top surface recombination velocity in cms^{-1}
S_{bot} = The bottom surface recombination velocity in cms^{-1}

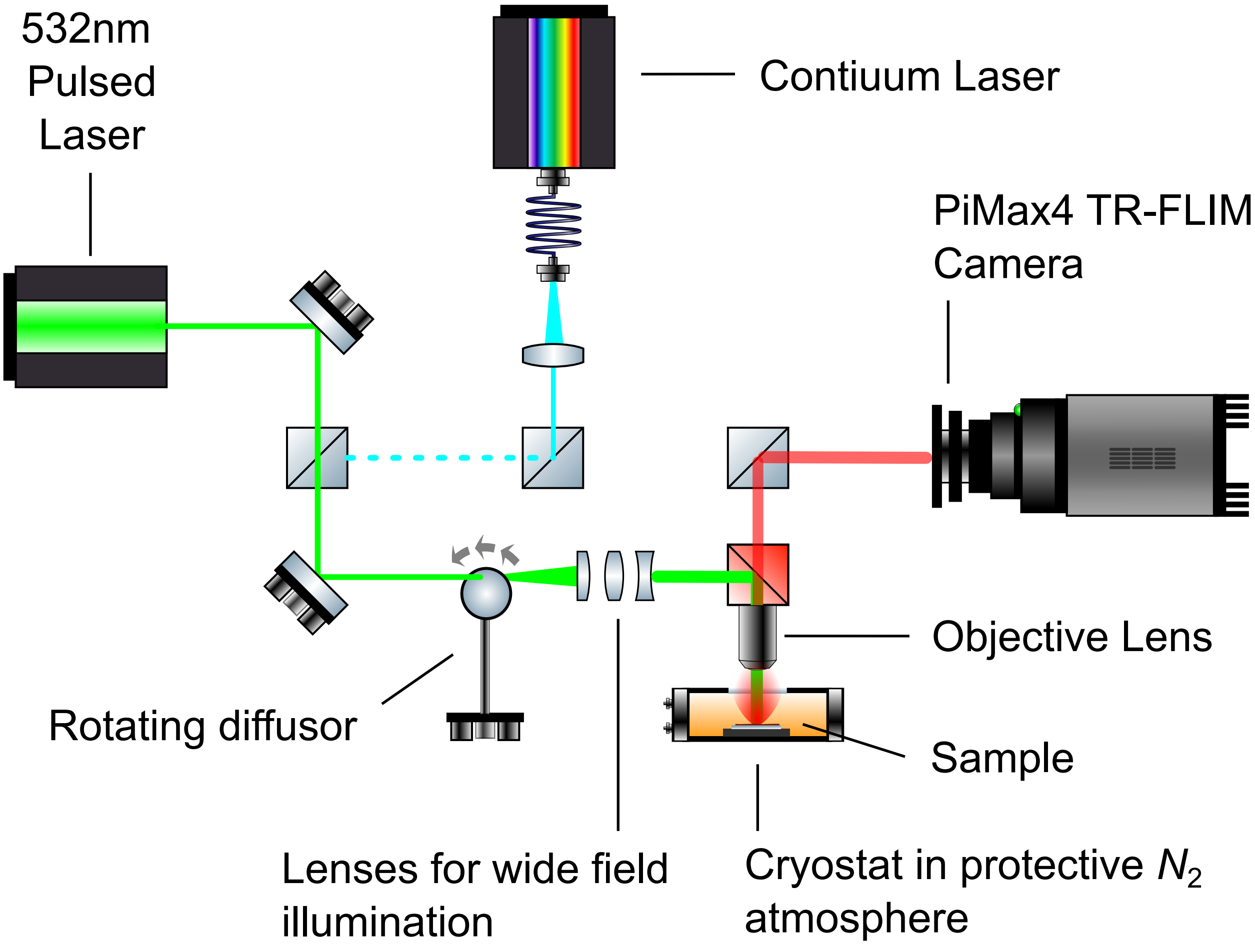

Figure 2.6: *Optical setup scheme of the TR-FLIM experiment.*

2.2 Experimental setup

The aim of this section is to describe how we obtained three experimental methods: one is the temporal super-resolution, the second the absolute calibration, the last is the signal to noise ratio estimation. Before describing these three methods, we present the general setup as well as good practices that allowed to increase the experimental work's quality.

2.2.1 Description of the setup

This subsection introduces the experimental TR-FLIM setup. A general description is sketched, then the two main illumination sources are described. Then triggering and time synchronization are briefly discussed.

General description

The experimental setup is described in Figure 2.6. The main optical path is the following. The illumination source can either be a 532nm pulsed laser —the Talisker —, or a tunable wavelength pulsed laser —the Fianium —. The laser light is homogenized via a rotating diffuser that is used to average out the speckle of the laser. Lenses are used to de-collimate the laser and allow for a wide field illumination. The laser light goes through a beamsplitter and an objective lens before it hits the sample. The sample emits light that is imaged through the same objective lens. The mixing of laser reflection and PL is filtered so that only the illumination reaches the TR-FLIM camera.

Illumination sources

Two main pulsed laser source are available. The first one is the Talisker laser, a pulsed 532nm laser. The pulses are $\approx$ 70ps long as measured by the manufacturer. Its intensity may be very high as this laser is intended for laser cutting applications. This high intensity allows us to work at the best of our homogenization strategies. Indeed, using the rotating diffuser is a very efficient way of reducing the speckle of the laser but it does greatly reduce the transmitted intensity —by at least two orders of magnitude. Therefore, the Talisker laser is very well suited for wide field imaging. This laser is used in the most of the experimental data, except in Chapter 5.

Parameters	Talisker	Fianium
Repetition Rate (kHz)	10-1000kHz	300-88000kHz
λ (nm)	532nm	450-800nm
Max fluence (ph.cm^{-2})	$> 10^{13}$	10^{9}

The Fianium laser is our second main source of illumination. It is composed of a white pulsed laser followed by a monochromator. The white light can be filtered out to only output light with a spectral width as low as 10nm —and as high as 100nm. The accessible wavelength range from 450nm to 850nm. The main issue with this laser is that the fluence is not constant on the whole wavelength range and that overall it is quite low. It took us a long time to find a way to obtain wide field illumination with this laser without reducing too much the intensity. **Marie Legrand**, a PhD student at IPVF, found the solution of using a square optical fiber directly imaged on the sample. The square fiber ensures very low speckle and sufficiently homogeneous illumination. This laser is used in the experimental data of the lambda study in Chapter 5.

Triggering

Both laser are pulsed and send a trigger signal to the camera. The trigger signal is a positive or negative voltage pulse. The camera detects it and takes it as the reference time $t = 0$. Then the user can set the time delay t_d after which we want to observe the photo-luminescence. At time $t = 1/f_{\mathrm{rr}}$, another voltage pulse reaches the camera and t represents the maximal time observable in a given experiment. The laser pulse hits the sample at some time delay t_{las} that depends on the laser, and on its repetition rate because the timing components of all the electronic equipment on the lab are frequency dependent. Thus, for each repetition rate and laser, t_{las} needs to be determined, for instance via dichotomy.

2.2.2 Good practices in experimental method

In this subsection, we list the main good practices employed or developed during this work on the experimental bench.

Samples in N_2

For perovskite based samples, many chemical reactions may occur in the presence of oxygen and or light [Cacovich *et al.* 2020]. Thus, we took steps to ensure the reproducibility of our measurements. One solution we found to reduce light soaking and chemical changes is to place the sample under Nitrogen gas atmosphere in a cryostat as sketched in Figure 2.6. We check the reproducibility by observing the stability of the decay after many repetitions of the same experiment.

Repetition for statistics

Another good practice we developed was to perform at least 2 repetitions in a row for each acquired decay cube. This process was greatly simplified by our automation codes, see section 2.3.4. The repetitions also allowed to discuss the statistics and uncertainty of our curves as discussed below.

Filters

The TR-FLIM camera is not spectrally resolved. That means that, as a regular camera, it will react on a wide spectral range. The light coming from the sample has at least two main spectral components: one from the laser reflection and one from the main PL peak of the studied sample. The laser reflection needs to be filtered out. The use of filters is of tremendous importance in this context. Moreover, as is explained in the next section, we devised an absolute calibration of the camera that requires careful spectral determination of the signal. Narrow band-pass filters need to be used to ensure that only light within a chosen interval hits the camera, for instance within tens of nanometers.

Laser reflections

Laser reflection are often an artifact that we want to eliminate from the signal, as it ”pollutes” the PL signal. But it is also a very effective way to obtain a map of morphology of the sample. Indeed, often the laser reflection is at relatively high intensity compared to the PL: reflection coefficients of surfaces usually amount to tens of percent while PL quantum yields, ie the ratio of number of output photons compared to the number of output photons are only of a few percents —and for the best available thin films. Therefore, this high intensity signal is very useful to find the focus (in z) and to compare the PL maps to the morphology maps. Care should be taken because the focus point depends on the wavelength: the focus point for the laser reflection might not be the same as for the PL. Moreover, with the wavelength-tunable laser, using two different wavelengths may lead to different information:

- A photon energy way higher than the bandgap will give the reflection of the surface
- A photon energy lower than the bandgap will give information on the bulk of the devices

See for instance in Figure 2.7 the reflection map at 600nm (absorbed, ie from the surface) and at 780 nm (not absorbed, ie from the bulk). Therefore laser reflections were used in this work as a tool to help the interpretation of PL maps and to help distinguish features from noise.

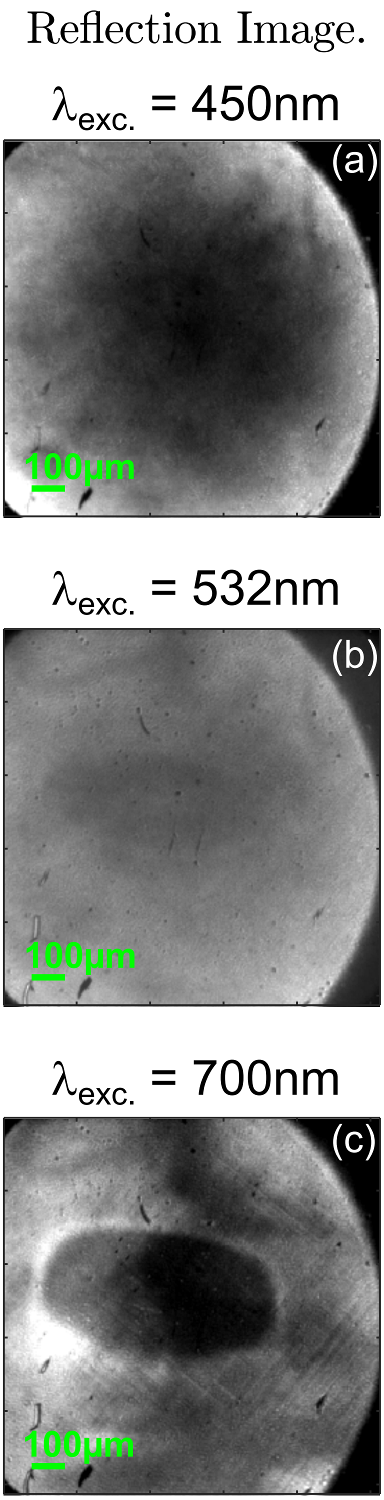

Figure 2.7: *Images of laser reflection for different excitation wavelengths at the exact same position. Focus was made for each of them. The sample is an IPVF baseline on glass, with a bandgap around* 760 *nm.*

2.2.3 The TR-FLIM camera

General introduction

The TR-FLIM camera at IPVF is a Princeton PiMAX4, doubly intensified EMiCCD time gated camera. In this thesis, we were interested in observing the decay images both **very shortly** (a few ns) after the laser pulse because the short time dynamics hold physical meaning, see Chapter 4, and **very long** after the laser pulse, because this is where the decay time is mostly initial-condition-independent, see Chapter 3. To be able to correctly measure these two regimes, we developed two methods: temporal super-resolution for the short-time, and absolute calibration of the camera to obtain a higher dynamic range for the long time. We describe how these two steps are achieved in the next sections. Finally, we also developed a statistical model to describe the camera's signal histograms that is described in Appendix E.

First we give a general description of the camera.

Description of the camera

In this section, we describe the main measurement apparatus used for our experimental data : the TR-FLIM camera.

The working principle is sketched in Figure 2.8. Incoming photons are first converted to electrons via a photocathode —that has a spectral response. Then, these electrons are multiplied via a Multichannel Plate. The electrons hit a phosphor screen where they convert back to (green) photons. The photons hit the CCD array. Upon reading the electrons excited in the array, another multiplication of these electrons is performed. The electrons are converted into analog digital unit (ADU or counts) via a gain F. Then an offset is added to all pixels to form the final numerical image.

The two main features are:

- **Doubly intensified EMICCD**. The signal is intensified in two main steps, one is via a multichannel plate (MCP) and the other is after the photons have been detected by the CCD. Both multiplication are controlled via a unique parameter of the camera called EMICCD gain.

- **Time gated camera**. This means that the shutter of the camera is opened or closed via temporal gates. This "shutter" is not a mechanical shutter, but rather implemented as a value of voltage applied to the first intensification step (MCP). If the voltage is low, electrons are not multiplied and close to no signal goes through. If the voltage is high, the electrons are multiplied and some photons reach the CCD array. These gates are controllable in width (ie during how much time the incoming signal is integrated) and in delay (ie when after the trigger pulse the acquisition starts).

The main camera parameters are the following:

- The multiplication gain parameter $EMICCD$. It ranges from 1 to 10 000 in the camera software. We note it I_{emiccd}.

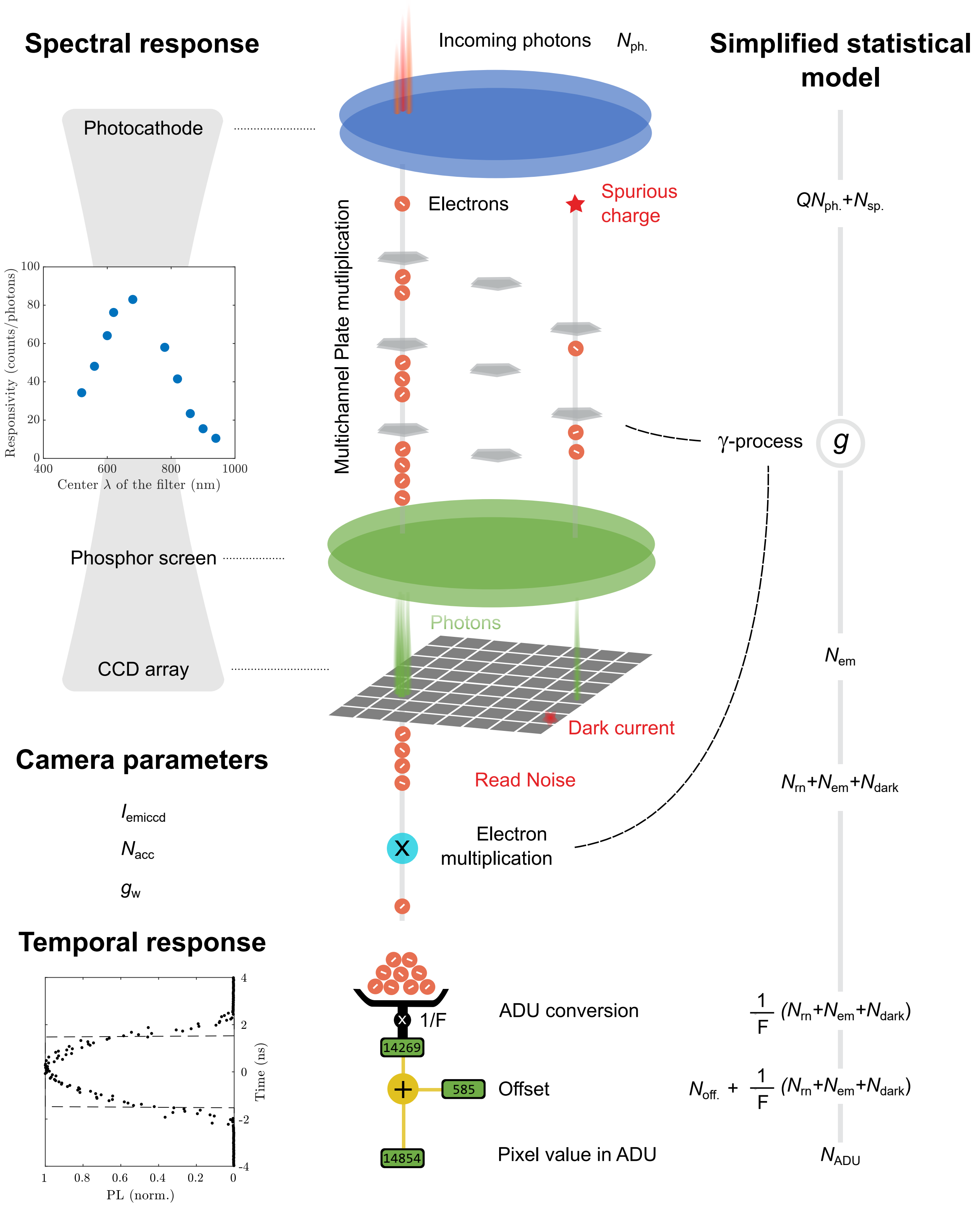

Figure 2.8: *Working principle of the TR-FLIM camera.*

- The number of accumulations to obtain one frame. It ranges from 1 to 65 000. This parameter is a hardware repetition of each of the experiment. We note it $N_{\text{acc.}}$.
- The gate width. This parameter plays on the integration time of the camera. It ranges from 480ps up to 1 ms. We note it g_w.

There are two main operation mode of the camera:

1. Sequential mode. In this mode one defines a gate width, a number of frame and the temporal positions of the starting gate and of the ending gate. The camera will acquire "sequential" frames in the sense that the gate delay of each frame will increase.
2. Repetitive mode. In this mode the gate delay and the gate width are the same for all the frames (which are therefore repetitive).

In the next section, we describe how we used the sequential mode to obtain the first new experimental method: the temporal super-resolution.

2.2.4 Obtaining temporal super-resolution to access the precise short-time dynamics of decays

In this subsection we present the temporal super-resolution method that allowed us to gain access to the short time dynamics. We first describe the time gating system of the camera, then explain how the super-resolution works.

The temporal gates

The TR-FLIM setup, as any other time resolved experimental setup, possesses an instrument response function (IRF) $h(t)$. This instrument response function originates from multiple elements of the setup, but mainly in our case from the laser temporal profile and the camera's own response function. As the laser's temporal duration does not excess 70 ps, the main limitation for the instrument response function of the setup is the camera's own response function as the minimal gate-width of the camera is 480 ps.

The camera's response function is actually a **parameter** that can be tuned. This parameter is referred to as the "gate-width" (GW, noted g_w). The gate is centered in some time delay t_d after the trigger pulse which is arbitrarily used to define $t_d = 0$. For our camera, the following gate-widths are available:

$$g_w = 480\,\text{ps}, 600\,\text{ps}, 660\,\text{ps}, 900\,\text{ps}, 980\,\text{ps}, 1.10\,\text{ns}, \quad \underbrace{1.2\,\text{ps}, \ldots}_{\substack{\text{continuous afterwards}\\ \text{with } 10\,\text{ps steps}}}$$

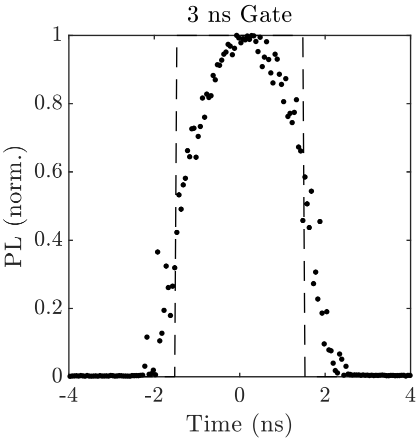

Figure 2.9: *(Points) Observed experimental gate* $h(t)$ *corresponding to a setting of* 3.00 ns, *normalized. (dots) Ideal square gate of width 3ns.*

In an ideal case, the gates would be step-like functions, equal to 0 outside of an interval of width g_w, where they would be equal to 1. However, experimentally it is of course not the case. The exact temporal shape of the gates not only is far from a step like function, but it also not a "$1-0$" or "on&off" function and its gates are not comparable to one another as their temporal functions are not simply scaled in time. For instance see Figure 2.9 for the 3.00 ns-long gate. We define the gate temporal gate profile by a function : $h(t, t_d, g_w)$.

Such temporal instrument response function has an impact on the measured signal, which is convoluted with the gate's temporal profile. Given an instrument response function $h(t)$, and an incoming signal $f(t)$, the output of the measurement $g(t)$ is obtained according to linear theory:

$$\underbrace{g(t)}_{\text{meas. signal}} = \int_{t'=-\infty}^{t'=+\infty} \underbrace{h(t-t')}_{\text{IRF}} \times \underbrace{f(t')}_{\text{signal}}\, dt' \tag{2.32}$$

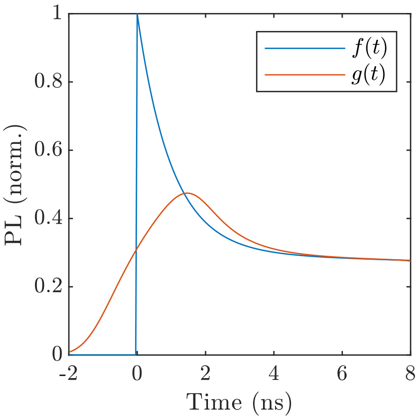

Figure 2.10: *Simulated decay in blue, and result of the convolution with the 3ns gate width in orange. Notice the time delay between the maxima and the value of the maximum that is lowered by the convolution.*

This equation simply states that the temporal gate *blurs* the incoming signal at time t with the signal that comes *shortly* after and shortly before time t. "Shortly", here, is to be understood as the width of the gate. In Figure 2.10, an example of this process is shown. We clearly see that convolution will prevent us to see major variations in our signal by blurring out any local derivative that would be more than approximately $1/g_w$ such as this discontinuous blue spike.

Statement 2.2.1. The camera can only ever measure the convoluted signal $g(t)$.

From a physicist's point of view, the convolution with the IRF is a difficulty in the way of observing the initial shape of the decay. As shown in the corresponding chapter of this thesis, there is physical information to gather in the initial time derivative of the signal.

We measured the instrument response function of the TR-FLIM with the following procedure: we acquired the laser reflection with different temporal gates in sequential mode. We used variations of time delays shorter than the gate width

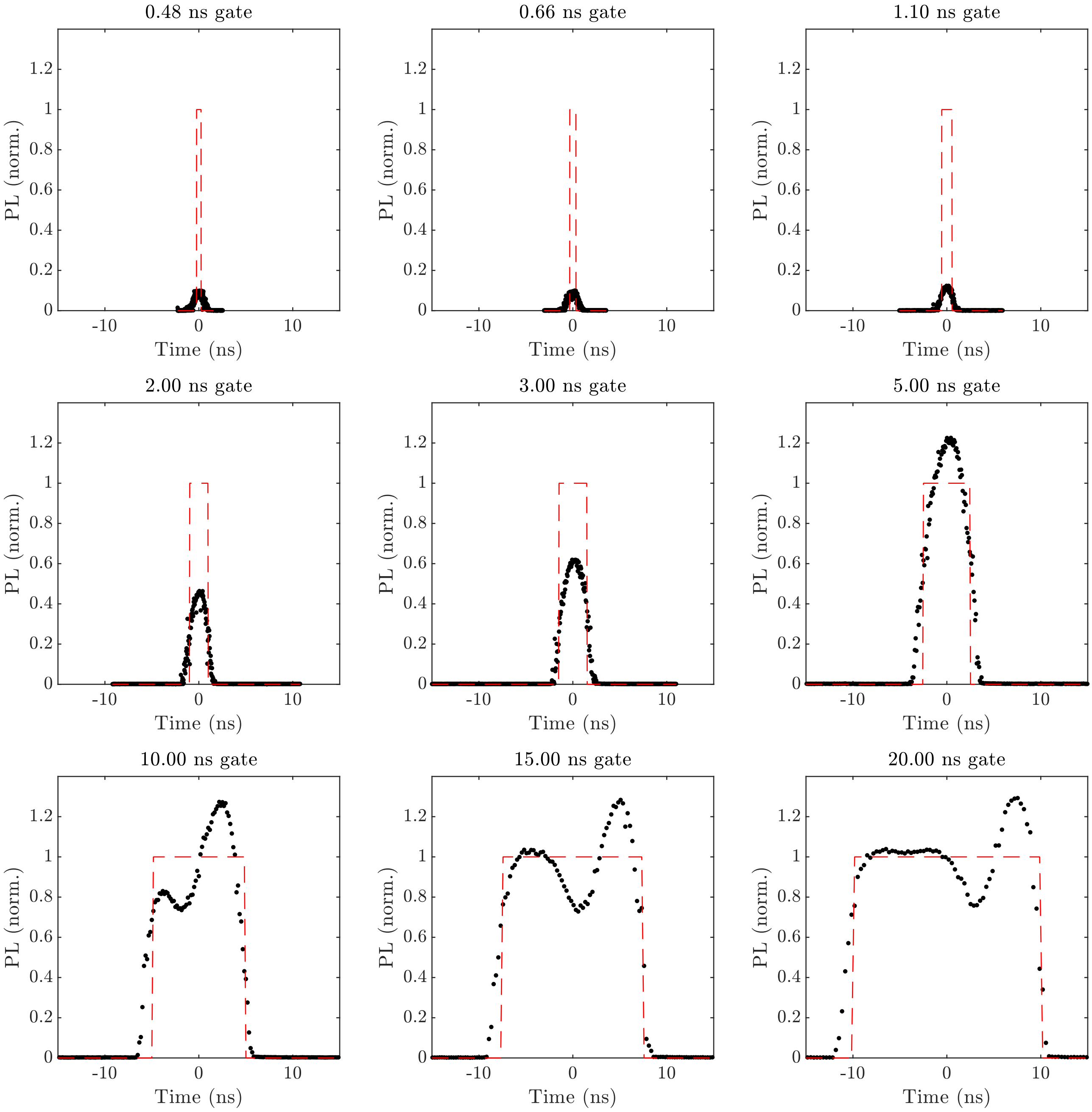

Figure 2.11: *Measured temporal gates of the TR-FLIM for nine settings of the camera. (black points) Experimentally observed signal, normalized with respect to the plateau intensity (see the* 20.00 ns *gate) ; (red dots) Square shaped ideal gate, of the corresponding gate width.*

to ensure that we resolve the gate itself, as sketched in Figure 2.13. As the laser temporal width is $\approx 70ps$ and the minimal gate is $480ps$, all is as if $f(t') \approx \delta(t')$ in Equation (2.32). In this case, $g(t) \approx h(t)$. We obtain the results shown Figure 2.11. In this Figure, we show the experimentally determined gate temporal shape $h(t', t_d = 0, g_w)$ compared to the ideal square shape that one would expect. For each experimental curve, we normalize the signal above noise to the value of the shoulder we see appearing for gates above 10 ns. We make at least three observations:

Statement 2.2.2.
1. The temporal gates are *not* square-shaped at the ns-scale.
2. The amplitude of opening of the gates varies substantially from one gate to the other. Notably, short-gates are rather dark.
3. The technical realization of the gate makes oscillations appear in their temporal profile.

This statement has a consequence in terms of the comparison of signals acquired with different gate widths. We want to describe how many photons the camera will integrate during one frame. In a simple picture we would have the following:

$$\underbrace{N_{\text{phot.}}}_{\text{Observed number of photons}} \propto \underbrace{\phi}_{\substack{\text{Incident flux}\\ \text{on one pixel}}} \times \underbrace{\Delta t}_{\text{Integration time}} \tag{2.33}$$

And, if things were ideal we would simply have:

$$\underbrace{\Delta t}_{\text{Integration time}} = \underbrace{g_w}_{\text{Gate Width}} \tag{2.34}$$

However this picture is a little too naive. We will show that if we want to keep the simple picture of Equation (2.33), we have to define a refined integration time, that depends on the gate-width setting $\Delta t(g_w) \neq g_w$.

In this regard we have to model the number of photons as:

$$\underbrace{N_{\text{phot.}}}_{\substack{\text{Observed number}\\ \text{of photons}}} \propto \underbrace{\phi(t_d)}_{\substack{\text{Incident flux}\\ \text{on one pixel}}} \times \underbrace{\int_{-\infty}^{\infty} h(t', t_d, g_w)\, dt'}_{\substack{\text{Integral of the gate}\\ \equiv I(g_w) \times g_w}} \tag{2.35}$$

Here, this assumes that the flux $\phi(t)$ is slowly varying between $t_d \pm g_w/2$. For each of the gate, we can compute the

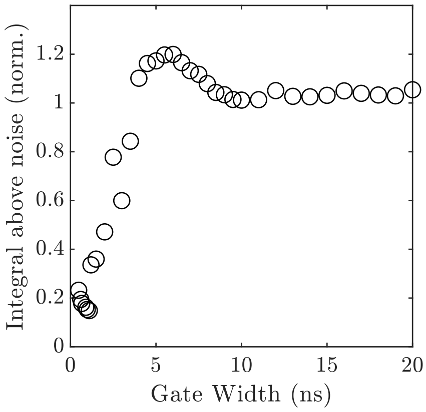

Figure 2.12: *$I(g_w)$, amplitude of the temporal integration of the gates presented in Figure 2.11, normalized by the expected integral of the square shaped red gates.*

integral of the signal above noise (integral of the black curve) and compare it to the expected integral (of the red curve). This quantity will be noted $I(g_w)$ and would be equal to 1 if the gates were square-shaped. The value of $I(g_w)$ is shown in Figure 2.12. We see that the obtained curve depends strongly on the gate for the gates below 10 ns, whereafter it is rather constant. It is interesting to notice that the oscillation visible for the 20 ns gate for instance, compensate itself in the sense that the obtained integral value for this gate is very close to 1.

We can make the following arbitrary (yet sensible) choice:

Statement 2.2.3. We define that for the gates after $g_w \geq 10$ ns,

$$I(g_w) = 1$$

and that for the gates before $g_w < 10$ ns the integral $I(g_w)$ is the one given by Figure 2.12.

Following our reasoning and definitions, let us state that:

Statement 2.2.4. If a number of counts $N_{c,1}$ is measured with the gate $g_{w,1}$. Then with the same input constant physical flux of light, and for any other gate $g_{w,2}$ we should have:

$$\frac{N_{c,1}}{I(g_{w,1})g_{w,1}} = \frac{N_{c,2}}{I(g_{w,2})g_{w,2}}$$

This rule allows to compare on an arbitrary axis two curves acquired with different gate widths. It will also help us calibrate absolutely our camera. Indeed, if we *know*—or set—the incoming photon flux on one pixel, then with the following statement, we can put any number of counts at any gate width on the same absolute scale.

Super-resolution and deconvolution

Now, to acquire a time resolved signal, one just has to slide t_d and observe the unfolding of the decay frame per frame, as sketched in Figure 2.13. The amazing capability of our camera is that :

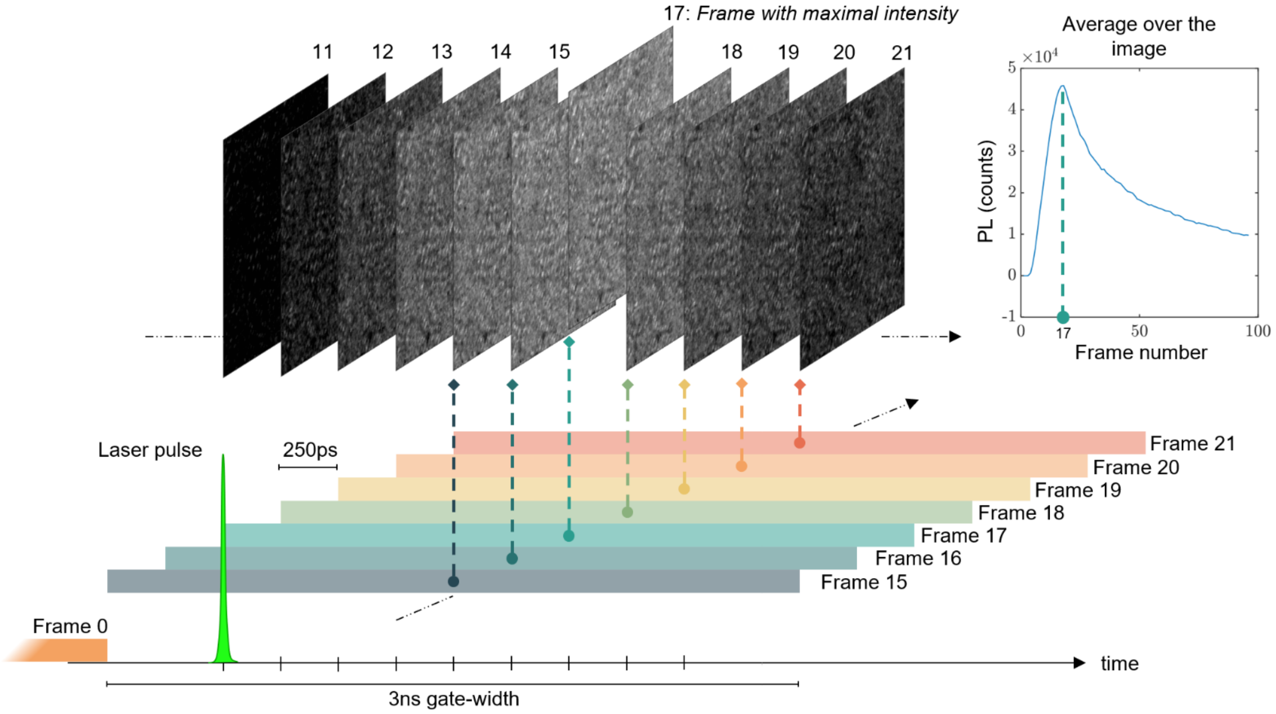

Figure 2.13: *TR-FLIM gating system used for super-resolution: the gates are slided with a time interval smaller than their temporal width.*

Statement 2.2.5. Principle of temporal super-resolution Even though the gate width is necessarily $g_w > 480ps$, the time delay of the center of the gate can be chosen with a 10ps precision.

This principle is what allowed us to plot all the points in Figure 2.11, and what is sketched in Figure 2.13 with a time delay difference of 250ps, that results in the round shape experimental decay in the top right part of this figure. Another example of experimental decay is given in Figure 2.14.

If the result of measurement is always convoluted, **can we recover the beginning of the decay?** For the deconvolution of experimental data, we used mainly 2 deconvolution procedures:

1. Fitting a convoluted phenomenological decay to the experimental data

2. Using Wiener filter in Fourier space

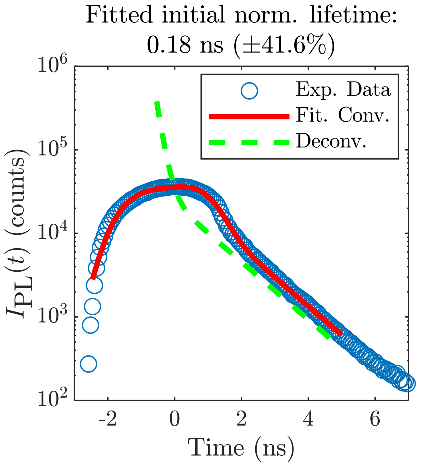

Figure 2.14: *(blue) Experimental decay of GaAs. (red) Result of the fitting of a bi-exponential decay convoluted by the 3ns gate. (green dots) Resulting "deconvoluted" bi-exponential decay*

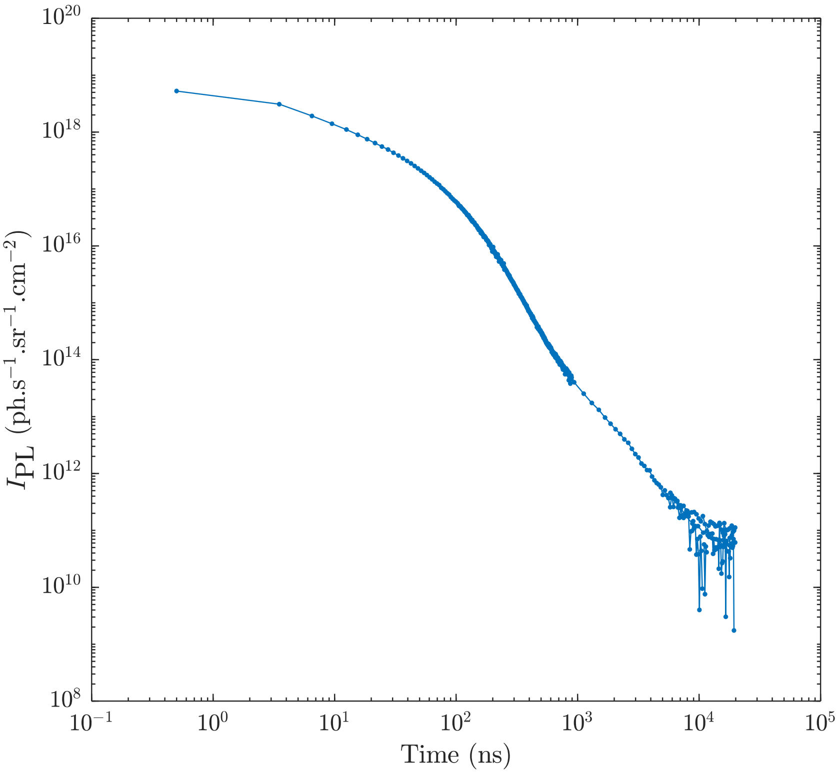

Figure 2.15: *Composite decay from multiple acquisitions put on the absolute scale showing the high dynamic range thus obtained. The sample was a full cell perovskite from the collaboration with Pavia University. The fluence was* $n_\gamma = 1.6 \times 10^{13}\,\mathrm{phcm}^{-2}$

An example of result of the procedure is given in Figure 2.14, where the blue points are experimental acquisition on GaAs with the super-resolved technique, the red curve is an modeled bi-exponential and post-convoluted curve, while the green one is the deconvoluted bi-exponential curve. We see that the red curve perfectly fits the experimental super-resolved acquired data. Then, it gives access to the shorter time dynamics in green. The fitted initial decay time of 0.18ns corresponding to the value obtained at $t = 0ns$ for the green decay, was confirmed by Streak camera acquisitions.

For most cases, when fitting more advanced models, such as the ones described in the first part of this chapter, the convolution with the gate is simulated on the experimental data. **Therefore, when fitting, we do not deconvolute the experimental data, we convolute the simulated data.**

2.2.5 Absolute calibration of the measurement setup to increase the camera's dynamic range

The aim of this section is to describe how we obtained the absolute calibration of the camera to be able to merge different acquisitions performed with different camera parameters. An example of the resulting high dynamic range is given in Figure 2.15. This absolute calibration will also allow for a high SNR method of decay time imaging, as presented in Chapter 3. The last section described what happens when the gate width is changed. Here, we take all other aspects into consideration: radiometric ones as well as the wavelength dependent and multiplication gains aspects.

Linearity and *relative* calibration

We introduce the:

Statement 2.2.6. Responsivity of the camera R**.** It gives the numerical number of counts obtained on the software for a given incoming absolute number of photons of wavelength λ reaching the entry point of the camera.

$$R\left(I_{\text{emiccd}}, \lambda\right) = \frac{\#\text{ of counts}}{\#\text{ of input photons of wavelengh } \lambda} \tag{2.36}$$

It is a function of the camera intensification parameters I_{emiccd}, and of λ. We define it for a number of accumulation equal to 1 and in the case of large gatewidth ie $I(g_w) = 1$. It represents the efficiency of detection due to the multiplication gain and spectral response of the elements.

To compare different curves acquired at different intensification parameter I_{emiccd}, we need to know how R scales with this parameter. This is the object of the present subsection while the wavelength dependent aspect is tackled in the next one.

We perform a simple experiment where a constant light source is imaged with different varying camera parameters, see Figure 2.16. We see an extraordinary linearity of the camera over the intensification parameter (a) and over the accumulation parameter (b).

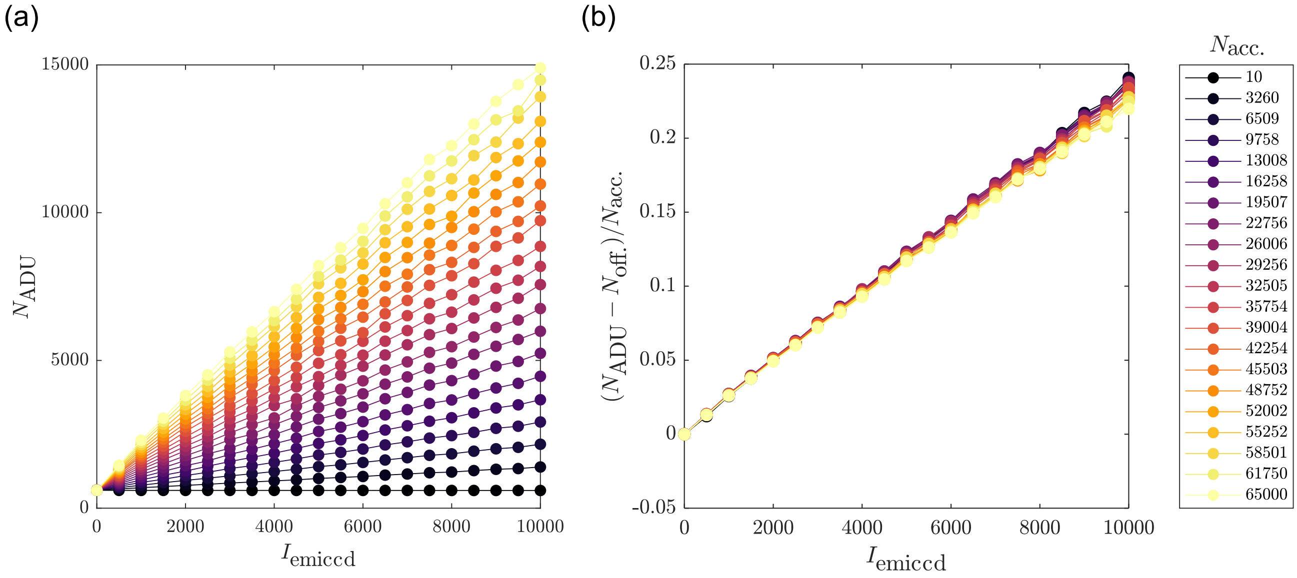

Figure 2.16: *(a) Value of counts observed when varying the intensification parameter I_{emiccd} for different values of $N_{\mathrm{acc.}}$; (b) Value of counts (minus 608 counts) normalized by the accumulation number $N_{\mathrm{acc.}}$. For (b) the curve at $N_{\mathrm{acc.}} = 10$ is omitted because of too low SNR. Experiments done with a 5 ns gate-width.*

These results allow us to write that the effect of both parameter is multiplicative, ie:

$$N_{\mathrm{ADU}} - N_{\mathrm{dark}} \propto I_{\mathrm{emiccd}} \times N_{\mathrm{acc.}} \tag{2.37}$$

Where N_{dark} is the number of counts obtained in the dark, $N_{\mathrm{dark}} \approx 608$ counts in this precise case. The exact composition of this dark signal is discussed below, on the origin of noise levels for our camera.

Finally, this proves our:

Statement 2.2.7. The camera Pi-MAX4 is linear with respect to both the I_{emiccd} and the accumulation $N_{\mathrm{acc.}}$ parameters. The linearity with respect to the accumulation number will be used in Statement 2.2.8 via Equation (2.45). For the intensification parameter, this implies that:

$$R\left(I_{_{\mathrm{emiccd}}}, \lambda\right) = \frac{I_{_{\mathrm{emiccd}}}}{5000} \times R\left(I_{\mathrm{emiccd}} = 5000, \lambda\right) \tag{2.38}$$

The value of $I_{_{\mathrm{emiccd}}} = 5000$ is taken as reference here because it was used for absolute calibration measurements.

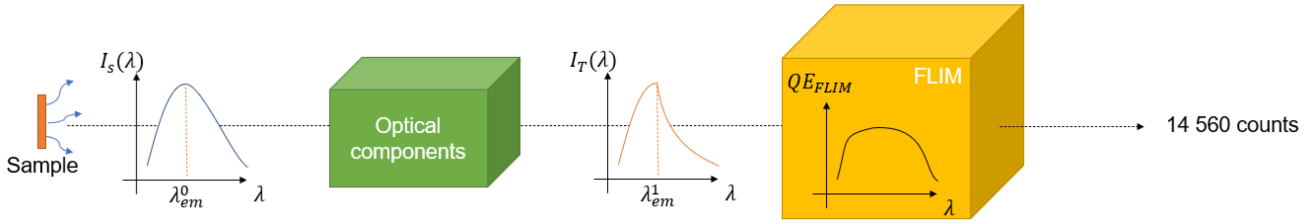

Figure 2.17: *Sketch of the elements to take into account in the TR-FLIM setup, where a chosen sample, in some chosen configuration of the setup, yield to a measurement of 14 560 counts on the sensor. We will show how to convert this arbitrary unit into absolute unit.*

This statement along with the Statement 2.2.4 on the impact of gate width allows the *relative calibration* of our camera. To obtain the *absolute* calibration, one needs to quantify the spectral response of the camera.

Optical and wavelength dependent aspects

The TR-FLIM's optical principles are depicted in Figure 2.17. We will not consider the temporal aspects in this specific subsection, but rather the optical ones, especially the wavelength dependent one. To do so, one can consider that everything discussed here happens in some short time equal to the gate width g_w.

The sample emits some light, with a spectrum:

$$\underbrace{I_s(\lambda, \Omega, \boldsymbol{r})}_{\substack{\text{Spectrum of the sample} \\ \text{just outside the surface} \\ \text{at position } \boldsymbol{r}\text{, angle } \Omega}} \equiv [\mathrm{ph\,nm^{-1}\,str^{-1}\,cm^{-2}\,s^{-1}}] \tag{2.39}$$

The quantity $I_s(\lambda)\delta\lambda\delta S\delta\Omega\delta t$ is the number of photons emitted with a wavelength between λ and $\lambda + \delta\lambda$ by a small surface δS within the solid angle $\delta\Omega$ and during a time δt.

Collection cone

The imaging setup will capture some solid angle Ω_S that depends on the numerical aperture of the lens. Each lens has a numerical aperture named NA. This aperture is linked to the angle of collection θ_c by:

$$\underbrace{\mathrm{NA}}_{\substack{\text{Numerical Aperture} \\ \text{of the lens}}} = n_{\mathrm{Air}} \sin(\underbrace{\theta_c}_{\substack{\text{Half angle} \\ \text{of collection}}}) \tag{2.40}$$

We have the following link between the solid angle of collection and numerical aperture of the lens:

$$\Omega_S = \pi \mathrm{NA}^2 \tag{2.41}$$

The solid angle of collection is the one to take into account to measure the absolute flux of light reaching the camera's input reticula. We define the flux of light reaching the camera as $I_T(\lambda)$. It is expressed as:

$$\underbrace{I_T(\lambda)}_{\substack{\text{Spectrum reaching}\\ \text{the camera}\\ [\text{ph}\,\text{nm}^{-1}\,\text{cm}^{-2}\,\text{s}^{-1}]}} = \pi\text{NA}^2 \times \underbrace{T_{\text{tot}}(\lambda)}_{\substack{\text{Total transmission}\\ \text{of the setup}}} \times I_S(\lambda) \tag{2.42}$$

Where we implicitly integrated over angles θ in the collection cone. As sketched in Figure 2.17, the transmission may change radically the spectrum coming from the sample. We will actually *use* this, by measuring the signal with notch filters (i.e. filters that only let pass certain wavelength for instance 780 ± 5 nm). This is actually **necessary** to obtain absolute quantitative information.

Projected size of pixels

The objective lens used has two main optical parameters: a numerical aperture NA and a magnification power M. The magnification power is used to image details and can range from x4 to x100. In any case the image is projected on the sensor with a magnification. The reverse perspective is that the pixels of the camera receive a diluted flux of light. One can think of projecting the pixels onto the sample's surface, being magnified. The real surface of one pixel of our camera is $S_{\text{p,real}} = (13\mu m) \times (13\mu m)$. If we use binning, for instance with a binning of $N_{\text{bin}} = 2$, the size of the binned pixel is $S_{\text{eff}} = N_{\text{bin}}^2 S_{\text{p,real}}$ The flux received by one pixel when using a lens of magnification M is therefore:

$$\underbrace{I_{\text{pix.}}(\lambda)}_{\substack{\text{Spectrum reaching}\\ \text{one (meta) pixel}\\ [\text{ph}\,\text{nm}^{-1}\,\text{s}^{-1}]}} = I_T(\lambda) \times \frac{\overbrace{N_{\text{bin}}^2}^{\text{Binning factor}} \times S_{\text{p,real}}}{\underbrace{M^2}_{\text{Magnification}}} \tag{2.43}$$

Notion of "responsivity" of the camera

The number of counts or ADU obtained for a given illumination $I_{\text{pix.}}(\lambda)$ is:

$$N_{\text{ADU}} = \int_0^\infty \underbrace{R(\overbrace{I_{\text{emiccd}}}^{\substack{\text{Camera Intensification}\\ \text{parameter}}}, \lambda)}_{\substack{\text{Responsivity}\\ \text{in } [\text{cts}\,\text{ph}^{-1}]}} I_{\text{pix.}}(\lambda) \overbrace{\Delta t_{\text{int.}}}^{\substack{\text{Integration}\\ \text{time [s]}}} d\lambda \tag{2.44}$$

Where we used the **Responsivity of the camera** R previously introduced. It is a function of the camera intensification parameters I_{emiccd}. It gives the numerical number of counts obtained on the software for a given incoming absolute number of photons spectrum $I_{\text{pix.}}\Delta t_{\text{int.}}$ reaching the pixels. The integration time $\Delta t_{\text{int.}}$ is the time during which the incoming flux is integrated. It equals as defined previously to:

$$\Delta t_{\text{int.}} = \overbrace{g_w}^{\text{Gate width}} \times \underbrace{I(g_w)}_{\substack{\text{Shape-factor}\\ \text{of the gate}}} \times \overbrace{N_{\text{acc.}}}^{\substack{\text{Number of}\\ \text{accumulations}}} \tag{2.45}$$

With the shape factor $I(g_w)$ discussed in the previous section.

The integral form of Equation (2.44) tells us that we loose the spectral information after having performed the TRFLIM measurement: even if we knew perfectly the responsivity R, the inversion of Equation (2.44) requires hypothesis on the emission spectrum.

Statement 2.2.8. To obtain the absolute flux of emission with the TR-FLIM setup, one **needs** to use notch band-pass filters of limited width $\delta\lambda$ and of center wavelength λ. In this case:

$$\begin{aligned} N_{\text{ADU}} \approx \overbrace{\pi \text{NA}^2}^{\text{Solid Angle}} &\times \overbrace{\frac{N_{\text{bin}}^2 \times S_{\text{p,real}}}{M^2}}^{\text{Proj. Pix. Size}} \times \overbrace{T_{\text{tot}}(\lambda)}^{\text{Total transmission}} \times \overbrace{\Delta t_{\text{int.}}}^{\substack{\text{Integration}\\ \text{time [s]}}} \\ &\times \underbrace{R(I_{\text{emiccd}}, \lambda)}_{\substack{\text{Responsivity}\\ \text{in [cts ph}^{-1}]}} \times \underbrace{I_s(\lambda)}_{\substack{\text{Spectrum of the sample}\\ \text{just outside the surface}}} \times \delta\lambda \end{aligned} \tag{2.46}$$

with:

λ = center wavelength of the notch filter
$\delta\lambda$ = band with of the notch filter
NA = numerical aperture of the objective lens
M = magnification of the objective lens
$S_{\text{p,real}}$ = real surface of one pixel: $(13\mu m) \times (13\mu m)$
N_{bin} = binning of the sensor: 1,2,4...
I_{emiccd} = camera intensification parameter
$\Delta t_{\text{int.}}$ = integration time $\Delta t_{\text{int.}} = g_w I(g_w) N_{\text{acc.}}$

In this case, the total transmission $T_{\text{tot}}(\lambda)$ will be a band pass filter of short width $\delta\lambda$.

To calibrate, we therefore need to measure the responsivity function $R(I_{\text{emiccd}}, \lambda)$. To do so, our strategy is the following:

1. Measure the responsivity as a function of wavelength with fixed $I_{\text{emiccd}} = 5000$.

2. Use our Statement 2.2.7 on the linearity of the camera to obtain the absolute calibration for all camera parameters.

Measuring the responsivity of the camera at one intensification parameter I_{emiccd}

Our choice was to perform the following simple procedure and is sketched in Figure 2.18. We chose some intensification camera setting I_{emiccd}. Then, with a lamp of calibrated (absolute) spectrum, along with bandpass filters, we measured the numerical output obtained with each filter. We also measured the transmission of all configurations and could compute the expected number of photons reaching the sensor. Thus, for this set of parameters of the camera, we obtained our absolute calibration measurement of $R(I_{\text{emiccd}} = 5000, \lambda)$. The gate width was chosen to be g_w =100 ns and we have $I(g_w = 100ns) \approx 1$. The accumulation number was varied depending on the notch filter used. Here are the optical parameters used for this experiment:

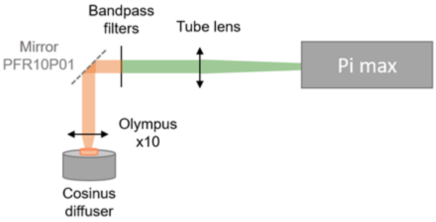

Figure 2.18: *Principle of the experiment to measure the responsivity.*

Information	Value
Objective lens	Olympus Plan N x10
NA	0.25
πNA^2	0.196
Magnification M	11.1
$S_{\text{p,real}}/M^2$ (m^2)	1.37×10^{-12}

In order to estimate the absolute photon flux received by the camera, we performed measurement of the transmission of each of the filters used, see the Appendix Figure E.1. With the experimentally determined transmissions, along with the parameters of the objective lens used, we could estimate the absolute photon flux reaching the camera. The results are presented in Table 2.1.

From this measurement and estimation of total flux, we are able to compute the responsivity function at $I_{\text{emiccd}} = 5000$, the result in presented in Figure 2.19. We see that the number of counts per photons is strongly dependent on the wavelength of the incoming photons. We remind the reader that this unit does make sense when the wavelength of the photons is known, which is the case here, up to 20 nm.

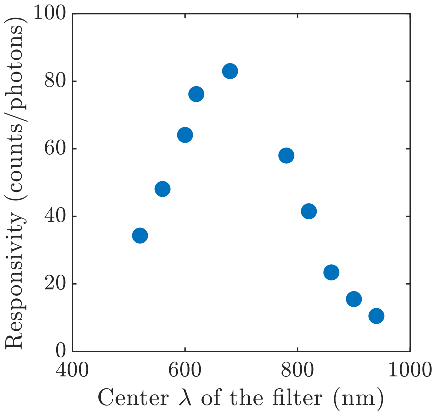

Figure 2.19: *Obtained responsivity function.* $R(I_{emiccd} = 5000, \lambda)$.

Generalization

Then, to generalize to other camera parameters, we used the *relative* calibration of the TR-FLIM camera, see the previous section. To generalize to other optical setups, we use the

λ (nm)	Transmitted radiance ($\mathrm{ph\,s^{-1}\,str^{-1}\,m^{-2}}$)		Collected Flux ($\mathrm{ph\,s^{-1}}$)	TR-FLIM		$R(\lambda)$
	Specs.	Exp.		$\Delta t_{\text{int.}}$ (s)	Mean Value (cts)	$I_{\text{emiccd}} = 5000$ ($\mathrm{cts\,ph^{-1}}$)
520	3.03×10^{18}	2.62×10^{18}	7.03×10^{5}	1.00×10^{-3}	24 148	34
560	4.95×10^{18}	5.01×10^{18}	1.35×10^{6}	5.00×10^{-4}	32 364	48
600	5.59×10^{18}	5.54×10^{18}	1.49×10^{6}	3.00×10^{-4}	28 609	64
620	6.76×10^{18}	5.67×10^{18}	1.52×10^{6}	3.00×10^{-4}	34 855	76
680	8.52×10^{18}	1.10×10^{19}	2.96×10^{6}	1.00×10^{-4}	24 574	83
780	1.59×10^{19}	1.74×10^{19}	4.27×10^{6}	1.00×10^{-4}	24 760	58
820	1.38×10^{19}	1.83×10^{19}	3.70×10^{6}	1.00×10^{-4}	15 380	42
860	1.85×10^{19}	2.39×10^{19}	4.97×10^{6}	3.00×10^{-4}	34 885	23
900	1.99×10^{19}		5.36×10^{6}	3.00×10^{-4}	24 916	15
940	2.37×10^{19}		6.37×10^{6}	3.00×10^{-4}	20 134	11

Table 2.1: *Determination of the input flux of photons, and of the responsivity of the camera, as measured with the described procedure.*

description given above, and simply change accordingly the numerical aperture and magnification (in case of change of objective lens), or the optical transmissions in case new elements are put on the optical path.

Absolute calibration formula

We finally obtain the following:

Statement 2.2.9. Absolute calibration formula. In the case of measurement with a band pass filter of center wavelength λ and width $\delta\lambda$, the absolute flux of photons emitted by the sample is:

$$\underbrace{I_s(\lambda) \times \delta\lambda}_{\substack{\text{Spectrum}\\ \text{of the sample}}} \approx \frac{(N_{\text{ADU}} - N_{\text{dark}})}{\overbrace{\pi \mathrm{NA}^2}^{\text{Solid Angle}} \times \overbrace{\frac{N_{\text{bin}}^2 \times S_{\text{p,real}}}{M^2}}^{\text{Proj. Pix. Size}} \times \overbrace{T_{\text{tot}}(\lambda)}^{\substack{\text{Total}\\ \text{transmission}}} \times \overbrace{g_w I(g_w) N_{\text{acc.}}}^{\substack{\text{Integration}\\ \text{time [s]}}} \times \underbrace{\frac{I_{\text{emiccd}}}{5000} \times R\left(I_{\text{emiccd}} = 5000, \lambda\right)}_{\substack{\text{Responsivity}\\ \text{in } [\mathrm{cts\,s\,ph^{-1}}]}}} \tag{2.47}$$

2.2.6 What is the uncertainty on the FLIM signal?

For the curious reader, we found in the literature and adapted a statistical description of the TR-FLIM. It allowed us to develop a way to predict the signal to noise ration only by measuring the signal (and not the noise!). This question is tackled in Appendix E.

2.3 Numerical methods

Among the tools we used for numerical methods, there are commercial simulation software, as well as home-made code. We principally coded three codes:

- A **data-observation software** to check the acquired experimental data *live* in the lab. This software, called VPL, allowed to increase greatly the quality of the experimental work by facilitating experimental mistake determination or distinguishing bad samples (with too low decay times).

- A suite of **automation software** for the experiments that allowed for new types of experiments to be conducted: numerous repetitions of the same experiments without manual input, experiments that depend on the time of the lab (light-soaking or ion movement experiments), experiments that link TR-FLIM acquisition and bias via the control of a Keithley Function Generator.

- A suite of **simulation and fitting** code based on the drift diffusion model. We developed a fitting procedure that can use as model both our own Matlab simulation as well as the commercial TCAD software Silvaco Atlas. Moreover, we took particular care in the use of fitting to determine parameters. We present our reasoning on the best method to fit parameters to our curves, notably by determining correlations and estimating the uncertainty on the fitted parameters.

2.3.1 Modeling software

In terms of modeling we used principally:

1. **SCAPS 1D**: this simulation tool was developed by Alex Niemegeers, Marc Burgelman, Koen Decock, Stefaan Degrave, Johan Verschraegen at the Department of Electronics and Information Systems (ELIS) of the

University of Gent, Belgium. This program can be used in the continuous wave regime to simulate device operation. See [Burgelman *et al.* 2013].

2. **Silvaco Atlas** is a commercial TCAD software. It allows among others for time resolved simulation of complex device architecture. We used it for spatial 2d-simulation as well as for the simulation of half cells and full cells (still undergoing).

3. **Home made Matlab simulation tool**. We coded a drift-diffusion simulation tool in Matlab with the function `pdepe` to solve the partial differential equation. The code results were validated against Silvaco Atlas and Baptiste Berenguier's code from IPVF.

2.3.2 Fitting methods

We developed and used various fitting procedures throughout this work. Fitting a model function $f(t, P)$ where t is the time and P a set of physical parameters onto N experimental data points $(I_{\mathrm{PL}})_{i\in[1,N]}$ consists in finding the set of parameters P for which one achieves the minimum of the residual function χ^2:

$$\chi^2(P) = \sum_{i=1}^{N} \|f(t_i, P) - I_{\mathrm{PL}i}\|^2 \qquad (2.48)$$

For instance $f(t, A, \tau) = Ae^{-t/\tau}$ for a mono exponential decay. Here, our notation is such that the fitting parameters are $P = (A, \tau)$. The uniqueness of the parameter set that achieves the minimum of χ^2, noted P_{min} is not guaranteed in general. To find the best parameters, most algorithms start from a parameter set P_0 and try to move slightly each of the component of P_0, then they decide which is the next parameter set P_1 by using the estimated gradients of χ^2 in each direction of P. As the number of fitted parameters (ie dimensions of P with our notations) increase, the problem becomes more and more complex, more and more initial point dependent, longer and longer to solve...

Fitting a model to experimental data requires delicate analysis, [Young 2015]. Many pitfalls can arise when using fitting methods. In this subsection, we will describe the main attention points to keep in mind when fitting, then we describe our fitting procedure and how it is capable of fitting multiple curves with only one underlying physical model.

Pitfalls of fitting decays

When using fitting algorithm to fit decays many pitfalls may arise.

Normalization

Decays are usually normalized by the observed initial value. It is important that discretization of the experimental data contain enough points to not "miss" the maximum. Moreover, due to the convolution with the apparatus response function —as described in the previous sections —, the exact maximal observed value is not equal to the observed one. The impact of the correct normalization is therefore two fold: have the correct value of the maximal intensity, and correctly place it in the time axis.

We will show in Chapter 4 how the "short time" dynamics are actually full of information on the physical behavior of samples under study.

Fitting the logarithm of the data

Decays often present exponentially decreasing time behavior —or even faster than exponential. This means that, when fitting data to a model, the terms of the sum in Equation (2.48) at long time t_i have less and less weight. Therefore, the fitting algorithm will not pay much time trying to make the model correspond to data points in these regions, compared to the regions where the residuals are higher.

To counter this, one may fit the logarithm of the I_{PL} so that the optimized $\chi^2_{\log}$ is:

$$\chi^2_{\log}(P) = \sum_{i=1}^{N} \|\ln\left(f(t_i, P)\right) - \ln\left(I_{\mathrm{PL}i}\right)\|^2 \tag{2.49}$$

Overfitting, parameter correlation and meta parameters

When fitting, one should always pay attention to parameter correlation. Parameter correlation is the fact that some parameters in P may have a somewhat similar effect on the objective function $\chi^2_{\log}$. Imagine two parameters $P = (p_1, p_2)$. We will say that they are perfectly correlated when there exists a line in parameter space along which the residual function $\chi^2_{\log}$ achieves its minimum. For instance if we imagine a model $f(t, \tau_1, \tau_2) = exp(-t/(\tau_1 - \tau_2))$ to fit data points generated with the model $e^{-t/500}$, then the minimal of χ^2 will be achieved on the line $\tau_1 - \tau_2 = 500$. τ_1 and τ_2 are perfectly correlated. (Times are in ns.)

In the example, the correlation is quite trivial and happens in the whole parameter space but for real cases it may happen only around the vicinity of the fitting result, ie around the best fitted parameters. It may also not be a perfect correlation but a partial one. Anti-correlation happens when one parameter increases and the other decreases along the line of minimum χ^2. Let us say that by *line* we do not mean *straight line* and the correlation may take more subtle forms as will be shown in the next chapters.

Correlation is measured between -1 and 1. Correlation close to 1 in absolute value means that a hyper-parameter is hidden in the model and that our model function contains actually too many parameters —as is the case for our example above. Hyper-parameters are the smallest ensemble of parameters that impact the model function. When fitting, one should always reduce at maximum the number of fitted parameters.

Estimating the uncertainty on the physical parameters

Estimating the uncertainty on the fitted parameters is rarely straightforward [Young 2015]. but techniques exist. Notably one needs to estimate uncertainty on data points (see Appendix E for the uncertainty on the FLIM signal). One method to obtain estimates of uncertainty on the fitted parameters is to select only a part of the experimental data points (a procedure called re-sampling) and perform the fit on this subset. With random drawings of the re-sampling datasets, one obtains a distribution of fitted parameters.

Simpler is better

When fitting, one should always try the simplest models first. For decays, a first —and possibly very wrong —fit, does bring information:

- It gives orders of magnitude for the parameters of more complex models
- It usually is much faster than fancy models
- It sets a bar of comparison for the residuals remaining after having fitted fancy models: it helps discuss the relevance of such models

2.3.3 Implementation of the fitting procedure

We implemented a fitting procedure in Matlab that has two main interesting features:

1. The ability to plugin Matlab models or Silvaco Atlas models
2. The ability to fit multiple curves —acquired say at different laser intensity and/or wavelength and or under some chosen bias—with the *same* underlying physical model

The main fitting model we used is the Matlab home-made code. The solver is coded with Matlab and uses the `pdepe` function. The equation solves for $\Delta n(z,t)$, then computes $I_{\mathrm{PL}}(t)$ as the trapeze-computed integral of $(\Delta n(z,t))^2$. Time convolution is also conducted with trapeze-computed integral with the formula:

$$I_{\mathrm{PL}}^{conv}(t) = \int_{-\infty}^{+\infty} dt' I_{\mathrm{PL}}(t') h(t-t')$$

with h defined as in Figure 2.11. The fitting is realized using `lsqcurvefit` method. Uncertainties are estimated using the `nlparci` method of Matlab for non-linear fitting techniques.

2.3.4 Automation of acquisitions

We developed a series of Matlab written codes for the automation of acquisition with the camera PiMax4. The camera software from Teledyne Princeton is called Lightfield, and can be controlled from external programming languages, such as Matlab. Thanks to this interface, one can **fully control the camera acquisitions parameters directly from Matlab**. The main parameters that our homemade code controls are the following:

- **The file name**. This may look futile but is actually at the heart of our experimental improvement. Indeed, our automatic code allows us to use consistent filenames all along an experimental session. It also allows to store information such as sample number, laser intensity, laser wavelength, applied bias (when applicable), etc. directly in the filename. One other information that is stored in the file name string is the **repetition number**. Repeating experiment has never been easier because thanks to our program we can track the exact same repetitions of experiments —and later combine them.

- **The acquisition parameters**. As discussed below the two main intensification parameters that are EMICCD and the number of accumulation. Both can be accessed via a reading function we found online and adapted to our case.
- **The gating parameters**. The gate delay and width may be modified at will by our program. This allowed us to draft a code of automatic setting of these parameters according to our design. One could think for instance for a program that increases the gate width of the acquisition until a certain Signal to noise ratio (SNR) is reached. We used it to quickly obtain long-time acquisitions with consistent camera parameters for different samples/days of experiments —which would otherwise be a tedious and potentially error-full process.

This series of program is a building block that helped us tremendously during this work mainly by reducing the number of human operations on the file. Typical **use cases** are:

- Repeating 10 times in a row the same experiment.
- For each sample, for each laser intensity, perform two different type of acquisition : one super-resolved at short time (say 100 points from $-5\,\text{ns}$ to $10\,\text{ns}$) and one that explores longer times (say 100 points from 0 to $1000\,\text{ns}$). If we want to perform say 5 repetitions of each individual combination, the naming, experiment opening and repeating would really require extreme patience and caution of the experimentalist.
- Launch a series of similar acquisitions but by saving the absolute time of the beginning of the experiment to track changes at the time scale of the minute our hour.

This **building block** may be used in the future for even more exotic applications.

2.3.5 Software to observe experimental results

Another cornerstone tool that we developed is a **graphical interface software** named VPL (Visualizing Photo Luminescence). This program has a simple purpose: being able to **visualize the obtained decays directly after acquisitions**, in a matter of seconds. The necessity is the following: one needs to make sure that the acquisitions are led correctly and that no artifacts are present. The camera's program was mainly built for imaging purposes and therefore does not allow to quickly visualize the decays, i.e. spatially integrated TR-FLIM cubes.

This program's purpose is also to compare live in the lab different decays obtained in different conditions, say at different laser intensity or wavelength —or to compare different regions of the same cube.

This software was coded from scratch via Matlab App Designer and is currently in version 4.7. Its features include ROI selection, basic fitting of decay times, comparison of different files, as well as displaying the acquisition parameters by reading the file metadata.

This software also contributed to the improvement of our experimental results.

2.4 Conclusion

In this Method and Tools chapter, we discussed first the theoretical models we used. We described the main physical parameters that come in play for the photo-luminescence which was our main tool for reaching the microscopic behavior of solar cells.

Second, we described the experimental setup and the precise characterization we performed on the TR-FLIM camera. This allowed us to obtain a relative and absolute calibration of the TR-FLIM setup. The statistical model used to describe the output histograms proved to be complementary to the calibration work done on averages. It allowed us to define a procedure to compute the uncertainty on our main signal : the photo-luminescence number of counts.

In a final part we discussed the numerical tools employed during this work. Code automation allowed for fast experiment look-up in the lab to increase reproducibility and error detection. Automation of acquisitions increased the reliability of the acquired data as well as allowed new type of experiments to be conducted. Fitting algorithms and methods were also discussed.

Chapter 3

Phenomenological interpretation of time resolved imaging photo-luminescence

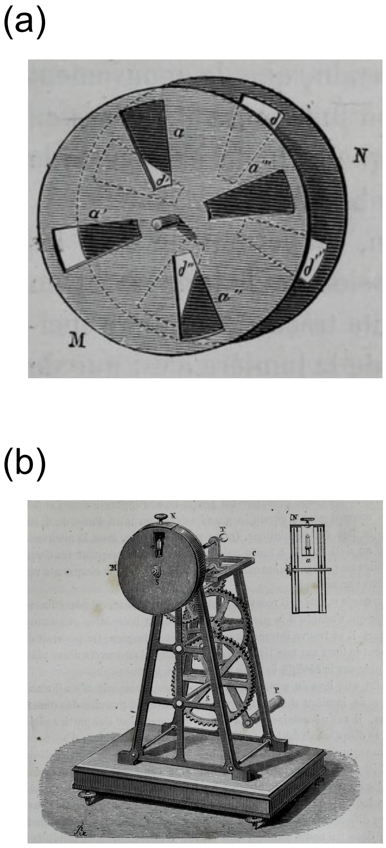

Figure 3.1: *Principle of the first time resolved fluorescence setup, the phosphoroscope, invented by Edmond Becquerel. Reproduced from [Becquerel 1867]. (a) The two disks. (b) The phosphoroscope.*

The very first time resolved setup to measure time resolved photo-luminescence is due to Edmond Becquerel in 1861 [Valeur and Berberan-Santos 2011, Becquerel 1867] and called the phosphoroscope, see Figure 3.1. It consisted of two disks composed of some open windows and some light-blocking windows. The principle was that one disk was used for excitation and the other for collection: their windows and light blocking regions were opposite so that the light of emission never goes through the collection path. By choosing the rotation frequency, one chooses the time delay of observation of the PL after the emission "pulse". His first interpretation was that the decay followed a mono exponential law:

$$I_{\mathrm{PL}}(t) = Ae^{-t/\tau} \tag{3.1}$$

Then, to explain the disgreement with his experimental data, he proposed a bi-exponential law:

$$I_{\mathrm{PL}}(t) = A_1 e^{-t/\tau_1} + A_2 e^{-t/\tau_2} \tag{3.2}$$

We see that very early in the field of time resolved photo-luminescence the phenomenological interpretation resulted in the measurement of decay times $\tau_{1,2,\ldots}$. In many recent papers in the semiconductor field the interpretation via Equation (3.1) and Equation (3.2) is still used [Adeleye *et al.* 2021, Zhang *et al.* 2020b]. Other phenomenological approaches such as the "stretched exponential" are widely used, in this Science article for instance [DeQuilettes *et al.* 2015].

The question of this manuscript is that of imaging recombination heterogeneities of perovskite-based solar cells. Computing images of "lifetime" therefore seems like the first way of doing so —especially because computing the maps from raw data is *very* fast compared to drift-diffusion fitting for instance. So the question of this chapter is the following: what can this phenomenological local interpretation tell us on the studied devices? What exactly can we conclude when observing two different decay times on an image? What is the best way to image the decay times?

The aim of this chapter is to demonstrate that decay times imaging can be used to characterize recombination inhomogenities on the studied samples, despite having numerous limits. We will show how decay time imaging allowed us to conclude on the homogeneity of the passivation induced by a 2d-layer onto 3d perovskite. We will also show how it allowed us to conclude on the increase of non radiative recombination is some areas of inhomogeneous $FAPbI_3$ crystals. **The problem that arises is** that the observed local decay times are not representative of defects only. For instance the excitation conditions or the local thickness can change the observed decay time. **What can be understood from our demonstration is** that phenomenological methods are useful for semi-quantitative imaging. We also propose a **new technique** for decay time imaging that relies on the camera's relative calibration.

We **first** evidence that the notion of "lifetime" can be misleading. We introduce a visualization tool for simulation that shows what physical processes cause the decays. We show that the best settings to use "decay-time" interpretation are: at *at long time* after the laser pulse and under *low excitation* conditions. **Second,** we show the application of the *regular* decay imaging technique to evidence the homogeneity of the passivation effect of 2d layer perovskite on top of 3d triple cation perovskite in state of the art samples. We show that the regular technique needs to be improved to increase the quality of the information it provides. **Finally,** we use a *new* method of decay time imaging, that we named Large Gate Acquisition (LGA) , to show the heterogeneity of $FAPbI_3$ layers annealed at different rates. We argue that the heterogeneity we observe is not explicable only by thickness variation but by a change of the local non radiative recombination rate.

3.1 Executive summary

Statement 3.1.1. Methods and theory.

1. The **term "lifetime"** is flawed and **should be avoided.** The term "decay time" is preferable.
2. We **introduce a new interpretation tool** for simulation called SIMPLED that explicitly shows *how* and *for how long* each physical phenomenon affects the PL decay.
3. **We developed a method** to image decay times with **higher precision** than we had earlier in the lab based on the calibration of our camera.
4. **Decay times measured are subject to many caveats** including : dependence on the local excitation condition, on local thickness, on measurement conditions.

Result 3.1.1. Decay times maps of $FAPbI_3$ thin films on glass hint that growth of microdomain leads to inhomogeneous defect density even inside large microdomains.

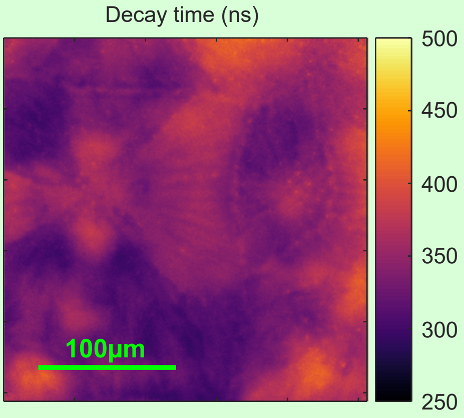

Result 3.1.2. Decay times maps of p-i-n solar cells with $Cs_{0.05}(MA_{0.17}FA_{0.83})_{0.95}Pb(I_{0.9}Br_{0.1})_3$ and additional 4-fluoro-phenylethylammonium (F-PEAI) layers show homogeneous passivation.

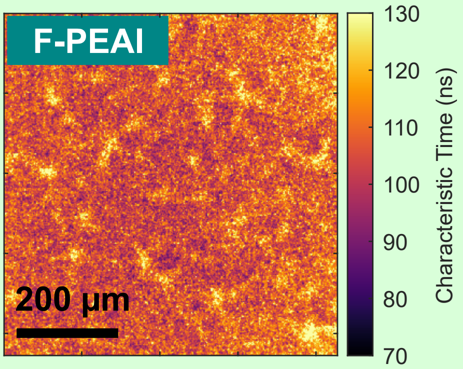

Result 3.1.3. Correlation of maps of $\Delta\mu$ and decay time τ measured on X-Ray damaged $Cs_{0.05}(MA_{0.14}FA_{0.86})_{0.95}Pb(I_{0.84}Br_{0.16})_3$ on Glass+FTO+TiO_2.

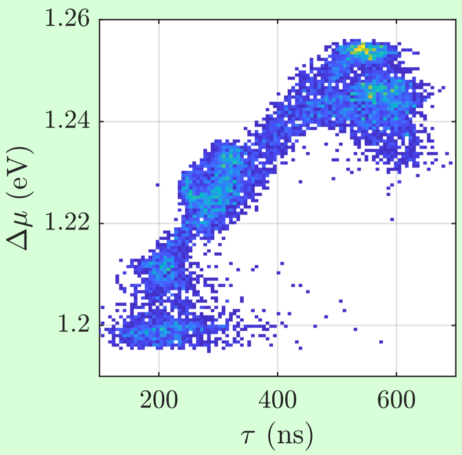

3.2 Why the lifetime notion is ambiguous

In this section, we show that the notion of lifetime is ambiguous for 2 main reasons: (i) multiple definitions of "lifetime" exist but not equal one to the other (ii) the lifetime is not only a measure of non radiative recombination because transport plays a role. To evidence more precisely the impact of transport we introduce a simulation tool that partially answers our title question "Why does the decay decay?". Therefore the first three subsections will show limits of the notion of lifetime (or decay time), but in the last we show that the local decay time correlates well with the quasi-Fermi Level splitting measured in continuous wave. For this, we will show a spatial pixel to pixel correlation between two images acquired on the exact same spot. Hence, this first section shows that the notion of decay time has limits but is nonetheless representative of the continuous wave operation of samples.

In the first subsection, we discuss toy models and definitions of lifetime in the literature. We show that multiple notions are called "lifetime" which is therefore ambiguous. Then, we discuss the impact of transport on the decay time. Next, we introduce and use a visualization tool (SIMPLED) to evidence that the decay time is influenced by both transport and surface recombination long after the pulse. This tool allows us to obtain the best conditions to measure decay times : at low excitation conditions and long after the pulse. Finally, we compare the decay time images to the continuous wave images of quasi Fermi Level splitting on the exact same spot of an inhomogeneous sample.

3.2.1 What is the lifetime? Definitions, toy models and flaws

Pulsed excitation: how it can affect the observed "lifetime"

In this subsection we discuss the notion of survival rate. Imagine a population of excited electrons at time t noted $n(t)$. We will note $\widetilde{\tau}$ the random variable that is the time of excitation of an electron. Let's assume that between t and $t+dt$ the population varies from $n(t)$ to $n(t+dt)$. Then, the probability for an electron to not "die" between t and $t+dt$ (survival rate) is linked to the density by:

$$P\left(\widetilde{\tau} \geq t+dt | \widetilde{\tau} \geq t\right) = 1 - \frac{n\left(t+dt\right)-n\left(t\right)}{n\left(t\right)} = 1 - \frac{dt}{n\left(t\right)} \times \frac{dn}{dt} \tag{3.3}$$

Thereby we obtain the following and intuitive formula where we assumed that n is a decreasing function of time:

$$\underbrace{P\left(\widetilde{\tau} \geq t\right)}_{\substack{\text{Probability that an e} \\ \text{has lftm} \geq t}} = \exp\left(-\int_0^t \frac{1}{n\left(t'\right)} \times \frac{dn}{dt}\left(t'\right) dt'\right) = \frac{n(t)}{n(0)} \tag{3.4}$$

With this intuitive formula we can give one definition of lifetime:

Statement 3.2.1. We define the "lifetime *in experiment E*", τ, as the average lifespan of electrons during *the experiment E*. In this case, knowing the temporal variation of $n(t)$, the density of excited electrons during this experiment, one may compute:

$$\tau \equiv \langle\widetilde{\tau}\rangle_{time} = \int_0^{+\infty} dtP\left(\widetilde{\tau} \geq t\right) = \int_0^{+\infty} dt\frac{n\left(t\right)}{n(t=0)} \tag{3.5}$$

We will give three examples to illustrate this definition.

1. In the case of the simplest model $n(t) = n_0 e^{-k_1 t}$ with $k_1 = 1/\tau_{\text{SRH}}$ the SRH time constant, see Statement 2.1.8. In this case we naturally obtain:

$$\tau \equiv \langle\widetilde{\tau}\rangle_{time} = \frac{1}{k_1} = \tau_{\text{SRH}} \tag{3.6}$$

2. For a radiative-recombination-only model with similar density of electrons and holes, one can show that the density evolves as:

$$n\left(t\right) = \frac{n_0}{1 + n_0 k_2 t} \tag{3.7}$$

   with k_2 the radiative recombination coefficient. In this case, the integral diverges: mathematically there is no mean "lifetime". As charges become less and less dense, the radiative process is slower and slower, explaining this divergence.

3. For a mix model with SRH and radiative recombination, one can show [Kirchartz *et al.* 2020]:

$$n\left(t\right) = \frac{n_0}{e^{k_1 t} + \left(e^{k_1 t} - 1\right) n_0 \frac{k_2}{k_1}} \tag{3.8}$$

   and in this case:

$$\tau \equiv \langle\widetilde{\tau}\rangle_{time} = \frac{1}{n_0 k_2} \ln\left(\frac{n_0 k_2}{k_1} + 1\right) \tag{3.9}$$

This last example is particularly striking: even in this very simplistic toy model with only bulk SRH recombination combined with radiative recombination, the definition of lifetime during the experiment is not equal to the SRH "lifetime" $1/k_1$. If one takes the limit of negligible radiative recombination, then Equation (3.9) does converge towards $1/k_1$. Notice also that Equation (3.9) shows the impact of the initial excitation condition here noted n_0. It is very unpleasant to obtain a lifetime that is not a characteristic of the semiconductor but that depends on excitation conditions.

Statement 3.2.2. In general, the lifetime is well defined if and only if the sample S **and** the experimental conditions E are well defined. The lifetime of sample S has no meaning unless the decay of S is purely mono-exponential. To obtain an information on the sample only, ie independent from the excitation conditions E, one has to choose *peculiar* conditions that are described below.

Continuous excitation: another notion of lifetime

In the continuous case, we can use the following definition for the lifetime. As we have a continuous regime we can write the equality between generation G and recombination R, see [Sinton and Trupke 2012]:

$$\tau_{\mathrm{cw}} \equiv \frac{n}{G} = \frac{n}{R} \tag{3.10}$$

For the simple model with radiative recombination and SRH:

$$G = k_1 n + k_2 n^2 \tag{3.11}$$

We obtain:

$$n = \frac{k_1}{2k_2}\left(\sqrt{1 + \frac{4Gk_2}{k_1^2}} - 1\right) \tag{3.12}$$

From which we determine the effective "lifetime" in the continuous regime to be:

$$\tau_{\mathrm{cw}} \equiv \frac{n}{G} = \frac{k_1}{2Gk_2}\left(\sqrt{1 + \frac{4Gk_2}{k_1^2}} - 1\right) \tag{3.13}$$

This expression may be written in the limiting case where $\frac{Gk_2}{k_1^2} \ll 1$. We write it "in inverse" mode because of reasons that will become clear in the next subsection (the total *rate* is the sum of all the *rates*). Up to order 1 in $\frac{Gk_2}{k_1^2}$:

$$\frac{1}{\tau_{\mathrm{cw}}} \approx k_1 + \frac{Gk_2}{k_1} \tag{3.14}$$

Therefore, even in continuous operation, the so called "lifetime" is injection dependent (through G). We also notice that the lifetime of continuous wave excitation is different from the pulse experiment one, unless one chooses condition where both become close to $1/k_1$, ie the low injection condition.

Full devices

For a full device, extraction of charges also takes place. Unless at open circuit, where the lifetime of charge carriers should come close to Equation (3.13). From the two following equations:

$$\begin{aligned} \Delta n^2 &= n_i^2 \exp\left(\frac{\Delta\mu}{kT}\right) \\ \Delta n &\approx G\tau_{\mathrm{cw}} \end{aligned} \tag{3.15}$$

One gets:

$$qV_{\mathrm{oc}} \approx \Delta\mu = 2kT \ln\left(\frac{G}{n_i}\tau_{\mathrm{cw}}(G)\right) \tag{3.16}$$

Where we write $\tau_{\mathrm{cw}}(G)$ to show how this quantity depends itself on the generation rate.

What is confusing is that theoretically the τ_{cw} put in Equation (3.16) is not the τ measured in the pulsed experiment Equation (3.9), even for these simplistic toy models that do not consider transport.

Statement 3.2.3. The notion of lifetime is flawed because in general the lifetime is dependent on the experimental conditions under which it is measured. To use this phenomenological notion, one should measure it in the lowest possible excitation conditions. Even then, the obtained rate is not necessarily relevant to explain device operation.

3.2.2 Comparison to continuous wave physics via Hyper Spectral imaging

In this subsection, we further discuss the comparison between pulsed and continuous wave experiments. This question has been the subject of some publications [Levine *et al.* 2018] but

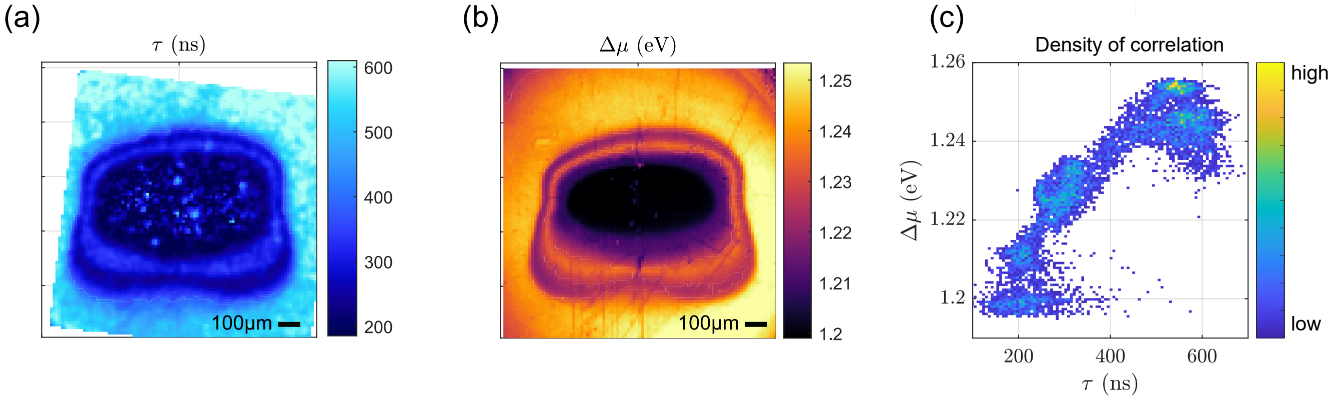

Figure 3.2: *(a) Decay time map (b) $\Delta\mu$ map (c) Pixel-pixel correlation where brighter color means higher density. The samples are $Cs_{0.05}(MA_{0.14}FA_{0.86})_{0.95}Pb(I_{0.84}Br_{0.16})_3$ deposited on Glass + FTO + TiO_2, and damaged by X-Ray on the center.*

here we tackle the local comparison of cw and tr behavior of the *same* sample. We compare the long time behavior of decays to the continuous wave characteristics, such as the continuous photo-luminescence intensity. Theoretical models such as Equation (3.16) give the link between "lifetime", open-circuit voltage and quasi-Fermi level splitting. But are those model accurate on real data? Our question is also: does the measurement of the pulsed "decay time" give a result that is relevant for continuous wave operation? We will prove that it is indeed the case.

We show an example of dataset where we could image locally exactly the same region in time resolved and in continuous wave excitation. We discuss the pixel-pixel correlation and find that it follows models such as Equation (3.16). From this model we are able to extract a measurement of the intrinsic carrier density of the perovskite film. Furthermore we are able to validate at the local scale the complementarity between hyperspectral and time resolved measurements.

One question that arises is the following: does the measured decay times match with the quasi-Fermi level splitting determination? This question can be reformulated into the following problem: how does our decay time imaging method compare to the well established hyperspectral imaging method? Or to put it into yet other words: do the measured decay times give information on the devices under study independently of the conditions under which they were measured?

To answer this question, we achieved to image the exact same region on the exact same sample on both the Hyperspectral (see [Delamarre 2013]) and TR-FLIM setup. The samples are composed of a IPVF perovskite baseline absorber

$Cs_{0.05}(MA_{0.14}FA_{0.86})_{0.95}Pb(I_{0.84}Br_{0.16})_3$ deposited on Glass + FTO + TiO_2, see Appendix C.1 for more details on the sample fabrication. The samples were exposed to X-Rays for different durations in order to perform X-Ray photo electron spectroscopy (XPS) analysis. XPS analysis allows for the precise characterization of the chemical bonds (and therefore species and their stoichiometry) present in the first nanometers of the studied layer [Cacovich *et al.* 2022a]. The samples were produced to study the degradation of the perovskite layer under X-Ray exposure. The particular sample we are using for the plots in this section was exposed 8 hours to X-Rays.The spot leaves a mark on the samples that is approximately 400 microns large. With this mark we can detect the location rather easily.

In Figure 3.2 we present mappings of decay time and of quasi-Fermi level splitting for the 8 hours spot. The mapping of decay time was obtained by fitting a dataset acquired under similar conditions as the ones described in Chapter 3.5 explained below. A mono exponential fitting was used in the temporal window of $[150, 600]$ ns. A Gaussian smoothing was applied on the data set of radius 2 pixels, for a 256 pixels wide image. Experiments were performed in protective atmosphere.

The quasi Fermi level map comes from a fitting of an hyperspectral imager (HI) dataset. This dataset was acquired with continuous wave illumination at 0.7 suns with a blue ($\lambda = 405nm$) LED in protective atmosphere. photoluminescence intensity was acquired locally and as a function of wavelength in the range [650 1000] nm. A fitting method based on the generalized Planck's law (Statement 2.1.1) was performed on the absolutely calibrated data set to obtain this map, see [El-Hajje *et al.* 2016].

A difficult and yet physically irrelevant task was performed to obtain the maps as presented in Figure 3.2 (a) and (b): we had to scale, rotate and translate the TR-FLIM decay times map to correspond to the QFLS map. This process was done by fitting the best transform in terms of correlation between the two maps. This explains why in Figure 3.2 (a), the image edges are rotated. We only plot the correlation for positions appearing in the two maps.

In Figure 3.2 (c) we present the local correlation between τ and $\Delta\mu$, where brighter color represents a higher number of pixels in this specific region. We see that there is a increasing relationship at the local level between both. This is expected with a relation ship such as Equation (3.16) that we recall here:

$$\Delta\mu = 2kT \ln\left(\frac{G}{n_i}\tau_{\text{cw}}(G)\right) \tag{3.17}$$

We discussed above that the decay time measured by TR-FLIM (or time resolved setups in general) τ is not always equal to the "lifetime" relevant to the continuous wave description τ_{cw}. However, we chose very low excitation conditions for the TR-FLIM acquisition and HI such as we assume that we have for this dataset:

$$\tau = \tau_{\text{cw}} \tag{3.18}$$

and therefore we expect in a very simplified model:

$$\Delta\mu \approx 2kT \ln\left(\frac{G}{n_i}\tau\right) \tag{3.19}$$

We stress that a more complicated model could be obtained via the use of Equation (3.13). The rest of this subsection shows that this more complicated model is not needed to interpret the data. A fit of Equation (3.19) on the whole dataset is presented Figure 3.3, red curve. We fitted only one parameter, G/n_i and obtain:

$$G/n_i = (1.33 \pm 0.01) \times 10^8 \text{ ns}^{-1}$$

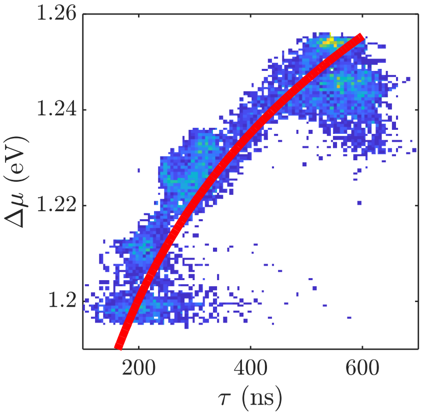

Figure 3.3: *Fitted correlation with Equation (3.19), with* $G/n_i = (1.33 \pm 0.01) \times 10^8$ ns^{-1}

The fit quality is acceptable, with a R^2 of 0.68. The obtained value can be compared to what is expected. HI measurements were performed at 7.25 mWcm^{-2} power. With a 405nm LED, a thickness of 400nm, we obtain $G = 3.7 \times 10^{20}$ cm^{-3}s^{-1}. This would give with our fitted value:

$$n_i \approx 3 \times 10^3 \text{ cm}^{-3}$$

This order of magnitude is very well in line with what is expected for a bandgap of 1.6 eV and densities of state similar than for other semiconductors, ie of the order of $N_{c,v} \approx 1 \times 10^{18}$ cm^{-3}.

The fact that this simplistic model is able to represent this highly non homogeneous dataset is remarkable. It implies that the intrinsic carrier density n_i was rather unaffected by X-Ray damage - that resulted mainly in a change of non radiative recombination.

To go into further details, we conducted a division of the τ and $\Delta\mu$ space into different regions, and observe *where* the corresponding pixels were located. The corresponding mappings are displayed in Figure 3.4. We have the following interpretation:

- The outer region is represented by the red and green (a) and (b) regions corresponding to decay times higher

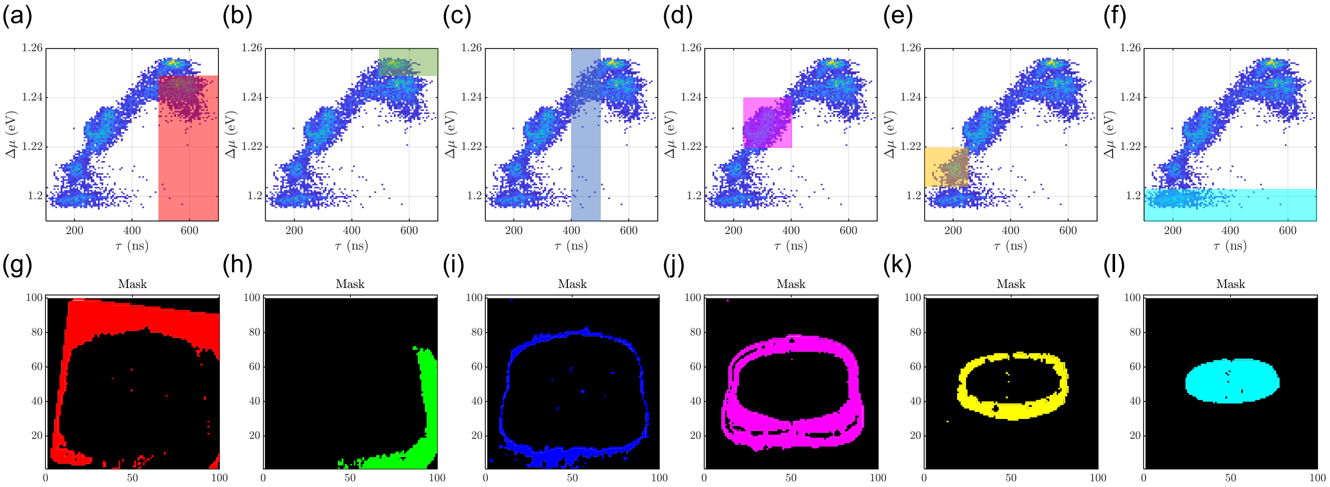

Figure 3.4: *Analysis of the areas of correlation. (first row) Masks chosen by hand in correlation space (second row) Corresponding pixels of the image with τ and $\Delta\mu$ values within the first mask in the first row.*

than 500 ns. The difference between the two regions likely results from a difference in illumination intensity in the hyperspectral acquisition resulting in a local change of G.

- Regions (c) to (e) represent three levels of rings around the X-Ray spot. The fact that a defined region in $(\Delta\mu, \tau)$ space results in such well defined spatial regions in the maps gives credit on the relevance of such correlation. Non radiative recombination increases as the distance to the spot edges decreases. The origin of these non radiative recombination could be explained by the electron current towards the spot due to electrons being ejected out of the sample by X-Ray absorption.
- Region (f) corresponds to the very center of the spot. We observe a wide range of decay times in this region. But as the luminescence levels inside the spot at long time is very low, we think that the transient data inside the spot comes with high uncertainty.

Statement 3.2.4. To conclude, we obtain a very coherent correlation between the pulsed experiment τ and the continuous wave $\Delta\mu$ at the local level. The analysis of the correlation gave us an estimate of the intrinsic carrier density of our film of $n_i \approx 3 \times 10^3$ cm^{-3}. The local analysis of the correlation evidenced that X-Ray damage mainly impacts non radiative recombination with a decreasing effect with the distance to the center.

This result indicates that if the decay time is measured in the correct way, it does represent non radiative recombination that are relevant to device continuous wave operation. But what is the "correct way"? Mainly at low fluence, and long after the initial condition, because, as the next section will evidence: transport does impact the measured value of decay time.

3.2.3 The impact of transport on the decay time

We will see in this subsection that when one includes transport in the equation, the decay time observed in the pulsed experiment is also modified.

As evidenced above, the best condition for the observation of an unaltered decay time are the low excitation conditions. In these conditions, radiative recombination may be considered negligible compared to non radiative recombination. Under this hypothesis, the drift-diffusion model Statement 2.1.8 may be solved analytically. This solution is analyzed in details in Chapter 5, as well as in [Maiberg and Scheer 2014, Weiss *et al.* 2019]. The axis are defined in Figure 3.5. Here we are interested in the following conclusion:

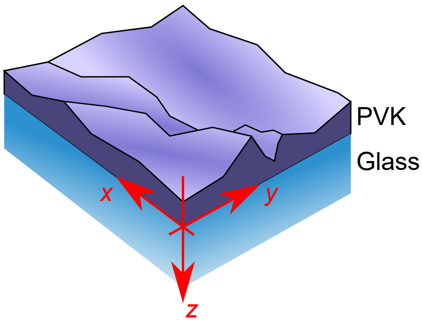

Figure 3.5: *Definition of the axis.*

Statement 3.2.5. In the case of negligible radiative recombination, the drift-diffusion model of Statement 2.1.8 may be solved analytically. It predicts that at long time the **carrier density** follows a mono-exponential decay:

$$\Delta n(z,t) \xrightarrow[t\to\infty]{} A_1 U_1(z) \exp\left(-\frac{t}{\tau_{\text{eff}}}\right) \tag{3.20}$$

with A_1 a constant, $U_1(z)$ a function of the space dimension z, and τ_{eff} the effective decay time that equals:

$$\frac{1}{\tau_{\text{eff}}} = k_1 + D\beta_1^2 \tag{3.21}$$

with β_1 the first strictly positive solution of the self-coherent equation:

$$\tan \beta_1 L = -\frac{D(S_{\text{top}} + S_{\text{bot}})\beta_1}{S_{\text{top}}S_{\text{bot}} - D^2\beta_1^2} \tag{3.22}$$

where

L = The device thickness
D = The diffusion coefficient
S_{top} = The top surface recombination velocity
S_{bot} = The bottom surface recombination velocity
k_1 = The bulk SRH recombination rate
τ_{eff} = The effective decay time **of the carrier population** (not of the PL).

Therefore, the inverse effective decay time τ_{eff} is the sum of a bulk contribution and of a surface/transport contribution:

$$\frac{1}{\tau_{\text{eff}}} = \frac{1}{\tau_{\text{bulk}}} + \frac{1}{\tau_{\text{surf+diff}}} \tag{3.23}$$

This decomposition is similar in its principles to Equation (3.14): the total rate is the sum of sub rates. To evidence the impact of diffusion and of the surface, let us use the simplifying hypothesis of (i) negligible bottom surface recombination. In this case, Sproul showed that a good approximation (less than 5% of error) of the solution of Equation (3.22) leads to [Sproul 1994]:

$$\frac{1}{\tau_{\text{eff}}} = \frac{1}{\tau_{\text{bulk}}} + \frac{1}{\underbrace{\frac{L}{S_{\text{top}}}}_{\text{Surface rec.}} + \underbrace{\frac{4}{D}\left(\frac{L}{\pi}\right)^2}_{\text{Diffusion}}} \tag{3.24}$$

There are two limiting case to understand from this expression: one is the case of very high surface recombination, ie $L/S_{\text{top}} \ll L^2/D$. In this case, the carriers have virtually infinite recombination at the top surface but recombination is still limited by the carrier supply chain: it takes time for carrier to diffuse to their almost certain death. Therefore, in this limit, the surface and diffusion time is limited by diffusion.

In the other extreme limit, almost no recombination takes place at the top surface. In this case, the surface and diffusion time becomes virtually infinite, because no carriers recombine at the top interface. In this limit, $\tau_{\text{surf+diff}} \longrightarrow \infty$ and therefore, the effective decay time becomes close to the bulk decay time, according to Equation (3.23).

Orders of magnitude. For a 300 nm thick absorber, with a diffusion coefficient of approximately $D = 1 \times 10^{-2}\,\text{cm}^2/\text{s}$, the diffusion part equals: $\tau_{\text{diff}} = \frac{1}{D}\left(\frac{L}{\pi}\right)^2 \approx 10\,\text{ns}$. For a surface recombination $S_{\text{top}} = 100\,\text{cm}\,\text{s}^{-1}$, then the surface time equals $\tau_{\text{surf}} = \frac{L}{S} = 300\,\text{ns}$. Therefore for practical application on perovskite, neglecting bottom surface recombination:

$$\frac{1}{\tau_{\text{eff}}} \approx k_1 + \frac{S}{L} \tag{3.25}$$

Therefore to conclude this subsection, we showed that transport had a major impact on the decay times that can contain information on the diffusion process in addition to non radiative recombination. Therefore **the decay time is not directly a measure of non radiative recombination**. The impact of transport for the continuous wave case is discussed in the literature, see [Sinton and Trupke 2012, Giesecke *et al.* 2010, Michl *et al.* 2012].

For the question of **lateral transport** we have the following remark. For the imaging cases, carriers will be able to travel laterally approximately one or two diffusion lengths which is defined by $l_D = \sqrt{D\tau}$. The diffusion length is much smaller than the pixel size of the images acquired for most cases, therefore the lateral diffusion does not need to be taken into account. Indeed, the diffusion length is expected to be at maximum $l_D \approx 1\mu m$ for the layers studied in this work, and for instance in Figure 3.2 the pixels are $10\mu m$ wide.

In the next subsection, we show a visualization tool that we developed to quantify what physical cause is responsible for the decay at each instant of time, including transport.

3.2.4 Why the decays decay: introducing a new interpretation tool, the SIMulated PL Element Decomposition (SIMPLED) plot

We saw that multiple processes are intertwined and act upon the observed decay time: at least bulk recombination, surface recombination and diffusion. To better understand and visualize the relative importance of each of the contribution, we developed the SIMPLED plot : SIMulated PL Element Decomposition. In this subsection we explain the theoretical background and show example use cases.

The SIMPLED analysis starts with one simple question: in a pulsed experiment why does the luminescence intensity decay? Why does "the decay" decay? If this question seems trivial, it holds physical interest in that it reveals that the PL signal is forged from multiple phenomena. To answer this question let us take a look at the derivative of the PL, from a theoretical point of view. By differentiating Eq. 2.11 and using the drift-diffusion equation 2.7, one can show that:

TR-PL Simulation @150sun

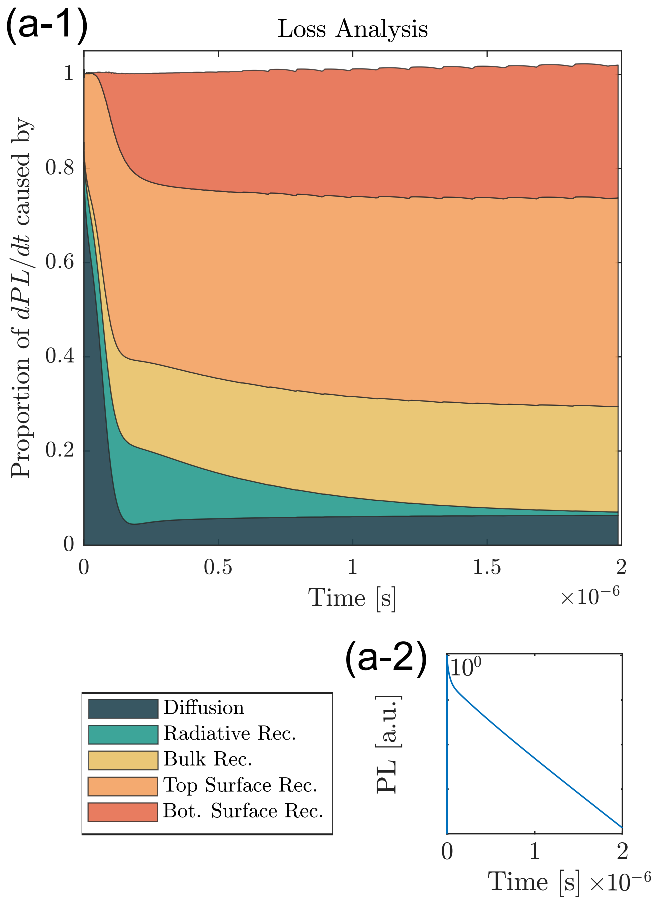

Electrical Simulation @1sun

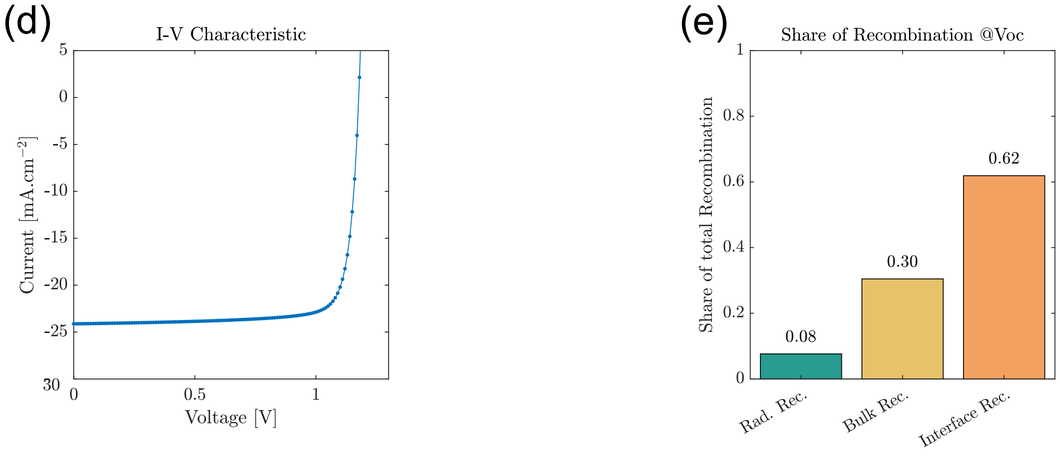

Figure 3.6: *SIMPLED plot. (Top Panel). TR-PL simulation performed on an absorber with the drift-diffusion model (Table 3.1), @150sun laser fluence, 2μs-long after which 98% of photo-generated carriers have recombined. (a-1). SIMPLED plot: Sources of the decay as a function of time. (a-2). Corresponding TR-PL decay (b). Integrated share of the derivative of the PL during the simulation per source. (c) Integrated share of recombination paths for carriers during the simulation. (Bottom Panel) Corresponding opto-electrical simulation with SCAPS1D (d). I-V curve for a pin device structure with the same absorber characteristics as for the left panel. Measures :* $V_{oc} = 1.18\ V$, $J_{sc} = 24.12\ mA.cm^{-2}$, $FF = 82.26\%$, $PCE = 23.35\%$. *(e). Share of recombination paths for carriers at* V_{oc}.

$$\frac{dI_{\mathrm{PL}}}{dt}(t) = -2A\Bigg[\underbrace{k_1\int_0^L dz\ \Delta n^2}_{\text{(i)}} + \underbrace{S_{top}\Delta n^2\left(z=0,t\right)}_{\text{(ii)}} + \underbrace{S_{bot}\Delta n^2\left(z=L,t\right)}_{\text{(iii)}} + \underbrace{D\int_0^L dz\ \left(\frac{\partial \Delta n}{\partial z}\left(z,t\right)\right)^2}_{\text{(iv)}} + \underbrace{k_2\int_0^L dz\ \Delta n^3}_{\text{(v)}}\Bigg] \tag{3.26}$$

Each of these terms can be given a physical interpretation: the first one is caused by bulk SRH recombination, the following two by top and bottom surface recombination while the (iv) one is due to diffusion. Let us stress here that diffusion alone can cause a decay, which might seem surprising. This comes from the definition of the local PL emission as the square of the excess carrier density which makes the global PL signal intensity dependant on the spatial carrier profile. This would not be the case for a doped material. The last term (v) is due to radiative recombination.

Method

Our SIMPLED method is the following:

1. Choose a set of parameters that describe the sample under study.
2. Use numerical simulation tools to obtain the function $\Delta n(z,t)$ for a given time and space interval.
3. Use Equation (3.26) to compute terms (i) to (v) that are functions of time only noted $R_{\text{(i)},\text{(ii)},\ldots}(t)$.
4. Use Equation (2.11) to compute the numerical values of $I_{\mathrm{PL}}(t)$
5. Normalize all the computed $R_{\text{(i)},\text{(ii)},\ldots}(t)$ by the function $I_{\mathrm{PL}}(t)$ to obtain the ratios $R'_{\text{(i)},\text{(ii)},\ldots}(t) = R_{\text{(i)},\text{(ii)},\ldots}(t)/I(t)$ that are between 0 and 1.

With this procedure, one can attribute a **weight** to each physical cause at each time of the decay. One can model these causes and observe their relative influence on the decay as a function of time by computing the given integrals.

Result

We apply this procedure and obtain the plot in Figure 3.6 (a), with the simulation parameters given in Table 3.1. In (a-1) the sources are plotted as a function of time, normalized

Symbol	Name	Value	Unit
α	Absorption coefficient	1.3×10^5	cm^{-1}
L	Thickness	500	nm
D	Diffusion Coefficient	4.5×10^{-3}	$cm^2\ s^{-1}$
k_2	Radiative Rec. Coefficient	2.9×10^{-11}	$cm^3\ s^{-1}$
k_1	Order 1 Rec. Coefficient	3.9×10^5	s^{-1}
S_t	Top Surface Rec. Velocity	50	$cm\ s^{-1}$
S_b	Bottom Surface Rec. Velocity	25	$cm\ s^{-1}$

Table 3.1: *Model Parameters for the SIMPLED analysis. These parameters were chosen as parameters representative of the triple cation perovskite layers on glass.*

at each instant of time. We can observe that diffusion is responsible for the short-time dynamics. We can observe that some recombination channels are only influential after some time, namely the bottom surface recombination and the bulk SRH recombination.

In (b) the overall share of PL decay per source is presented, as the share of each source to the sum of the derivative over the time of the simulation. We see that diffusion is responsible for most of signal decay, and therefore, the decays need to be carefully interpreted, especially at short time. In comparison, we plot in (c) the recombination paths: the proportion of each type of recombination. The two interfaces play an important role in the overall recombination of the carriers. We also note that diffusion plays a role during the complete decay, not only at short time. This is compatible with the theoretical equations for instance Equation (3.21) where diffusion explicitly appears. Moreover we stress that radiative recombination appear to shortly become negligible compared to other sources of decay. This could be puzzling because the radiative recombination represent 100% of our signal! The reason behind this is the realization that even if we use radiative recombination as our inspection tool, they only represent a small "perturbation" term compared to the other processes at play such as diffusion but mainly non radiative recombination.

One could wonder how the pulsed laser experiment compares to the continuous wave excitation of the sun. This comparison is done in the bottom panel of Figure 3.6. We used a simulation software named SCAPS 1D [Burgelman *et al.* 2000] to simulate a device with the same absorber as the one used to simulate the left panel. In (d) the main figure of merit for a solar cell is plotted: the IV curve, while we present the share of recombination at V_{oc} in (e). SCAPS 1D does not distinguish between the two surfaces in this case, this is why they are grouped under the "Interface Rec." category. Overall we see that the share of recombination is quite similar to (c): the interfaces play an import role in both cases. The radiative recombination are smaller in the electrical case, as expected because the pulsed simulation was performed at substantially higher excitation intensity. Even if the comparison between the excitation in the pulsed and continuous regime is not necessarily straightforward, as evidenced above.

From the SIMPLED analysis, we can say that the TR-PL experiment can be difficult to interpret as many microscopic causes play a role in the final shape of the decay. However, the leading recombination relevant for the IV curve and therefore energy application, are expressed in the time resolved PL pulsed experiment. This shows the great potential of correct measurement of the cell via TR-PL as a tool to analyze the recombination paths in the device.

Statement 3.2.6. The SIMPLED tool shows that after some time (that depends on the excitation conditions, order of magnitude for triple cation perovskite: 200ns) the distribution of causes of the PL decay remains constant in time. This time region with the constant distribution is the one where the decay usually becomes monoexponential. This mono exponential decay is a mixture of interface recombination, bulk recombination as well as diffusion.

This is in total agreement with the description given above for the value of the effective decay time, for instance Equation (3.23).

The SIMPLED visualization also helps in understanding what parameters may be obtained from which part of the experimental decay curve. For instance radiative recombination only takes place at short time and high excitation conditions. This will be employed in Chapter 4 when the scaling law for the short time will be introduced.

3.2.5 Conclusion

Therefore we showed in this section that the notion of "lifetime" is ambiguous. Many definitions exist and it is rarely independent on excitation conditions. Moreover, the decay time for the pulsed experiment may contain information on diffusion in addition to non radiative recombination. Nevertheless, if measured in the lowest possible fluence and long after the pulse, one can obtain decay times that compare very well to continuous wave measurement. The SIMPLED analysis allows to visualize the best conditions to find the correct measurement regime.

3.3 Measuring decay times images: methods, examples, pitfalls

In the previous section we showed how careful one needs to be when using the notion of lifetime or decay time. In this section we present the opportunities brought by this measurement technique in terms of imaging: when used with care, decay time imaging does bring insight on the recombination inhomogeneities of the sample(s) under study.

In a first subsection we present result obtained *with a basic technique* on state of the art double cation triple halide and 2d-passivated perovskite layers from a collaboration with the University of Pavia. These results show how **decay time imaging proves homogeneous passivation of the samples.**

Then we present a *new technique* we developed, named LGA for "Large Gate Acquisition", and its application to $FAPbI_3$ samples, from another collaboration with EPFL, that exhibit wonderful lateral inhomogeneities. We discuss the interest of the technique in terms of signal to noise ratio, as well as its limitations. We show that together with thickness measurement, **the decay time imaging technique can show inhomogeneities in the non radiative recombination** within pseudo-grains of the grown $FAPbI_3$.

Finally we show some promising results obtained on the technique itself with a (last) collaboration with INRIA, trying to answer the following question: what is the best way to compute the decay times map from a given dataset? Regularization algorithms show promising improvements of the reliability of the obtained decay time map.

3.4 Lifetime imaging to prove the homogeneity of passivation on state of the art perovskite

This subsection is based on a publication in collaboration with Pavia university and Giulia Grancini's group. Our publica-

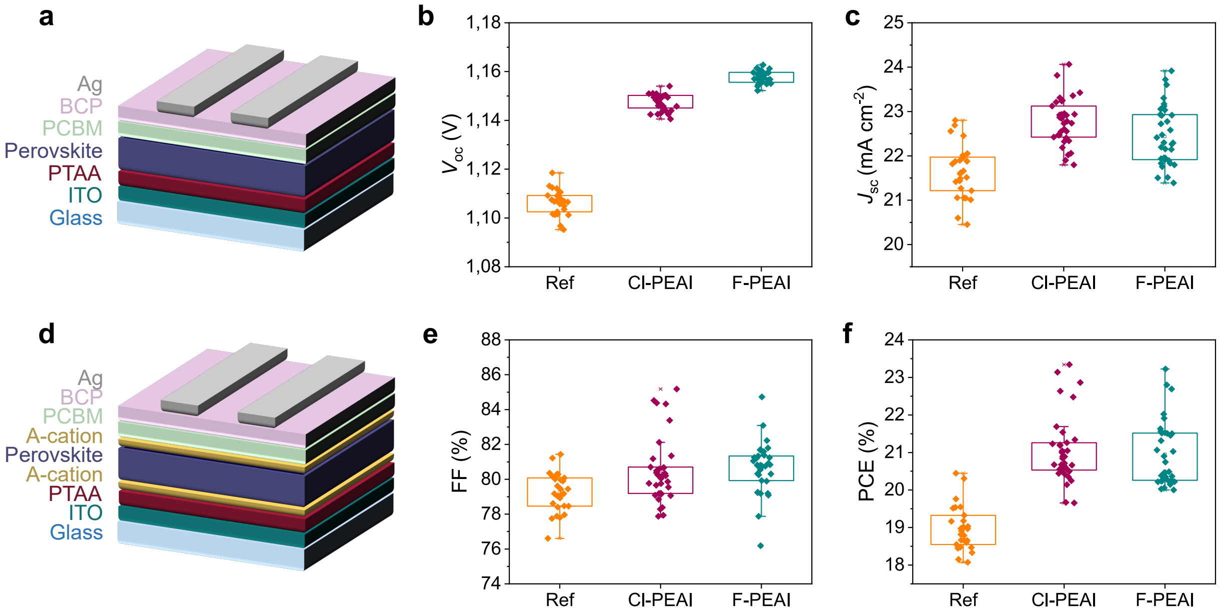

Figure 3.7: *Electrical characterization of the samples. Schematic of the reference samples (a) and of the A-cation p-i-n devices with dual interfacial modification (d). Photovoltaic characteristics of reference (orange), Cl-PEAI (purple) and F-PEAI (teal blue) devices. b) Open circuit voltage (V_{oc}) c) Short circuit current (Jsc) e) Fill Factor (FF) f) Power conversion Efficiency (PCE). Reproduced from [Cacovich* et al. *2022a]*

tion is available at: [Cacovich *et al.* 2022b]. **We use text of the publication in this text.** This collaboration aimed at characterizing the passivation of full cells by the addition of a "2d"-perovskite layer. In this subsection we show how decay time imaging may be used to evidence the homogeneity of passivation effects of 2d layers in perovskite bases pin solar cells. We also show that the "regular" technique we employed needed to be improved in order to get better signal to noise ratio. With the regular technique we were able to compare samples from one to the other but not obtain clear inside-sample comparison of decay times. The new LGA technique is presented in the next section.

3.4.1 Description and main findings of the study

In this study, we focused on the passivating role of 2d perovskite layers on state of the art inverted pin perovskite solar cells from the collaboration with Pavia University. We proved that their main effect was to passivate the interface between the perovskite and the ETL, the interface with the HTL being only slightly improved. Specifically, two large organic A- site cations, i.e. 4-chloro-phenylethylammonium iodide (Cl-PEAI) and 4-fluoro-phenylethylammonium iodide (F-PEAI), were introduced at the interfaces of the perovskite absorber with both hole transport layer (HTL) and electron transport layer (ETL). Questions regarding the physics behind the modified interfaces are still open [Kim *et al.* 2021]. Issues regarding the completeness of the coverage of the passivating layer [Mahmud *et al.* 2020], whether a 2D perovskite is formed or not [Sutanto *et al.* 2020, Rahmany and Etgar 2021], and the possible effects on carrier extraction remain not fully understood. In a more general way, several studies focused on the recombination dynamics at the perovskite/selective interfaces by tracking the photoluminescence signal and its intensity[Kirchartz *et al.* 2020, Krückemeier *et al.* 2021a, Goetz *et al.* 2020]. For instance, the contributions of bulk and interfacial recombination currents were decoupled through the measurements of the quasi-Fermi level splitting (QFLS) of the individual layer by all-optical techniques [Sarritzu *et al.* 2017]. Stolterfoht and co-workers used transient and absolute PL imaging to visualize non-radiative recombination pathways at modified perovskite/C_{60} [Stolterfoht *et al.* 2018] electron transport layer. In this study we combined steady-state and time-resolved multidimensional photo-luminescence imaging techniques to probe the main opto-electronic and transport properties of the optimized p-i-n devices.

The devices under investigation follow a p-i-n structure, as shown in Figure 3.7 a and d. The mixed cation double halide composition is ($Cs_{0.05}(FA_{5/6}MA_{1/6})_{0.95}Pb(I_{0.9}Br_{0.1})_3$), with an addition of piperidinium salt [BMP]+[BF4]20,21-. Three different types of cells were fabricated: a reference cell (Figure 3.7 a) and devices with dual interfacial modification by F-PEAI and Cl-PEAI cations (Figure 3.7 d). The main photovoltaic characteristic parameters for the reference cell and the A-cations devices are reported in Figure 3.7 b, c, e and f. The addition of the cations induced an increase of all the main photovoltaic characteristics. The PCE of the devices in which both absorber interfaces were modified by A-cations is clearly enhanced, exhibiting values up to 23.34% for the Cl-PEAI and 23.22% for the F-PEAI. In particular, we can note a clear increase of the Voc from 1.10 V for the reference to 1.15 V using Cl-PEAI and exceeding 1.16 V using F-PEAI, which corresponds to a tenfold decrease of the dark current, i.e. of the carrier recombination rate. The current also slightly improved, in contrast with some previous observations in the literature, where the full formation of a 2D perovskite layer was acting as a blocking layer [Sutanto *et al.* 2021]. Remarkably, fill factor reached values up to 85 % on the Cl-PEAI and

F-PEAI devices, within the highest ever reported for halide perovskite solar cells. Also, the devices do not show any hysteretic behavior.

To evidence the role of passivation of these layers, we used photo-luminescence imaging techniques, both time resolved (TR-FLIM) and spectrally resolved (Hyperspectral). We used the main advantage of photo-luminescence studies: they can be performed on unfinished devices, ie thin films on glass and half cells. We also measured the full cells. Thanks to this step by step measurement we evidenced that the passivating role of F-PEAI and Cl-PEAI takes place at the ETL/Perovskite interface. Indeed, no clear passivation effect was observed on thin films and on half devices with the HTL. The main results are presented in Figure 3.8 where spectra as well as temporal decays are displayed for full cells and thin films. In Figure 3.8b, the obtained QFLS for the different stacks are displayed, evidencing that the passivation mainly takes place at the ETL/perovskite interface.

In this section, we focus more precisely on the homogeneity of the passivation that our imaging techniques allow to verify. We will develop more on the quantitative models in Chapter 4.

3.4.2 Decay time imaging

As explained in the Methods chapter, we performed experiments in Nitrogen atmosphere, homogeneous illumination by the Talisker laser (532nm) at low repetition rate (40kHz). We have two sets of acquisitions for each sample, one with a fluence of $1.5 \times 10^{12}\,\mathrm{phcm}^{-2}$ (high fluence) and one with a fluence of $1 \times 10^{11}\,\mathrm{phcm}^{-2}$ (low fluence).

We use the high fluence acquisition to compute the decay times map because the low fluence acquisition presented too low SNR at long time. This is one of the limit of this dataset, because we showed that the decay time imaging needs to be performed in the **lowest** excitation possible. This is why we spent time after this study to design a new technique to perform high SNR low fluence decay time imaging: the LGA (Large gate acquisition) technique.

A x10 objective was used in confocal configuration, and the laser was filtered out with a dichroic beam splitter as well as with a long pass filter. Each acquisition was repeated two times in a row to check for any reproducibility issue (none was found) and to obtain a better average signal to noise ratio. To obtain the mapping of the decay time, we used our TR-FLIM acquisitions. One issue that arises is the noise at the level of each pixel. To be able to average out noise at the local level, we performed a temporal mean of the logarithm of decays

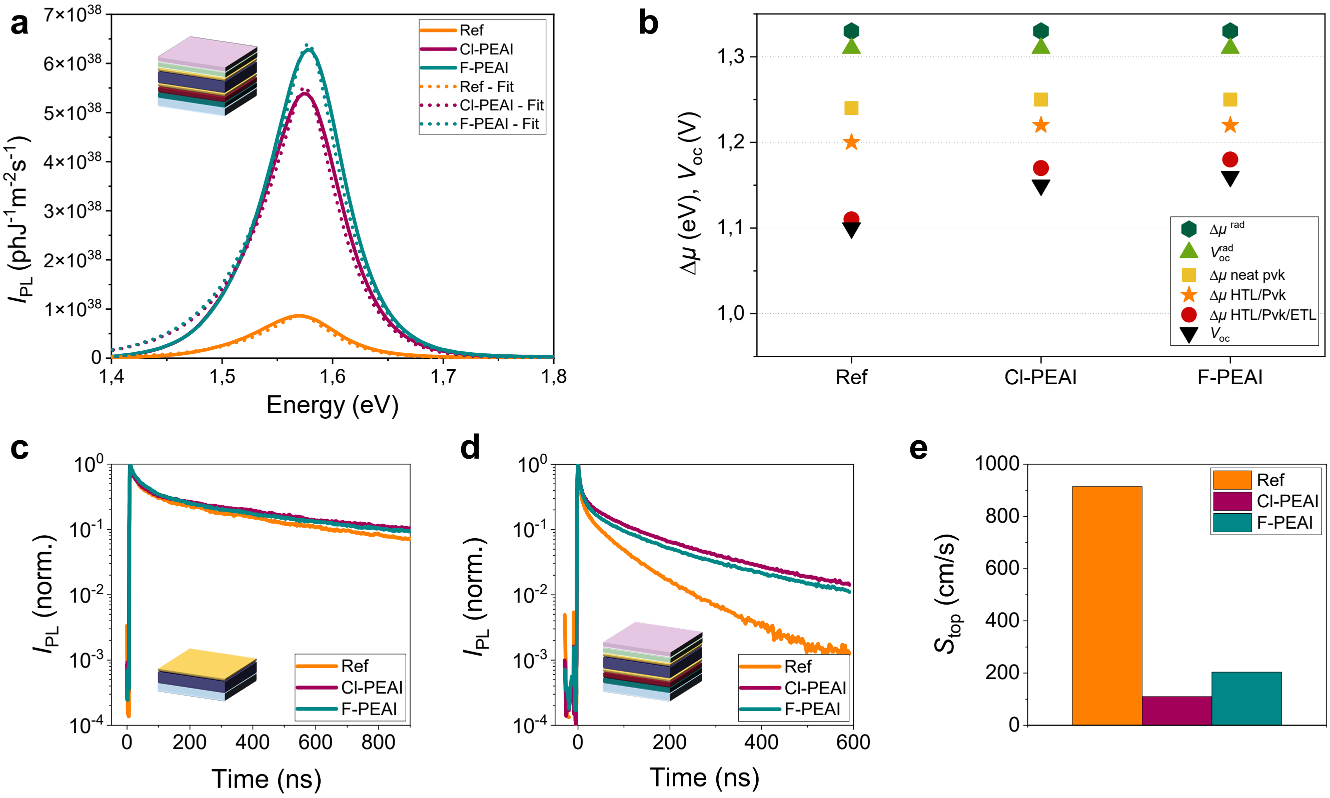

Figure 3.8: *Spatially averaged photo-luminescence analysis in the continuous wave and time resolved regime. a) photo-luminescence average spectra and corresponding fits acquired on the stack glass/ITO/PTAA/perovskite/PCBM/BCP samples. PL spectra were acquired on reference (orange), Cl-PEAI (purple) and F-PEAI samples (teal blue). b) QFLS values extracted from PL spectra for neat perovskite, half cells and full devices compared with radiative QFLS* $\Delta\mu_{rad}$*, open circuit voltage* V_{oc} *and radiative open circuit voltage* V_{oc}^{rad} *. TR-FLIM (spatially integrated) decays acquired at* $1 \times 10^{11}\,\mathrm{phcm}^{-2}$ *fluence for c) perovskite layers deposited on glass, top illumination and d) full cells without top bottom electrode, top illumination. e) Comparison of the fitted top surface recombination rate on full devices. Reproduced from [Cacovich et al. 2022b]*

of each pixel on different temporal windows noted $[t_i; t_{i+1}]$. Namely, we averaged the decays in the logarithm space and created a new dataset PL':

$$PL'\left(\frac{t_i + t_{i+1}}{2}\right) = \exp\left(\frac{1}{t_{i+1} - t_i}\int_{t_i}^{t_{i+1}} dt \log\left(PL(t)\right)\right) \tag{3.27}$$

This is justified in the case of a mono-exponential decay, which we expect here after ≈100ns after the pulse. We used the following time windows limits:

$$\{t_i\} = [90 \quad 140 \quad 190 \quad 290 \quad 490] \text{ ns} \tag{3.28}$$

This principle is sketched in Figure 3.10 on a decay obtained by the taking the spatial average over the whole image.

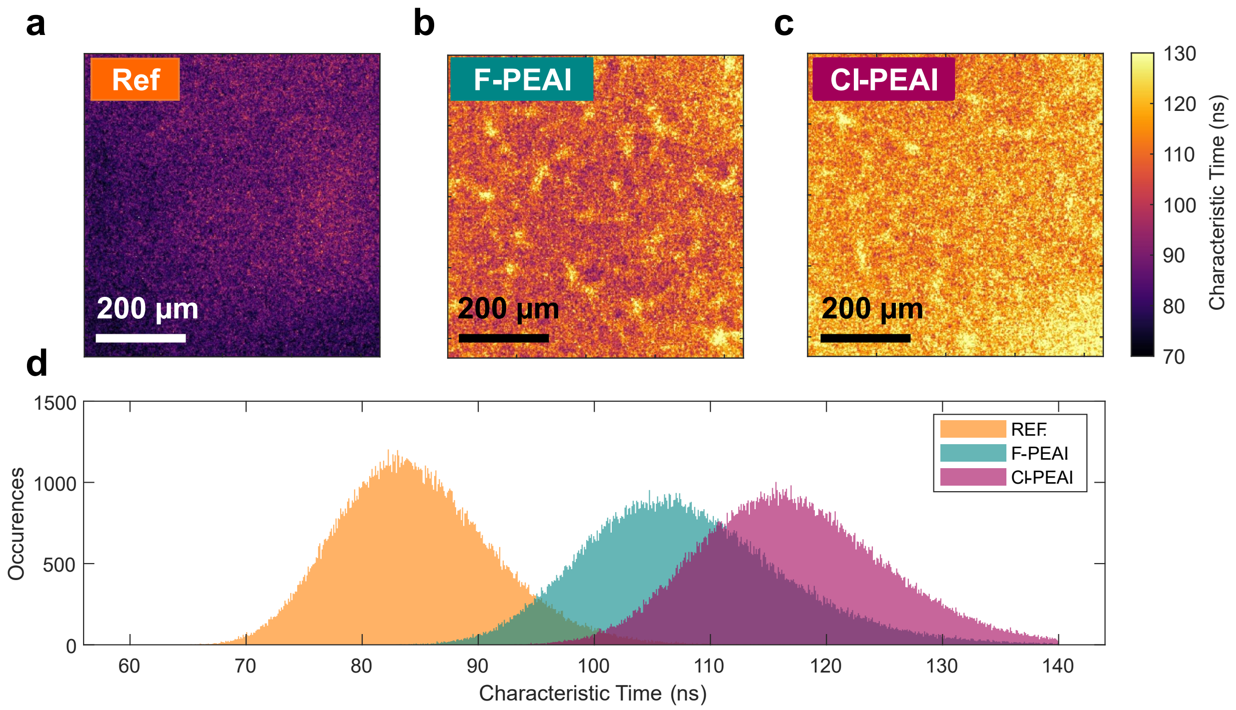

Figure 3.9: *(a-c) Map of decay time obtained on full-stacks (glass/ITO/PTAA/perovskite/BCP/PCBM) for the high fluence (1.5* 10^{12} *ph.cm*$^{-2}$*) acquisition for the reference and two passivation strategies. (d) Histograms of the corresponding decay times values. Reproduced from [Cacovich et al. 2022b]*

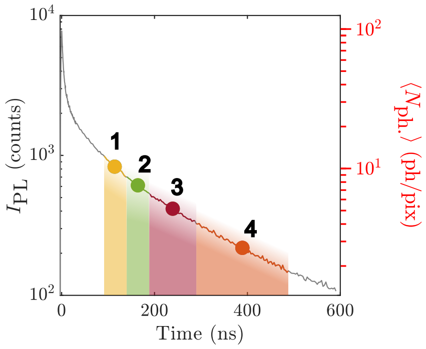

Figure 3.10: *Principle of computation the decay time meta images. We obtain 4 frames from averaging all the frames in the shaded intervals as exlained in Equation (3.27). Decay from the high fluence acquisition for the Cl-PEAI full cell.*

This principle could be called ”a posteriori” large gates imaging. A posteriori because we do this computation after the acquisition, and not during as is shown in the next section. ”Large gate imaging” because we artificially increase the gate width to obtain better SNR, see the discussion below.

We obtained a set of 4 values of PL’ for each pixel, shown in Figure 3.11 for the Cl-PEAI acquisition, from which we extracted the local decay time.

3.4.3 Discussion on the obtained decay times images

The decay time results are presented in Figure 3.9. Overall, an excellent homogeneity was achieved at the 1 mm^2 scale for the F-PEAI and Cl-PEAI samples. The histograms of Figure Figure 3.9 (d) display that the difference between reference and modified samples in terms of non-radiative recombination is statistically significant. The mean decay time on the maps extracted from the high fluence acquisitions are found to be 84.6 ns for the reference, 107.9 ns for the F-PEAI and 117.35 ns for Cl-PEAI. The images of the passivated layers show a slightly wider distribution of decay time, compared to the reference sample with a standard deviation of 6.7ns for the reference and 8.7ns and 8.2 ns for the F-PEAI and Cl-PEAI, respectively. This analysis provides us with an approximate estimate for the uncertainty and noise level on the images. The **decay time maps thus show the homogeneity of the interfacial cation addition treatment** resulting in a uniform improvement of decay times for the A-cation modified devices, further confirming the reduction of non-radiative recombination.

Therefore we evidenced an homogeneous passivation effect of the 2d layers on the perovskite full cells. But this passivation effect on the decay times could potentially also come with a decrease of the output current of the devices, which would render it rather useless for solar cell application. It is not the case, as electrical IV curve measurement showed, see Figure 3.7. The short circuit current is even slightly improved by the 2d layer deposition. Moreover, the open circuit voltage does follow the trend obtained in continuous wave photo luminescence and of the found decay times. Therefore the 2d layers do reduce non radiative recombination while not blocking the charges.

3.4.4 Discussion on the signal to noise ratio of the regular decay time technique

In terms of number of incoming photons, with our camera calibration we are able to put the intensity of Figure 3.10 in units of incoming photons per pixel per frame, see the red right axis on the figure. We used the procedure described in Statement E.2.2.

We see that the number of photons per pixel and per frame is quite low: it reaches levels close to unity, and this even for the high fluence acquisition. For Poisson processes, where we expect an error in square root of the incoming signal, this low number of photons goes along a high uncertainty on the signal. With our a posteriori averaging procedure where we average N frames, we would at maximum increase the SNR of our newly created frame by a factor $\sqrt{N}$. (To show that, one can assume that Equation (3.27) is written as a sum of random variable of similar Poisson like distribution. Then, many hypothesis are needed the main one being that the PL intensity is constant in time.). For frame 4, the number of averaged frames is $N = 65$ so this gives us a maximal improvement of the SNR by a factor 8. With a signal intensity of approximately 3 ph per frame and per pixel, it started from a SNR of $\sqrt{3} \approx 1.7$ to a final SNR of maximum $SNR_{\text{a post.}} \approx 13$.

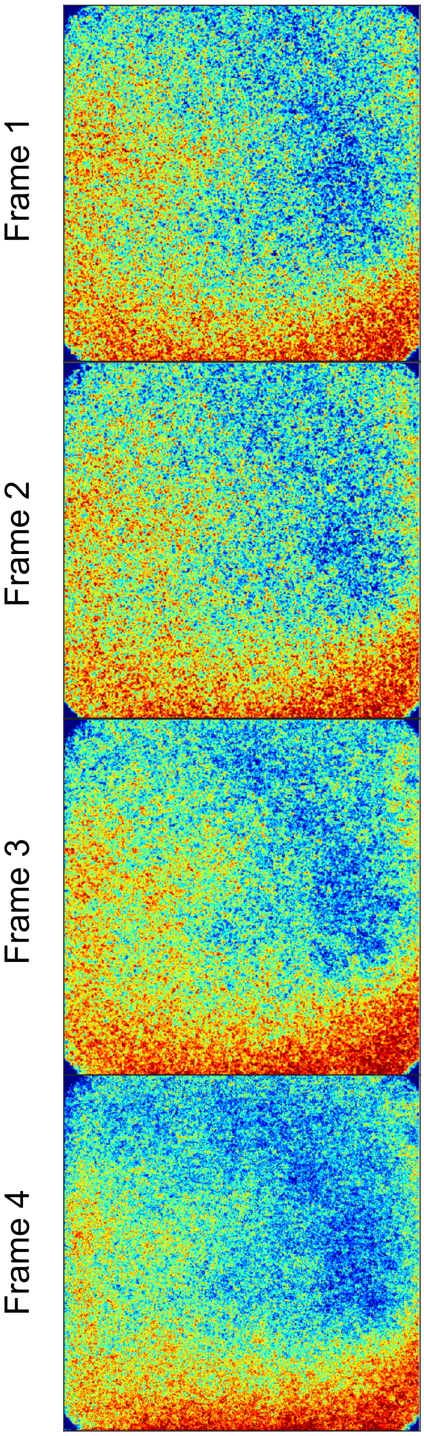

Figure 3.11: *The obtained 4 frames for the CL-PEAI acquisition after averaging, see Figure 3.10. The colorscale is individual to each frame and does not allow to compare one frame to the other.*

Result 3.4.1. Therefore, we showed how decay time imaging may be used to evidence the homogeneity of passivation effects in perovskite based pin solar cells. Nonetheless, the ”regular” decay time imaging technique does suffer from low SNR.

3.5 New method for lifetime imaging for the characterization of $FAPbI_3$ polycrystals

We developed a new decay imaging technique for the study of $FAPbI_3$ thin films, thanks to collaboration with Sandy Sanchez at EPFL in Michael Graetzel's group. A publication was just accepted [Sánchez *et al.* 2022] and the results here are partially taken from this publication. The main question of this paper concerns the quality of the obtained $FAPbI_3$ films as a function of the heating rate of their annealing. Indeed at room temperature, $FAPbI_3$ should thermodynamically convert to a “yellow” δ non-perovskite phase that is cubic Pm-3m as shown by neutron diffraction. The interesting phase for PV application is the ”black” α phase, which can become meta-stable at room temperature after annealing. In this study, the annealing system developed by Sanchez and coworkers is used at different heating rates [Sanchez *et al.* 2018, Sánchez *et al.* 2019, Sánchez *et al.* 2020a, Sánchez *et al.* 2020b, Sánchez *et al.* 2021]. Our role in the collaboration was to perform luminescence imaging on samples in the α perovskite phase obtained with **three different heating rates** designated S1, S2, S3 in this text. We were able to use **time resolved decay time imaging to evidence that the micro domains formed during the annealing do not have homogeneous recombination properties**. Moreover, between micro domains, high recombination as well as spectrally shifted emission occurs.

To obtain this result we needed a new decay time imaging technique: designated as ”Large Gate-width Acquisition” or LGA. We saw in the previous section how low the SNR of decay time images could be. We proposed a ”a posteriori large gate width” method that did increase the SNR. Here the large gates are used *during* the acquisition. Increasing the gate width has two effects. One, it naturally increases the number of photon per frames, as the amount of time the camera is acquiring is increased. But as shown in Figure 2.12, the camera sensibility is also increased for higher gatewidths compared to the 3 ns gatewidth for instance. These two effects allow for even higher SNR to be reached. Moreover, using the "repetitive mode" of the camera, a higher number of repetitions of the same acquisitions may be measured than in the "sequential mode" that has a capped number of accumulations.

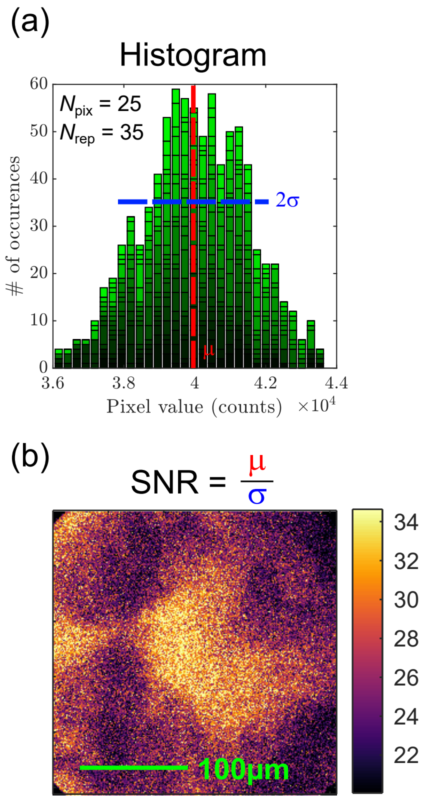

Figure 3.12: *Histogram of the first frame for 25 pixels in position X= [100,105] and Y=[200,205]. Each shade of green represents the histogram of one of these pixels. They are stacked to illustrate the general trend. (b) Signal to noise ratio mapping for Frame 1.*

3.5.1 Description and main findings of the study

The process of Dr Sanchez leads to highly stable black $FAPbI_3$-based perovskite solar cells using the optimal film crystallization processing parameters, with an annealing time of just 640 ms. They achieved a 18.5% power conversion efficiency (PCE) with the champion device in the absence of any additives, incurring merely a 10% loss in PCE during maximum power point tracking for 1500 h under full solar intensity exposure of the devices (in Nitrogen).

The samples we studied at IPVF were however simpler: $FAPbI_3$ layers on Glass+FTO annealed with three different rates designated by S1, S2 and S3. The samples show grain domains with varying size depending on the rates.

3.5.2 Description of the "LGA decay time technique"

We use the repetitive mode of the camera as well as the automation codes, described in the Methods chapter. The principle is to assemble multiple "one"-frame-acquisitions with varying gate width and delay into one cube of data. To assemble them, one needs the calibration function of our camera, as also described in the Methods section. **The calibration of the camera is the key that allowed us to create the LGA technique.** For this dataset, the following parameters were used for the acquisition: Each individual acquisition uses $N_{\text{acc}} = 65000$ accumulations.

Frame	Delay (ns)	Gate Width (ns)
1	0	3
2	180	10
3	280	30
4	480	60
5	780	100
6	1280	100
7	1780	100
8	2280	300
9	2780	300

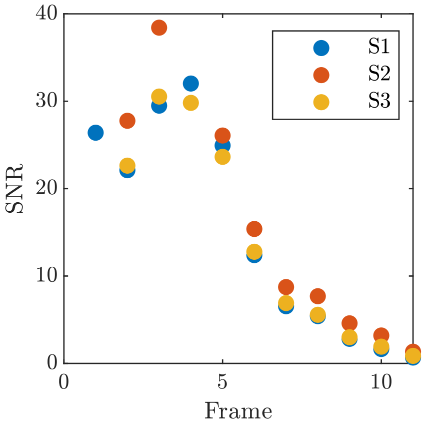

Figure 3.13: *Computed SNR as a function of frame number for our acquisitions. The three curves correspond to the three samples.*

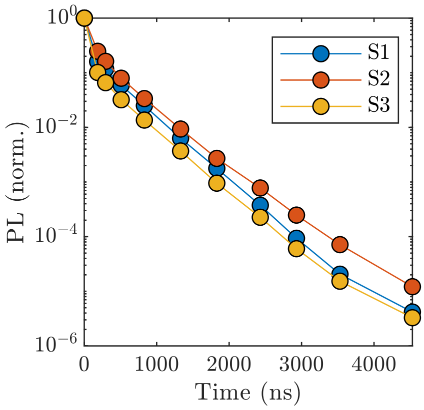

Figure 3.15: *Decays averaged over the whole image for the three samples.*

Each frame was acquired with a number of repetitions $N_{\text{rep}} = 35$ to obtain high enough SNR. This number of repetition allows us to compute a mapping of the signal over noise ratio, see Figure 3.12 (b). We obtain the local histogram for each pixel, but to allow for better visualization we display in (a) the histogram of values for 25 pixels forming a square of width 5 pixels. This histogram is the distribution of count values obtained over the 35 repetitions for the ensemble of 25 pixel for Frame 1. We obtain local SNR values in Figure 3.12 (b) above 20 and up to 34 for the brighter pixels. The mapping of histogram here is obtained by the *observation* of the standard deviation and average values over a series of repetitions.

Our new method allows for a better observation of decays at long time, with SNR of all frames but the last three being higher than 5, see Figure 3.13. The large gates combined with high number of accumulations do improve the overall SNR. Notice how the SNR slightly increases with frame number for the first 4 frames: despite an intensity that is lower (because the PL decays) the change of gate width results in a higher SNR.

The corresponding images are displayed in Figure 3.14. For each sample a laser reflection map was acquired. We display in column (ii) the average images (over 35 repetitions) for the different times. One can observe the change of SNR "by eye", as the last three images look rather noisy.

With these acquisition and the calibration, we may obtain the average decays over the images, see Figure 3.15. The three average decays present similar behavior: this is because the analysis on decay times needs to be performed locally. We want to stress to the reader that the visible range of photoluminescence intensity spans over 6 orders of magnitude in this plot. This broad dynamic range is allowed by the extraordinary capability of our TRFLIM camera.

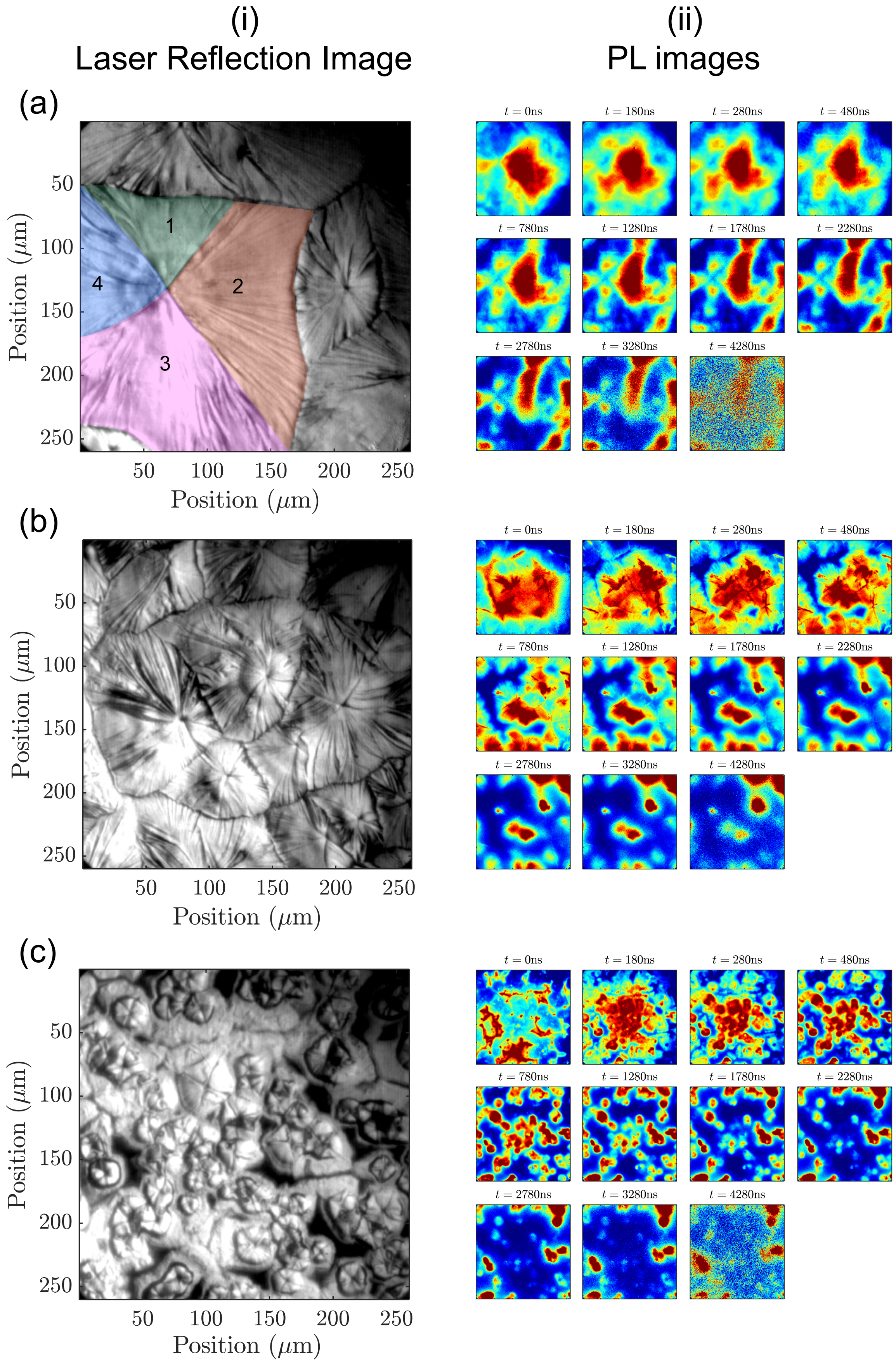

Figure 3.14: *(i) Laser reflections (ii) Average images of I_{PL} at different gate delays. (a) S1 (b) S2 (c) S3. We colored and numbered four quadrants of one micro domain in sample S1.*

3.5.3 Decay time imaging

To obtain the decay time maps we fit a non-convoluted bi-exponential decay locally on the TR-FLIM cubes. The fitting interval was set to the whole time interval. Qualitatively we observed that the interest of the bi-exponential fit is that the "short"-decay time (not analyzed here) allows to reduce the noise on the long decay time. The decay time map image is then obtained as the long characteristic time of the bi-exponential decay. We obtain the decay times maps shown in Figure 3.16, where the first line are the maps of "short" decay time and the second the one of "long" decay time, ie $\tau_2 = \tau_{\text{eff}}$. We observe that the cores of the grain micro-domains generally show higher decay times, around 500ns, than the rest of the micro-domain - particularly the "valleys" that have a decay time around 250ns (see the dark blue regions in Figure 3.16 (f)). Moreover, we observe that for some micro-domains, the decay time is not similar in all its four quadrants (see in the center image).

Figure 3.16 (g) presents the histograms of τ_{eff} values for the three samples under study. One can compare the histograms of decay times value obtain for this dataset for the three samples shown here, to the histograms of the previous dataset shown in Figure 3.9. Here we clearly see multiple peaks in the histograms of values that correspond to different regions on the image, whereas in Figure 3.9 we had obtained a more homogeneous distribution caused by the homogeneity of the samples under study. Moreover we see that sample S1 has a distribution different from sample S2 and S3. Particularly, it does not show regions of too low decay time. We attribute this to the facts that the domains are much larger for S1 than for the other two samples.

We argue that there are hints that the valley regions are more defective than the core of the microdomains. To do so, we discuss the impact of thickness on the measured decay time in the next section.

3.5.4 Discussion on the impact of thickness on the decay time

We used an Olympus LEXT confocal microscope to map the local thickness of the films and obtained Figure 3.17. Olympus claims their accuracy on thickness is of the order of 200nm. The locations probed are unfortunately not exactly the one probed via TR-FLIM, but are representative of each of the thin films. We see that some local variations can amount to $\Delta z = 350\,\text{nm}$ for S1 and up to a few microns for S2 and S3.

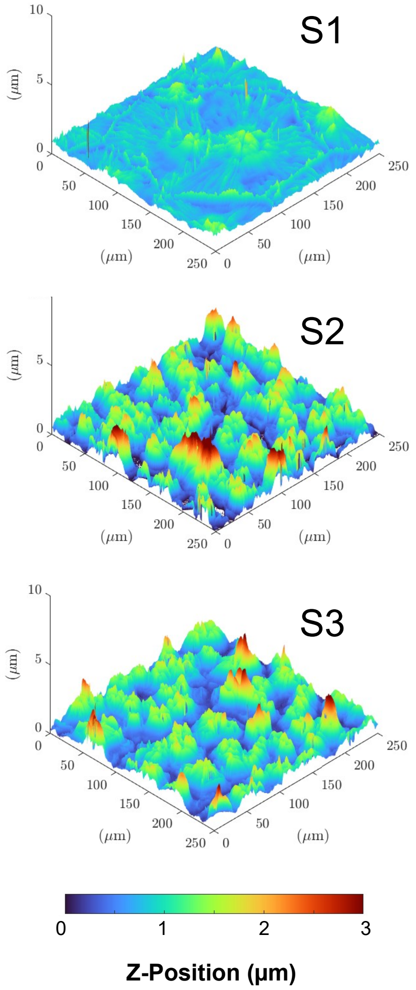

Figure 3.17: *Thicknesses obtained with confocal microscope. It is not the same position on S1, S2 and S3 as the TR-FLIM acquisition but the obtained values are nontheless representative of the TR-FLIM acquisitions.*

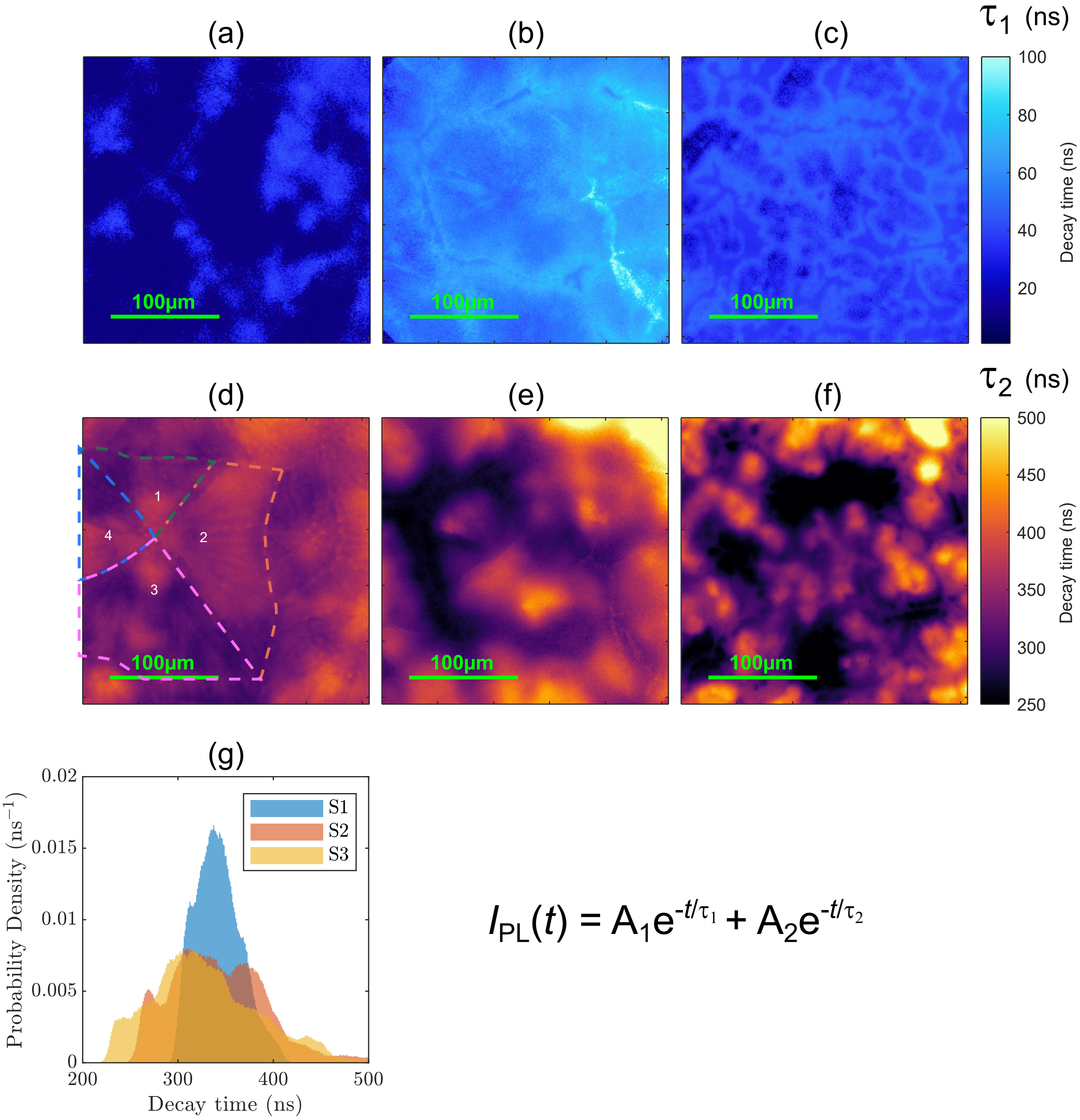

Figure 3.16: *Decay times maps. (first row) Maps of fitted* τ_1 *for (a) S1, (b) S2, (c) S3 (second row) Map of fitted decay time* $\tau_2 = \tau_{eff}$ *for (d) S1, (e) S2, (f) S3. (g) Histogram of values of decay times* $\tau_2 = \tau_{eff}$ *for the three maps (d), (e) and (f). We indicated by dots on (d) the position of the four quadrants of one micro domain in sample S1.*

This change of thickness may lead to a change of decay time. Below, we use models to suggest that the valleys are not only thinner than the core of the micro domains, they are also more defective, at least for sample S1. This means that thickness alone cannot explain the change of decay time observed in Figure 3.16.

We consider two regions (see Figure 3.16 (d) and Figure 3.17):

- Region 1 : core of the domain; $\tau_{\text{eff},1} \approx$ 500ns ; $L_1 \approx 1500nm$
- Region 2 : "valley"; $\tau_{\text{eff},2} \approx$ 250ns ; $L_2 \approx$ 500nm

In this case, one can show that the ratio of surface recombination velocities of the core ($S_{\text{top},1}$) and of the valley ($S_{\text{top},2}$) are above:

$$\frac{S_{\text{top},2}}{S_{\text{top},1}} = \frac{L_2}{L_1} \times \frac{\frac{1}{\tau_{\text{eff},2}} - \frac{1}{\tau_{bulk}}}{\tau_{\text{eff},1} - \frac{1}{\tau_{bulk}}} \geq \frac{L_2}{L_1} \times \frac{\tau_{\text{eff},1}}{\tau_{\text{eff},2}} \approx 0.66 \qquad (3.29)$$

The far right value of this equation is the limit of the ratio in the case of negligible bulk recombination. Any additional bulk recombination would reduce the discrepancy. For instance, if we assume a bulk lifetime of 1µs, then the ratio of surface recombination $\frac{S_{\text{top},2}}{S_{\text{top},1}}$ would be greater than 100%. If the bulk lifetime of the film is below $\tau_{\text{bulk}} \leq 1000ns$, then $\frac{S_{\text{top},2}}{S_{\text{top},1}} \geq 1$. It is therefore likely that the "valley" region has higher surface recombination than the "core" of the micro domain.

Statement 3.5.1. Decay time imaging is able to show that the films of $FAPbI_3$ are highly inhomogeneous. Micro domains appear, as well as "valleys" in between them. The higher annealing rate S1 leads to wider micro domains. Local thickness reduction may explain partly the drop of effective decay times between the micro domains and the valley, but numerical application suggests that non radiative recombination also increases in the valleys compared to the micro domains.

Therefore the new LGA method introduced for decay time imaging proved to yield higher signal to noise ratio than the previous method. It was developed thanks to the calibration work of the camera. Such new method allows us to study more precisely the samples's recombination inhomogeneities.

3.6 New algorithms for data treatment: regularization functions

In the previous section, we used a bi-exponential fitting approach. This allowed us to artificially "regularize" our data by giving some more freedom to the fitting algorithm for the long decay time. There also exist more accurate regularization functions when working with imaging. As a perspective to this chapter, we present preliminary results obtained on regularization.

Mainly, the regularization function has the following working principle. Instead of fitting each pixel independently one from the other, when using regularization function, we try to fit the whole map at the same time. The regularization function is a cost imposed on the fitted parameters to make sure that two pixels close to one another end up having fitting results that are also close to one another.

One example of regularization function would for instance be the norm of the gradient of the fitted decay times over the image. Having high local gradients of decay time means that locally the decay time may change abruptly. There are physical reasons to think that the reverse is true: diffusion will smooth decays as evidenced in the next section, spatial convolution with the point spread function of the camera also occurs and does effectively blur the observed signal. Therefore it is *reasonable* to expect that the local fitted decay time has *low* gradients.

This question was the subject of a collaboration with INRIA, and of the internship of Etienne Soret. Preliminary results are shown in Figure 3.18 where we compare in (a) a regular pixel per pixel fitted map with (b) a map obtained with a regularization procedure (total variation) and the l_2 norm and with (c) a map obtained with a regularization procedure (total variation) and the Huber norm. We observe that the total variation algorithms yields to the apparition of features that were blurred out in the regular procedure. Such algorithms are a promising way to obtain more precise and noise independent decay times maps. They are currently under study at IPVF.

3.7 Conclusion

In this chapter we discussed what happens long after the laser pulse has hit the sample. We showed that different definitions of lifetime exist, rendering this notion difficult to use. Particularly, we detailed the information contained in the effective

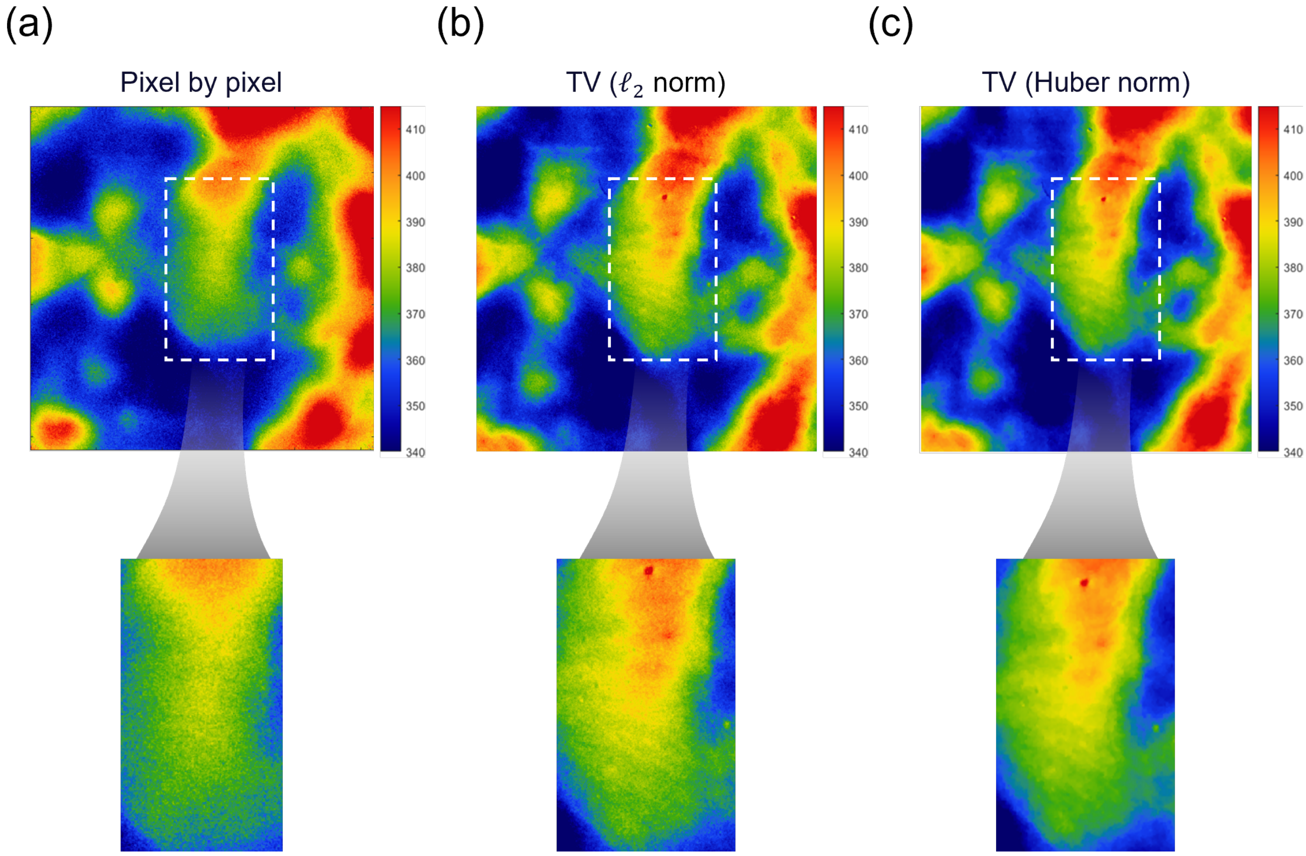

Figure 3.18: *(a) Decay time map obtained with the local fitting of the decay time. (b) Decay time map obtained with the total variation regularization and* l_2 *norm (c) Decay time map obtained with the total variation regularization and the Huber norm*

decay time measured in the pulsed experiment. We compared both theoretically and experimentally the lifetime in pulsed and in continuous wave experiments. We were able to validate at the local scale the complementarity between hyper-spectral continuous wave and time resolved pulsed measurements. From this correlation we obtained an estimation of the intrinsic carrier density of $Cs_{0.05}(MA_{0.14}FA_{0.86})_{0.95}Pb(I_{0.84}Br_{0.16})_3$. By precisely studying the correlation maps, we quantified the impact of X-Rays on the perovskite layer.

In a second part, we showed that the decay time imaging technique is nonetheless powerful when used with care. We used a regular technique to show that the deposition of a 2d passivation layer on state of the art perovskite based pin solar cell was homogeneous.

In a third part, we imaged $FAPbI_3$ poly-crystals annealed at different rates that crystallize in the metastable α phase. We developed a new decay time imaging technique, based on the calibration of our camera, to increase the SNR. We were able to obtain decay time images with low uncertainty. We discussed that our result hint at a non homogeneous defect state inside ”micro-domains”: with valleys that would present higher non radiative recombination than core of the micro-domains.

Then, a doubtful reader may wonder the interest of the time resolved experiments over the continuous wave ones—given that the experiments are more difficult to perform. A short answer would be: with the time resolved setup, what is really unique is that we can observe materials *shortly* after the laser pulse, when many physical processes are yet to occur. This is why our next chapter will focus on the short time dynamics.

Chapter 4

Local fluence dependent short-time PL dynamics: insight on non radiative recombination, doping and diffusion processes of perovskite absorbers

The aim of this chapter is to demonstrate three main results. **One**, perovskite absorbers, as exotic as they are considered, show TR-PL decays very close to what usual models for semiconductor predict. Their PL decays are very well described by the drift-diffusion model over orders of magnitude of incoming laser fluence. **Two**, we tackle the issue of obtaining a mapping of the top surface recombination velocity. To do so, we introduce a new technique based on the "short-time" derivative of the decay as a function of laser fluence. We show that one can use the drift-diffusion-compatible behavior of perovskite as well as the fact that their diffusion is "slow" to devise this technique. That technique outputs the radiative recombination coefficient as well as an effective non radiative recombination coefficient. This technique is easily applicable to images. We show its application to the determination of the local top surface recombination velocity of an IPVF baseline triple cation perovskite. **Three**, we come back on one of the main hypothesis of our short-time scaling: the fact the perovskite layers are lowly doped. We prove it experimentally and locally. We show how we can image local doping densities from absorbers by looking at the scaling of their absolute PL intensity at time $t = 0ns$ as a function of the excitation fluence. This allows us to demonstrate the close-to-intrinsic nature of all the perovskite films we have been able to observe, and to discuss the non existence of collateral doping from doped charge transport layers.

The problem that arises is to be able to measure **local** quantitative recombination parameters from the PL signal. It is actually the combination of two problems: having millions of datasets inside images, and being able to use the $I_{\mathrm{PL}}(t)$ function to extract recombination and transport parameters. **What can be understood from our demonstration is** that using the excitation intensity as a probe of perovskite absorbers combined with "short-time" analysis allows to probe radiative recombination related quantities: local doping and local radiative recombination coefficient.

Table of contents

Executive summary

Result 4.0.1. Short-time scaling. In the cases of (i) slow diffusion of carriers, (ii) high absorption of incident light and (iii) deep defects, one obtains the following scaling for the initial normalized derivative of the PL intensity:

$$\left.\frac{dI_{\mathrm{PL}}^{norm}}{dt}\right|_{t=0} = -2(k_1 + 2\alpha S_{top} + \alpha^2 D) - \frac{4}{3}k_2\alpha n_\gamma$$

Result 4.0.2. Application to imaging S_{top} for triple cation perovskite.

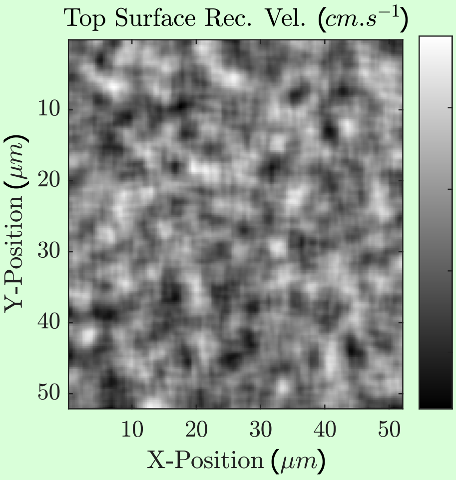

Result 4.0.3. Intensity scaling. For the pulsed experiment, one expects the following scaling valid in the slow diffusion and high absorption case:

$$I_{\mathrm{PL}}(t = 0ns) = Kn_\gamma \left(n_\gamma + \frac{N_{\mathrm{dop}}}{\alpha}\right)$$

with n_γ the laser fluence, α the absorption coefficient, K a constant, and N_{dop} the doping density.

Result 4.0.4. Imaging a transition region in a perovskite on TiO_2 region.

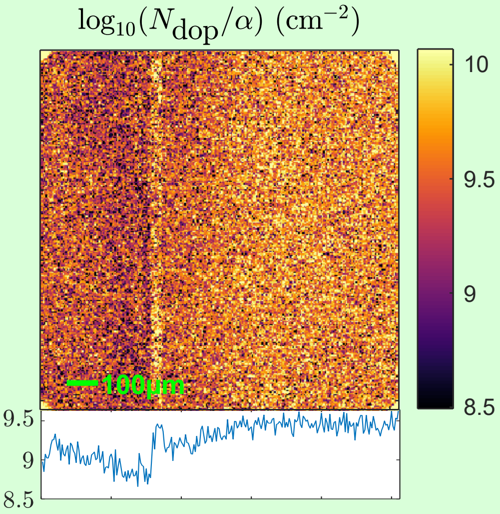

4.1 Perovskite absorbers exhibit TR-PL decays that are compatible with the drift-diffusion model

In this section, we will give elements of answer to the following question: does the drift-diffusion model account well for the TR-PL decays of perovskite absorbers? We will show that decays of perovskite absorbers are well explained by the drift-diffusion model described in Statement 2.1.8 and this for multiple excitation fluences. This model, with a correctly adjusted parameter set, allows to describe the TR-PL intensity of the absorber under different excitation condition. The fact the drift diffusion model applies to perovskite absorbers was already evidenced in the literature including by our team [Bercegol *et al.* 2018]. The novelty of our work is that we succeeded in finding models where not a single parameter is fluence dependent. For each of the three examples we give, the models we provide have only one input parameter that varies with fluence... the fluence itself.

First we will discuss the necessity of probing $I_{\mathrm{PL}}(t)$ at different fluences. Then, we will show three examples of fitting the drift diffusion model onto experimental data to obtain information on their recombination and diffusion parameters. Finally, we will discuss the limits of this approach.

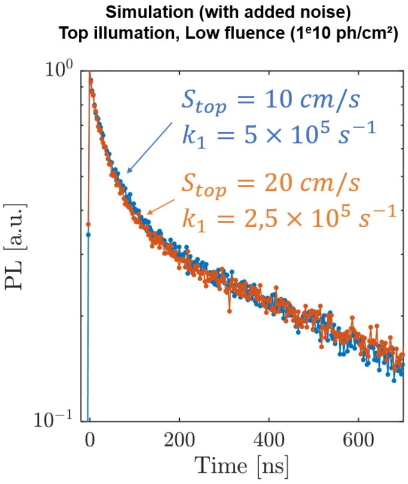

Figure 4.1: *Simulation with added noise of the drift-diffusion model of Statement 2.1.8, with two different parameter sets.*

4.1.1 One decay: too many parameters possible

The drift-diffusion model of Statement 2.1.8 may be seen as a function that takes as input the physical parameter set and that outputs the time dependent PL intensity. Two questions can arise. The mathematician may ask: is there a theoretical unique correspondence between one TRPL decay and the set of parameters? The physicist may ask: with the experimental noise available to our measurement, do I stand a chance to apply this supposed correspondence?

It would be convenient that the answers to these two question be "yes" but it is not so. At least the second question can be answered negatively, as can be hinted by Figure 4.1. In this Figure, we simulate two decays with the drift-diffusion model with two different parameter sets, and add random Gaussian noise to the decays. We see that the difference between them is lost in the error bar that the noise creates.

Therefore, measuring only one decay per sample does not allow to necessarily obtain all of the parameter set behind this decay. However, some parameters may still be recovered, as will be discussed more thoroughly in Chapter 5. In general, it is therefore preferable to perform experiments with different excitation conditions, to reduce the parameters set possible [Weiss *et al.* 2019, Bercegol *et al.* 2018]. In this chapter we study the impact of the laser fluence, ie the number of incident photons per pulse.

4.1.2 Multiple decays: examples and results

In this subsection we prove that the drift-diffusion model allows for the close description of multiple fluence-TR-PL decays three different perovskite absorbers. In the following subsections, we **work with the spatially averaged decays**. In the conclusion of this section, we discuss the (im)possibility to apply drift-diffusion fitting to images.

The **aim** of the three examples we provide is similar: **quantify non radiative recombination via defects**. Whether these defects are bulk or surface is tackled in Chapter 5. Here, for the last two examples we simply assume that surface recombination is dominant.

In the **first subsection** we study an IPVF triple cation baseline absorber, with data and text extracted from our publication [Vidon *et al.* 2021]. The aim was to quantify non radiative recombination. We discuss two fitting strategies and the presence of shallow defects. In the **second subsection**, we quantify the impact of etching of the IPVF perovskite baseline with Ar ion bombardment for X-Ray photo electron Spectroscopy (XPS) measurements. We show that surprisingly, the non radiative recombination are not dramatically increased after the Ar atoms have extruded out the perovskite and reduced its thickness. **Finally**, we quantify the impact of PEAI, Cl-PEAI, F-PEAI passivation on perovskite absorbers on glass from the collaboration with Pavia university (presented in Chapter 3.4). We show that the three passivation strategies have little effect on surface recombination for absorbers on glass.

The three different studies show that the TR-PL decays are well described by the drift-diffusion model. They will also prove that triple cation perovskite exhibits slow diffusion.

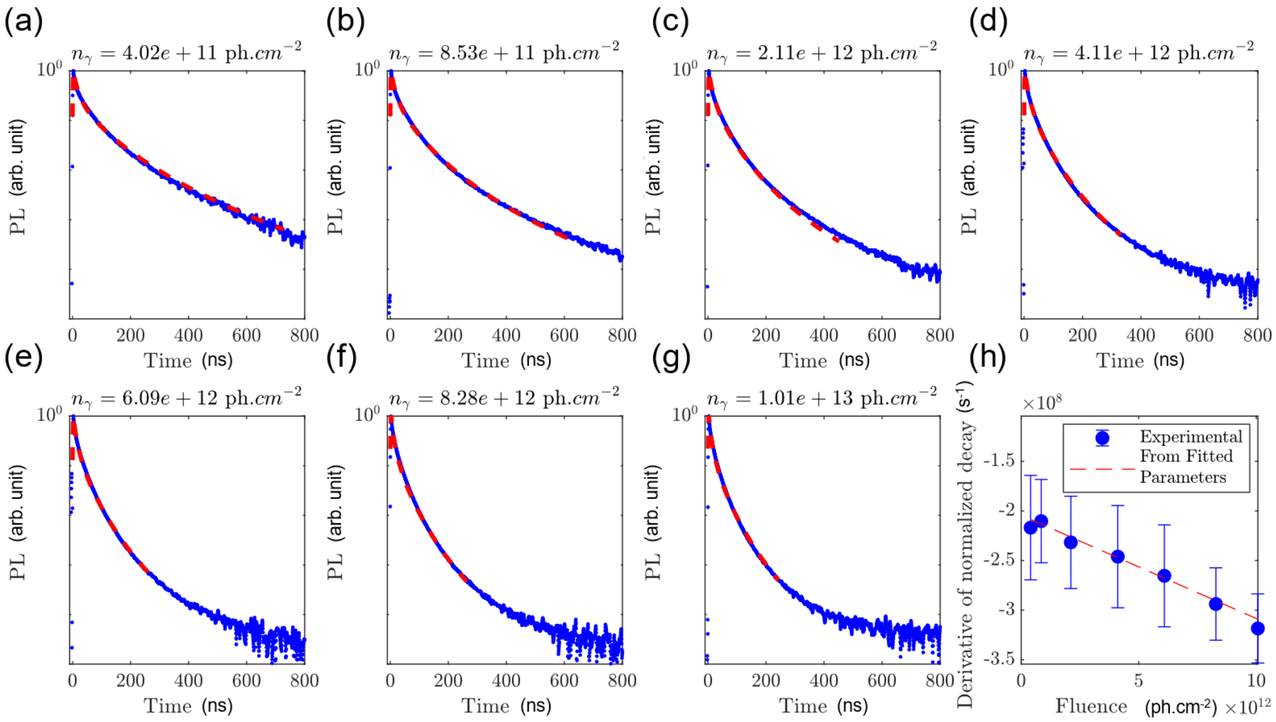

Figure 4.2: *Fitting the long decays with of Triple-Cation Perovskite with the Drift Diffusion Model, Strategy 2. (a-g) Fitting result (red dotted line) compared to experimental data (blue points). The experimental curves are a composition of the super-resolved decays and regular decays. The model is fitted until a level of* 5×10^{-4} *is reached by the experimental curves, which corresponds to the last tolerable SNR. The extracted parameters are given in Table Table 4.1. (h) Scaling of the short-time derivative: from the model fitted parameters included in the theoretical formula of the scaling (red dotted line) vs. measured on the experimental deconvoluted curves (blue points). The interval for the determination of the derivative was set to be from 0.5 to 2.5ns after the maximum of the decay is reached. Error bars come from linear fitting of the log decay, which is the method used for derivative estimation.*

Symbol	Name	Value	Uncertainty	Unit
α	Absorpion coefficient	6.5×10^4	n.a.	cm^{-1}
L	Thickness	500	n.a.	nm
k_2	Radiative Recombination Coefficient	1.2×10^{-10}	n.a.	cm^3s^{-1}
S_{bot}	Bottom Surface recombination velocity	0	n.a.	$cm.s^{-1}$
D	Diffusion Coefficient	3.54×10^{-3}	6%	cm^2s^{-1}
k_1	Order 1 Recombination Coefficient	9.23×10^6	2%	s^{-1}
N_{bulk}	Trap-Related Density for bulk defects	4.9×10^{15}	5%	cm^{-3}
S_{top}	Top Surface recombination velocity	600	8%	$cm.s^{-1}$
N_{top}	Trap-Related Density for surface defects	1.7×10^{14}	25%	cm^{-3}

Table 4.1: *Model Parameters, Strategy 2. These model parameters correspond to usual parameters for perovskite absorbers, along with fitted parameters (lasts five lines, with uncertainties).*

4.1.3 Defect quantification for perovskite on glass

In this section we describe the drift diffusion fitting of the baseline perovskite from IPVF that was used for our publication [Vidon *et al.* 2021]. The aim of this subsection is to show that the drift-diffusion fitting allows to obtain quantitative information on defects (bulk and surface) for the triple cation perovskite layer. This drift-diffusion result will then be used to validate the new method we propose in section 4.2.2.

We performed TR-FLIM experiments on triple cation perovskite thin films ($Cs_{0.05}(MA_{0.17}FA_{0.83})_{0.95}Pb(Br_{0.17}I_{0.83})_3$) deposited on glass substrates, see Appendix C.1. The acquisitions were carried out by applying a wide-field pulsed illumination ($\lambda = 532$nm) in a protective N_2 atmosphere at the temperature of 20°C to prevent light soaking effects [Péan *et al.* 2019]. Each acquisition was repeated three times and good reproducibility was obtained. We acquired images with a 3ns-long exposure gate. We used the super-temporal resolution of the camera described in section 2.2.4, by acquiring one image every 250 ps during 19.5 ns, see Figure Figure 4.8 (a). Thus, we obtained sub-nanosecond-resolved images and decays. We also acquired *regular* data cubes, by taking one image every 3ns from $t = -21$ ns up to $t = 879$ ns, as shown in the inset of Figure Figure 4.8 (b).

To obtain estimates of the recombination parameters of the perovskite thin film, we performed drift-diffusion fitting of the long decays. The models and assumptions we used are described in Statement 2.1.8, with one slight difference for the non radiative recombination in this case. **The simplest defect model of Statement 2.1.8 did not describe well our experimental data.** We tried to fit the simplest model but found unsatisfactory result. Therefore, we introduced a more general model of recombination from SRH theory, described in Equation (2.19), namely we replaced:

$$k_1 \Delta n \longrightarrow k_1 \frac{\Delta n^2}{\Delta n + N_{bulk}} \tag{4.1}$$

And for the top surface recombination velocity:

$$S_{top} \Delta n \longrightarrow S_{top} \frac{\Delta n^2}{\Delta n + N_{top}} \tag{4.2}$$

The two densities N_{top} and N_{bulk} could be named "defect related densities" and are discussed in the next subsection. They are not the defect densities themselves, but rather the equilibrium occupation of the traps. We chose to set the bottom surface recombination velocity S_{bot} to 0, because recombination at the interface between glass and perovskite was proven to be negligible, and because our tests to include it in the fit were inconclusive.

All the 7 curves were fitted **simultaneously** with only one physical model on various time-spans that corresponded for each curve to the time where $I_{\mathrm{PL}}^{norm} > 5 \times 10^{-4}$. The fitting procedure was described in section 2.3.3. There were 5 fitted parameters: D, k_1, N_{bulk}, S_{top}, N_{top}.

We were able to reproduce the behavior of our experimental data with **only one parameter set for all fluences**, see Figure 4.2. In blue the experimental data and in red the fitted model. The fitted parameters are given in Table 4.1. The correspondence is excellent with all the curves. Not only does our model reproduce the behavior of our sample over 2 orders of magnitude of intensity of excitation, but it also reproduces quite closely the scaling of the short-time derivative as a function of fluence, as shown in Figure 4.2 (h) —scaling that we will introduce in the next section. This means that the model we fitted both represents the short-time and the longer-time dynamics of our sample.

Discussion on the obtained parameters

We found $k_1 = (9.23 \pm 0.19) \times 10^6\ s^{-1}$, which could be interpreted as a bulk lifetime $\tau = 1/k_1 = (108 \pm 3)\ ns$. This is compatible with values found in the literature in terms of orders of magnitude and precedent values obtained by our group [Bercegol *et al.* 2018]

Less expected and less commonly used as a parameter in the literature is the trap-related density for bulk defects $N_{bulk} = (4.9 \pm 0.3) \times 10^{15}\ cm^{-3}$. This density can be related to the difference in energy between the trap energy and the closest band but also to the effective density of states of the corresponding band, see Equation (2.19) that we reproduce here:

$$\frac{dn_{e,h}}{\mathrm{dt}} \approx -\frac{n_e n_h - n_i^2}{\tau_h \left(n_e + N_c e^{-(E_c - E_t)/kT}\right) + \tau_e \left(n_h + N_v e^{-(E_t - E_c)/kT}\right)} \tag{4.3}$$

In this expression, only one (or less) of the exponential term is not negligible at room temperature. If we assume that the defects are close to the conduction band, then given our definition Equation (4.1):

$$N_{bulk} = \frac{N_c}{2} \exp\left(\frac{E_t - E_c}{kT}\right) \tag{4.4}$$

Our model cannot be used to determine which band the defect is closest to, nor can it disentangle if N_c or E_t has a

	D	S_{top}	N_{top}	k_1	N_{bulk}
D	1.00	0.10	0.78	-0.25	0.78
S_{top}	0.10	1.00	0.45	-0.57	0.29
N_{top}	0.78	0.45	1.00	-0.64	0.44
k_1	-0.25	-0.57	-0.64	1.00	0.12
N_{bulk}	0.78	0.29	0.44	0.12	1.00

Table 4.2: *Correlations between fitted model Parameters, Strategy 2.*

major contribution for the value of N_{bulk}. Temperature studies might bring more insight to these questions. What our model can prove is that this density is not negligible compared to photo-generated carrier density for our sample at long time after the pulse, even if the uncertainty for this value is quite large.

The top surface recombination velocity was found to be $S_{top} = (6.0 \pm 0.5) \times 10^2\ cm.s^{-1}$. This value is in the high range of what was already found for such materials, but in the low range compared to III-V materials. The top surface defect related density $N_{top} = (1.7 \pm 0.4) \times 10^{14}\ cm^{-3}$ was found to be much smaller than N_{bulk}. This could indicate that the nature of the defects at the top interface is different than the bulk defects. If one assumes that $N_{top} = \frac{N_c}{2} \exp\left(\frac{E_t^{top} - E_c}{kT}\right)$ then the ratio of the two densities gives access to their energy difference, which we estimate with

$$E_t^{bulk} - E_t^{top} = kT \ln\left(\frac{N_{bulk}}{N_{top}}\right) \tag{4.5}$$

This results in $E_t^{bulk} - E_t^{top} \approx 85\ meV$.

The diffusion coefficient we obtain is equal to $D = (3.54 \pm 0.21) \times 10^{-3}\ cm^2 s^{-1}$. This corresponds to a mobility of approximately $0.14\ cm^2 V^{-1} s^{-1}$, in line with previous studies done at IPVF [Bercegol *et al.* 2020], and in the literature (even if this value is debated).

The correlation between the fitted parameters are given in Table 4.2. We see that some correlation coefficients are high: between N_{top} and D as well as N_{bulk} and D which indicates that the fit is not certainly determining the effects of these coefficients. A similar effect happens for k_1 and N_{top} as well as for S_{top} and k_1. This last correlation will be detailed in Chapter 5.

Conclusion on this dataset.

Our baseline's behavior is well described by the drift diffusion model and exhibit "slow" diffusion compared to

III-V or Si absorbers. To describe correctly our dataset, we had to complexify slightly the defects models by not neglecting the defect related densities N_{top} and N_{bulk}. These defects are not negligible at small fluence or when the carrier density approximates $1 \times 10^{15}\,\mathrm{cm}^{-3}$. This result will be discussed further in chapter 4.3 where "doping" densities of this order of magnitude are found by a different technique.

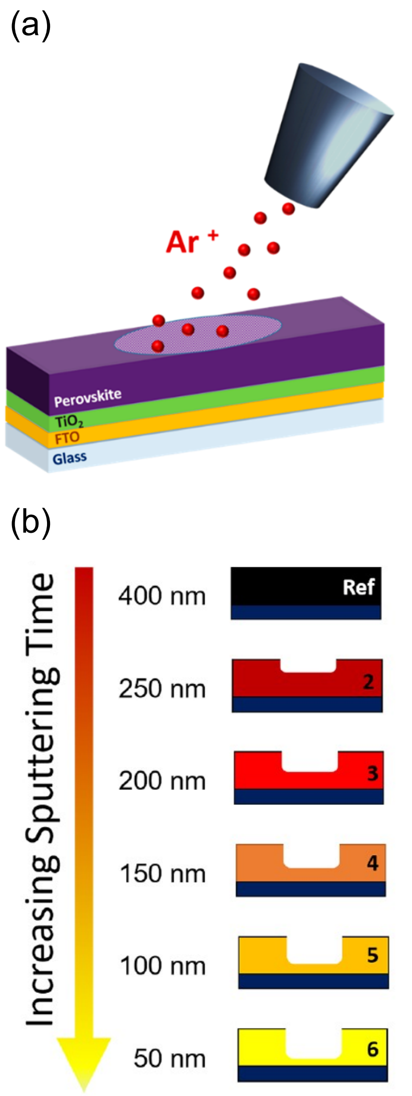

Figure 4.3: *Principle of the study with ILV. (a) Prnciple of Ar bombardment and composition of the stack. (b) Estimated thicknesses of the layers for the studied samples. Adapted from [Cacovich* et al. *2022a]*

4.1.4 Ar etching does not lead to drastic increase of surface recombination of triple cation half-cells

This study was done in collaboration with the X-Ray photo electron spectroscopy team, partly at Institut Lavoisier de Versailles. It led to the following publication [Cacovich *et al.* 2022a] which we co-authored. We quote some of the results in this section.

In this section we apply the drift diffusion model to the study of the degradation of the recombination properties of the triple cation perovskite after etching with bombardment of Argon ions. We performed Argon etching at different levels and studied the impact in terms of recombination properties of the perovskite layer. The major question this study is: **does profiling generate perturbations and degradation of the perovskite in bulk from an optoelectronic point of view?** In this work, the impact of mono-atomic Ar+ sputtering on triple-cation perovskite layers is explored on half-cells, see the structure in Figure 4.3 (a). The question of the in-depth redistribution of the elemental components as a function of the perturbation is essential. Both chemical and optical modifications are studied for different sputtering times to have a better understanding on the sputtering process and the level of the eventual induced perturbation.

At ILV, they perform depth profiling photo electron spectroscopy. To do so, Ar ions are sputtered on the perovskite layer to etch it slightly see Figure 4.3 (b). Then a XPS spectrum is recorded to obtain information on the chemical composition and bonds present near the surface (over a few nanometers), and then the process is repeated. Following this technique allows to obtain the XPS spectra as a function of the position in thickness of the sample.

With TR-FLIM and Hyperspectral characterization, we were able to **prove that the Ar etching did not increase drastically non radiative recombination**. This could be surprising knowing how fragile certain perovskite layers may be.

Symbol	Name	Value	Unit	Comment
L	Thickness	Varied for each curve	nm	From the expectation
α	Absorption coefficient	5×10^4	cm^{-1}	Estimated from absorption measurements
k_2	Radiative Recombination Coefficient	3×10^{-10}	$cm^3 s^{-1}$	Fitted on the thin film reference
S_{bot}	Bottom Surface recombination velocity	0	$cm.s^{-1}$	Hypothesis to compare the impact on the top surface
D	Diffusion Coefficient	1×10^{-2}	$cm^2 s^{-1}$	Fitted on the thin film reference
k_1	Order 1 Recombination Coefficient	9.23×10^6	s^{-1}	Fitted on the thin film reference

Table 4.3: *Fixed Model Parameters for the fitting of Figure 4.4*

Experimental Results and fitting.

We studied 4 different thicknesses with TR-FLIM, the reference at around 400 nm, as well as Ar-etched 250 nm, 200 nm and 150 nm. Medium fluence ($n_\gamma = 4 \times 10^{11}$ phcm^{-2}) decay curves are shown and compared in Figure 4.4 (f). Qualitatively, it can be seen that the four decays are not so different one from the other, despite the three colored one coming from samples having been etched. To go further in the analysis, we used drift-diffusion model fitting, as shown in Figure 4.4 (a-b-d-e) for the four samples. We used the drift-diffusion model of Statement 2.1.8. To simplify the procedure we performed a first fit on the reference sample (not etched). This allowed us to estimate values for D, k_2 and k_1, see Table 4.3. Then we fixed the values of these parameters for all the regions. For the etched regions, we fitted only one parameter : the top surface recombination velocity S_{top}.

The model parameters are presented in Table 4.3. We chose to estimate and not fit the bulk recombination coefficient k_1 to 10^6 s^{-1} as this value is close to what we found previously for our baseline perovskite. We also performed a first fit on the reference thin film on glass to estimate the diffusion coefficient and radiative recombination coefficient k_2.

To analyze the impact of the etching on the recombination, we fitted for each set of curves (a-d of Figure 4.4) the drift diffusion model with only one varying parameter: the top surface recombination velocity S_{top}. The results are given in Figure 4.4 (c). We observe once again very close correspondence from the model to the experimental data. We observe that the top surface recombination velocity is found to decrease with the decreasing thickness. This suggests that the

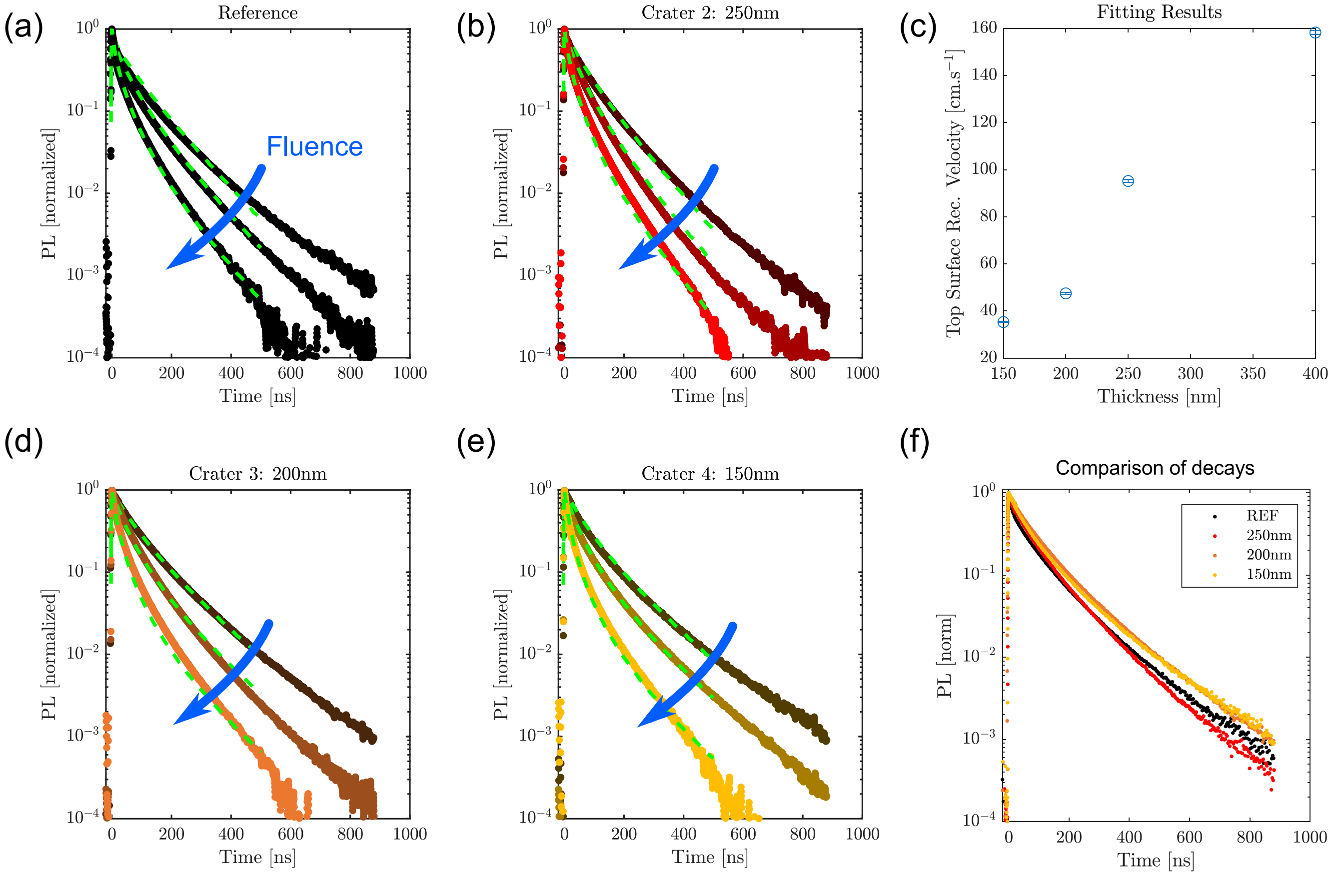

Figure 4.4: *DD-fitting of perovskite from IPVF, Ar etched. (a-d) Experimental decays at three fluences (4, 10, 30 $\times 10^{11}$ ph.cm^{-2}, from top to bottom) overlaid with the fitting model (green dashes). (e) Fitted top surface recombination velocity as a function of the thickness of the Ar etched crater. (h) Comparison of the different samples at the lowest fluence.*

etching did not compromise the quality of the surface.

Now to discuss the result we need to discuss whether top surface recombination actually play a role for this parameter set. We can do it with the SIMPLED method presented in section 3.2.4. With the fitted parameters

- bulk non radiative recombination account for 22% (400nm-thick device) to 27% (150nm-thick device) of all recombination at 1 sun equivalent illumination,
- top-surface recombination account for 77% (400nm-thick device) to 71% (150nm-thick device)
- radiative recombination account for the rest.

We could also discuss the fact of applying a ”thin-film-like” model onto data obtained on half cells. Here, we think it is reasonable for two reasons. One, the simplest model should

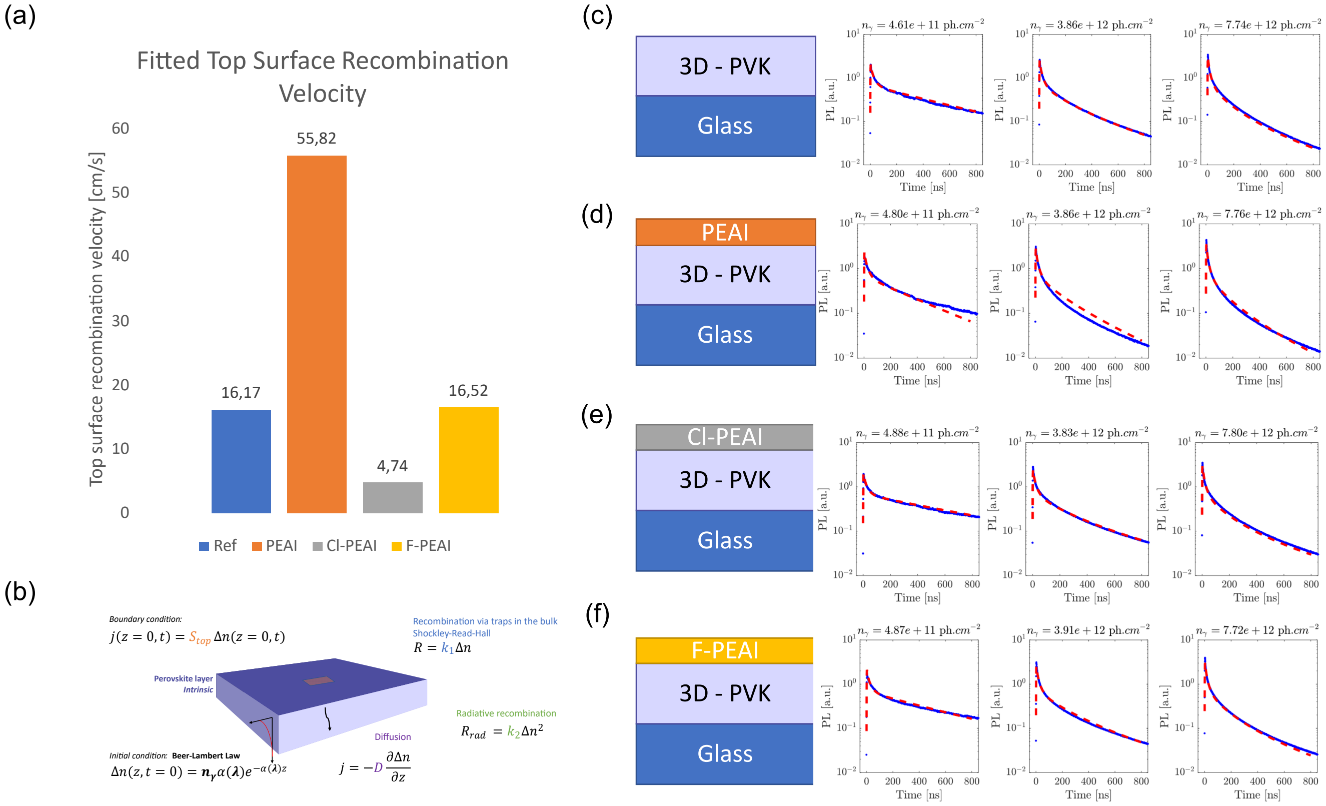

Figure 4.5: *DD-fitting of perovskite from Pavia University. (a) Fitted top surface recombination (b) Scheme of the model (c-f) Experimental results in blue, fitted curves in dotted red. Fitting parameters and methods are given in the text.*

always be favored, two for half cells and full cells, we will show in Chapter 6 that they behave as thin films for the medium to high fluences, which is the range of fluences used for this specific study.

Conclusion.

Therefore, drift-diffusion fit allowed us to prove quantitatively that the impact of the Ar etching on the TR-PL decay was quite low. This was further confirmed by Hyperspectral measurement as shown in [Cacovich *et al.* 2022a]. Thus, the XPS measurement as a function of thickness are validated.

Once again, the perovskite under study show decays compatible with usual models and with rather slow diffusion.

4.1.5 PEAI passivation is negligible for perovskite on glass samples

Finally, we applied our model to the samples from the collaboration with Pavia university, described in chapter 3.4.

We studied similar perovskite composition, see Appendix C.2. The fitting aimed at describing the passivation effect of 2d-perovskite deposited on top of a 3d-triple-cation perovskite. In this section we use the films deposited on glass. **We evidence that the passivation effect of the 2d-layer is quite negligible for the thin films**. However, as evidenced in Figure 3.7 in the previous chapter, the open circuit voltage increases with the deposition of such layer. After further study of different stacks, we concluded that the role of this passivation layer was to mitigate defects forming at the perovskite/ETL interface.

Here, to study quantitatively the role of this layer on thin films on glass, fluence-dependent TR-FLIM acquisitions we performed in protective atmosphere. We present the results, as well as the fitting results in Figure 4.5. Four sample are studied, one reference and 3 samples with added 2d-layers, one with the PEAI molecule, and the two others with modified molecules F-PEAI and Cl-PEAI.

In order to gain quantitative insight on these devices, we performed drift-diffusion fitting with the drift diffusion model of Statement 2.1.8. We adopt the following strategy.

First we fit only the reference sample to find the values of k_1, S_{top}, k_2, and D. They are given in Table 4.4, along with the other fixed parameters. We find a diffusion coefficient in the range of the previously found one for the IPVF baseline which has a close composition —highlighting once more the slow diffusion happening in this material. The radiative recombination coefficient is found almost one order of magnitude less than for the two previous studies on the perovskite IPVF baseline. We attribute this difference to a possible increase of photon recycling for these films that exhibit very high bulk decay times. Indeed we find $1/k_1 = 2.5\,\mu\text{s}$ which is at least one order of magnitude higher than for our baseline. The correlations between parameters are given in Table 4.5. They are relatively low except for the correlation between S_{top} and k_1. This correlation is discussed in more details in the discussion section.

Second, we fit for all samples the top surface recombination velocity on all samples, as the only fitted parameter, the others being fixed to what was found for the reference, according to Table 4.4. The fitted results are displayed in Figure 4.5 (a) while the fitting curves are shown in dashed red in (c-f). Figure 4.5 (b) is a representation of the drift diffusion model. We see an excellent agreement between the fitted curves and the model, over one order of magnitude of excitation intensity. Except for the PEAI sample (d), the modeled curves are very close to the experimental ones. The

Symbol	Name	Value	Uncertainty	Unit
α	Absorption coefficient	1.3×10^5	n.a.	cm^{-1}
L	Thickness	500	n.a.	nm
S_{bot}	Bottom Surface recombination velocity	0	n.a.	$cm.s^{-1}$
k_2	Radiative Recombination Coefficient	2.9×10^{-11}	2%	cm^3s^{-1}
D	Diffusion Coefficient	4.5×10^{-3}	3%	cm^2s^{-1}
k_1	Order 1 Recombination Coefficient	3.9×10^5	7%	s^{-1}

Table 4.4: *Model Parameters, for the fit of Figure 4.5. The first (top) part of parameters are fixed from measurement/design. The last three result from a fit of the reference device.*

	k_1	S_{top}	D	k_2
k_1	1.0000	-0.9865	-0.4814	-0.5191
S_{top}	-0.9865	1.0000	0.5614	0.4895
D	-0.4814	0.5614	1.0000	0.6814
k_2	-0.5191	0.4895	0.6814	1.0000

Table 4.5: *Correlations between fitted model of Table 4.4*

results in terms of top surface recombination velocity in (a) show that the Cl-PEAI does result in a passivation with a value going from 16 cms^{-1} to 5 cms^{-1}. The F-PEAI shows no clear passivation while the PEAI sample actually displays an increase of the top surface recombination.

These result highlight that the passivation strategy does operate slightly for Cl-PEAI thin films, but has a neutral role for F-PEAI. The reason for this is that the perovskite/N_2 interface shows already quite low surface recombination. The positive role of the passivation was far more evident when we measured TR-FLIM on half cells or full cells, as evidenced in Figure 3.8.

To conclude, let us take a step back and write that once again, the simple drift-diffusion model correctly accounts for the TR-PL decays of the perovskite thin films with a good accuracy over orders of magnitude of fluence. It shows limits for the devices with added PEAI (especially for the neat PEAI).

4.1.6 Discussion and Limits of drift-diffusion fitting

In the three previous cases, we displayed how the drift-diffusion model can accurately describe the luminescence behavior of perovskite based thin films. The fitting technique

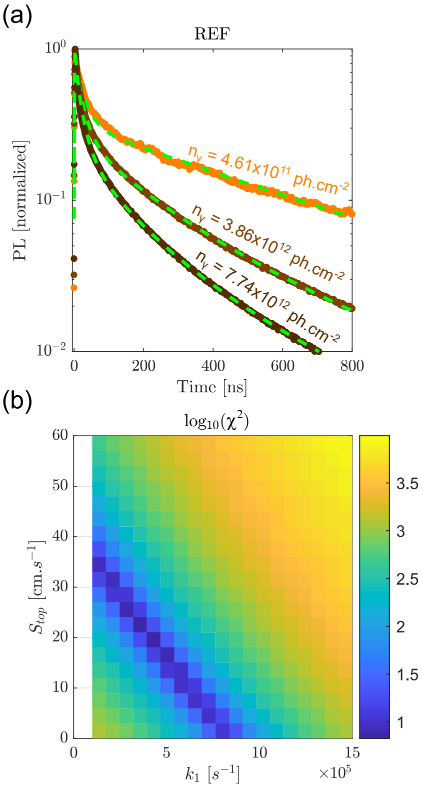

Figure 4.6: *(a) Fitting result on samples from Pavia University (b) Map of residual error of the fit around the obtained results. Blue corresponds to a small error, yellow to a high one.*

allowed us to describe the passivation or the absence of degradation of the films, or evidence the presence of possible shallow defects. However, this technique has drawbacks. The first one is **the correlation between the fitted parameters**. The second one is the **difficulty to apply this technique to images** because the fit is quite time consuming.

We evidenced in Table 4.2 that the correlation between parameters can be high (in absolute value). The correlation between k_1 and S_{top} was found close to -1. This effect can be visualized in Figure 4.6 (b) where we took the previous fitting result shown as well in (a) and computed the $\log \chi^2$. χ^2 was introduced in Equation (2.48). It represents the "distance" between the fitted curve and the model. A higher value meaning a less precise fitting (in yellow in the figure). In Figure 4.6 (b) we vary k_1 and S_{top} in the model and compute the distance between the model curves and the experimental ones. The blue line indicates a high number of couples (k_1, S_{top}) that yield a model close to the experimental data. This line means that what our fitting strategy is able to determine is rather a coefficient that would be S_{top}/k_1 or the inverse. A minimum exists on this line but we do not think it holds specific meaning, as noise could easily change its position. Therefore: the drift-diffusion model can lead to fitting parameters that are highly correlated. In this case, we can assume that our strategy does not allow to determine accurately both parameters but rather their ratio or product. This is why, when comparing samples, we used a 2 step strategy where we estimated k_1 (or fitted it), and looked only at the variation of S_{top}.

The second limit of this drift-diffusion fitting approach is that it is not easily applicable on images. Indeed, it can take up to a few hours on a modern computer to fit a map of parameters onto one dataset. In Figure 4.7 we present an example of such difficulty. We use the dataset presented in section 4.1.5, and fit the reference sample map with the drift-diffusion fit pixel per pixel. The original acquisition is 512x512 pix^2. In (a) we use a high binning to obtain a map of 30x30 pix^2. It took a few **hours** to compute. In (b) we use a 90x90 pix^2 map. It took a few **days** to complete and was interrupted due to errors. Even though we fitted only one parameter: S_{top}.

Another factor to take into account are the numerous fits necessary before obtaining the right one, to fine tune the intervals, check for errors etc. This time limit could be overcome in the future or with strategies to fasten the code. This strategy was not followed —we rather searched and found another way to image recombination parameters.

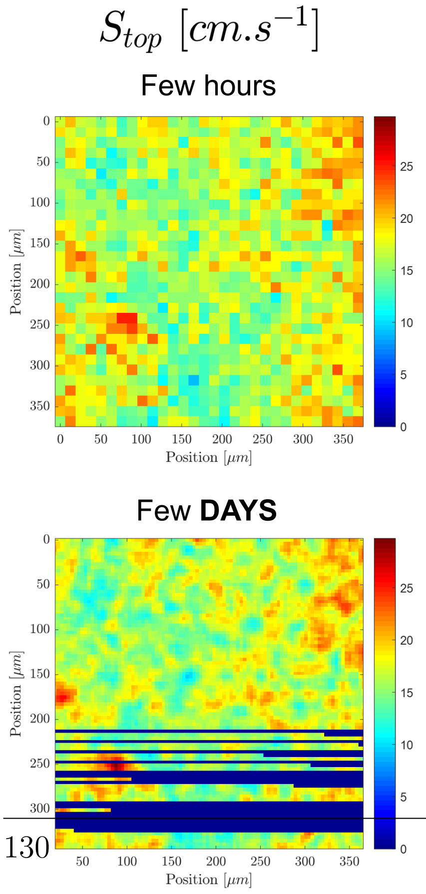

Figure 4.7: *(a) Map of fit-*

4.2 Obtaining an image of the top surface recombination velocity of triple cation perovskite with a new approach: the initial derivative

This section describes a new technique we developed to **image recombination parameters of perovskite absorbers**. It is based on the observation of the initial derivative of the $I_{\mathrm{PL}}(t)$ signal shortly after the laser pulse. **This section is based on our publication [Vidon *et al.* 2021]**. We took extracts of this publication to write this section.

4.2.1 Motivation

As discussed in the general introduction of this manuscript, the TR-PL experiments are rather easy to perform but difficult to interpret. [Hutter *et al.* 2020, Dequilettes *et al.* 2019]. We repeat some of the arguments but with new light shaded on them. To date, two main approaches are employed in the literature:

1. One based on phenomenological fitting of the decays, as explained and used in Chapter 3. Fitting functions such as mono-exponential, bi-exponential [Son *et al.* 2016], stretched exponential [DeQuilettes *et al.* 2015, Yamada *et al.* 2017, Wang *et al.* 2019a], tri-exponential [Zhang *et al.* 2014] are arbitrarily chosen. We saw that the fitted decay time constants and parameters mix recombination and diffusion. We also saw that to get the most physically significant observation one needs to look at the long time dynamics and at low fluence. For this regime, the signal to noise ratio of the images might become an issue.

2. The second method relies on a microscopic drift-diffusion model to describe the dynamics of carriers transport and recombination [Ahrenkiel and Lundstrom 1993, Baloch *et al.* 2018, Kirchartz *et al.* 2020, Maiberg and Scheer 2014, Trimpl *et al.* 2020, Bercegol *et al.* 2020] as was explained above in chapter 4.1. However, this interpretation method has multiple drawbacks. First of all, parameter correlation. Another major drawback appears when one wants to interpret images, as evidenced

in the previous section.

Thus, to accurately map local transport parameters, new approaches in modeling as well as data treatment are required.

In this section, we establish a theoretical relationship that allows for the direct determination of physical parameters *without* using drift-diffusion **fitting**. This method directly outputs coefficients that are related to physical parameters via theoretical formulae. Our approach is based on a scaling law we derived for the time-derivative of the transient PL signal computed just after the laser pulse.

Other groups used the derivative of the PL signal to describe different physical phenomena. For instance, Krogmeier and co-workers [Krogmeier *et al.* 2018] defined a differential lifetime of halide perovskite closely linked with such derivative [Ahrenkiel and Lundstrom 1993]. Saba and co-workers displayed the initial derivative as a function of laser fluence studied on $\mathrm{MAPbI_3}$ and $\mathrm{MAPbI_{3-x}Cl_x}$ perovskite [Saba *et al.* 2014]. However, only in few publications [Kanevce *et al.* 2014, Maiberg and Scheer 2014] were the theoretical components of the PL derivative directly associated to their physical origin, i.e. carrier diffusion, recombination in the bulk or at the interfaces via traps and radiative recombination. In these publications, the derivative is computed in a general and thus integral form. As no specific analytical form for the inhomogeneous photo-generated carrier density profile $\Delta n(z,t)$ is considered, the integrals are not computed.

We propose to compute the expected theoretical derivative and integrals at 'short—time' after the pulse, when one can make an assumption on the photo-generated carrier density spatial profile based on Beer-Lambert's law. We obtained a law that is linear in laser fluence. Starting from this law and from the observation of the short time derivative of the PL signal, it is possible to extract accurate values of physical parameters such as the external radiative recombination coefficient or top surface recombination velocity. This method can also be applied for the analysis of three-dimensional datasets, acquired with imaging systems, although very precise signal is needed for local application. One of the benefits of considering only the beginning of the decays stands in the high signal-to-noise ratio of the curves in this temporal window.

4.2.2 A theoretical scaling law for the initial derivative of the PL decay

We use a general model, namely the drift diffusion model described in Statement 2.1.8, with a slight modification of the defect regime to include shallow defects, already introduced in section 4.1.3, namely we use for the bulk defects:

$$k_1 \Delta n \longrightarrow k_1 \frac{\Delta n^2}{\Delta n + N_{bulk}} \tag{4.6}$$

For the top surface recombination velocity:

$$S_{top} \Delta n \longrightarrow S_{top} \frac{\Delta n^2}{\Delta n + N_{top}} \tag{4.7}$$

And for the bottom surface recombination velocity:

$$S_{bot} \Delta n \longrightarrow S_{bot} \frac{\Delta n^2}{\Delta n + N_{bot}} \tag{4.8}$$

We propose to give a theoretical approximation to the following quantity:

$$\left.\frac{dI_{\mathrm{PL}}^{norm}}{dt}\right|_{t=0} = \frac{1}{I_{\mathrm{PL}}(t=0)} \times \left.\frac{dI_{\mathrm{PL}}}{dt}\right|_{t=0} \tag{4.9}$$

We recall the definition of I_{PL} which is given in Equation (2.11):

$$I_{\mathrm{PL}}(t) = A \times \int_0^L \Delta n^2(z', t)\, dz' \tag{4.10}$$

With A a constant, see the discussion around Equation (2.11). For the derivative we have:

$$\left.\frac{dI_{\mathrm{PL}}}{dt}\right|_{t=0} = 2A \times \int_0^L \Delta n(z', t=0) \frac{d\Delta n}{dt}(z', t=0) dz' \tag{4.11}$$

Within the drift-diffusion model, the derivative of the carrier density is for $t > 0$:

$$\frac{\partial \Delta n}{\partial t}(z,t) = -D \frac{\partial^2 \Delta n}{\partial z^2} - k_1 \frac{\Delta n^2}{\Delta n + N_{bulk}} - k_2 \Delta n^2 \tag{4.12}$$

With this equation, along with the definitions of the PL signal and the recombination terms one may compute:

$$\begin{aligned} \frac{dI_{\mathrm{PL}}}{dt} = -2A \Bigg[& k_1 \int_0^L \frac{\Delta n^3}{\Delta n + N_{bulk}}\, dz' + k_2 \int_0^L \Delta n^3\, dz' + D \int_0^L \left(\frac{\partial \Delta n}{\partial z}\right)^2 dz' \\ & + S_{top} \frac{\Delta n^3(z=0,t)}{\Delta n(z=0,t) + N_{top}} + S_{bot} \frac{\Delta n^3(z=L,t)}{\Delta n(z=L,t) + N_{bot}} \Bigg] \end{aligned} \tag{4.13}$$

A similar equation may also be found in [Maiberg and Scheer 2014].

Statement 4.2.1. Approximations 1/2 We then make the **main approximation** that we can compute the integrals with a carrier distribution equal to the Beer-Lambert initial condition. This approximation is justified in the case of perovskite absorbers because they appear to have slow diffusion, as evidenced in the previous section and also as evidenced in the literature [Bercegol *et al.* 2018]. This slow diffusion renders accessible the "before-diffusion" distribution of carriers to the camera's temporal response function (3ns). Therefore we assume that we can replace in Equation (4.13):

$$\Delta n(z, t = 0^+) \approx n_\gamma \alpha e^{-\alpha z} \tag{4.14}$$

In this case, the $I_{\mathrm{PL}}(t = 0)$ definition yields:

$$I_{\mathrm{PL}}(t = 0) = A \times \int_0^L \Delta n^2(z', t = 0)\, dz' \tag{4.15}$$

$$= A n_\gamma^2 \alpha^2 \int_0^L e^{-2\alpha z'}\, dz' = \frac{A n_\gamma^2 \alpha}{2} \left(1 - e^{-2\alpha L}\right) \tag{4.16}$$

We need compute the following integrals valid within this approximation:

$$\int_0^L \Delta n^3\, dz' = \frac{n_\gamma^3 \alpha^2}{3} \left(1 - e^{-3\alpha L}\right) \tag{4.17}$$

$$\int_0^L \left(\frac{\partial \Delta n}{\partial z}\right)^2 dz' = \left(-n_\gamma \alpha^2\right)^2 \int_0^L e^{-2\alpha z'}, dz' = \frac{n_\gamma^2 \alpha^3}{2} \left(1 - e^{-2\alpha L}\right) \tag{4.18}$$

The first integral in Equation (4.13) is computed in the Appendix Appendix F, the general result being :

$$I = \int_0^L dz \frac{\Delta n^3}{\Delta n + N_{bulk}} = n_\gamma^2 \alpha \left[\left(\frac{N_{bulk}}{n_\gamma \alpha}\right)^2 \ln\left(\frac{\frac{N_{bulk}}{n_\gamma \alpha} + 1}{\frac{N_{bulk}}{n_\gamma \alpha} + e^{-\alpha L}}\right) + \frac{1}{2} - \frac{N_{bulk}}{n_\gamma \alpha} - \frac{1}{2} e^{-\alpha L} \left(e^{-\alpha L} - 2\frac{N_{bulk}}{n_\gamma \alpha}\right) \right] \tag{4.19}$$

The top and bottom recombination terms give:

$$S_{top} \frac{\Delta n^3(z = 0, t)}{\Delta n(z = 0, t) + N_{top}} = n_\gamma^2 \alpha^2 S_{top} \frac{1}{1 + \frac{N_{top}}{n_\gamma \alpha}} \tag{4.20}$$

$$S_{bot} \frac{\Delta n^3(z = L, t)}{\Delta n(z = L, t) + N_{bot}} = n_\gamma^2 \alpha^2 S_{bot} e^{-2\alpha L} \frac{1}{1 + \frac{N_{bot} e^{-\alpha L}}{n_\gamma \alpha}} \tag{4.21}$$

Finally one can compute the scaling in the general case, which would give a horrid formula that would be pointlessly written here. However, this general form can be simplified by considering the case where:

Statement 4.2.2. Approximations 2/2

1. High absorption. In the case of highly absorbed wavelength: $e^{-\alpha L} \ll 1$ (leading to simplify Equation (4.16), Equation (4.17), Equation (4.18), and neglect Equation (4.21) in front of Equation (4.20))
2. Deep defects. $\frac{N_{bulk}}{n_\gamma \alpha} \ll 1$ (leading to simplify I), and $\frac{N_{top}}{n_\gamma \alpha} \ll 1$ (leading to simplify Equation (4.20)). The case of the approximation of the integral I, appearing as a factor of the term proportional to k_1 in Equation (4.13), is discussed below.

This gives us a simplified scaling valid in the high absorption and deep defects approximation.

Result 4.2.1. In the cases of (i) slow diffusion of carriers, (ii) high absorption of incident light and (iii) deep defects, one obtains the following scaling for the initial normalized derivative of the PL intensity:

$$\left.\frac{dI_{\mathrm{PL}}^{norm}}{dt}\right|_{t=0} = -2\left[k_1 + 2\alpha S_{top} + \alpha^2 D\right] - \frac{4}{3}k_2 \alpha n_\gamma \quad (4.22)$$

This equation relates the derivative of the normalized decay curve just after the laser pulse to the model parameters, notably to the **experimentally accessible parameters**: the fluence n_γ and the laser-wavelength-dependent absorption coefficient $\alpha(\lambda)$.

The **slope** of this linear function of n_γ gives a direct access to the product αk_2. The absorption coefficient can be measured via other methods such as Fourier transform photocurrent spectroscopy [Lin *et al.* 2020, Holovský *et al.* 2017] or ellipsometry [Löper *et al.* 2015]. Therefore, one can extract a direct measurement of the external radiative recombination coefficient k_2.

The **intercept** of the scaling gives a direct access to the quantity $k_1 + \alpha^2 D + 2\alpha S_{top}$. There is a major difference between the intercept of the scaling at short time and the (long-time) observed decay time: the spatial distribution of the carriers. For the short-time intercept, the distribution of carriers follows Beer-Lambert's law, while for the decay time a more homogeneous distribution is reached (not entirely homogeneous due to surface recombination). These two distributions explain the difference in terms of theoretical formulae between these two characteristic times of the system (see Equation (3.21)).

Equation (4.22) suggests **two sets of experiments**. The first one consists in measuring decays when varying the laser fluence at a given laser wavelength. This approach has been widely employed in the literature [Bercegol *et al.* 2018, Trimpl *et al.* 2020, Kirchartz *et al.* 2020, Krogmeier *et al.* 2018]. In this case, one could explore how the initial slopes of the relative decays exhibit a linear relationship with laser fluence. The other set of experiments would consist in varying the laser wavelength at fixed laser fluence. Then, as long as the high absorption condition $e^{-\alpha L} \ll 1$ is fulfilled, one expects a polynomial of order 2 in α for the initial derivative (a generalized version of the scaling for the low absorption case is given below). Combining the two methods would give access to most of the model parameters: k_1, D, S_{top}, k_2, without any use of complex numerical methods.

The first set of experiments is described in the following, while the second set of experiments will be the subject Chapter 5.

4.2.3 Experimental application of the scaling law to averaged decays

To validate the proposed model, we performed TR-FLIM experiments on IPVF's triple cation perovskite thin films ($\mathrm{Cs_{0.05}(MA_{0.17}FA_{0.83})_{0.95}Pb(Br_{0.17}I_{0.83})_3}$) deposited on glass. The samples were presented above in section 4.1.3

In Figure 4.8 (b), we plotted sub-nanosecond-resolved decays acquired at different laser fluences (varying from 4×10^{11} to 1×10^{13} ph.cm^{-2}) and averaged over the whole image. The corresponding scaling is shown in Figure 4.8 (c), in blue dots. The derivative was computed as the slope of a linear fit of the natural logarithm of the PL between 0.5 and 2.5ns. Two data sets are considered: in the former the derivative was performed on the raw decays shown in Figure 4.8 (b) while in latter we computed the derivative on the results of a deconvolution algorithm applied to the decays (the decays are shown in the appendix Figure F.5). Then, we fit linearly the points of Figure 4.8 (c), to obtain the slope $a = -4/3\alpha k_2$ and intercept $b = -2\left[k_1 + \alpha^2 D + 2\alpha S_{top}\right]$ of the scaling law. For the raw dataset, we obtained values of $a = -(5.7 \pm 0.6) \times 10^{-6}$ cm^{2}s^{-1} and $b = -(1.24 \pm 0.03) \times 10^8$ s^{-1}, whereas for deconvoluted dataset we find $a = -(1.07 \pm 0.15) \times 10^{-5}$ cm^{2}s^{-1} and $b = -(2.06 \pm 0.08) \times 10^8$ s^{-1}.

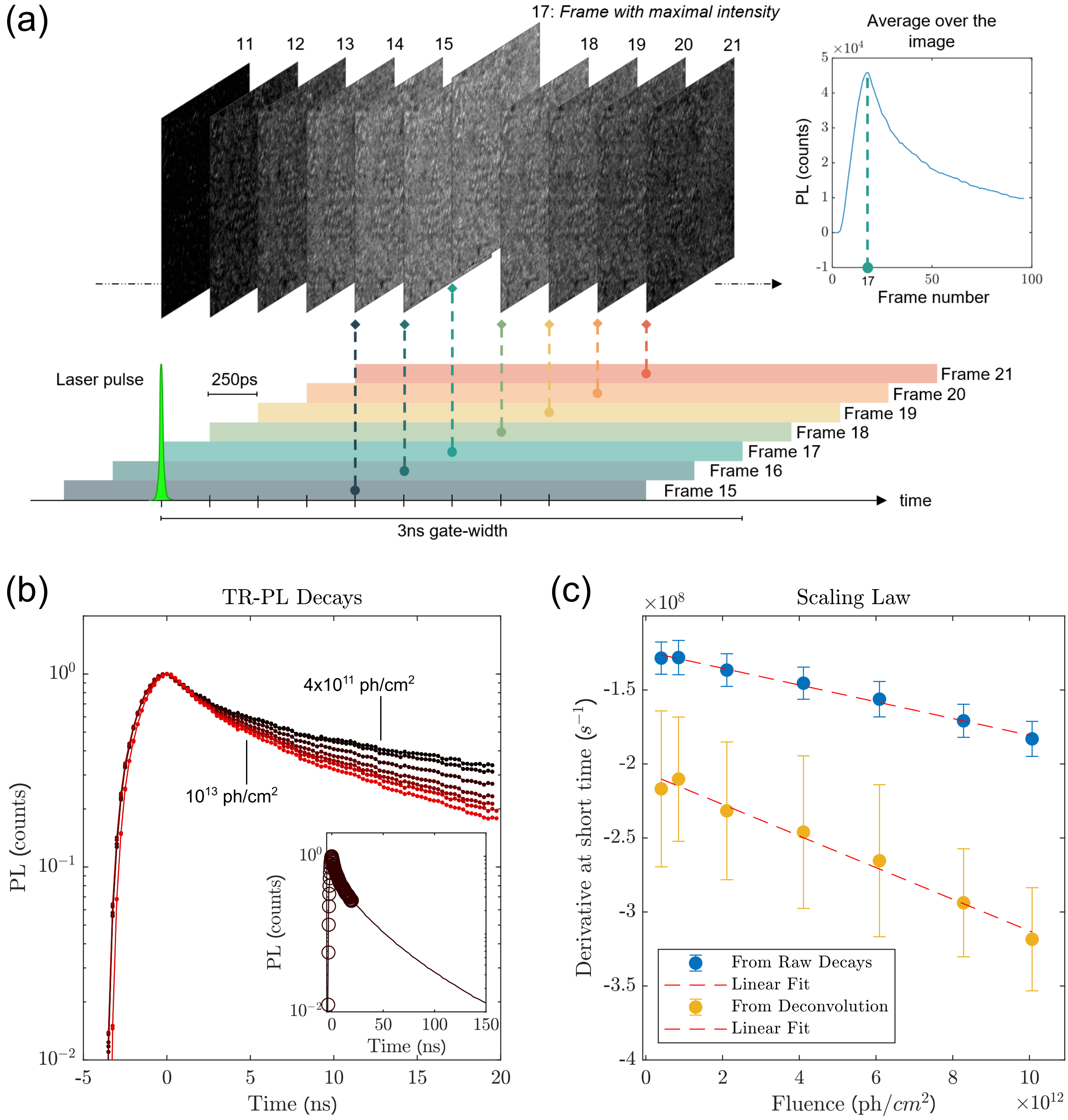

Figure 4.8: *Experiments on triple-cation perovskite* ($Cs_{0.05}(MA_{0.17}FA_{0.83})_{0.95}Pb(Br_{0.17}I_{0.83})_3$) *thin films in inert atmosphere. (a). Scheme of the sub-nanosecond-resolved TR-FLIM acquisitions. Top right is the obtained decay averaged over the images. All images share the same colorscale (from* 3.5×10^4 *to* 6×10^4 *counts). (b). TR-PL intensity as a function of time for different fluences. (b-Inset) Comparison of the sub-nanosecond-resolved curves (open circles) with the regular decays resolved at 3 ns (line). Only the first 150 ns of the regular and longer decay (that lasts up to* $t = 879$ *ns) are shown. (c). Relative slope fitted on the decays between* 0.5 *ns and* 2.5 *ns as a function of laser fluence: (blue) measured on the raw decays; (yellow) measured on the deconvoluted decays. Error bars are given by the fitting function, see Supplemental Material Section 2 on numerical uncertainty. The curves were fitted by using a linear function (dotted line):* $y = a \times x + b$*. The parameters found for the raw scaling are :* $a = -(5.7 \pm 0.6) \times 10^{-6}$ $\mathrm{cm^2 s^{-1}}$ *and* $b = -(1.24 \pm 0.03) \times 10^{8}$ $\mathrm{s^{-1}}$*. The parameters found from the scalings from deconvoluted decays are :* $a = -(1.07 \pm 0.15) \times 10^{-5}$ $\mathrm{cm^2 s^{-1}}$ *and* $b = -(2.06 \pm 0.08) \times 10^{8}$ $\mathrm{s^{-1}}$*. Reproduced from [Vidon et al. 2021]*

The deconvolution algorithm is discussed in details in Appendix F. Here, we make three remarks on the impact of temporal convolution. One, the order of magnitude of the parameters is similar for both results after and before deconvolution. Two, characterizing the apparatus response function allows for the use of deconvolution algorithms. These algorithms are especially efficient in the high signal to noise regions, which is exactly our temporal window of interest when computing the short-time derivative. Three, the use of deconvolution algorithms is necessary because the characteristic timescales of the material's decay are comparable to the temporal resolution of our camera. We want to stress that deconvolution would not be necessary for the study of materials with longer characteristic time scales.

For the rest, we use the results from the deconvoluted dataset ($k_2\alpha_{532nm} = (8.0 \pm 1.1) \times 10^{-6}\,\mathrm{cm^2 s^{-1}}$) to estimate the transport parameters of the perovskite layer.

Result 4.2.2. Assuming an absorption coefficient at the laser wavelength (532 nm) $\alpha = (6.5 \pm 1) \times 10^4$ cm^{-1} from previous measurements, and in line with literature values for this composition and laser wavelength [Brenes *et al.* 2019], we can extract the value of the external radiative recombination coefficient $k_2 = (1.2 \pm 0.4) \times 10^{-10}$ cm^{3}s^{-1} by using Equation (4.22). Moreover, we can provide lower and upper bounds for the multiple parameters expressed in the intercept coefficient. The bulk lifetime $\tau = 1/k_1$ would in this regard be such that $\tau \geq 10$ ns, which is highly expected for triple cation perovskites. The diffusion coefficient would be less than $D \leq 2.4 \times 10^{-2}$ cm^{2}s^{-1}, corresponding to a mobility $\mu \leq 0.9$ cm^{2}s^{-1}V^{-1} at ambient temperature. For the top surface recombination velocity, one finds that $S_{top} \leq 790$ cm.s^{-1}. All of these conditions are in agreement with literature results on triple cation perovskites [Brenes *et al.* 2019], and with our previous results [Bercegol *et al.* 2018].

4.2.4 Using the scaling law to image non radiative recombination

Homogeneous perovskite sample

To use the scaling locally, we use the acquired cube $I_{\mathrm{PL}}(x, y, t)$. We use a binning of 11 pixels, for all pixel (i, j) of the new map, the decay is composed of the signal of all the pixels in the square $(i \pm 5, j \pm 5)$. For each decay, the deconvolution algorithm is applied. Then the derivative is computed. Thus, for each pixel a scaling of derivative as a function of fluence is established.

We show local slope and intercept in Figure 4.9. We can observe that the two maps Figure 4.9 (a,d) are greatly **negatively correlated** as highlighted by Figure 4.9 (c). This

Intercept of the scaling law (s-1)

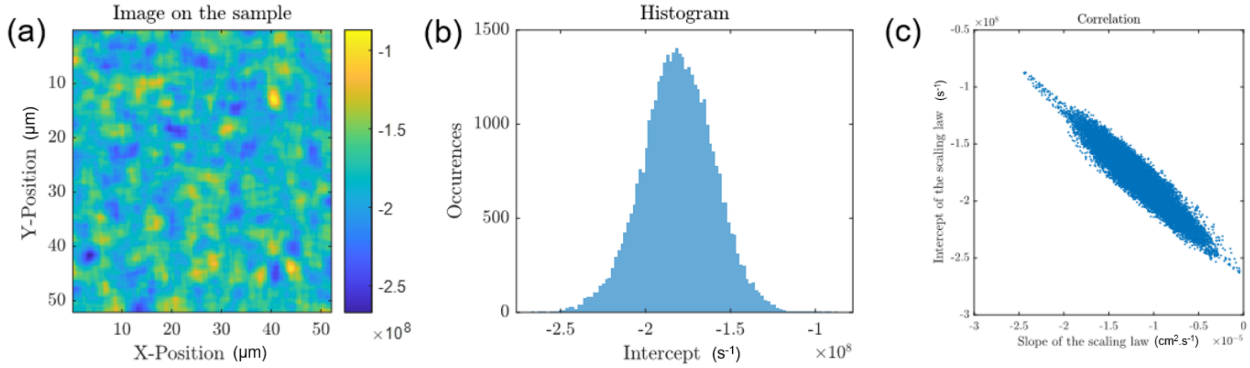

Slope of the scaling law (cm2.s-1)

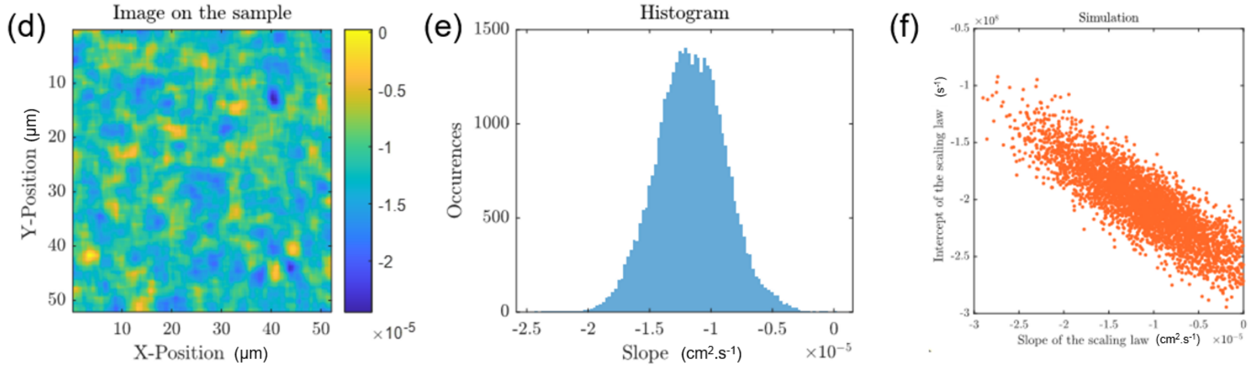

Figure 4.9: *Local determination of parameters. (a-b). Map and histogram of the fitted intercept for the local scalings. (d-e). Map and histogram of the fitted slope for the local scalings. (c) Experimental correlation between the two obtained parameters. The 7 fluences acquisitions were used at a local scale. A binning of* 10 *pixels is applied, meaning that all pixels are averaged out on a square of size* 10×10 *pixels. For each pixel decays are obtained. The derivative of the deconvoluted decays are computed between 0.5 and 2.5ns. The derivatives are assembled to form the scaling, which is linearly fitted. (f) Simulated correlation. Simulation of fitting linear curves with each point being multiplied by a relative error of 20%. This plot shows the fitted intercept as a function of fitted slope after noise has been simulated.*

negative correlation can have two origins: it could have a physical meaning or it could come from noise on the experimental result. To distinguish the two, we tested the case of adding noise to simulations to see if such correlation would appear. It does, as evidenced in Figure 4.9(f). To perform this test, we simulated 2000 scalings from an original perfectly linear scaling with values of intercept and slope equal to the values we found experimentally on the average decay. From this perfectly linear scaling composed of ten points, we generated Gaussian noise centered on 1 and of standard deviation 0.2. For each of the ten points, a random variable is drawn and multiplied to the original point. Thus we simulate a 20% error on all the acquired points. We then apply a linear fit and obtain a slope and intercept. We do this 2000 times and plot the correlation between the intercept and slope in Figure 4.9 (f) for these 2000 couples of intercept and slopes. We can observe a linear negative correlation between the fitted intercepts and fitted slopes, exactly as what is observed on our experimental data (c). **We conclude that we cannot attribute the observed negative correlation to a physical origin, it may come from the noise.** Thus, the independent measurement of the local slope and intercept requires very precise measurements.

However, one advantage of our approach over phenomenological fitting is that it allows to make hypothesis based on physical considerations. In the situation currently under scrutiny, we can assume that the bulk properties of the film are uniform, and that heterogeneities are caused by local differences in the local top surface recombination velocity.

Under this hypothesis all local scalings should have the same slope, since the absorption coefficient α and the external radiative recombination coefficient k_2 are considered constant.Therefore, under this approximation, only the intercept of the scalings should vary locally, and its variation is attributed to a variation in local surface recombination velocity, see Equation (4.22). We fix the slope of local scalings to the value we obtained from the spatially averaged decays, $a = -(1.07 \pm 0.15) \times 10^{-5}$ cm^{2}s^{-1}, and compute only the local intercept. Doing so, we obtained a map of the local intercept of the scaling.

By using values for the bulk SRH recombination parameter k_1 and the diffusion coefficient D as fitted in section 4.1.3, it is possible to extract **a map of the local top surface recombination velocity** S_{top} as shown in Figure 4.10 (a). In Figure 4.10 (b) we show a vertical cross section of the map. We can see variations that are above the estimated error bars. To justify our assumption that local surface recombination is the origin of the variation of the intercept, we evaluate, from Equation (4.22) and the chosen parameter set, that top surface recombination account for 76% of the value of the intercept. We can thus conclude that the scaling law, combined with hypothesis on the material under study, allows us to observe local variations of recombination parameters in a direct way.

In-Homogeneous perovskite sample

To further verify that our technique allows for the interpretation of imaging data, we report here an analysis carried out on a triple cation perovskite thin film after being exposed to an X-ray beam, similar to that of section 4.1.4. We ac-

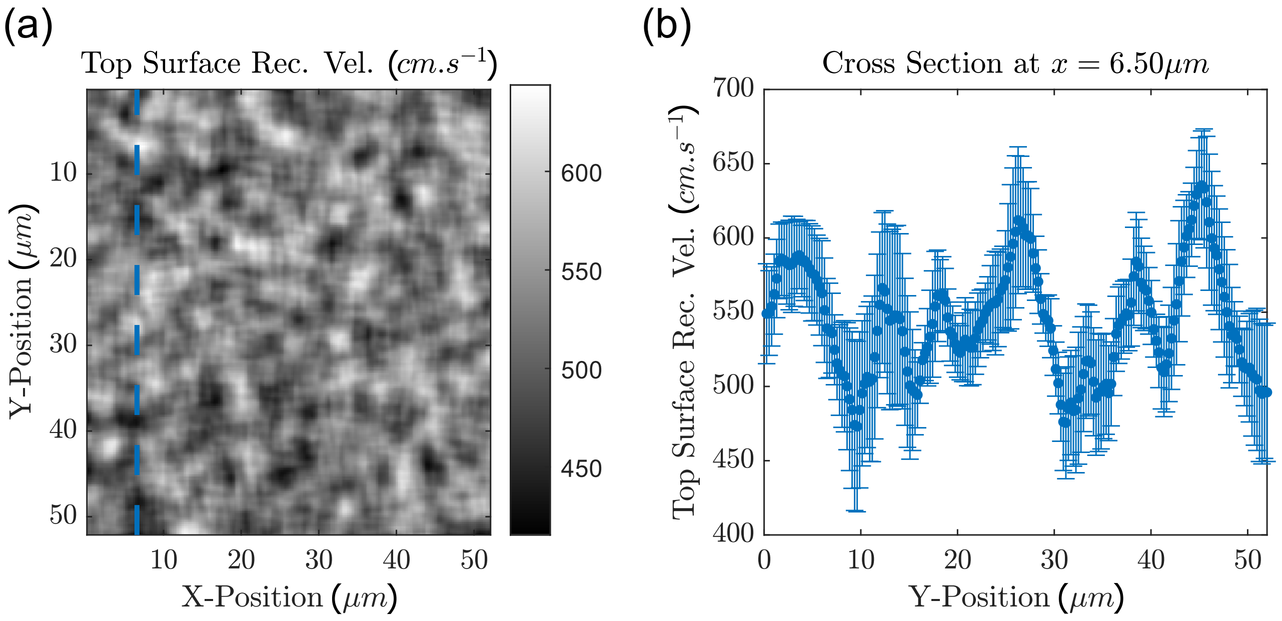

Figure 4.10: *Local determination of parameters. (a). Map of top surface recombination velocity from the fitted local intercepts of the local scalings. The 7 fluences acquisiton of Figure 4.8 were used at a local scale. A binning of* 11 *pixels is applied, meaning that all pixels are averaged out on a square of size* 11×11 *pixels. For each pixel, seven decays are obtained, corresponding to seven fluences. The derivative of the deconvoluted decays are computed between 0.5 and 2.5ns. The derivatives are assembled to form the scaling, from which the intercept is fitted. The slope for all points is set to* $a = -1.07 \times 10^{-5}$ cm^{2}s^{-1}. *To obtain the map of local intercept, we compute locally the average of the ensemble* $E = \{\text{derivative} - a \times \text{fluence}\}$. *For the uncertainty, we compute* $std(E)/\sqrt{\#E}$, *with* $\#E$ *the number of elements in* E. *Then we use Equation (4.22) and the assumed values for the other parameters to compute the map of* S_{top} *from the map of the intercept. The parameters were estimated at* $D = 3.54 \times 10^{-3}$ cm^{2}s^{-1}, $k_1 = 9.23 \times 10^6$ s^{-1}, $\alpha = 6.5 \times 10^4$ cm^{-1}. *(b) Vertical cross section of map (a) at* $x = 6.5\,\mu$m. *Reproduced from [Vidon et al. 2021]*

quired time resolved maps and applied the scaling law. In Figure 4.11(a) and Figure 4.11(c) we show the maps of the intercept and of the slope, respectively. In both cases, the X-ray spot is clearly visible, proving that the transport properties of the material have been modified by the X-rays. We then consider two points: the first one on the pristine area (red) and the second one within the X-Ray spot (green) and we plot the corresponding scaling in Figure 4.11(d). On one side, we can notice that the slope of the scaling is similar in the two cases, indicating that the radiative recombination parameters, namely k_2 and α, did not evolve due to X-ray exposure. On the other side, the intercept values varied from -1×10^{-7} s^{-1} to -2×10^{-7} s^{-1}, demonstrating an increase of the non-radiative recombination processes in the beam exposed region. This result in a in-homogeneous sample gives credit to the interest of the scaling technique to gather map-

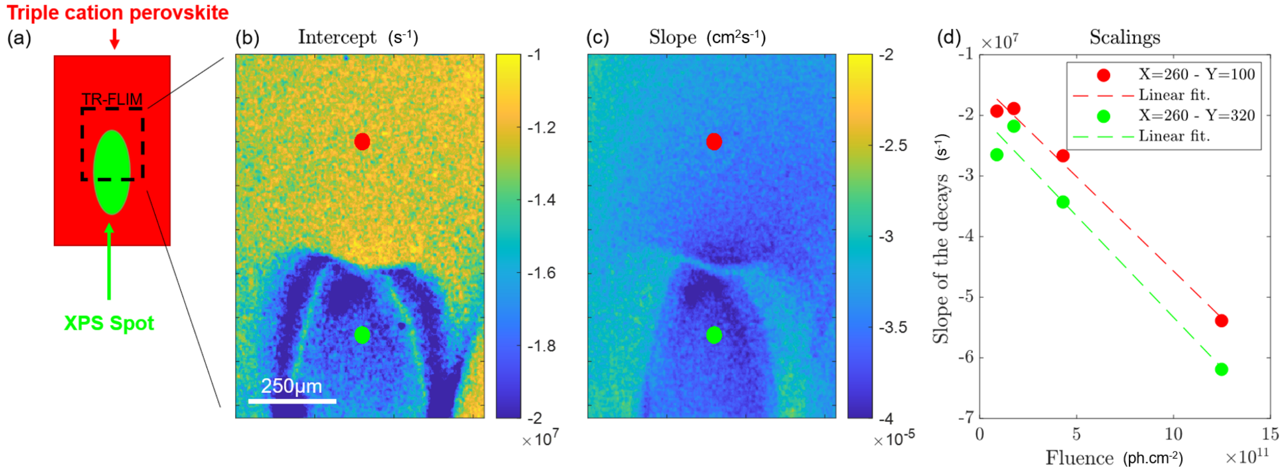

Figure 4.11: *(a) Scheme of the perovskite sample on glass analyzed via XPS. (b) Map of the intercept of the scaling law. (c) Map of the slope of the scaling law. (d) Two local scaling corresponding to the points in red and green in (b) and (c). We observe that while the slope of the scaling is similar inside and outside the region exposed to X-Rays, the intercept of the scaling has changed. This means that the X-Rays did not modify the radiative recombination parameters* k_2 *and* α*, but did induce more non radiative recombination.*

pings of recombination parameters.

4.2.5 Discussion

In this section, we discuss the obtained results. First, we comment on the values of the parameters obtained with this technique. Then, we compare this technique with regular drift-diffusion fitting and we demonstrate that using the scaling law leads to a higher level of accuracy in the determination of parameters. Next, we discuss the validity of the assumptions leading to Equation (4.22), describing the scaling law and extend the formula to other hypothesis. Finally, we discuss the limits of the proposed technique and possible future improvements.

Obtained values

By following the scaling law approach, we obtained a value for the external radiative recombination coefficient k_2 equal to $k_2 = (1.2 \pm 0.4) \times 10^{-10}$ cm^{3}s^{-1}. According to Brenes et al. [Brenes *et al.* 2019], the internal radiative recombination coefficient of $Cs_{0.05}(MA_{0.17}FA_{0.83})_{0.95}Pb$- $(Br_{0.17}I_{0.83})_3$ perovskite is of the order of $k_2 = 2.0 \times 10^{-10}$ cm^{3}s^{-1}, while the external radiative recombination coefficient, evaluated taking into account photon recycling, is of the order of $k_2^{ext} =$

1.0×10^{-11} cm^{3}s^{-1}. Firstly, we can observe that our technique is able to obtain a value close to what is expected for such materials. Secondly, the value we find is close to the internal radiative recombination coefficient as was expected by our simulations of the impact of photon-recycling in the present case, see the Appendix Appendix F. The difference between the value given in [Brenes *et al.* 2019] and ours can have different origins. One is the overall uncertainty on this parameter which is still not determined with precision for triple cation perovskite. Two, the obtained value is dependent on the measure of the absorption coefficient at the laser wavelength α. Three, we showed that the temporal convolution has an impact on the determination of the radiative coefficient. This calls for a more detailed study on the best method to deconvolute the signal and obtain the most precise estimate. Therefore, we conclude that the scaling law allows to extract a direct value for the external radiative recombination coefficient which, in the present low photon-recycling case, is close to the internal radiative recombination coefficient.

Comparison to the drift-diffusion fit

In order to ascertain the accuracy of the parameters we obtain from this measurement technique, we performed a comparison with the drift-diffusion fit of longer decays. The parameter that our scaling was able to determine is the radiative recombination coefficient k_2. Therefore, we implemented two fitting strategies. One in which k_2 is used as a fitting parameter, named Strategy 1, and one where we fixed k_2 to the value obtained by the scaling measurement, named Strategy 2. For both, we also fit D, k_1, N_{bulk}, S_t, N_{top}. We fitted the 7 TR-PL curves all together at once and with only one model for all the curves: no parameter is changed as a function of fluence. Results of Strategy 2 fit were presented in Figure 4.2. For Strategy 1 and 2, the fitted parameters are available in Table 4.6.

We compared the results of the two fitting strategies: comparable values for the fitted parameters were obtained in the two cases. In addition, the uncertainties on the fitted parameters were reduced when considering the value of k_2 determined by the scaling (see the representation in Figure 4.12). In particular, the uncertainty on N_{top} goes from 42% when k_2 is a free fitting parameter to 25% when k_2 is fixed. Finally, the value of the radiative recombination from the drift-diffusion fit is $k_2^{dd} = (1.16 \pm 0.07) \times 10^{-10}$, which is fully compatible with the value obtained with the scaling. Therefore we

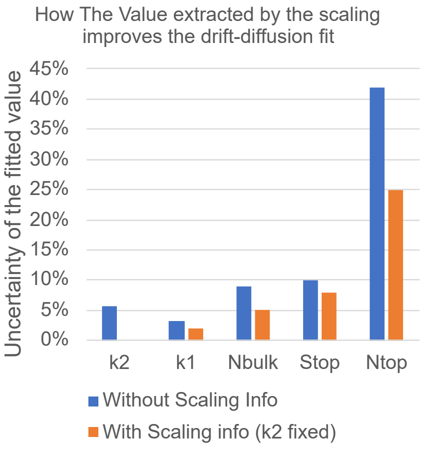

Figure 4.12: *Uncertainties of Table 4.6 represented for the two strategies.*

Symbol	Name	Strategy	Value	Uncertainty	Unit
D	Diffusion Coefficient	1	$(3.49 \pm 0.30) \times 10^{-3}$	9%	cm^2s^{-1}
		2	$(3.54 \pm 0.21) \times 10^{-3}$	6%	cm^2s^{-1}
k_1	Order 1 Recombination Coefficient	1	$(9.20 \pm 0.30) \times 10^{6}$	3.3%	s^{-1}
		2	$(9.23 \pm 0.19) \times 10^{6}$	2%	s^{-1}
N_{bulk}	Trap-Related Density for bulk defects	1	$(4.9 \pm 0.4) \times 10^{15}$	9%	cm^{-3}
		2	$(4.9 \pm 0.3) \times 10^{15}$	5%	cm^{-3}
S_{top}	Top Surface recombination velocity	1	640 ± 62	10%	$cm.s^{-1}$
		2	600 ± 50	8%	$cm.s^{-1}$
N_{top}	Trap-Related Density for surface defects	1	$(1.7 \pm 0.7) \times 10^{14}$	42%	cm^{-3}
		2	$(1.7 \pm 0.4) \times 10^{14}$	25%	cm^{-3}
k_2	Order 2 Recombination Coefficient	1	$(1.16 \pm 0.07) \times 10^{-10}$	5.6%	cm^3s^{-1}

Table 4.6: *Fitted Parameters.Comparison between Strategy 1 (k_2 fitted) and Strategy 2 (k_2 fixed to the value from the scaling). Residuals for Strategy 1 were 57.01 a.u. and for Strategy 2, 57.66. For Strategy 2 the value of k_2 was fixed to 1.2×10^{-10} cm^3s^{-1}.*

conclude that the scaling law is complementary to regular drift-diffusion fitting.

Approximations used

The experimental observation of the linear scaling proves that our assumptions were reasonable. Namely, four main assumptions led to Equation (4.22): (i) the intrinsic nature of the perovskite material, which, according to this experiment, is doped less than 3×10^{16} cm^3. We will explore the question of the doping density of the layers in the last part of this chapter, chapter 4.3; (ii) at short-time, in our experimental conditions, one can neglect the defect related densities N_{bulk} and N_{top} in front of the photo-generated carrier density - which is also confirmed by the values found for these parameters by the drift-diffusion fitting presented above; (iii) no high order Auger-like recombination were observed, as they would lead to a term $\propto n_\gamma^2$ in the scaling (see the formula of the scaling in this case and a more detailed discussion in Appendix F); (iv) at short time, the spatial profile of the carriers is both close to Beer-Lambert initial condition and following the drift diffusion equation. Short-time is therefore defined as the time during which this approximation is valid.

Limits

However, we also note that our technique has two main experimental limitations. The first one, is due to the camera's temporal response function. To reduce the gap between experimental measurements and theoretical models, we used deconvolution algorithms, as discussed below. It is worth noting that this limitation is not due to our method but it is a common issue to all time-convoluted signals. The second limit is related to the use of the scaling law approach to map transport parameters. We observed that noise on the local decays creates a negative correlation between the intercept and the slope fitted at a local level. This renders difficult the determination of the two parameters independently at the local scale when the variations on the sample are of the order of the sensitivity of the technique. However, the correlation could potentially also occur for physical reasons, but, to this date, our measurements cannot distinguish the two. This limitation can be surpassed when hypothesis are made on the nature of the material under study, or when the spatial variations are greater than the sensitivity.

4.2.6 Additional information

Additional details are given in Appendix F including: a discussion on the role of photon recycling and out-coupling, a discussion on the role of deconvolution, a formula with Auger recombination, additional computation details, and an extension to the low absorption regime.

4.2.7 Conclusion

Therefore, we introduced a **new technique** that allows to **image** recombination parameters. It succeeds in answering two challenges: it is compatible with imaging and fast analysis (≈1min to obtain the local results) and it is quantitative and not phenomenological. This technique however has some limitations and we discussed the impact of photon recycling, temporal convolution, noise artifacts extensively.

This short-time fluence dependent slope brought us some information on radiative recombination as well as non radiative recombination. One of the main hypothesis leading to the scaling was that radiative recombination was of order 2, ie $\propto \Delta n^2$ in the range of considered photo-generated densities. But we have a means of quantifying if this is the case or not. We will now introduce and apply another technique that also uses the beginning of the decay, but this time its absolute intensity: $I_{\mathrm{PL}}(t = 0ns)$. This technique is a promising way to obtain maps of local doping density.

4.3 $I_{\mathrm{PL}}(t=0)$ vs. fluence : a proof of the lowly-doped nature of perovskite absorbers

In this section, we show how we can use the scaling of the relative intensity of PL at the beginning of the decay $I_{\mathrm{PL}}(t=0)$ as a function of the fluence n_γ to obtain mappings of doping levels of absorbers.

4.3.1 Theoretical concept and comparison to the continuous wave case

In any out of equilibrium experiment, the net intensity of PL emission from the sample will scale as:

$$I_{\mathrm{PL}} \propto \left(\Delta n_e + n_e^0\right)\left(\Delta n_h + n_h^0\right) - n_i^2 \tag{4.23}$$

We will assume that all the densities at play are much greater than n_i so that we can neglect the last term in Equation (4.23). If doping is present in the material, Equation (4.23) may still be used, but the excess carrier density of one type of carriers may become negligible compared to the doping density.

Pulsed case

In the case of a pulsed laser, at short time, the number of excess carriers at $t=0$ will be, see Statement 2.1.7:

$$\Delta n_e(t=0) = \Delta n_h(t=0) \propto \underbrace{n_\gamma}_{\text{Fluence}} \propto \underbrace{P_{\mathrm{las}}}_{\text{Laser power}} \tag{4.24}$$

One can discuss how short is short time. The main hypothesis here are : it is smaller that any recombination time constant of the material and it is smaller than the charge separation time. Under these hypothesis:

$$\Delta n \equiv \kappa P_{\mathrm{las}} \tag{4.25}$$

As it is unusual for a material to be n-doped and p-doped, we will note N_{dop} the density of dopants, irrespective of their n- or p- nature. With this extra hypothesis, we obtain that:

$$I_{\mathrm{PL}}(t=0) \propto \underbrace{\kappa P_{\mathrm{las}}^2}_{\substack{\text{Order 2}\\\text{term}}} + \underbrace{N_{\mathrm{dop}} P_{\mathrm{las}}}_{\substack{\text{Order 1}\\\text{term}}} \tag{4.26}$$

Therefore we see that observing the scaling of the intensity of PL at short time as a function of the laser power (or fluence) allows to extract a value for the doping density of the material. By observing the transition from order 1 to order 2 when the laser power increases, one can estimate N_{dop}/κ. Even more,

TR	doped	intr.
Low Fluence	1	2
High Fluence	2	2

Table 4.7: *Order of I_{PL} as a function of laser fluence. Qualitative summary.*

this can be applied locally on the imaging data sets. Such scaling was evidenced in [Saba *et al.* 2014] where Saba and co-authors showed a scaling of power two over a wide range of intensities for $\mathrm{MAPbI_3}$ and $\mathrm{MAPbI_{3-x}Cl_x}$. However, they focus on the high excitation range and do not exhibit the low excitation data. In [Feldmann *et al.* 2019], such order 2 scaling is also displayed, but the low fluence data is not shown. In [Wolff *et al.* 2021], the scaling of the decay time (rather than the intensity) is discussed, as well as comparison with continuous wave data.

Continuous wave case

In the intrinsic case and in continuous wave, as described in Equation (3.12):

$$n = \frac{k_1}{2k_2}\left(\sqrt{1+\frac{4Gk_2}{k_1^2}}-1\right) \tag{4.27}$$

where G is the generation rate that is proportional to the laser power P_{las}:

$$G \equiv \kappa' P_{\mathrm{las}} \tag{4.28}$$

Therefore, we find:

$$I_{\mathrm{PL}}^{\mathrm{cw}} \propto \frac{2}{k_1}G - \frac{k_1}{k_2}\left(\sqrt{1+\frac{4k_2}{k_1^2}G}-1\right) \tag{4.29}$$

For the sake of simplification we can consider

- the low generation case where $4Gk_2 \ll k_1^2$, in this case : $n \propto G$ and
$$I_{\mathrm{PL}}^{\mathrm{cw}} \propto P_{\mathrm{las}}^2 \tag{4.30}$$
- The high generation case where $n \propto \sqrt{G}$ and
$$I_{\mathrm{PL}}^{\mathrm{cw}} \propto P_{\mathrm{las}} \tag{4.31}$$

In the literature, such results on continuous wave were discussed in [Levine *et al.* 2018]. A more detailed discussion of rates and orders in the continuous wave case was given in [Draguta *et al.* 2018], as well as some applications to imaging. They show the transition between order 2 at low generation and order 1 at higher generation for perovskite based solar cells and thin films.

CW	doped	intr.
Low G	2	2
High G	1	1

Table 4.8: *Order of I_{PL}^{cw} as a function of laser power. Qualitative summary.*

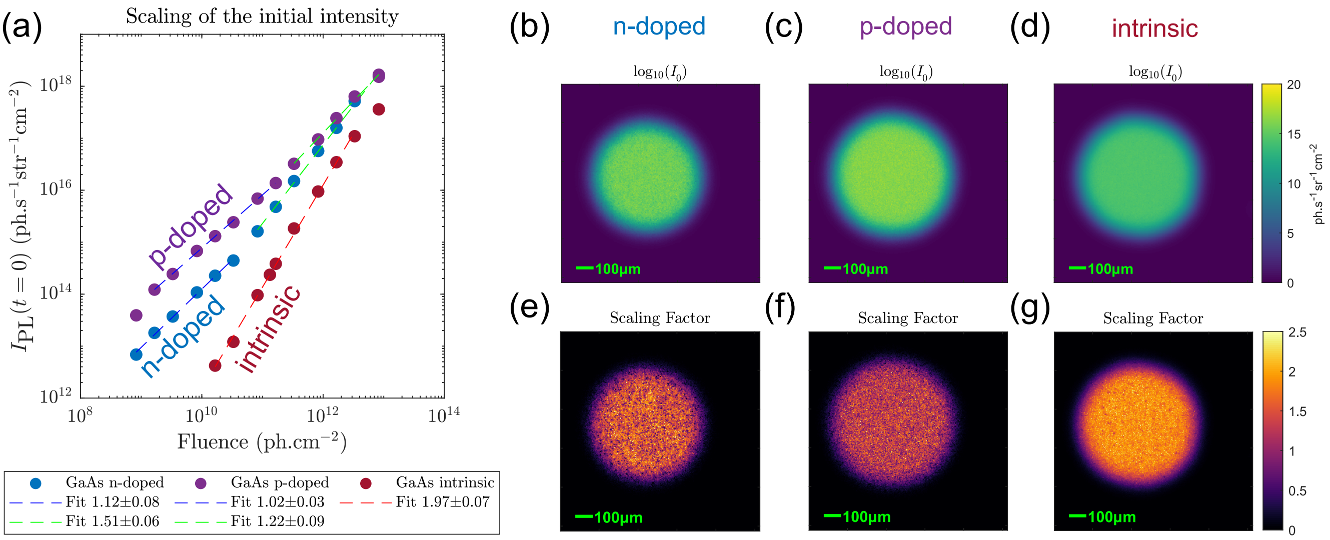

Figure 4.13: *TR-FLIM Power study of GaAs wafers using the absolute calibration. (a) Intensity of the maximal point of the decay as a function of laser fluence. (b-d) Maps of the 10-based logarithm of the absolute intensity fitted via Equation (4.33) (e-g) Maps of the fitted scaling factor of* $\log(I_{PL})$ *vs.* $\log(n_\gamma)$ *with* n_γ *the fluence. A slope of 2 is indicative of intrinsic nature.*

Comparison

The two scaling have opposite behavior for intrinsic or lowly doped absorbers: in cw the low fluence case should yield a order 2 behavior while an order 1 behavior is expected below the doping concentration for the tr experiment. At high fluence the cw experiment would yield to a order 1 behavior while the tr experiment should yield an order 2 scaling.

4.3.2 Experimental validation with GaAs

We perform experimental acquisitions on three commercial GaAs wafers: one intrinsic ($L = 350\,\mu\mathrm{m}$), one p-doped ($L = 350\,\mu\mathrm{m}$) and one n-doped ($L = 450\,\mu\mathrm{m}$). We use the TR-FLIM with the Talisker laser in quasi punctual illumination and vary the intensity of excitation. The three wafers have a fairly low decay time, of the order of 3ns, which is the order of magnitude of the temporal gate we use for this experiment.

We obtain for each of the wafers a series of decays corresponding to each fluence. We use the absolute calibration of the camera to estimate the absolute number of photons reaching the sensor. The experimental results are shown in Figure 4.13.

In Figure 4.13 (a) we plot the average intensity over the spot size as a function of the laser fluence for the three samples. The intrinsic sample scales with an order 2 manner, as expected from the theoretical point of view. A slight saturation seems to appear at the highest fluence which is expected as well (if the order 2 would continue indefinitely, the PLQY would become greater than one at some point). The n-doped sample has a higher PL intensity than the intrinsic - as expected because the doping carriers increase the $n_e n_h$ product in the low fluence range. We see a order 1 scaling for the fluences up until approximately 3×10^{10} ph/cm^2. After that fluence, an order of 1.51 is found. For **the p-doped wafer** a similar behavior is observed. The intensity of PL at low fluence is even more intense than for the n-doped wafer. Moreover the transition between the order 1 behavior and the higher order seems to start at a fluence of approximately 2×10^{11} ph/cm^2, one order of magnitude higher than for the n-doped wafer. Both of these observations (higher PL intensity, higher fluence transition) point towards a **higher doping density for the p-doped wafer rather than the n-doped one**.

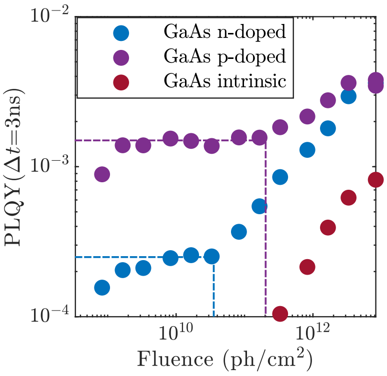

Figure 4.14: *Effective PLQY at the maximum of the decay computed as* $PLQY = 2\pi * (3ns) * I_{PL}(t = 0ns)/n_\gamma$

From these measurements we can also compute the effective PLQY at time $t = 0ns$, or rather during a time equal to the decay time observed for these samples around $\tau = 3ns$. To do so we compute it as:

$$PLQY(\Delta t = \tau) = \tau \times \frac{2\pi I_{\mathrm{PL}}(t = 0ns)}{n_\gamma} \tag{4.32}$$

This definition compares the photons output of the sample during a time Δt and the photon input. It is plotted in Figure 4.14. We clearly see a transition from a constant as function of fluence to a linear behavior for the doped samples. We zoomed in on the region where it is more visible. No constant behavior is observed for the intrinsic wafer. The values found are rather low but there are a few phenomena that could explain this. First, these wafers were un-passivated and therefore subject to a high density of defects at the surfaces (with a decay time of the order of 3ns). Two, we neglect the laser reflection in this computation, which would reduce the real incoming photon flux. Three, we only look at the beginning of the decay which gives us a lower limit for the real PLQY value. Still, even GaAs devices in the literature can have PLQY in cw of the order of 10^{-3} at low intensity [Zhang *et al.* 2020a].

In Figure 4.13 (b-g) we show the same analysis conducted on the images. We fit locally the following model:

$$\log_{10}(I_{\mathrm{PL}}(t = 0ns)) = f \times \log_{10}(n_\gamma) + \log_{10}(I_0) \tag{4.33}$$

We plot $\log_{10}(I_0)$ in Figure 4.13 (b-d) and f in Figure 4.13 (e-g). The fits are conducted in the low fluence region $n_\gamma <$

$3 \times 10^{10}\,\mathrm{ph/cm^2}$. The local values correspond to the average values, with no specific local variation observed. We attribute the visible variations to local noise. Let us comment on the order of magnitude for $\log_{10}(I_0)$. For GaAs, the diffusion of carriers is very fast (tens of ps) compared to the gate width of the camera (3ns). Therefore we can assume that the photogenerated carriers have homogenized in thickness. For the doped wafers we then expect that:

$$I_{\mathrm{PL}}(t = 0ns) \approx k_2 \int_0^L dz\ n_e n_h \tag{4.34}$$

$$\approx \underbrace{k_2 N_{\mathrm{dop}} \frac{\alpha_{\mathrm{GaAs}}(532\mathrm{nm})}{L}}_{\equiv I_0} n_\gamma \tag{4.35}$$

For GaAs, $k_2 \approx 7 \times 10^{-10}\,\mathrm{cm^3/s}$, the thicknesses L are approximately 400 μm for the three devices and $\alpha_{\mathrm{GaAs}}(532\mathrm{nm}) \approx 1 \times 10^5\,\mathrm{cm^{-1}}$. By averaging over the spot we find $I_0(\text{n-doped}) = 2.5 \times 10^{15}\,\mathrm{ph/s/str/cm^2}$ and $I_0(\text{p-doped}) = 1.4 \times 10^{16}\,\mathrm{ph/s/str/cm^2}$. This corresponds to doping densities: for the p-doped wafer $N_A = 8.4 \times 10^{16}\,/\mathrm{cm^3}$ and for the n-doped $N_D = 1.5 \times 10^{16}\,/\mathrm{cm^3}$.

Comparison with cw data

We tested punctual illumination at high fluence ($\Delta n > 10^{17}\ cm^{-3}$) for the three samples and found scalings of order 1 for the three samples.

Conclusion

Therefore we showed the interest of the technique of measuring the intensity at time $t = 0ns$ for the determination of doping densities. We showed that at low fluence, doped semiconductors exhibit order 1 behavior and intrinsic semiconductors and order 2 behavior as a function of laser fluence. Next, we use this tool on perovskite absorbers to prove their intrinsic nature.

Result 4.3.1. For the pulsed experiment, one expects the following scaling valid in the slow diffusion and high absorption case:

$$\log(I_{\mathrm{PL}}(t = 0ns)) = \underbrace{\log(K)}_{\text{Fit Param. 1}} + \log(n_\gamma) + \log\left(n_\gamma + \underbrace{\frac{N_{\mathrm{dop}}}{\alpha}}_{\text{Fit Param 2}}\right) \tag{4.36}$$

with n_γ the laser fluence.

4.3.3 Imaging results on various perovskite compositions

In this section we use the PL_0 technique to evidence that all of **the perovskite absorbers that we were able to study exhibited very low doping,** ie most of them showed intrinsic-like behavior at fluences comparable to 1 sun, see Figure 4.15. We also studied half cells as well as full cells in top and bottom configuration. We did not observe doping or order 1 behavior either for full cells or half cells: this suggests that the assumed doping of the CTL in the classical pin configuration does not translate into the doping of the perovskite layer. We finally show results on $FAPbI_3$ samples discussed in chapter 3.5. The results show spatial inhomoegeneity of both the value of the constant K and of the doping density N_{dop}/α.

Comparing different perovskite compositions

In Figure 4.15, we plot the scaling obtained for various perovskite compositions studied during this work. They all exhibit order 2 behavior for fluences higher than $n_\gamma > 1 \times 10^{10}\,\text{phcm}^{-2}$. At lower fluences, order 1 behavior is shown. This allows to estimate that **for the layers under study, $N_{\textbf{dop}}/\alpha$ is of the order of $1 \times 10^{10}\,\text{cm}^{-2}$.** In terms of density, it would yield to an order of $N_{\text{dop.}} \approx 1 \times 10^{15}\,\text{cm}^{-3}$.

What could this doping density be? The "doping" could actually be the defect density of charged defects that act as dopants for the perovskite layers. This is only an hypothesis we have at this stage, and this needs further confirmation.

Discussion on the impact of the wavelength. With the green laser $\lambda = 532nm$, for slow diffusion materials such as perovskite, we only probe the surface at $t = 0ns$. Therefore, we could obtain different $N_{\text{dop.}}$ values for different wavelength of excitation (this experiment has not been tried).

Impact of FTO and TiO_2 on half cells

We use the technique on images acquired on a half cell composed of Glass+FTO+TiO_2+PVK analyzed in the bottom illumination configuration as sketched in Figure 4.16 (d). The samples were deposited at IPVF, see Appendix C.1 for more details. The laser reflection shown in (a) displays the transition region between the TiO2 (right) and TiO2-free zone (left), as sketched in (d). We fit the following model to the data (valid in the slow diffusion and high absorption case):

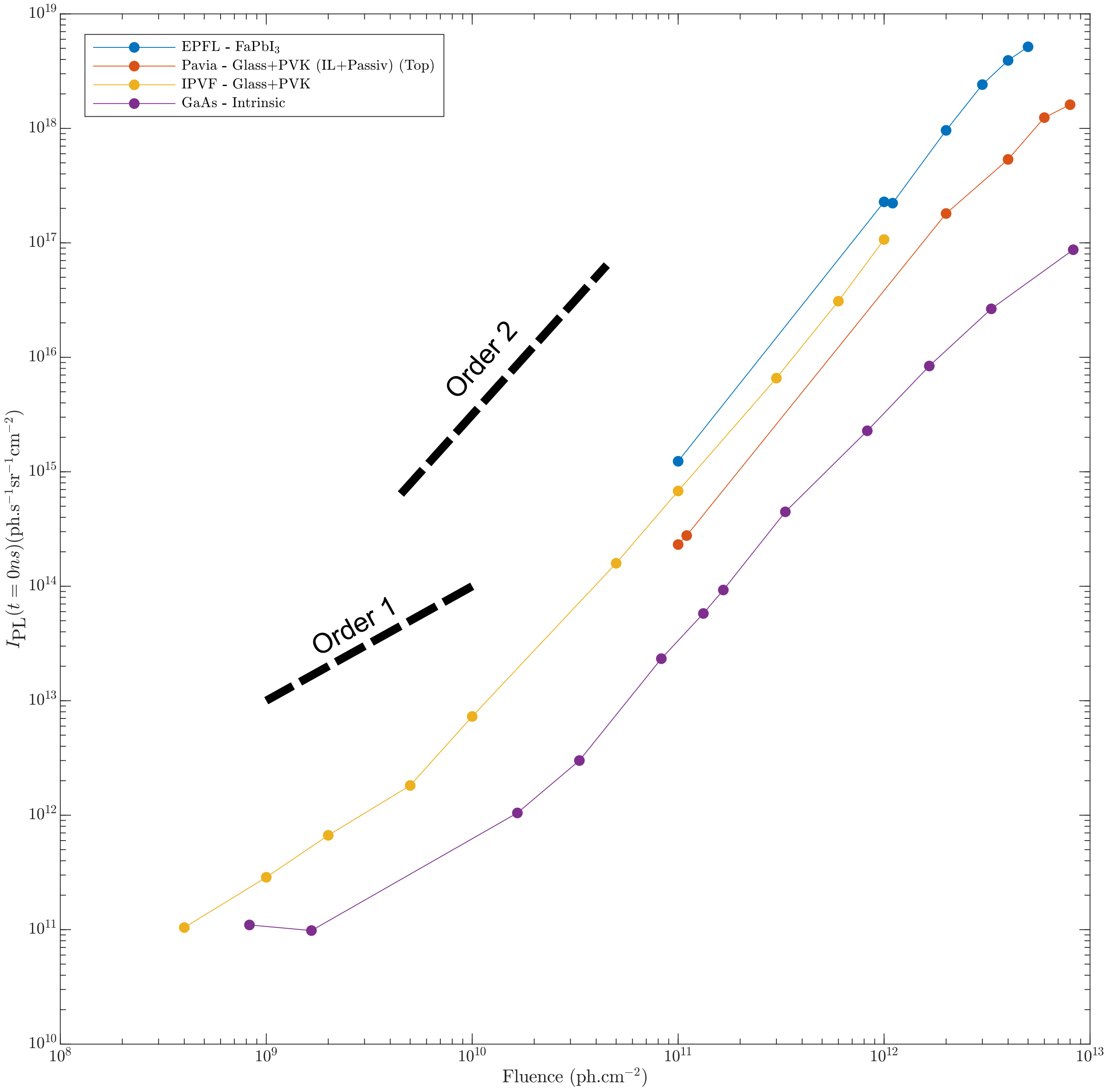

Figure 4.15: *Scaling of $I_{PL}(t = 0ns)$ for various samples acquired during this work.*

$$\log(I_{\mathrm{PL}}(t=0ns)) = \underbrace{\log(K)}_{\text{Fit Param. 1}} + \log(n_\gamma) + \log\left(n_\gamma + \underbrace{\frac{N_{\mathrm{dop}}}{\alpha}}_{\text{Fit Param 2}}\right) \tag{4.37}$$

This is just Equation (4.26), re-written with logs and as a function of laser fluence and not power. The resulting fitted maps for the half cell are shown in Figure 4.16 (b) and (f), while an example of local fitting is shown in Figure 4.16 (e). The curve in Figure 4.16 (c) is the pixel-pixel correlation of the maps shown in (b) and (f).

Interpretation of the constant K. We observe a clear transition in terms of the parameter $\log(K)$ in (f) when observing the TiO_2 and not TiO_2 region. The right side shows stripes characteristic of the deposition of this material via spray coating. The vertical separation visible in the laser reflection (a) is gives rise to a clear increase of K. The constant K is a combination of many physical parameters. One is the local illumination intensity. Indeed, if a small factor is applied locally on the estimated n_γ it would mainly (but not only) be taken into account by the fitting in the K parameter. Second is the local radiative recombination coefficient value $k_2(x,y)$ which could potentially vary, for instance with local variations of bandgap. Third is the local escape probability of photons. Indeed, the local probability of escape $p_e(x,y)$ at some position x, y also comes in as a multiplicative factor on the local $I_{\mathrm{PL}}(x,y)$ signal. Here the presence of the TiO_2 layer seems to slightly decrease K, which could be explained by a different light coupling in this region from the FTO-PVK interface of the left. The impact of the reflection coefficient is discussed below.

Interpretation of the doping N_{dop}/α. In Figure 4.16 (b) we plot the map of the parameter N_{dop}/α. This map shows a transition from the left region, with a value of $\approx 1 \times 10^9\,\mathrm{cm}^{-2}$ to the right region with $\approx 3 \times 10^9\,\mathrm{cm}^{-2}$. The fact that we observe a transition does not seem to be very correlated to the map of K, as the correlation is rather pointlike in (c) —the points at very low doping corresponding to noise on the map and not to a particular region. Therefore, the variation of effective doping density does hold physical information not redundant with K. We see that the perovskite in contact with TiO_2 seems to be slightly doped. For a wavelength of 532 nm, we expect $\alpha \approx 1 \times 10^5\,\mathrm{cm}^{-1}$. This would lead to $N_{\mathrm{dop}} \approx 1 \times 10^{14}\,\mathrm{cm}^{-3}$ out of the TiO_2 zone and up to $N_{\mathrm{dop}} \approx 3 \times 10^{14}\,\mathrm{cm}^{-3}$. This order of magnitude is very low compared to other semiconductors. In particular, it is most interesting to see that the doped TiO_2 does not dope so much

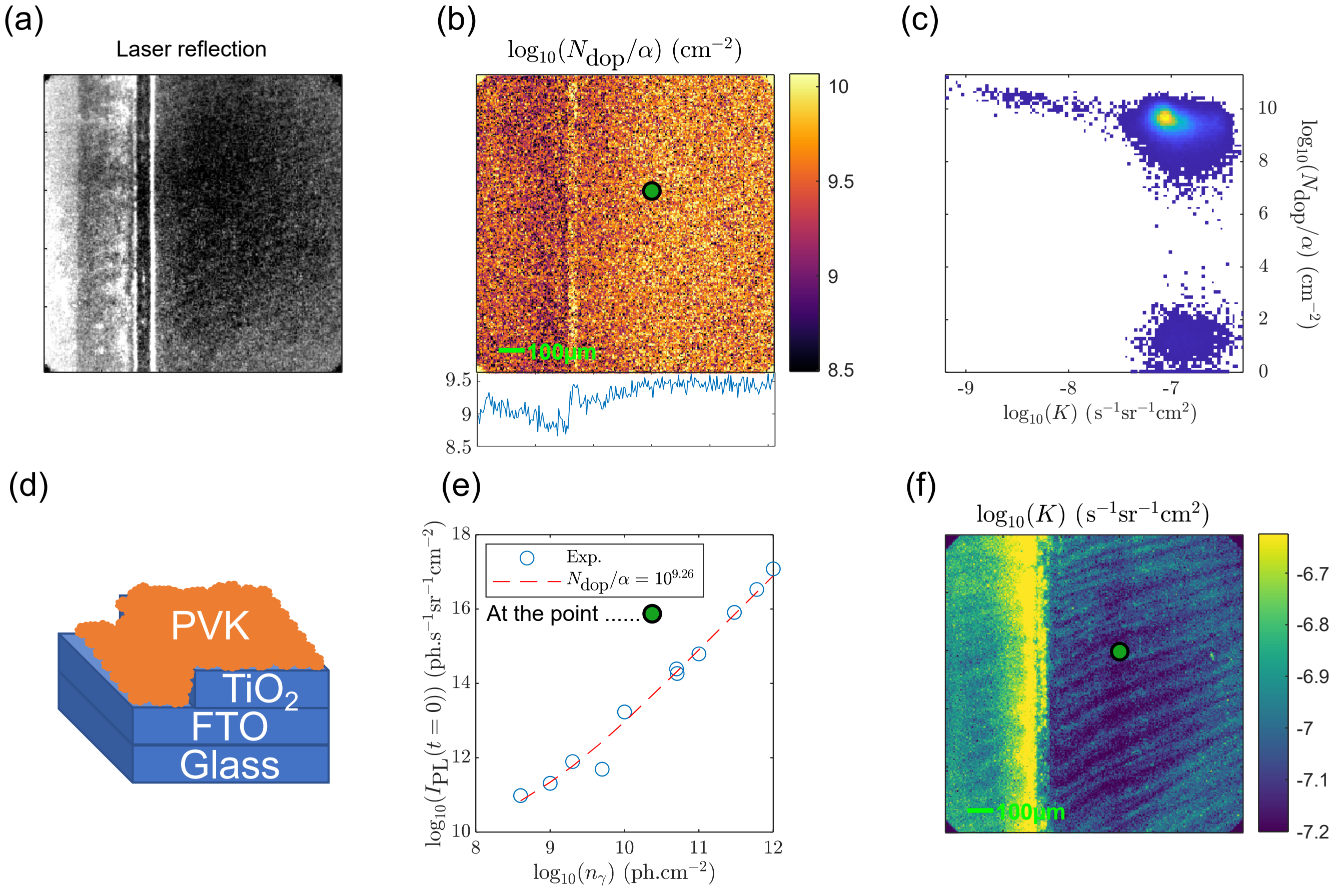

Figure 4.16: *Scaling of $I_{PL}(t=0ns)$ for the half cell Glass+FTO+TiO2 observed from the bottom. (a) Laser reflection map (b) Fitted parameter 2 of Equation (4.37) (c) Correlation between the two local fitted parameters. Brighter color correspond to higher number of pixels. (d) Scheme of the imaged area. (e) Example of local scaling at the green point and correspondind fit. (f) Fitter parameter 1 of Equation (4.37).*

the perovskite layer. This could be the case for two reasons: either the TiO_2 is not doped as we expect it to be or there exists a difference in affinity leading to a barrier for the electrons going from the TiO_2 to the perovskite. Interestingly, we saw a similar result when using illumination from the top-perovskite side.

Impact of the change of local reflection. In Figure 4.16 (a) we see that the reflection map is not uniform. This has an impact on the density of carriers that is photogenerated. If $R(x,y)$ is the reflection coefficient, then we obtain:

$$\log(I_{\rm PL}(t=0ns)) = \log(K) + \log(1-R(x-y))\log(n_\gamma) + \log\left(n_\gamma + \frac{N_{\rm dop}}{\alpha(1-R(x,y))}\right) \quad (4.38)$$

Therefore, we see in Equation (4.38) that if the reflection coefficient is higher, the transition between order 1 and order 2 scaling is expected at higher fluence. We see in Figure 4.16 (a) that the reflection is higher on the left region (without TiO_2). However, this does not translate in a higher local value of transition fluence, we even observe the contrary. Therefore we can say that the observed variation in D_{dop}/α of Figure 4.16 (b) is not an artifact due to a change of reflection coefficient.

$FAPbI_3$ samples

We used our model to image in-homogeneous samples of $FAPbI_3$ of the same kind as presented in chapter 3.5. The three samples correspond to three different (flash-)annealing rates, sample 1 being the fastest rate. The fluences observed range from $1 \times 10^{11}\,\mathrm{phcm}^{-2}$ to $5 \times 10^{12}\,\mathrm{phcm}^{-2}$. We plot the results of fitting of model Equation (4.37) in Figure 4.17. We can observe that as the annealing rate decreases (ie in the order 1,2,3), the presence of regions with $N_{\mathrm{dop}}/\alpha \approx 1 \times 10^{10}\,\mathrm{cm}^{-2}$, increases —see the yellowish zones in column (b). The zones correspond to some of the black zones in the reflection maps. Here we need to acknowledge that our fitting result gives a pseudo-doping density lower than our lowest fluence. Therefore, this interpretation needs to be confirmed by further measurements. Still, we argue that the fact that this pseudo doping spatially corresponds to precise zones in the reflection map does give credit to our interpretation. In column (c) we show mappings of the constant K. In these maps we observe that most of the black zones in the reflection maps (a) appear brighter in (c). With complementary Hyperspectral cw measurements, we were able to show that these dark zones actually show slightly higher emission in the high energy range than the center. This change of emission would imply local changes in the band parameters that could translate in a modification of the value of k_2, leading to the observed modification of K.

4.4 Conclusion

In this chapter, we focused on the interpretation of decays as a function of the incident laser fluence.

In the first section, we showed that perovskite absorbers are very well described by usual models such as the drift diffusion model. We evidenced it by applying the drift diffusion fitting method onto multiple perovskite coming from different labs and subject to X-ray or not. The models gave us the clue that in thickness diffusion for perovskite material takes place

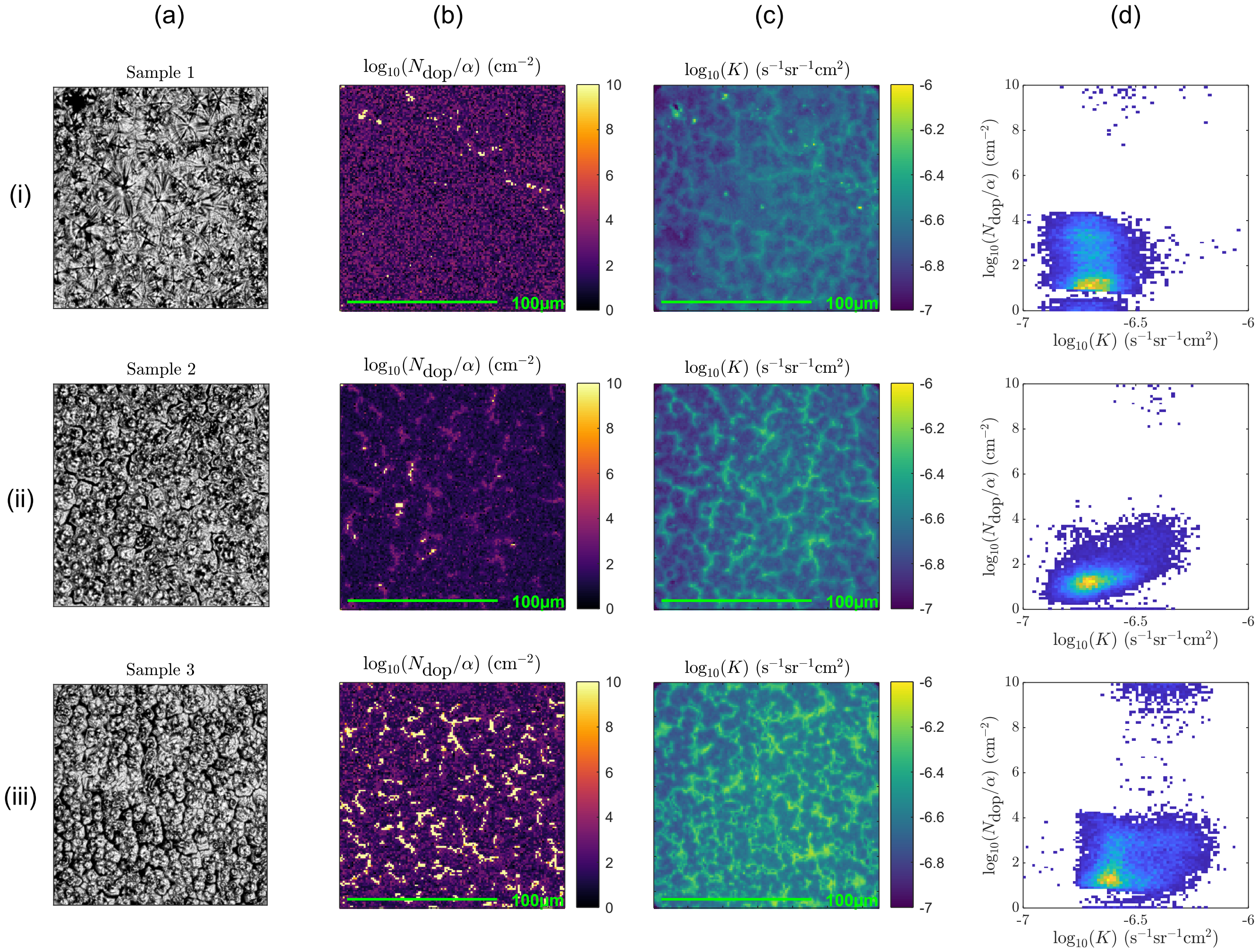

Figure 4.17: *Scaling of $I_{PL}(t = 0ns)$ for the FAPbI$_3$ samples. The three lines correspond to sample 1, 2 and 3. Column (a): Laser Reflection map. Column (b) Fitted N_{dop}/α. Column (c) Fitted K. Column (d) Correlation between the mas (b) and (c).*

slowly compared to 1 ns. This fitting technique is irrelevant for imaging applications today as it is too slow to apply.

In the second section, we introduce a new technique that we developed to overcome this imaging challenge while still having a link to the microscopic models. This so called ”scaling law” technique uses the initial normalized derivative of the decays as a function laser fluence to obtain the radiative recombination coefficient as well as a parameter linked with non radiative recombination and diffusion. This technique is justified from a theoretical point of view. We found a good agreement when we applied this technique to our baseline rather homogeneous perovksite but also when applying it to samples with areas exposed to X-rays. This technique evidenced that the radiative recombination coefficient was not modified by the X-rays, but the non radiative recombination were increased. This technique will be further studied as a function of laser wavelength in Chapter 5.

In the third section, we showed another tool to map properties of perovskite based materials: the observation of the scaling of the absolute intensity of PL as a function of laser fluence. We showed how this technique applied to usual GaAs wafers correctly distinguished the doped and intrinsic wafers in terms of the order of the scaling going from 1 for a doped wafer to 2 for an intrinsic one. We applied this technique on our datasets, using our absolute calibration of the TR-FLIM camera. The application of this technique evidenced that **all the thin films we were able to measure showed very light doping** ($< 10^{15}$ cm^{-3}) if any. The images allowed to evidence inhomogeneities of doping for the FAPbI$_3$ samples. We also showed that, surprisingly, the perovskite was not doped when put in contact with doped extraction layers. This points toward a possible band misalignment between the perovskite and its neighbor layers.

Therefore, all this chapter showed how the fluence of the laser coupled with advanced methods, simulation and calculus allowed us to obtain maps of: radiative recombination coefficient, top-surface recombination velocity and local doping. We also hinted at a major issue concerning non radiative recombination measurement: distinguishing top surface recombination velocity from bulk defects is far from obvious. In the next chapter we will discuss this question and introduce two methods to answer the following question: are the defects in the bulk or at the surface?

Chapter 5

Distinguishing bulk from surface recombination locally

We saw in the previous chapter how the short-time dynamics of the decays contained information on most of the recombination and transport parameters. We proved that the non-radiative recombination at the interfaces and in the bulk played a closely tied role —the correlation between them rendering their unique determination difficult. **The problem that appears is** that the process of diffusion ensures that carriers will be subject both to traps in the bulk and at the interfaces. In order to gain more insight on *where* the efforts need to be made to improve the devices, we need to be able to distinguish interfacial non-radiative recombination from bulk ones. **The aim of this chapter is to demonstrate** that one can distinguish bulk from surface defects by using different excitation wavelengths when performing TR-FLIM experiments. By using larger and larger wavelengths, the photo-generated carrier density is more and more homogeneous in thickness.

In a first section, we justify our question and introduce the problem, as well as the state of the literature on this matter. We also discuss the exact solution of the drift-diffusion model and how this solution can shed new light on this problem. In a second section, we use our short-time scaling introduced in Chapter 4 and study perovskite samples as a function of wavelength. We argue that using the scaling law allows to distinguish surface from bulk recombination. As a proof of concept, we use this technique to estimate the surface recombination velocity of perovskite with decays from punctual illumination. In the third part we tackle the application of this technique to images, we apply this method to the study of X-Ray exposed triple cation perovskite and give images of top surface recombination velocity as well as bulk lifetime. We thus demonstrate that there exists different regions affected in the bulk around the X-Ray beam spot. We discuss the reliability of this technique and compare it to another technique that we adapted from one found in the literature.

Table of contents

Executive summary

Statement 5.0.1. Methods and theory. Two methods are introduced to distinguish bulk from surface recombination:

1. The short-time-scaling-method, that relies on the observation of the short-time derivative multiple decays obtained with different wavelengths of excitation.
2. The δ_1-method, that relies on the observation of the long-time mono exponential decay and its projection on the y-axis at $t = 0$. Possibly usable with only one decay.

We show that we are able to obtain coherent result with these two methods both locally and on average.

Result 5.0.1. Application of the short-time scaling method to the averaged decays of triple-cation perovskite.

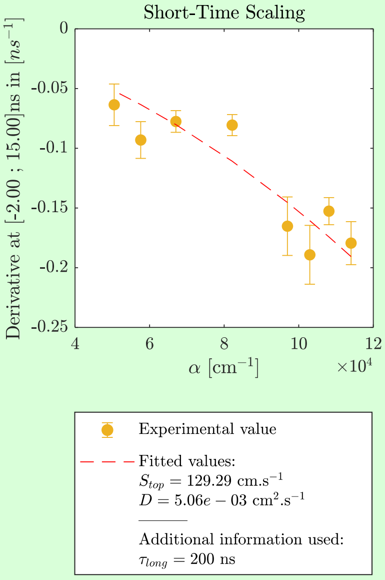

Result 5.0.2. Obtained mappings of top surface and bulk recombination for an X-Ray damaged half cell of triple cation perovskite with the short-time scaling method.

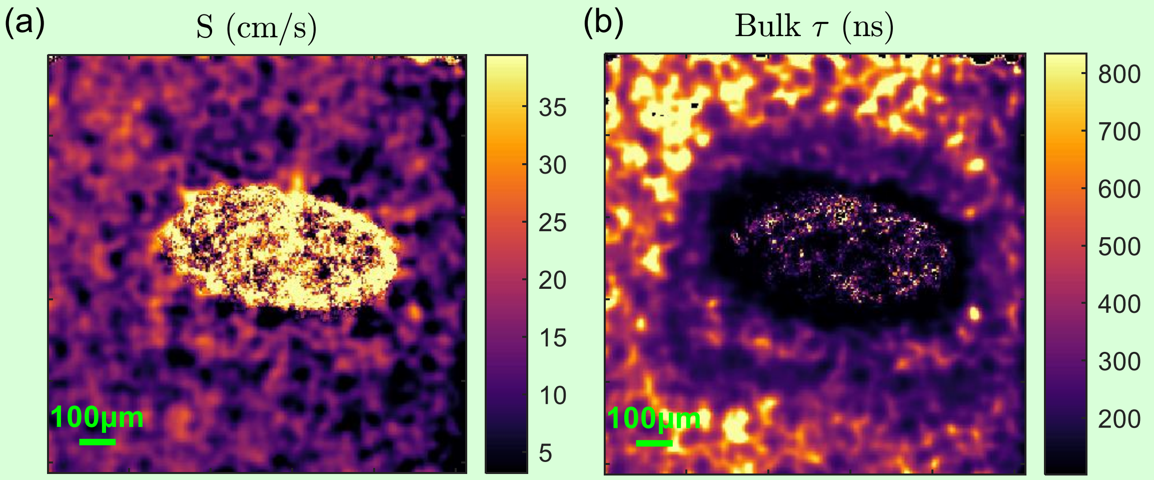

5.1 What is the bulk, what is the surface, why are they often difficult to distinguish? Two methods to distinguish them.

If the reader are *mathematicians*, it may strike them that we allow ourselves to easily distinguish the bulk from the surface of a layer. But as *physicists* we have ways of answering such concerns, and the first part of this section will tackle the exact definition of bulk and surface. Next we will give some literature review on the subject, mainly to show techniques that were developed to answer the question of distinguishing the two types of recombination. Finally, we will describe the exact solution of the simplified drift diffusion model. This will allow us to gain more insight on the techniques developed in the literature, as well as giving us tools to apply to the experimental case.

5.1.1 Theoretical considerations: does this question make sense?

Let us gain in precision on the exact problem we want to solve. We consider an element of surface of our sample, say a thin-film on glass. Let us consider that it contains a total number $N_{\mathrm{tot.}}$ of defects per cm^2 and a local density at thickness z, $N_{\mathrm{def.}}(z)$. These defects could have different spatial distribution in the thickness of the device. Most of the defects could be close to the top surface or rather homogeneously distributed, or any other distribution $N_{\mathrm{def.}}(z)$ that amounts to:

$$N_{\mathrm{tot.}} = \int_0^L N_{\mathrm{def.}}(z')\,dz' \tag{5.1}$$

The question of surface or bulk defect could be formulated as such: for the device under study, is there a way for us to determine if the distribution of defects is closer to the surface dominated case (a) or to the homogeneous case (b)?

The two situations give rise to different decays, see Figure 5.1. In this Figure, two decays (in (b)) are obtained via drift diffusion simulation, with two different defect spatial distributions depicted in (a) and parameters given in Table 5.1.

The two defect distributions however **share the same integral value**, ie $N_{\mathrm{tot.}}$ is the same. We can observe that the decays are different both at short time and at long time, with a long lifetime that is different even though the total number of defects is similar for both. This allows us to state:

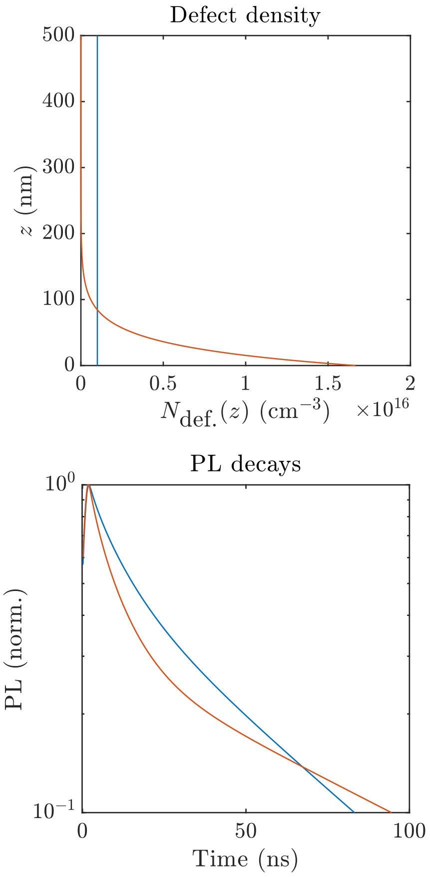

Figure 5.1: *Simulation of two different decays (bottom) obtained from two different spatial distributions of defects (top). The spatial distributions of defects have the same integral value* $N_{tot.}$.

Statement 5.1.1. Different defect spatial distributions lead to different decays, even if they all represent the same total number of defects. Even the *decay time* may be different.

Therefore, there is hope that one can use decays to distinguish spatial distributions of defects.

Parameter	Value
D	$1 \times 10^{-2}\,\mathrm{cm}^2\,\mathrm{s}^{-1}$
$N_{\mathrm{def.}}(z)$	see Figure 5.1 (a)
σv_{th}	$1 \times 10^{-8}\,\mathrm{cm}^3/\mathrm{s}$
$k_1(z)$	$\sigma v_{th} N_{\mathrm{def.}}(z)$
k_2	$9 \times 10^{-11}\,\mathrm{cm}^3/\mathrm{s}$
α	$9 \times 10^{4}\,\mathrm{cm}^{-1}$
L	$500\,\mathrm{nm}$
n_γ	$1 \times 10^{10}\,\mathrm{cm}^{-2}$

Table 5.1: *Parameters used for Figure 5.1*

5.1.2 The surface recombination velocity

Usually, a simpler model is considered to take the spatial distribution of defects into account. A surface recombination velocity S_{top} is considered in the literature, as a boundary condition for the charge carriers and a *flat* recombination rate k_1 is considered in the bulk [Wurfel 2005]. At the top interface $z = 0$, the surface recombination velocity is defined as:

$$\underbrace{D\frac{\partial \Delta n}{\partial z}(z=0,t)}_{\substack{\text{Current "flowing out".} \\ (\mathrm{cm}^{-2}\,\mathrm{s}^{-1})}} = S_{\mathrm{top}}\Delta n(z=0,t) \tag{5.2}$$

There is a correspondence between this definition and the number of defects $N_{\mathrm{def.}}(z)$ we introduced above. **We have to define some height z_s defining a volume for what we call "the surface".** This correspondence is found by equating the number of charges flowing out in one model, to the number of recombination happening in the "surface" volume of height z_s:

$$S_{\mathrm{top}}\Delta n(z=0,t) \approx \sigma v_{th} \underbrace{\int_0^{z_s} N_{\mathrm{def.}}(z')\Delta n(z=z',t)\,dz'}_{\substack{\text{If } z_s \ll \left(\frac{\partial}{\partial z}\frac{N_{\mathrm{def.}}(z)\Delta n(z)}{N_{\mathrm{def.}}(0)\Delta n(0)}\right)^{-1}: \\ \approx z_s N_{\mathrm{def.}}(0)\Delta n(0,t)}} \tag{5.3}$$

With σv_{th} the product of the defects capture cross section and thermal velocity, see Statement 2.1.4. If z_s is sufficiently small compared to the derivative of the function $\left(\frac{\partial}{\partial z}\frac{N_{\mathrm{def.}}(z)\Delta n(z)}{N_{\mathrm{def.}}(0)\Delta n(0)}\right)^{-1}$, the integral may be approximated by the value at $z = 0$ times the width of the interval. The approximate link between the S_{top} and $N_{\mathrm{def.}}$ is therefore:

$$S_{\mathrm{top}} \approx z_s \sigma v_{th} N_{\mathrm{def.}}(z=0) \tag{5.4}$$

Therefore, the surface recombination model is a crude way of approximating the spatial shape of the defect density. It amounts to model it as a discontinuous distribution with some defect density close to the surface, and another in the bulk of the material.

Statement 5.1.2. Definition of the bulk and surface recombination. We define the surface by using a thickness z_s, small compared to the total thickness of the sample L. The top surface recombination are the recombination happening in the slice of thickness z_s, they are described by the top surface recombination S_{top} linked to the density of defects by Equation (5.5):

$$S_{\text{top}} \approx z_s \sigma v_{th} N_{\text{def.}}(z=0) \tag{5.5}$$

The bulk is defined as the rest of the thickness of the device. Non radiative recombination are described by the bulk recombination coefficient (or its inverse the bulk recombination lifetime) by:

$$1/\tau_{\text{bulk}} = k_1 = \sigma^b v_{th} \langle N_{\text{def.}} \rangle_{\text{Bulk vol.}} \tag{5.6}$$

with possibly a different capture cross section σ^b than the top defect.

5.1.3 How is surface recombination distinguished from bulk recombination in the literature?

Distinguishing the location of non-radiative recombination has long been of interest to improve photovoltaic devices efficiencies. Therefore, in the literature, many techniques were used to distinguish bulk recombination, characterized by a bulk lifetime τ_{bulk}, from the (top) surface recombination characterized by a surface recombination velocity (SRV) S_{top}. The techniques employed to make this distinction all rely on the following principle: one has to somehow change the surface to volume ratio of recombination, see Figure 5.2.

A series of methods rely on the fabrication and comparison of multiple devices of different thicknesses but with similar surface state, see Figure 5.2(a). These multi-sample approaches are well suited when it comes to analysis of wafers —with very controllable thicknesses and very reproducible fabrication procedures. These techniques have been used on

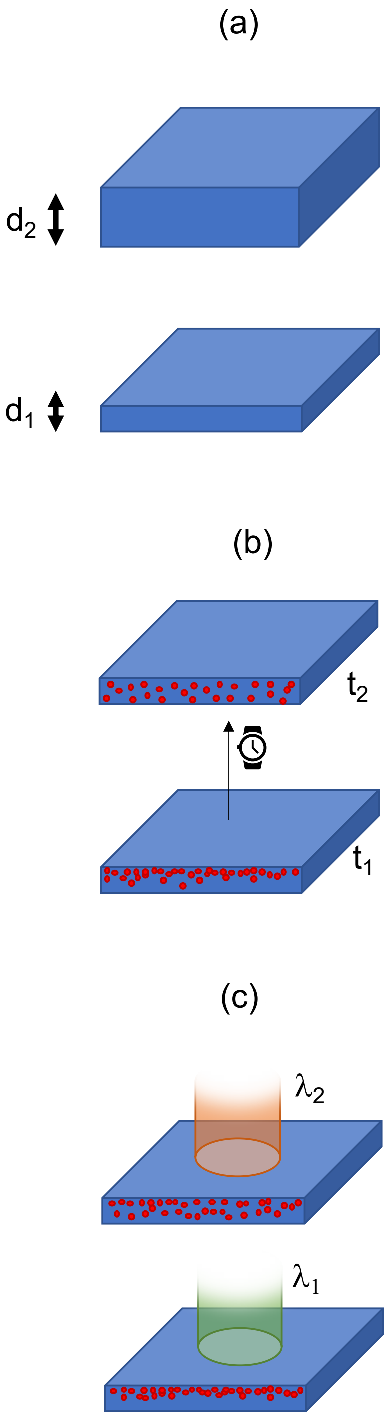

Figure 5.2: *Ways of playing with the surface to volume ratio of the carrier density. (a) Different thicnesses (b) With diffusion and time (c) With different wavelength of excitation.*

Silicon wafers [McKelvey 1982], III-Vs [Ahrenkiel 1992], CdTe [Zhao *et al.* 2014, Taheri *et al.* 2021], but have also been used recently to rule out "bulk" recombination inside the electron transport layers of recent perovskite-based PV cell architectures [Warby *et al.* 2022]. These methods are not suited for analyzing a specific device but rather give results on a series of samples. It is therefore impossible to obtain any image of local surface to bulk recombination ratio for a given sample with these techniques.

Since the 80's, researchers developed methods to change the surface to volume ratio of recombination without relying on the laborious fabrication of extra samples. In a seminal work [Eränen and Blomberg 1984], Eränen et al propose a method to determine S_{top} and τ_{bulk} from photo-conductivity decays (PCD) by comparing the dynamic just after the laser pulse and the dynamic after diffusion, an approach that inspired our work on TR-PL decays in [Vidon *et al.* 2021] and Chapter 4. Usually, PCD measurements do not allow good spatial resolution and are therefore unfit for imaging application. In a following work [Luke and Cheng 1987], Luke and Cheng studied the theoretical relaxation and diffusion of carriers inside a Silicon wafer after excitation via a laser pulse. They suggested four different methods (including a so called and self-explanatory "two-wafer method" as well as a "dual slope method" somewhat similar to Eränen's method) to distinguish S_{top} and τ_{bulk}. In these cases, time plays the role of change of surface to volume ratio through the diffusion process following a pulsed excitation, see Figure 5.2(b).

Following up [Buczkowski *et al.* 1991], Buczkowski et al. suggested to excite carriers inside Silicon wafers with multiple light excitation energies. They argued that doing so was a clever way of tuning the surface to volume ratio of recombination – at least at short time – as the absorption coefficient of semiconductors change by orders of magnitude with the excitation photon energy. They were followed by Gaubas et al and many more research papers [Gaubas and Vanhellemont 1996, Ling and Ajmera 1991, Gaubas *et al.* 2018, Palais and Arcari 2004, Kousik *et al.* 2003, Ling *et al.* 1998, Ogita 2013, Ahrenkiel and Dashdorj 2015].

A reasonable question at this stage could be: why were all these methods necessary? Part of the answer is contained in a recent publication [Heinz *et al.* 2017] by Heinz and coworkers: all the techniques presented in the literature are highly sensitive to experimental noise. This uncertainty prevents separation of τ_{bulk} and S_{top} from one single measurement. Even when multiple measurements are done, a high correlation links

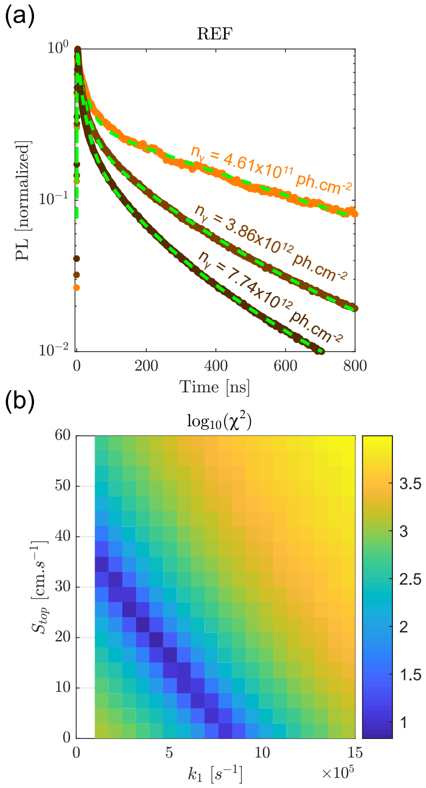

Figure 5.3: *(a) Fitting result on samples from Pavia University (b) Map of residual error of the fit around the obtained results. Blue corresponds to a small error, yellow to a high one.*

these quantities, as shown in the correlation plots of Heinz et al and in this work in Figure 4.6, reproduced in Figure 5.3 for convenience. Wang et al [Wang and Kampwerth 2014] also displayed this correlation curve. They proposed continuous wave measurements to obtain a second correlation curve, and used the intersection of both to theoretically distinguish between bulk and surface non radiative recombination. However, since, to the best of our knowledge, they did not show experimental application.

With continuous wave measurement, imaging of surface recombination was obtained for Si technology: for Si wafer in [Michl *et al.* 2012], or for Si cells in [Giesecke *et al.* 2010].

If most of the cited works above focused on Silicon-based devices, today's intensely studied class of material are perovskite. Distinguishing their bulk and surface properties is a key challenge today [Kumar *et al.* 2020]. Recently [Yang *et al.* 2015, Yang *et al.* 2017] Yang and coworkers, used different excitation wavelengths to study the transient reflectance response of perovskite mono crystals, such as $\mathrm{MAPbI_3}$ and were able to extract diffusion coefficients, top surface recombination velocity as well as bulk lifetime. To the best of our knowledge, these are the only published time resolved measurements done with multiple excitation wavelengths on perovskite materials.

Therefore, if many publications already introduced wavelength dependent measurements to distinguish bulk from surface recombination, only a few of them focused on perovskite based material and none of them (to the best of our knowledge) provided images of these recombination parameters for perovskite layers. This chapter describes our take at obtaining such images for perovskite based films from TR-FLIM measurements in order to characterize their spatial surface recombination and bulk inhomogeneity.

To do so, we will use two techniques: one new technique which is the extension of the short-time scaling introduced in section 4.2.2, and another adapted from a technique introduced by [Gaubas and Vanhellemont 1996]. We are interested in these two methods because they are the only one we found, to this date, to be applicable to time resolved photoluminescence *imaging*. Therefore, they are the only methods available to us able to image spatial inhomogeneity in the surface to bulk recombination ratio on perovskite samples. To describe both techniques before applying them, we will take a detour to theory: we will use the drift-diffusion model to link microscopic parameters to observables on the decay, see Figure 5.4.

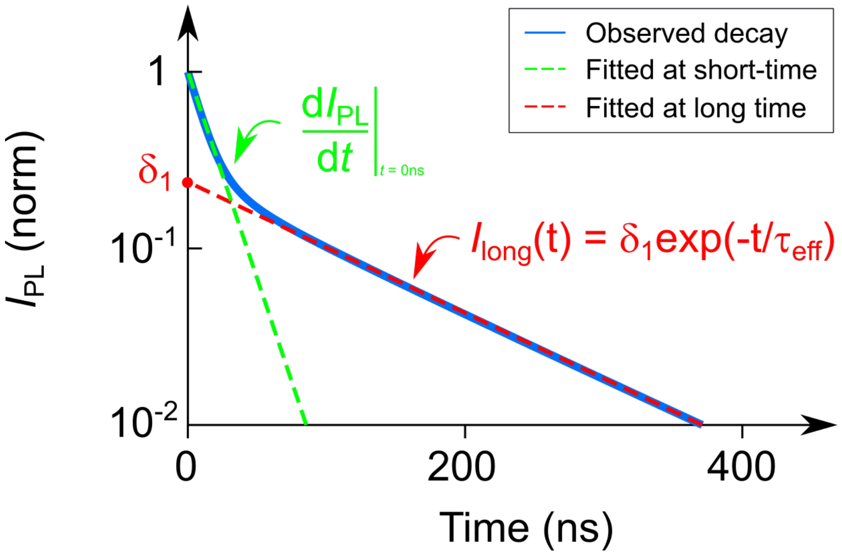

Figure 5.4: *Definition of the "observable" that can be fitted on some experimental decay (in blue).*

5.1.4 Solving analytically the simplified drift diffusion model

When one measures some experimental decay, one can fit or "observe" a few quantities as sketched in Figure 5.4. Looking at the short time, one can fit the initial derivative as sketched in green. Looking at the long time, a mono-exponential decay is found with decay time τ_{eff} and amplitude δ_1. In this subsection, we will consider a theoretical resolution of the drift diffusion equation to link the microscopic parameters, mostly S_{top} and τ_{bulk}, to the observables described in Figure 5.4. We will deduce from this resolution two methods to extract S_{top} and τ_{bulk} from the observables.

We can only solve it analytically in the case where recombination is *linear* in Δn. Therefore, **we will assume in this subsection that radiative recombination are negligible**, ie that we are at low enough fluence so that $k_2 n_\gamma \alpha \ll k_1$.

In the linear case, the solutions to the drift diffusion equation are actually sums of eigenfunctions (see the recent paper by [Weiss *et al.* 2019]) so that:

$$\Delta n(z,t) = e^{-k_1 t} \sum_{k=1}^{\infty} A_k U_k(z) e^{-t/\tau_k} \tag{5.7}$$

With:

A_k = coefficient determined by initial condition
$U_k(z)$ = eigenfunction determined by model parameters
τ_k = decay time of the corresponding eigenfunction

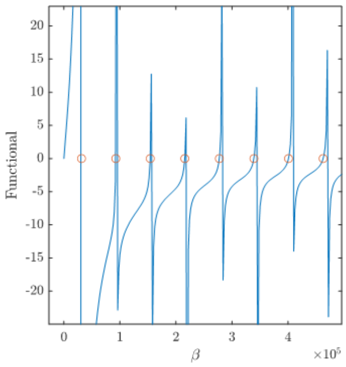

Figure 5.5: *Example of the determination of solutions to the self coherent Equation (5.8)*

The eigenfunctions are determined by solutions of a self-coherent equations **that only depends on model parameters**. One has to find the values β_k (cm^{-1}) such that:

$$\tan \beta_k L = -\frac{D\left(S_{\text{top}} + S_{\text{bot.}}\right)\beta_k}{S_{\text{top}} S_{\text{bot.}} - D^2 \beta_k^2} \tag{5.8}$$

These solutions has an infinite number of positive solutions that are labeled with $k = 1, 2, ...$, see a visual representation in Figure 5.5. The solutions of this equation are unfortunately difficult to find analytically in the general case. One can solve the equation numerically nonetheless. Once the solutions are found, the corresponding **eigenfunctions** exist:

$$U_k(z) = \cos(\beta_k z) + \frac{S_{\text{top}}}{D\beta_k}\sin(\beta_k z) \tag{5.9}$$

They form a basis of solutions of the drift-diffusion equation with the given boundary conditions. They all ensure that the derivative at $z = 0$ and $z = L$ respect the S_{top} and $S_{\text{bot.}}$ boundary conditions. For a given initial condition $\Delta n_0(z)$ we obtain the coefficients A_k via a projection onto the set:

$$A_k = \frac{\int_0^L \Delta n_0(z) U_k(z)\, dz}{\int_0^L (U_k(z))^2\, dz} \tag{5.10}$$

For instance, if we consider the usual initial condition of $\Delta n_0(z) = \alpha n_\gamma e^{-\alpha z}$ then we can obtain the following projections, see Figure 5.6.

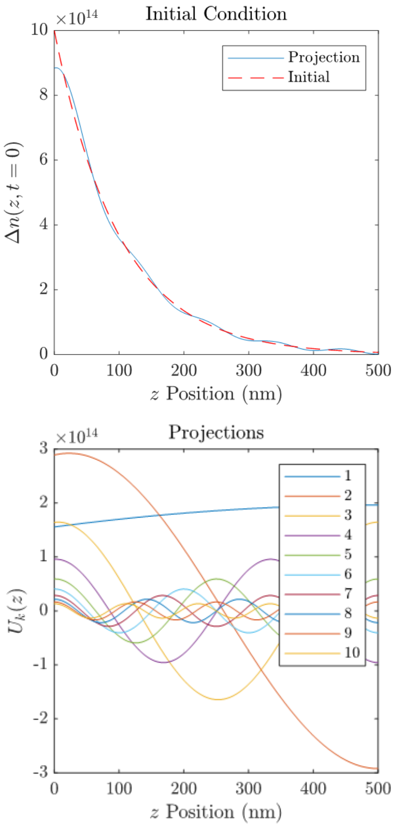

Figure 5.6: *Example of the determination of projections of the initial solution onto the basis of solutions of the dd-equation.*

Now each of these eigenfunctions will be associated with its own lifetime τ_k. The lifetime of solution k is defined as:

$$\tau_k = \frac{1}{D\beta_k^2} \tag{5.11}$$

Here is an example of the lifetimes τ_k found for the case where the parameters are $D = 1 \times 10^{-2}\,\mathrm{cm^2\,s^{-1}}$, $S_{\text{top}} = 100\,\mathrm{cm\,s^{-1}}$, $S_{\text{bot.}} = 0\,\mathrm{cm\,s^{-1}}$ and $L = 500\,\mathrm{nm}$:

k	β_k (cm^{-1})	$1/\beta_k$ (nm)	τ_k (ns)
1	13065,42	765,38	585,8
2	65846,2	151,87	23,06
3	127232,41	78,6	6,18
4	189549,71	52,76	2,78
5	252120,27	39,66	1,57
6	314794,39	31,77	1,01
7	377520,77	26,49	0,7
8	440277,15	22,71	0,52
9	503052,35	19,88	0,4
10	565840,1	17,67	0,31

We see that in this case only the 4 first eigenfunction have a lifetime of the order of 3 ns. This means for instance that it is enough to consider only the first 4 eigenfunctions to describe the spatial distribution of charge carriers at $t = 3ns$. We also note that they correspond to the high eigenlengths $1/\beta_k$ and we can find a justification for this: the process of diffusion will erase any "spikes" of short size (compared to the sample size) very quickly while larger variations will take longer to be flattened.

The exact number depends on the model parameters and mainly on the value of the diffusion coefficient, see the map in Figure 5.7. This number increases when D decreases as diffusion becomes slower and slower. When the top surface recombination velocity S_{top} increases, we see a slight decrease of the number of eigenfunctions required.

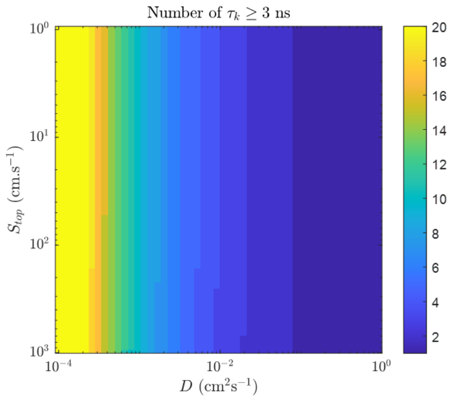

Figure 5.7: *Number of eigen values with lifetime above 3 ns (capped at 20).*

At long time only the first eigenvalue will matter and therefore:

Statement 5.1.3. At long time, the decay **of carriers** will become mono-exponential with a characteristic decay time τ_{eff} equal to :

$$\frac{1}{\tau_{\text{eff}}} = k_1 + D\beta_1^2 \tag{5.12}$$

with β_1 the smallest positive solution of Equation (5.8). In the case of negligible bottom surface recombination and where $S_{\text{top}}L \ll D$, one obtains:

$$\frac{1}{\tau_{\text{eff}}} = k_1 + \frac{S_{\text{top}}}{L} \tag{5.13}$$

To obtain the **decay time of the photo-luminescence**, a **factor 2** should be multiplied to this expression due to bi-molecular recombination.

We provide in Appendix G.1 two discussions: one is on the theoretical definition of the top to bulk recombination ratio, the other is on approximations for A_k, β_k in the case of neglected bottom surface recombination.

5.1.5 The A_1-δ_1 method

In this subsection, we adapt a method presented in the literature by Gaubas and coworkers in [Gaubas and Vanhellemont 1996]. This method allows, under certain hypothesis, to obtain estimates of the bulk recombination coefficient τ_{bulk} and of the top surface recombination velocity S_{top}. The main idea is the following: measuring the intercept A_1 or δ_1 of the long time scale decay gives access to $\beta_1 L$ which in turn can be used to estimate S_{top} and hence separate the contributions from the bulk and from the surface.

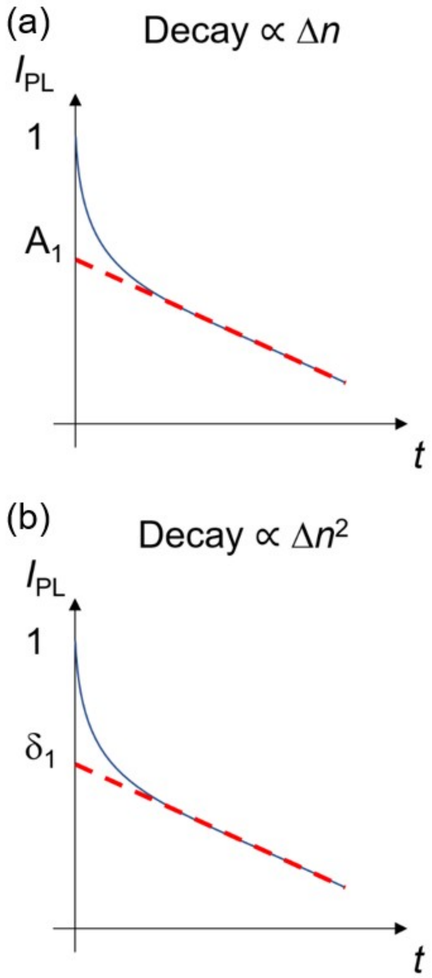

Figure 5.8: *(a) Scheme of the definition of A_1 for a **doped** semiconductor. (b) Scheme of the definition of δ_1 for the case of an **intrinsic** semiconductor.*

We adapt the method of Gaubas et al by changing two of its features:

- We adapt the method presented for doped semiconductors to intrinsic semiconductor. We name A_1-method the method presented originally by Gaubas and coworkers for doped semi conductors, while we name δ_1-method the method for intrinsic semiconductors. What changes is the link between the intercept and $\beta_1 L$, as discussed below.
- We apply the method to images acquired via TR-FLIM.

We will directly introduce the principle of the δ_1 method. The "A_1" method is called as such because the main idea is to measure the value A_1 as defined in Equation (5.10). How? by measuring the long-time behavior of the decay.

Indeed, following Equation (5.7), at long time we expect:

$$\Delta n(z,t) \underbrace{\approx}_{t\longrightarrow\infty} e^{-k_1 t} A_1 U_1(z) e^{-\eta_1 t} \tag{5.14}$$

Therefore, when applying decay-time fitting (as extensively discussed in Chapter 3), we usually obtain the value of decay time, but one can also obtain the value of "the intercept", see Figure 5.8. If we compute the PL intensity in the intrinsic case:

$$I_{\text{PL}}(t) = K \int_0^L \Delta n^2 dz \tag{5.15}$$

$$\underbrace{\approx}_{t\longrightarrow\infty} K A_1^2 \int_0^L U_1(z)^2 dz e^{-2(k_1+\eta_1)t} \tag{5.16}$$

At $t = 0$, we can use Equation (5.7) to compute that:

$$I_{\text{PL}}(t=0) = K n_\gamma^2 \alpha^2 \int_0^L e^{-2\alpha z} dz \tag{5.17}$$

Hence when we fit the long time normalized decay, as sketched in Figure 5.8, the function fitted at long time is:

$$\underbrace{\frac{I_{\text{PL}}(t)}{I_{\text{PL}}(t=0)}}_{\text{Norm. Decay curve}} \underbrace{\approx}_{t\longrightarrow\infty} \underbrace{\frac{A_1^2 \int_0^L U_1(z)^2 dz}{\frac{n_\gamma^2 \alpha}{2}\left(1-e^{-2\alpha L}\right)}}_{\equiv \delta_1} e^{-2(k_1+\eta_1)t} \tag{5.18}$$

It may seem to be a complicated formula but actually, given the definitions above we have that U_k only depends on β_k, S_{top}, and D.

$$\delta_1 = \frac{2}{n_\gamma^2 \alpha \left(1 - e^{-2\alpha L}\right)} \times \frac{\left(\displaystyle\int_0^L U_1(z) n_\gamma \alpha e^{-\alpha z} dz\right)^2}{\displaystyle\int_0^L U_1(z)^2 dz} \tag{5.19}$$

In the simplified case of negligible bottom surface recombination, we have the following property:

Statement 5.1.4. Computing S_{top} from the measurement of δ_1, and estimation of L, α and D. In the simplified case of negligible bottom surface recombination, δ_1 is a function of α and β_1 and L **only**. It equals:

$$\delta_1(\alpha, \beta_1, L) = \frac{4\alpha\beta_1}{(1 - e^{-2\alpha L})(\alpha^2 + \beta_1^2)^2} \frac{\left(\alpha + \beta_1 \tan(\beta_1 L) - \alpha e^{-\alpha L} \sec(\beta_1 L)\right)^2}{\tan \beta_1 L + \beta_1 L \sec^2(\beta_1 L)} \tag{5.20}$$

with sec the secant function equal to $1/\cos$. This function is strictly decreasing in the interval $\beta_1 \in [0,\ \frac{\pi}{2L}]$. Given an experimental value of δ_1, and estimates for L and α, one can therefore obtain a unique value of β_1 in the interval $[0,\ \frac{\pi}{2L}]$.
With this estimate for β_1, one may compute the top surface recombination velocity as:

$$S_{\text{top}} = \frac{D}{L} \beta_1 L \tan(\beta_1 L) \tag{5.21}$$

This statement sketches the following method to obtain an estimate of S_{top} from the observation of δ_1 and the knowledge or estimation of D, L and α. In theory, this estimation only needs the measurement of one decay.

Unfortunately, there is a limitation to this method: as always, temporal convolution with the camera's response function needs to be taken into account. Indeed, here δ_1 is measured on the *normalized* decay curve. But the convolution does not act as a multiplication constant applied to the whole decay, instead the maximal value of the decay is heavily reduced because it is the zone of the decay where temporal variations are higher:

$$I_{\text{PL}}^{\text{th}}(t = 0ns) > I_{\text{PL}}^{\text{conv}}(t = 0ns) \tag{5.22}$$

Therefore, the temporal convolution reduces the observed value of the maximal intensity of the decay. Therefore:

$$\underbrace{\delta_1^{\text{conv}}}_{\text{Measured.}} \geq \underbrace{\delta_1^{\text{th}}}_{\text{Theoretical.}} \tag{5.23}$$

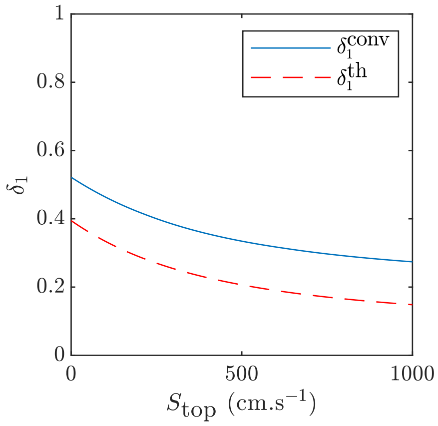

Figure 5.9: *Numerical computation of δ_1 convoluted and theoretical as a function of S_{top}. Parameters used were* $L = 500\,\mathrm{nm}$, $D = 1 \times 10^{-2}\,\mathrm{cm^2 s^{-1}}$, $\alpha = 1 \times 10^{5}\,\mathrm{cm^{-1}}$,$g_w = 3\,\mathrm{ns}$.

And this might lead to difficulties of interpretation. For this reason, we can also compute the convoluted δ_1^{conv} by estimating the error committed on the maximum value numerically. We do so in Figure 5.9. We see that the convoluted value is higher than the theoretical one for the same parameters. Once this artefact is taken into account, one can just use the blue curve to find S_{top} from the local value of δ_1^{conv}. We take it into account inFigure 5.9 by using the following principle: with a value for S_{top}, D, n_γ, L and α, one can compute the values of A_k and therefore estimate the beginning of the decay with Equation (5.7). Then, the convolution can be applied on this decay to estimate the ratio of $I_{\mathrm{PL}}^{\mathrm{th}}(t = 0ns)/I_{\mathrm{PL}}^{\mathrm{conv}}(t = 0ns)$. We then apply this ratio tvo δ_1^{th} to obtain δ_1^{conv}.

Statement 5.1.5. Proposed method: δ_1-method. To obtain the local top-surface recombination velocity S_{top} and τ:

1. Measure 1 TR-FLIM decay at the smallest possible fluence n_γ to correspond to the linear recombination regime necessary for this theory to apply.

2. Fit the local long decay time τ_{eff}, and the local intercept to the exponential decay at the origin δ_1.

3. With the assumed values of D, thickness L and absorption coefficient α, compute the *unique* chart δ_1^{conv} vs. S_{top}.

4. Use the chart to find for each pixels the value of S_{top} from the value of δ_1^{conv}.

5. Use the value of S_{top} and Equation (5.12) to find the local the bulk non radiative recombination rate $k_1 = 1/\tau$

Before applying the δ_1 method, we discuss in the next subsection the short time scaling method.

5.1.6 The wavelength study — a new method to obtain images of top surface recombination velocity and bulk lifetime

The idea of the study with a varied excitation wavelength λ_{ex} is not new in the literature, though this experiment is rarely done in the pulsed regime. This is especially the case as this requires either to have a white pulsed laser and a filter of tunable wavelength - both of which are expansive or to own multiple pulsed lasers of different wavelengths, another expansive solution. The experimental challenge resides in the dependence of the transmission of most optical components on wavelength in the optical path. This renders difficult the exact tuning of laser fluence for instance.

The main effect of changing the excitation wavelength is to change the initial carrier distribution, see Figure 5.10. By choosing the wavelength, we change the ability of the material to absorb the photons close to the surface. In the high absorption case (a), most of the photons are absorbed at the top. In the lowly absorbed case (b), the distribution of charges is more homogeneous. The concept of the lambda short-time-study is to use this change of initial condition to observe the change in the initial recombination rate. From this observation, one could be able to **separate the contribution of bulk non radiative recombination from surface non radiative recombination**. However one other physical process may mix in our interpretation: diffusion of carriers. We will indeed prove that the hallmarks of diffusion and surface recombination on the observed signal can be difficult to distinguish experimentally.

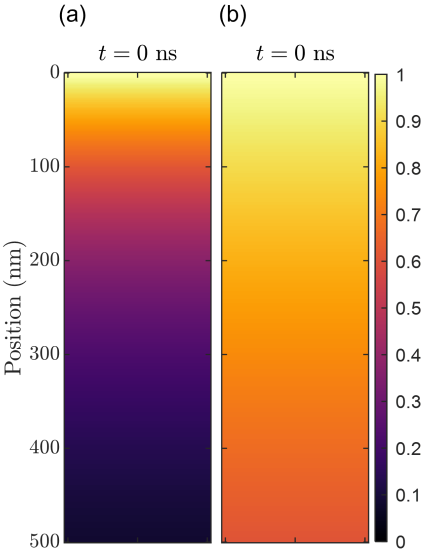

Figure 5.10: *Normalized spatial distribution of carrier at $t = 0$ following Beer Lambert's law: $\Delta n(t = 0, z) = n_\gamma \alpha e^{-\alpha z}$ with (a) $\alpha = 1 \times 10^5\,\text{cm}^{-1}$ (b) $\alpha = 1 \times 10^4\,\text{cm}^{-1}$*

Here, we present the theoretical framework used for the interpretation of the acquired signal as a function of the excitation wavelength. We showed the following equation in section 4.2.2:

$$\left.\frac{dI_{\text{PL}}^{\text{norm}}}{dt}\right|_{t=0} = -2k_1 - \left[\frac{4}{3}k_2 n_\gamma + 4S_{\text{top}}\right]\alpha(\lambda) - 2D\alpha(\lambda)^2 \tag{5.24}$$

Equation (5.24) was obtained with three main hypothesis: (i) that the material is intrinsic thus allowing to write that $I_{\text{PL}} \propto \Delta n^2$; (ii) that the photo-generated carrier density at time $t = 0$ is close to Beer Lambert's law ; (iii) that the absorption at the excitation wavelength is high, i.e. $e^{-\alpha(\lambda)L} \ll 1$.

Here we are going to use the tunable wavelength laser to perform experiments as a function of the excitation wavelength λ, thus changing the initial photo-generation through the absorption coefficient $\alpha(\lambda)$. We cannot choose the absorption coefficient behavior as a function of the wavelength but we can measure it and use its variation to obtain various initial conditions.

To help us reduce the number of parameters, we can use the relationship between the decay time at long time τ_{eff} and S_{top}, D, k_1 given in Equation (5.12). This relationship allows us to reduce the number of parameters because we can measure τ_{eff} and thus express for instance k_1 as a function of τ_{eff}, D and S_{top}. This expression is not analytic.

Statement 5.1.6. Proposed method: short-time scaling. To obtain the local top-surface recombination velocity S_{top} and τ:

1. Measure N TR-FLIM decays at the same position with different excitation wavelength λ but similar fluence n_γ.
2. Measure the long decay time τ_{eff} for all curves, and check that it is similar for all curves.
3. Measure the short-time decay slope on the normalized decays
4. Estimate or measure the absorption coefficient $\alpha(\lambda)$ for the wavelengths used.
5. Fit the local scaling law equation Equation (5.24) combined with Equation (5.12) to obtain the maps of S_{top} and τ

In the next section of this chapter we show the application of the scaling law method on one example without imaging, as a proof of concept. We find results that are compatible with the long decay times (by design) but also with the δ_1 observable.

5.2 Experimental validation of the scaling law technique without imaging: 2d-3d perovskite

In this subsection, we present experimental application of the wavelength study to samples using a surface passivation strategy. This section will prove how our measurements are able to determine that for all the devices under study, **the main source of non-radiative recombination is the top surface.** However, the passivation showed only a slight effect on the decays. The results prove to be compatible with the δ_1-method as well as the observation of the long decays.

5.2.1 Samples and methods

We analyzed three samples from the collaboration with Pavia university, see Figure 5.11: a reference sample of perovskite on glass. A sample with a bulk modification : addition of ionic liquids (IL) in the perovskite mixture that were shown to improve fill factors. And a last sample with IL and an additional surface treatment: the A-cation "2d"-passivation layer discussed in chapter 3.4.

We performed TR-FLIM measurements on these samples. We used the tunable wavelength pulsed laser as well as a 532nm pulsed laser. For each of the sample two different excitation sources were used: (i) a laser at constant number of photons per pulse, but with a varying wavelength, and (ii) a 532 nm laser with varying fluence. We thus performed on the same samples both a *wavelength* study and a *power* study. Unfortunately, the laser with changing wavelength is not powerful enough to perform imaging, and therefore the curves with varying wavelengths are not spatially resolved. Imaging with this technique is tackled in Chapter 5.3. Here we give a proof of concept of the technique on decays (and not images).

Samples were placed in chamber with a slight over pressure of nitrogen obtained with an incoming flux of N_2 at room temperature. The excitation laser had a repetition rate of 153 kHz. Its intensity was varied so that all excitation wavelengths have the same fluence, ie number of photons per centimeter square per pulse around $n_\gamma = 1 \times 10^{10}\,\mathrm{ph cm^{-2}}$. The objective lens used was an Olympus x10. A bandpass filter centered around $\lambda = 780\,\mathrm{nm}$ was used to only obtain the emission of the perovskite. The camera acquisitions were repeated 3 times and averaged.

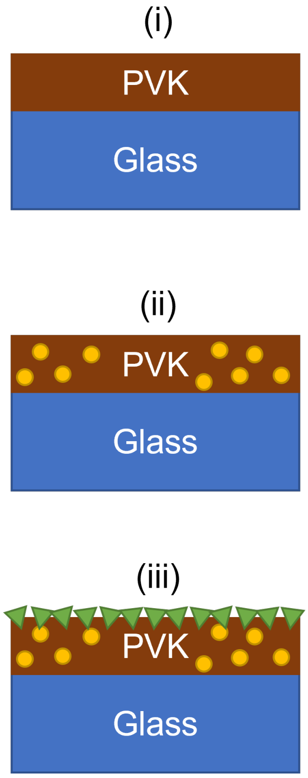

Figure 5.11: *Scheme of the samples used. (i) Reference perovskite layer (ii) Perovskite layer with ionic liquids (IL) responsible for better fill-factor (iii) Perovskite layer with ionic liquids (IL) and additional 2d layer perovskite as surface treatment.*

5.2.2 Decays and observable

The decays obtained for the three samples are shown in Figure 5.12. The decays were obtained after average over a circular region of interest of radius 15 pixels corresponding to a radius of 17.5 µm, see Figure 5.13.

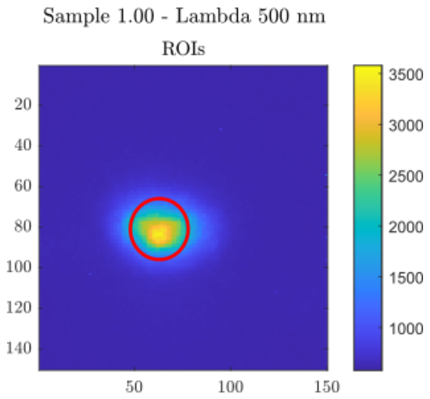

Figure 5.13: *Region of interest. Spatial axis are in pixels (not binned). Color axis is in counts.*

We see that the three sample have the same qualitative

(a) REF PVK (Top)

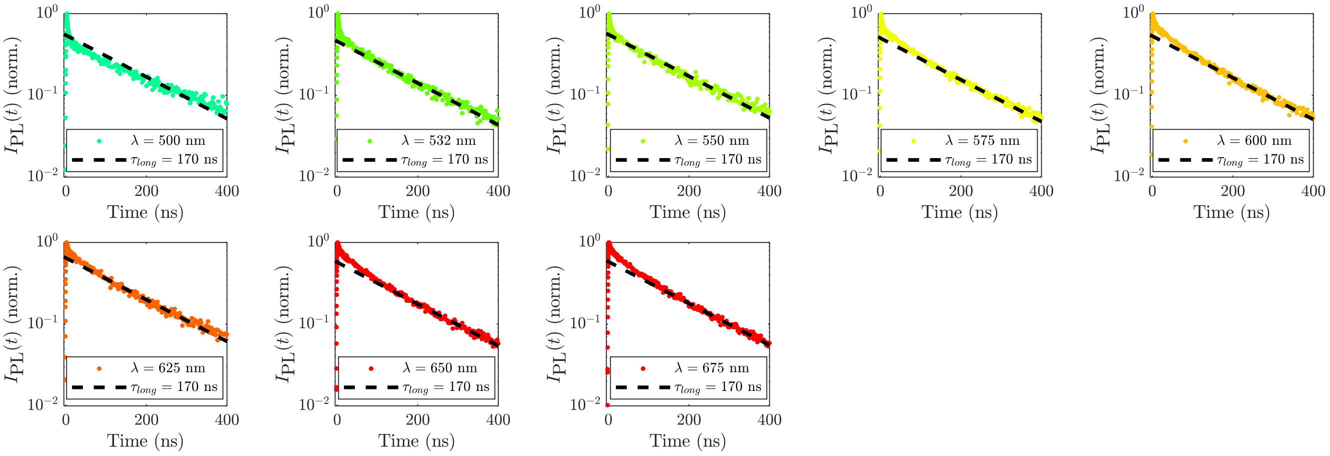

(b) IL (Top)

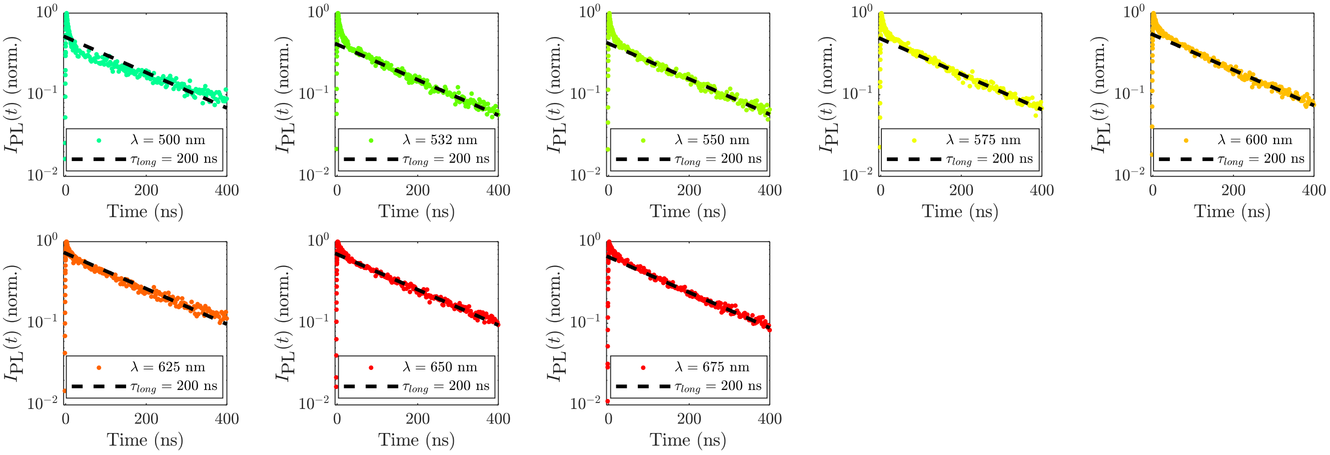

(c) IL + Passivation (Top)

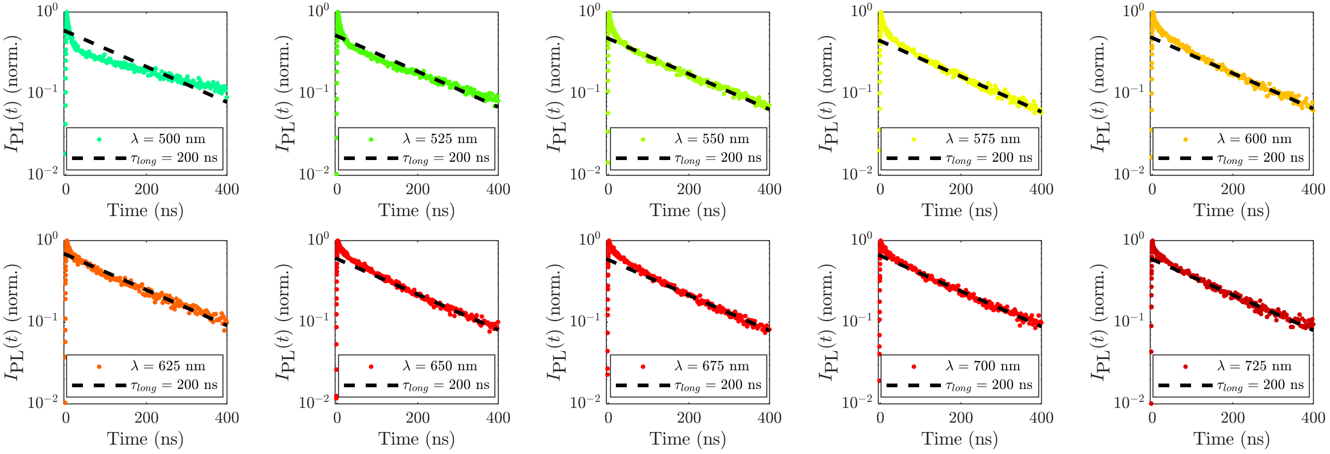

Figure 5.12: *Decays at different excitation wavelengths for the three samples, normalized to their maximal value.*

behavior : at short time, shorter wavelengths lead to faster decays. The measurement of the derivative at short time will showcase this phenomenon.

We observe that the reference sample (i) has an effective decay time around $\tau_{\text{long.}} = 170\,\text{ns}$. We also observe that the long decay time of all the curves for sample (ii) and (iii) seem to be around $\tau_{\text{long.}} = 200\,\text{ns}$. There are however a few exceptions. For instance, the 500nm curve for sample (iii) IL+Passivation clearly shows a dissimilar behavior. The reasons for this are not well understood by us at present. This could be linked with the 2d passivation layer, as this layer is semiconducting with a band gap around $\lambda = 520\,\text{nm}$.

From these measurements, the initial derivative of the decays may be computed. To do so, we use the fitting method with an bi-exponential decay convoluted with the temporal gate of the camera. To estimate the uncertainty and obtain a robust value, we use the *bootstrap* method to re-sample our experimental points and obtain a result that is more robust to noise, see an example in Figure 5.14. We choose the interval $[-2\,\text{ns}; 15\,\text{ns}]$.

We apply our technique and obtain the derivative shown in Figure 5.15. **First**, we can see that as the excitation wavelength increases, the initial derivative is reduced, irrespective of the sample. To understand this effect, one has to imaging that with the increasing wavelength we also have an increase of penetration depth at $t = 0$, namely $1/\alpha(\lambda)$. This effect leads to a *slower* decay and this could be explained by two phenomena: (i) the reduction of the impact of diffusion as the initial distribution is more and more homogeneous; (ii) the reduction of the number of carriers close to the surface traps that could mean that the surface of the samples are more defective than the bulk. The rest of this section will show how one can distinguish one effect from the other.

Second, we see that the samples have distinct short time behavior from one another. Mainly, the reference sample has the faster initial decays over the whole excitation wavelength range. However, we also observe that the dependence on wavelength is quite similar between the three samples. If the shape qualitatively looks as the one of a linear behavior, we could argue that the three samples share the same *slope* but have distinct *intercepts*. We also observe that sample (ii) IL and sample (iii) IL+Passivation are close one to the other - even if for most wavelengths, sample (iii) as the slowest decay.

To go further in the analysis and use our Equation (5.24). To become quantitative, we need to represent the derivative as a function of $\alpha(\lambda)$. To do so, we need to determine the absorption coefficient as a function of wavelength.

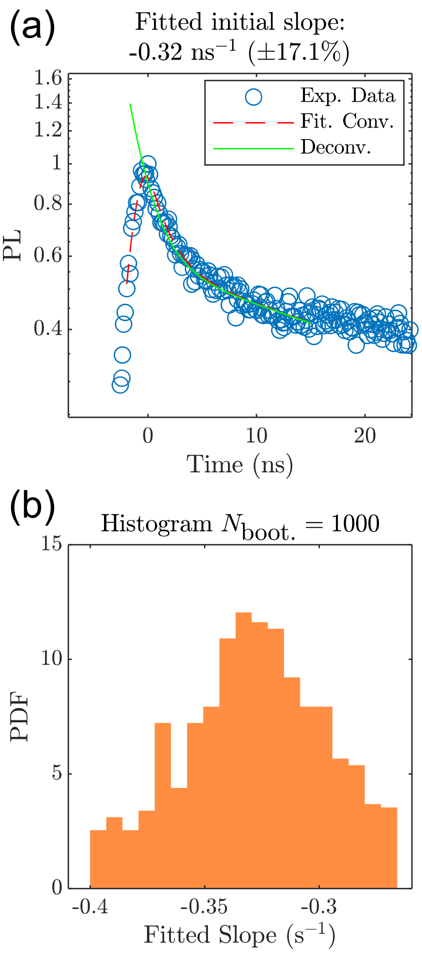

Figure 5.14: *Determination of the short-time slope via fitting of a bi exponential convoluted decay. Example on the 500nm curve for the reference sample. (a) Decay and fitted exponential between -2 ns and 15 ns. (b) Application of the bootstrap algorithm and distribution of fitted initial slopes with* $N_{\text{boot.}} = 1000$.

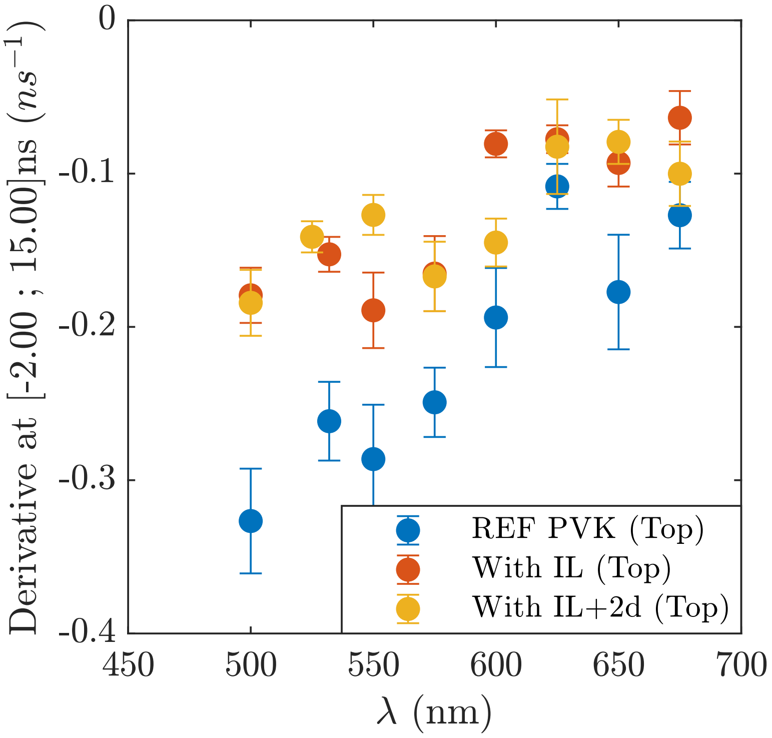

Figure 5.15: *Initial derivative as a function of excitation wavelength. Error bars from bootsrap procedure,* $N_{boot.} = 50$. *Mono-exponential convoluted fit between* $[-2\,\text{ns}; 15\,\text{ns}]$.

5.2.3 The scaling law and its quantitative estimation of S_{top} and D

Following the method presented in Statement 5.1.6, we estimate the absorption coefficient of the material under study via Absorptance measurement with a FTIR setup. More details are given in the corresponding subsection. This gives us the precious function $\alpha(\lambda)$. We note no clear difference in terms of absorptance from the 3 different samples and therefore use the same function to turn λ into α.

Short-time scaling method results

The analysis is presented for the "IL" sample in Figure 5.16. In (a) we plot the derivative as a function of α, with the corresponding model of Equation (5.24). We measured a long time effective decay time of $\tau_{\text{eff}} = \tau_{\text{long}} = 200\,\text{ns}$. We used, as prescribed in the method, the Equation (5.12) to eliminate one of the unknowns : the bulk lifetime $\tau = 1/k_1$. The results are the following: $D = 5 \times 10^{-3}\,\text{cm}^2\text{s}^{-1}$ ($\pm 58\%$), $S_{\text{top}} = 130\,\text{cms}^{-1}$ (high uncertainty) and τ is found to be much larger than τ_{eff},

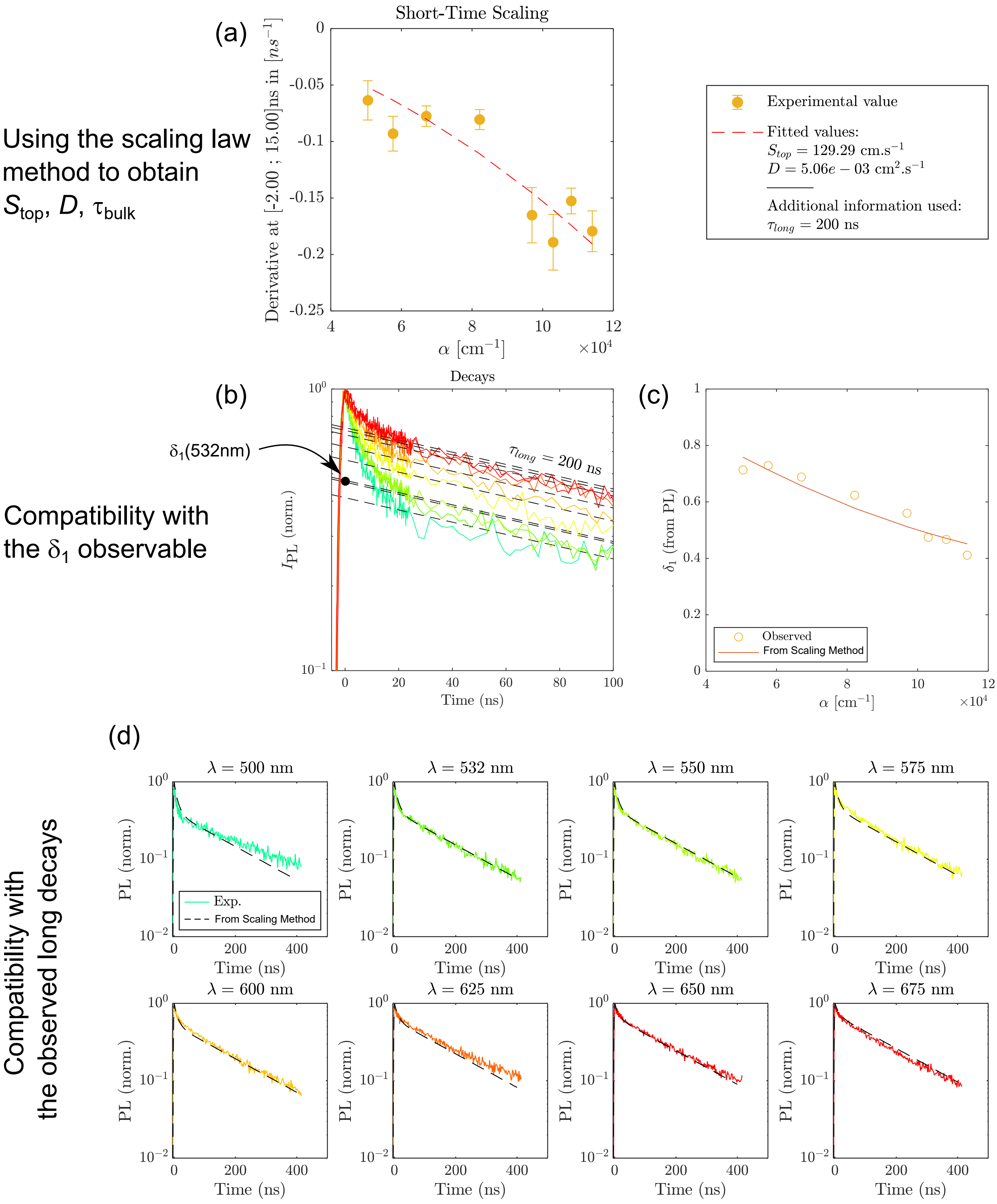

Figure 5.16: *Application of the scaling technique as a function of laser wavelength for the Ionic Liquid sample (ii). (a) Initial derivative and fitting with the scaling law method. (b) Observed decays and values of δ_1. (c) Values of δ_1 vs. the model obtained via the scaling method. (d) Application of the model obtained via the scaling model to the long time dynamics and comparison to the experimental data.*

virtually infinite. Therefore the fitting finds that defects are most probably surface defects and that the bulk plays a very negligible part in the non radiative recombination. We find a diffusion coefficient that is very compatible with what we found with the drift-diffusion technique for similar samples, see Table 4.4. It would correspond to a carrier mobility of $\mu = 0.2\,\mathrm{cm}^2\mathrm{s}^{-1}\mathrm{V}^{-1}$. The top surface recombination shows high uncertainty. This uncertainty is not satisfactory but we think it is over-evaluated because the compatibility with the other figures of merit is high.

Compatibility with the δ_1-method

In Figure 5.16 (b) we display the decays normalized, along with the dotted fitted mono exponential behavior at long time. We particularly highlight where on the graph the value of $\delta_1(532nm)$ can be read. By fitting the long decays with a mono-exponential decay of the form $\delta_1 e^{-t/\tau_{\mathrm{eff}}}$, we find δ_1 for all wavelengths. In Figure 5.16 (c) we plot as circles the values found as a function of α. We then plot the theoretical curve for δ_1^{conv}, as predicted by Equation (5.20) and the convolution, with the parameters that the short-time scaling found. To be clear: we do not apply the δ_1 method here: we only compare the observed δ_1 values to the theoretical curve. The results are fully compatible with the observed values of δ_1 for all wavelengths. Therefore the short-time scaling is confirmed by the δ_1-method.

Compatibility with the longer decays

In Figure 5.16 (d) we plot each individual decay in color with the corresponding modeled curve in dotted black. To obtain the model curve, we use the drift diffusion simulation with input parameters equal to the ones obtained by the short-time scaling (a). We find very compatible behavior both in terms of long time and intermediate time behavior. The only exception is the $\lambda = 500nm$ curve, for a reason we cannot explain.

Conclusion

Thus, the short-time lambda scaling law technique is confirmed to yield parameters both compatible with the long decays and with the δ_1-method.

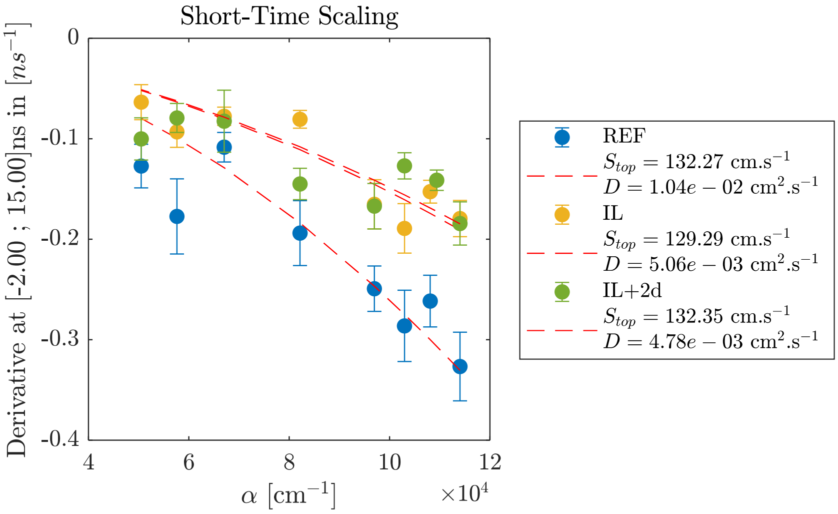

Figure 5.17: *Application of the scaling technique as a function of laser wavelength for the three samples.*

5.2.4 Discussion on the results of the scaling law

Sample to sample comparison

To go further, we compare in Figure 5.17 the scaling-lax technique for the three studied samples, where a similar data treatment as for sample (ii) is done.

We observe that the two samples with ionic liquids behave similarly with no clear difference between them, the fitted parameters are similar. The main difference is with the reference sample (i). The scaling law technique attributes the difference to an increased diffusion coefficient: a factor 2 with the other samples is found. The top surface recombination remains at the same level. We note that this would not explain the slight difference in τ_{eff} that we observed.

Therefore, the ionic liquid addition is correlated with a reduction of the diffusion coefficient. No clear passivation is observed with the addition of the 2d layer, but this is compatible with the study on the impact of these 2d-layers, presented in chapter 3.4 and [Cacovich *et al.* 2022a]. The samples under scrutiny revealed to show little bulk recombination.

Uncertainties and applicability of the method

We want to stress out that even though the found results seem straightforward to obtain, this is not so. There are a lot of choices necessary to obtain the results: the method to obtain the derivative, the intervals to fit the long decay times, the estimation/measurement of the absorption coefficient measurement. These choices result in the careful application of the technique and should be studied more extensively in the future.

However, our scaling law technique does find correct diffusion and recombination coefficients compatible with the behavior of the samples over a wide range of excitation wavelengths. This experimental confirmation comforts our idea for the application to imaging, described in the next section.

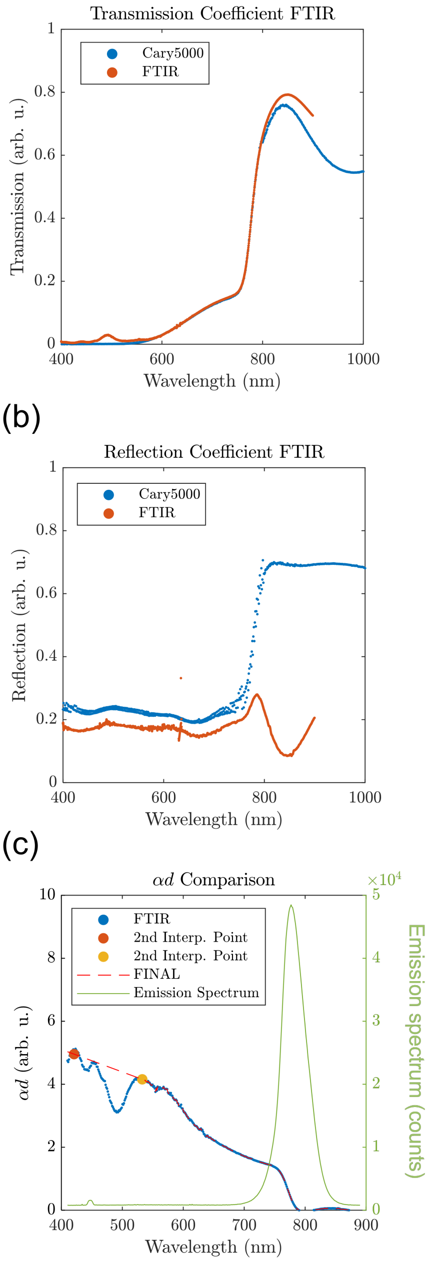

Figure 5.18: *(a) Transmission measured by two setups (b) Reflection measured by two setups (c) Absorption coefficient obtained.*

Determination of the absorption coefficient as a function of wavelength

The determination of the absorption coefficient is a topic of its own and we will merely here describe our measurement to do so. We measured the samples with two apparatus and obtained the spectra for transmission and reflection given in Figure 5.18 (a) and (b). The two apparatus are a UV-VIS Cary 5000 and a FTIR (Fourier Transform InfraRed spectroscopy) Nicolet iS50R . We see a bump in the transmission around 490nm for the spectrum measured with the FTIR setup which we think is not due to the sample. To determine α we use a simple model described by Pankove, see [Look and Leach 2016]. It relates the absorption coefficient times thickness to R and T via:

$$\alpha d = -\log_{10}\left(\frac{(1-R)^2}{2TR^2}\left(\sqrt{1+\frac{4T^2R^2}{(1-R)^4}}-1\right)\right) \tag{5.25}$$

We show the resulting curve in Figure 5.18 (c), along with the emission spectrum (in green). We chose to ignore the bump in the αd curve by performing a linear interpolation between the two points shown in Figure 5.18 (c). We measured the thickness to be approximately 380 nm. We saw no differences between the three samples studied in terms of their reflection and transmission spectra.

Many techniques exist to determine the absorption coefficient α and more complicated model could be implemented, such as a “top/bottom” measurement of R and T, or ellipsometry measurement. None of these techniques give access directly to α.

5.3 Imaging the top surface recombination velocity and bulk lifetime: the impact of X-Ray radiation on the recombination of perovskite half cells

In this last section we present results obtained with the two techniques of Statement 5.1.6 and Statement 5.1.5: the scaling law technique of our making, and our adaptation of the δ_1 technique of Gaubas et al. [Gaubas and Vanhellemont 1996]. We perform both techniques on images, which was a real challenge to obtain, we describe briefly why in the first subsection. Then we show the results of both techniques applied to the study of X-Ray damaged half cells. We show how the techniques are able to display that X-Rays create a zone of bulk defects rather than surface defects. Finally we discuss why these techniques yield compatible results.

5.3.1 Experimental challenges

Obtaining images with the lambda scaling law technique was very difficult. The main reason was because the tunable-wavelength laser we have in the lab, the Fianium (see the description in Chapter 2) **is not intense enough**. Yet, for imaging application, one needs to both dilute spatially the laser pulse and to get rid of the laser speckle. To get rid of speckle we usually use a rotating diffuser that randomizes the speckle and leads to the observation of flat images. But this operation reduces by order of magnitudes (one at least) the laser intensity. This rendered impossible "flat" images to be obtained with the Fianium.

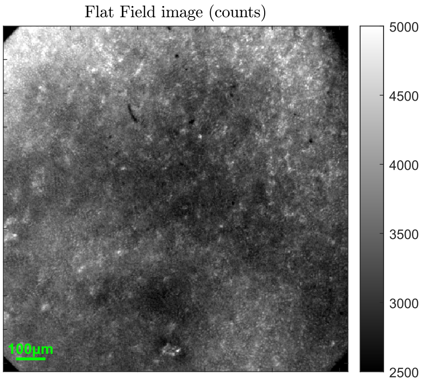

Figure 5.19: *Flat field image acquired on a piece of paper in the cryostat, under the square fiber illumination.*

Until Marie Legrand, a PhD Student, found another solution to get rid of the Speckle. Her elegant solution was to use an optical fiber with a square-shaped core leading to the random superposition of modes inside the fiber. This large square-shaped core was then imaged directly onto the sample's surface (without the rotating diffuser). The obtained images were rather flat, see Figure 5.19. Of course, this is not perfectly flat but with a ratio of standard deviation over mean of 0.15, we considered that we could use this technique to image samples.

5.3.2 Distinguishing the effect of X-Rays on perovskite degradation

We tackled the question of the impact of X-Ray exposure onto perovskite half-cells. This set of samples was already used in this thesis in section 3.2.2 for the comparison between the quasi Fermi level splitting $\Delta\mu$ and the decay time τ. The half cells have been exposed to X-Rays and we see a damage zone appear. The question we want to tackle is: **are the defects created in the bulk or on the surface of the perovskite layers?**

To answer this question, we propose to apply the two methods previously discussed: the scaling law method, explained in Statement 5.1.6 and the δ_1 method in Statement 5.1.5. Therefore we (i) measured TR-FLIM decays for a range of wavelengths above the bandgap; (ii) estimated the absorption coefficient for the selected excitation wavelengths. (iii) computed for each TR-FLIM dataset the map of initial derivatives; and (iv) computed the local top (S_{top}) and bulk (τ) recombination parameters from Equation (5.24).

5.3.3 Results

In Figure 5.20, we apply steps (i) to (iii) of this method to IPVF half-cell constituted of a stack of glass / fluorine doped tin oxide (FTO) / compact titanium oxide (c-TiO2) / triple-cation double halide perovskite with a nominal stoichiometry of $\text{Cs}_{0.05}(\text{MA}_{0.14}, \text{FA}_{0.86})_{0.95}\text{Pb}(\text{I}_{0.84}, \text{Br}_{0.16})_3$. The samples were irradiated via a X-Ray beam for 8h, leaving a defective zone as detailed in [Cacovich *et al.* 2022a]. We use two excitation wavelengths at 650nm and 532nm. In Figure 5.20(b) we show the average decays over the whole image for these two wavelengths, while Figure 5.20(c) and (e) show the images for $t = 0$, 2, 4, 6, 8 and 10 ns after the laser pulse for the 650nm and 532nm respectively. These acquisitions are made using the combination of 25 repetitions of the same experiment to increase the SNR. Despite this, we see that the noise on the images is high. This is due to the experimental challenge of having intense enough widefield illumination with our wavelength tunable pulsed laser as explained in the previous subsection. In Figure 5.20 (d) and (f) we show maps of initial derivative for the two datasets. They were computed as the linear fit of the local decay in the range 0 to 150ns. We observe, as expected that the image for the 532nm acquisition is darker than the image at 650nm – which is compatible with Equation (5.24).

Then, we present in Figure 5.21 (a) and (b) the resulting

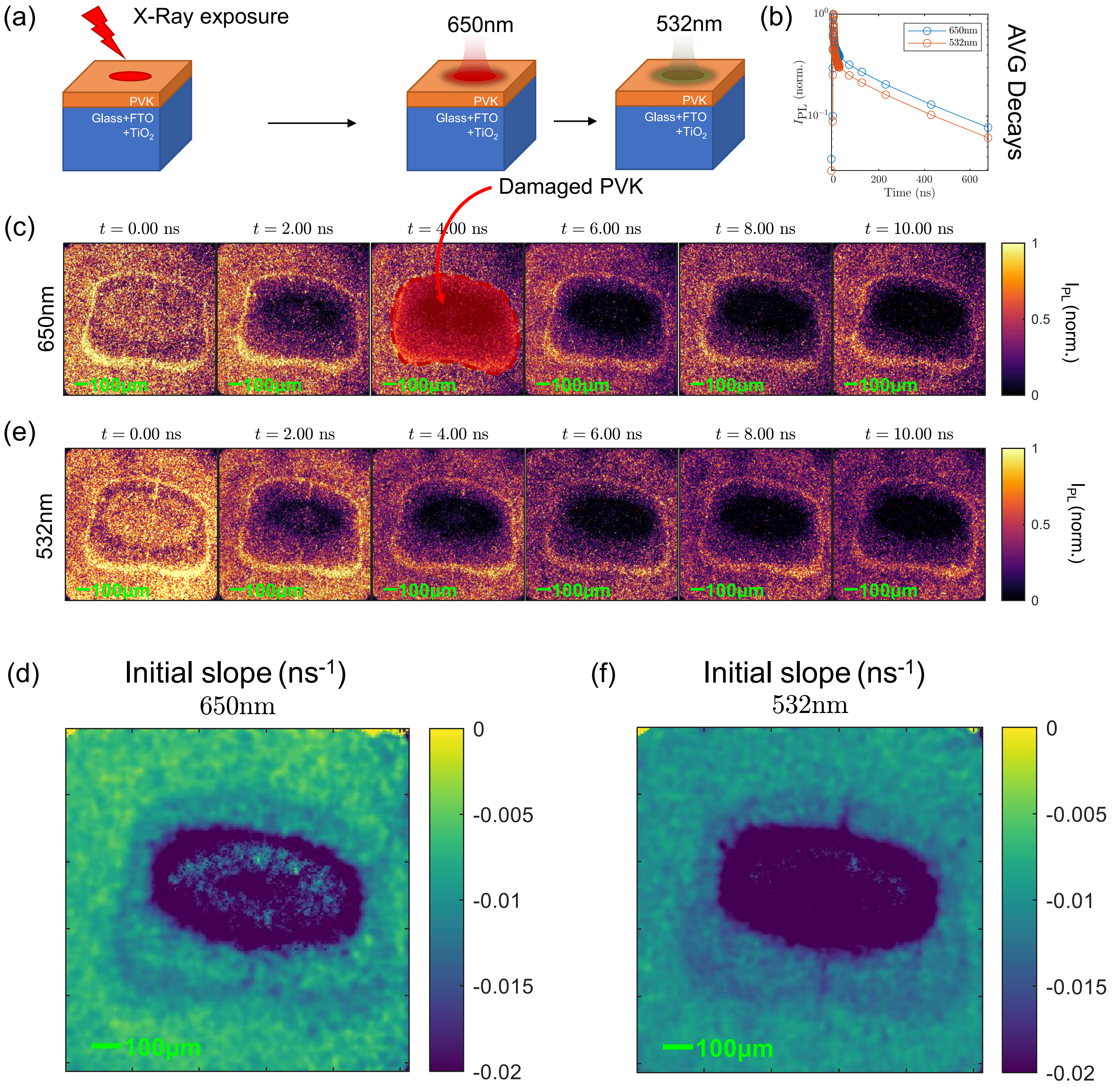

Figure 5.20: *λ-TR-FLIM Experiments lead on* $Cs_{0.05}(MA_{0.14}, FA_{0.86})_{0.95}Pb(I_{0.84}, Br_{0.16})_3$ *half cells. (a) illustration of the XPS experiment and the wavelength analysis at 650 nm and 532 nm (b) average decays over the whole image for these two wavelengths. (d) and (f) maps of initial derivative for the two datasets. (c) and (e) show the images for* $t = 0$, *2, 4, 6, 8 and 10 ns after the laser pulse for the 650nm and 532nm respectively*

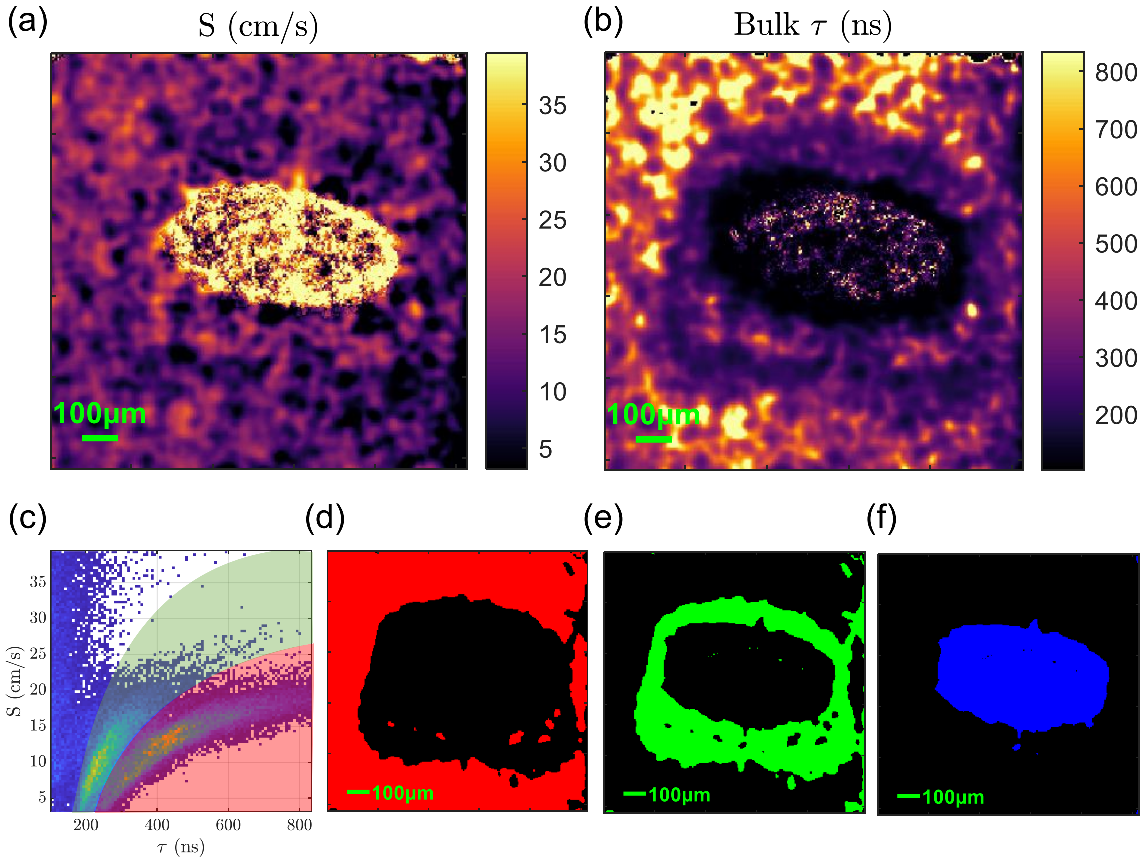

Figure 5.21: *Determination of the local surface and bulk recombination parameters with the scaling law method. (a) and (b) resulting maps of top surface recombination velocity Stop and bulk non radiative constant .(c) pixel correlation of the two obtained maps. Three distinct regions that qualitatively correspond to three regions of bulk lifetime : (d) "high bulk lifetime region" in red, (e) intermediate region in green which corresponds to the outskirts of the spot, and (f) the other pixels in blue.*

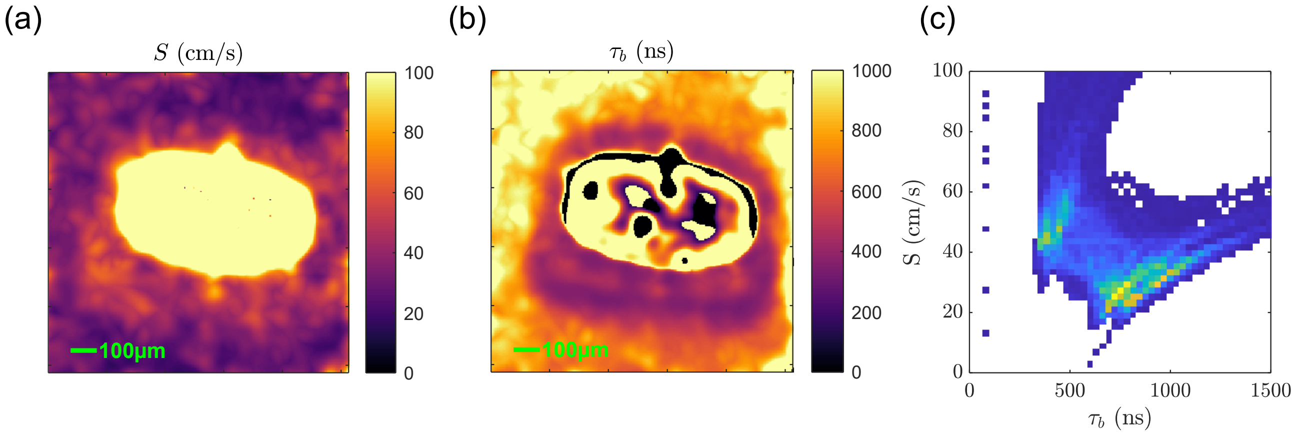

Figure 5.22: *Determination of mappings of S (a) and τ_{bulk} (b) with the δ_1 method. In (c) is presented the pixel pixel correlation.*

maps of top surface recombination velocity S_{top} and bulk non radiative constant τ. The maps are obtained using the two maps of Figure 5.20 (d) and (f) along with a simplified version of Equation (5.24) valid in the slow diffusion and low fluence case:

$$\left.\frac{dI_{\text{PL}}^{\text{norm}}}{dt}\right|_{t=0} \approx -2k_1 - 4S_{\text{top}}\alpha(\lambda) \tag{5.26}$$

We use the following values for $\alpha(\lambda)$: $1 \times 10^5\,\text{cm}^{-1}$ and $0.5 \times 10^5\,\text{cm}^{-1}$ for 532nm and 650nm respectively. For each pixel of the map, we have two values of the initial derivative and we determine the local value of slope and intercept of Equation (5.26) to obtain the maps of τ and S_{top}. We can observe on the map of S_{top} a rather homogeneous surface recombination velocity, except in the very center. On the map of τ, we see however that three regions appear: the pristine perovskite, the outskirts of the X-Ray spot and the spot itself. The bulk decay time is in this regard reduced each time. In Figure 5.21 (c) we plot the pixel correlation of the two obtained maps. We observe three distinct regions in this plot that qualitatively correspond to three regions of bulk lifetime τ. Following the shape of correlation, we define the "high bulk lifetime region" in red as the pixels corresponding to the values of S_{top} and τ in the red quadrant of Figure 5.21 (c). Their spatial position is displayed in red in Figure 5.21 (d). We see that all these pixels correspond to the pristine perovskite. Similarly, we define the intermediate region in green in Figure 5.21 (d) and show the corresponding positions of pixels in (e). This corresponds to the outskirts of the spot. In (f) we display the other pixels in blue.

5.3.4 Discussion

The results obtained via the scaling-law method allowed us to define regions in the correlation plot that correspond to regions on the image that have **physical meaning**: the exterior of the spot, its immediate outskirts, and the very center. The fact that this is the case does make us confident in the fact that the results in term of recombination parameters as well hold some physical meaning. This physical meaning is that: **X-Rays created defects mainly in the bulk of the perovskite**. This result is compatible with the fact that X-Rays are supposed to penetrate the sample homogeneously in the ≈500nm thickness with expected absorption coefficient lower than $1 \times 10^3\,\text{cm}^{-1}$ [He *et al.* 2022]. In XPS, only the first nanometers are probed but this does not come from the X-Ray distribution but rather from the fact that the electrons that have a chance of getting out of the layer are only those close to the top surface. Therefore, the fact that the defects are created in the bulk seems compatible with the underlying physical cause.

To compare the obtained results to the δ_1-method, we apply it on the same datacubes (we use the one acquired at 532nm). The method is described in Statement 5.1.5 and the results are shown in Figure 5.22. In (a) and (b) we plot the obtained maps for the top surface recombination velocity and the bulk lifetime. In (c) we plot the pixel-pixel correlation. First, let us state that we find similar orders of magnitude for the parameters, namely S_{top} in the order of $50\,\mathrm{cm s^{-1}}$ and τ in the order of 500 ns. Second, in terms of effects of the X-Ray we find a similar trend for the bulk lifetime: a drastic reduction in the outskirts region. Third, we see a slight difference in terms of top surface recombination: the δ_1-method predicts a slight increase in the outskirt region, while it is less visible for the scaling law method. Nevertheless, the increase is far more limited than the reduction of bulk lifetime. Finally, the correlations seem to be compatible with one another, we recognize the general shape. A word on the central zone of the spot for all the images: we deem that this region presents too low signal to be interpreted (see Figure 5.20(c))and choose to limit the discussion to the outskirts and outside regions.

Finally, we discuss the validity of our approximation to turn Equation (5.24) into Equation (5.26). The low fluence approximation is easily verified when computing the fluence dependent term around $n_\gamma = 1 \times 10^{10}\,\mathrm{ph cm^{-2}}$. The approximation that needs to be discussed is the fact that we neglected the term $-2\alpha^2 D$. For a highly absorbed wavelength, such as the green $\lambda = 532\,\mathrm{nm}$, $\alpha \approx 1 \times 10^5\,\mathrm{cm^{-1}}$. With $D \approx 5 \times 10^{-3}\,\mathrm{cm^2 s^{-1}}$, the diffusion term of Equation (5.24) equals $0.1\,\mathrm{ns^{-1}}$, a value almost one order of magnitude higher than what we find on the images of Figure 5.20 (d). This could mean that we overestimate the absorption coefficient for this wavelength. We think that our approximation can be interpreted as considering that the diffusion term is constant over the image, and looking only at the variations in terms of S_{top} and τ. Finally, the approximation on the scaling method seems to be confirmed by the similarity of the results with the δ_1-method.

5.4 Conclusion

In this chapter, we asked the following question: how to obtain maps of top surface recombination and bulk lifetime?

We first discussed the notion of surface and bulk by defining a thickness z_s. We then introduced two methods to obtain estimates of the surface and bulk recombination parameters from the observable of the decays. One method is an adaptation of a method introduced by [Gaubas and Vanhellemont 1996] to the case of intrinsic semiconductors: the δ_1-method. The other method is based on the scaling law we introduced for the time derivative of the decay around $t = 0ns$ as a function of laser wavelength: the scaling-law-method.

Then, we applied the scaling law method on a set of decays that were not spatially resolved. We performed experiments with triple cation perovskite from Pavia university and the tunable-wavelength-pulsed-laser at our disposal. By using both the short-time information as well as the long decay time, we were able to fit the short-time derivative as function of α for the three samples. It gave us values for the diffusion coefficient D, as well as top surface recombination S_{top}. The bulk lifetime was found to be much greater than the other recombination times. The values found were compatible with other characterization methods, notably the δ_1-method. The long decays simulated with the model parameters obtained from the short time scaling are very close to the observed long decays. All of this proved the interest of the technique and gave us confidence in the parameters found.

Finally, we were able to scale to the imaging application. After having found how to overcome the experimental challenge that we were facing with our small-intensity tunable-wavelength-laser, we applied the short-time scaling to the study of defects caused on the perovskite by X-Ray exposure. We obtained maps of top surface recombination velocity as well as bulk lifetime that indicated that most of the created defects are bulk defects and not surface defects. We imaged different zone of around the spot that correspond to different area in the correlation plot of S_{top} and τ_{bulk}. To confirm this finding, we also performed the δ_1-method that gave results mostly compatible both in terms of comparison top vs. bulk but also on the quantitative values found.

Therefore, we gave two possible techniques to image top and bulk recombination parameters. From a practical point of view, the δ_1-method is easier to perform as only one excitation wavelength is necessary in principle. The two methods gave compatible results both in the case of a surface-dominated or mixed surface-bulk recombination scenario.

Now, for the last step on this journey of imaging properties of perovskite thin-films, we go toward the mountains of "Devices" where we meet the challenge of: "What distinguishes the decays of full cells, from half-cells from thin films on glass?” and its corollary; ”Can we image extraction properties of perovskite cells with TR-FLIM?”

Chapter 6

Towards devices: are interfaces recombining or extracting carriers?

In the previous chapter, we mainly focused our theory and modeling efforts towards the interpretation of images of decays on thin films on glass to observe spatial inhomogeneities. In this chapter we will tackle the question of images of decays of half cells and full cells, as an opening towards further perspectives. The structure of this chapter is summarized in Figure 6.1.

The questions one can have when observing half cells or full cells are the following: are the charges well transferred to the charge transport layer (CTL). Are the bands correctly aligned? Is the interface between one CTL and the absorber defective? And of course we would like to find answers to these questions *locally*, ie on images. It is still unclear today in the literature (and to us) to which of these questions TR-PL (or TR-FLIM) is able to answer. For instance some authors interpret fast decays on "quenching" layers as a (positive) sign of extraction [Wang *et al.* 2019b, Zhang *et al.* 2017, Roldán-Carmona *et al.* 2015] or others as a (negative) hallmark of recombination. The interpretation of the decays requires care because the impact of extracting layers may have different effects on the observed decay times: charges could be transferred to the charge extraction layers, capacitive charging of the electrodes could occur, ion motion could change the electronic landscape. Theses effects are linked to the presence or build up of **electric fields in the devices** and to **charge extraction to the CTL**, see Figure 6.1.

For conventional semiconductors, the question of the interpretation of decays on half cells and full devices has already been studied: for CIGS for instance by Maiberg and cowork-

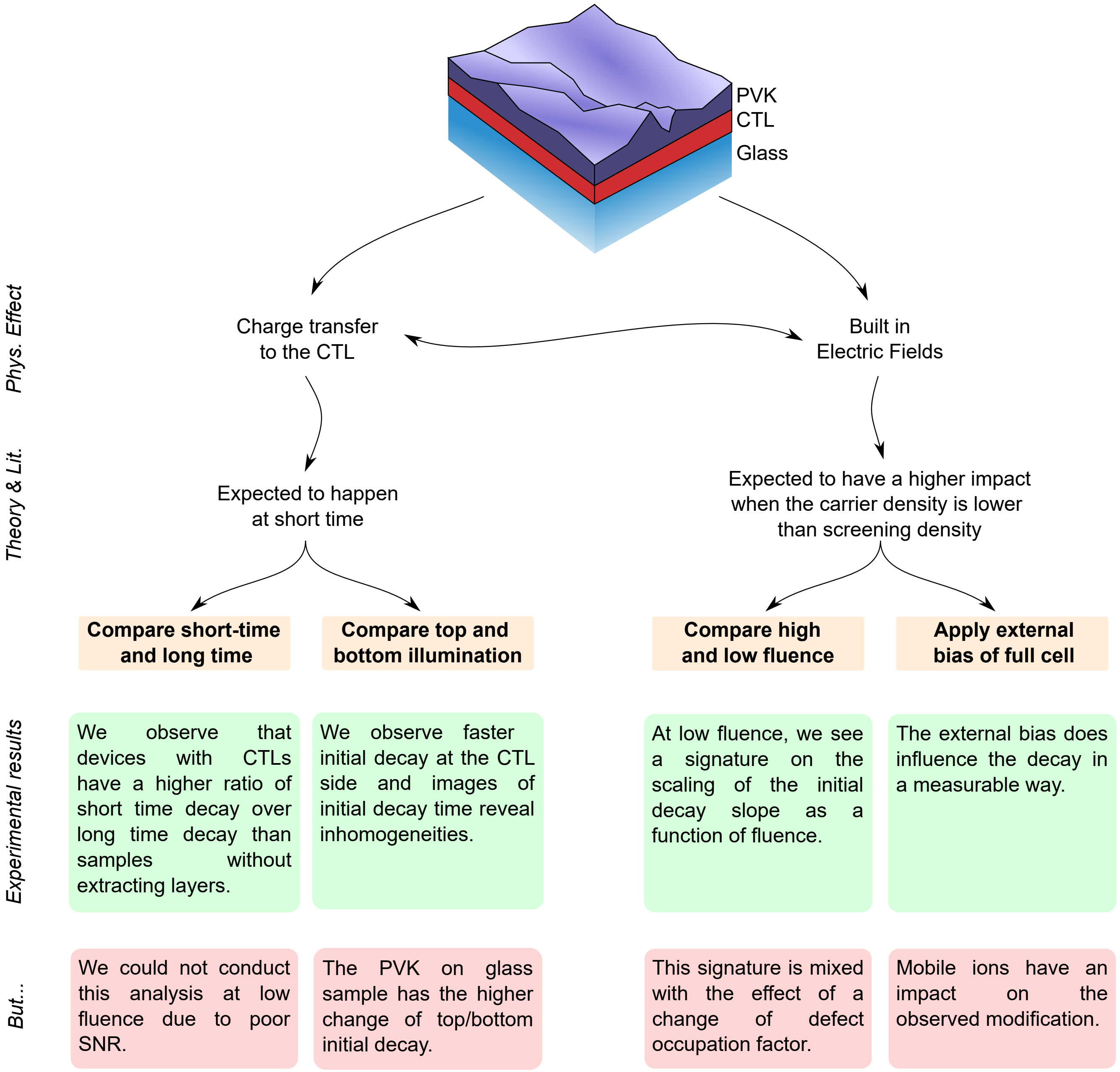

We observe that devices with CTLs have a higher ratio of short time decay over long time decay than samples without extracting layers.

We observe faster initial decay at the CTL side and images of initial decay time reveal inhomogeneities.

At low fluence, we see a signature on the scaling of the initial decay slope as a function of fluence.

The external bias does influence the decay in a measurable way.

We could not conduct this analysis at low fluence due to poor SNR.

The PVK on glass sample has the higher change of top/bottom initial decay.

This signature is mixed with the effect of a change of defect occupation factor.

Mobile ions have an impact on the observed modification.

Figure 6.1: *Main results discussed in this chapter. The physical effects and theoretical as well as literature orient our research with four main focus points. We obtained partial results for each of the four.*

ers [Maiberg *et al.* 2015], for Si in [Dashdorj *et al.* 2004] and for GaAs hetero-structures in [Rosenwaks *et al.* 1994]. These articles already point to the following observations:

1. If built-in electric fields are present in the structure, the photo-generated charges will follow its direction and might, by doing so, screen it almost completely if enough charges are present. Contrary to the usual thin films, half cell and full cells may then present electron and hole spatial separation **that would result in a fast decay at low fluence**.

2. During the decay, there exist different phases: such as carrier separation, "discharging" of the effective capacity formed, non radiative recombination.

3. The observed decay times are therefore not easily interpreted

However, only a few papers question the interpretation of TR-PL decays when perovskite absorbers are in contact with one or two charge transport layers. The main group that tackled this question for $MAPbI_3$ cells, is Thomas Kirchartz and Uwe Rau's group in Jülich via papers such as : [Krückemeier *et al.* 2021a, Krückemeier *et al.* 2021b]. The case of perovskite solar cells is specific for four main reasons: (i) they show very slow carrier diffusion ($D \approx 1 \times 10^{-2}\,\mathrm{cm}^2/\mathrm{s}$); (ii) they show very low doping ($N_{\mathrm{dop.}} \leq 1 \times 10^{14}\,\mathrm{cm}^{-3}$); (iii) Ions of the structure appear to be even slower moving charges; (iv) The extraction layers could have rather low conductivity leading to electric field variations within these layers.

Rau's group focuses on $MAPbI_3$ devices while our focus is on triple cation mixed perovskite, which proved to have even slower diffusion coefficient than $MAPbI_3$ —hindering the comparison between the two system. Nevertheless, their simulations with TCAD software show that the decay at low fluence for full cell devices should be very fast. Our own simulation on half devices also show this behavior.

Therefore these two main facts are accepted in the literature:

1. At **high fluence**, ie high photo-generated carrier density, there is not much difference between the decays of full-cells, half-cells, and thin films on glass.

2. At **low fluence**, effects due to the extracting layers and built in electric fields can modify the shapes of decays.

In the rest of this chapter we designate by "extraction properties" the band alignment and transport properties that shape the band diagram of the half cell or the full cell. For instance the doping of the charge transport layers, or the difference in electron affinity between the perovskite and the charge transport layers $\Delta\chi$. **Those "extraction parameters" in the end control the built in electric field and the amount of charges transferred**.

Therefore, in this last and prospective chapter, we will tackle the following open question: **can we observe signatures of charge transfer and/or of electric fields from the TR-FLIM acquisitions on half-cells and full devices?**

This question is still under study at the moment when we write this manuscript. This chapter aims at showing the state of our interpretation when tackling the specific case of imaging **local** extraction and recombination properties of triple cation double halide perovskite films, half cells and full cells. We will use the indicators that were introduced in the previous chapters: namely the $I_{\mathrm{PL}}(t = 0ns)$ scaling with fluence, the $dI_{\mathrm{PL}}/dt(t = 0ns)$ scaling with fluence and the long decay time observation $\tau_{\mathrm{eff.}}$. We show in this chapter two different ways to answer the question of interpretation: one is via the observation of a layer by layer sample set at different fluences and in a top and bottom approach, the other is via the application of bias on full cells.

In a first part, we present the experimental results we obtained on a series of samples built in a "layer by layer" approach: a thin film on glass, two half cells and a full cell. We tackle the three first columns of Figure 6.1. We mainly show that the behavior of faster decay at low fluence is observed for half devices and full cells, but *also* for the films deposited on glass (column 3 of Figure 6.1). This challenges the possibility to attribute this behavior to the presence of CTL and to link it to their extraction properties. We propose a model that explains the behavior of thin films on glass based on a change of defect occupation factor. Moreover, we discuss the possibility and interest to analyse the images both at short and long time while comparing the top and bottom acquisitions (first two columns of Figure 6.1).

In a second part, we describe a proof of concept for an experiment with applied bias (column 4 of Figure 6.1). We evidence that the decays evolve at the scale of the second/minute after the bias is applied. We discuss observables linked to this “slow” variation and attribute this change to ion motion. To prevent or lower ion motion, the possibility of applying pulsed bias is discussed. We introduce the application of pulsed biases by referring to a publication of our group. For this work, we modeled the effects of pulsed biases on the local decay of a lateral channel structure.

These two approaches all show how complicated the problem of interpreting a decay measured on a half of full device is, and each brings its new difficulty to tackle. But all of these difficulties can be seen as *opportunities*. The influence of the defect occupation factor at low fluence could lead to precise imaging of their dynamics. The presumed movement of ions on the decays could be imaged and quantified.

Thus, we do not have a definite answer to give to the title-question of this chapter, but we do have hope that the approaches we present give convincing perspective for future work and hopefully future scientific results.

Table of contents

6.1 Step by step building of the cell and using a fluence study to impact the screening of the electric field

In this section, we study experimental results obtained on a set of four samples, see Figure 6.2: (a) a thin film on glass, (b) a half cell with the electron transport layer (ETL), (c) a half cell with the hole transport layer (HTL) and (d) a full cell. In this dataset, we explore the following idea: we use the fluence to compare two situations:

1. At low fluence: we expect that electric fields and/or extraction could occur and would be of higher impact when the photo-generated charge density is low.

2. At high fluence: we expect that electric fields are screened.

Therefore, we use the fluence as a stressor that should change the impact of extraction and of the electric field. Another "stressor" is to **image sample from both sides**. Indeed, especially for half cells, we expect that **extraction properties would only take place when the sample is illuminated from the CTL side**.

To monitor the impact of the stressor we will use the indicators previously introduced: namely the $I_{\mathrm{PL}}(t=0ns)$ scaling with fluence (chapter 4.3), the $dI_{\mathrm{PL}}/dt(t=0ns)$ scaling with fluence (section 4.2.2) and the long decay time observation $\tau_{\mathrm{eff.}}$ (Chapter 3).

In the first subsection, we discuss the comparison in terms of the impact of fluence. We argue that if extraction properties have an effect, it is mixed with the impact of defect dynamics due to background doping/defects. **In the second subsection**, we compare the top and bottom acquisitions and argue that there is nonetheless a part of the initial signal that could be attributed to extraction. We propose a qualitative interpretation method based on a plot of τ_{long} vs. τ_0 (inverse of the initial slope). We apply this interpretation locally on images as a proof of concept.

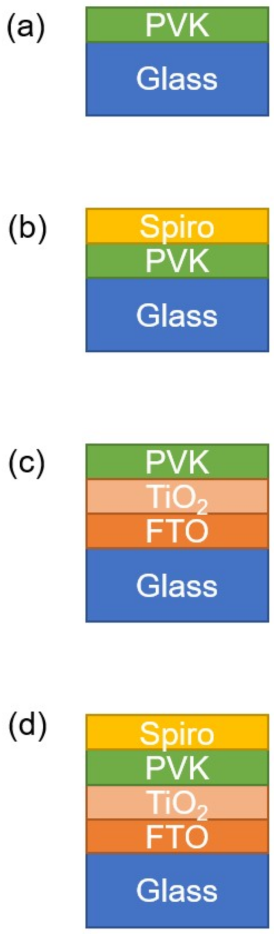

Figure 6.2: *Description of the samples used in Figure 6.3*

6.1.1 Comparing high and low fluence: interplay between defect dynamics and extraction properties

We will show that: (i) contrary to what we expect in the high fluence case (section 4.2.2), the initial slope increases

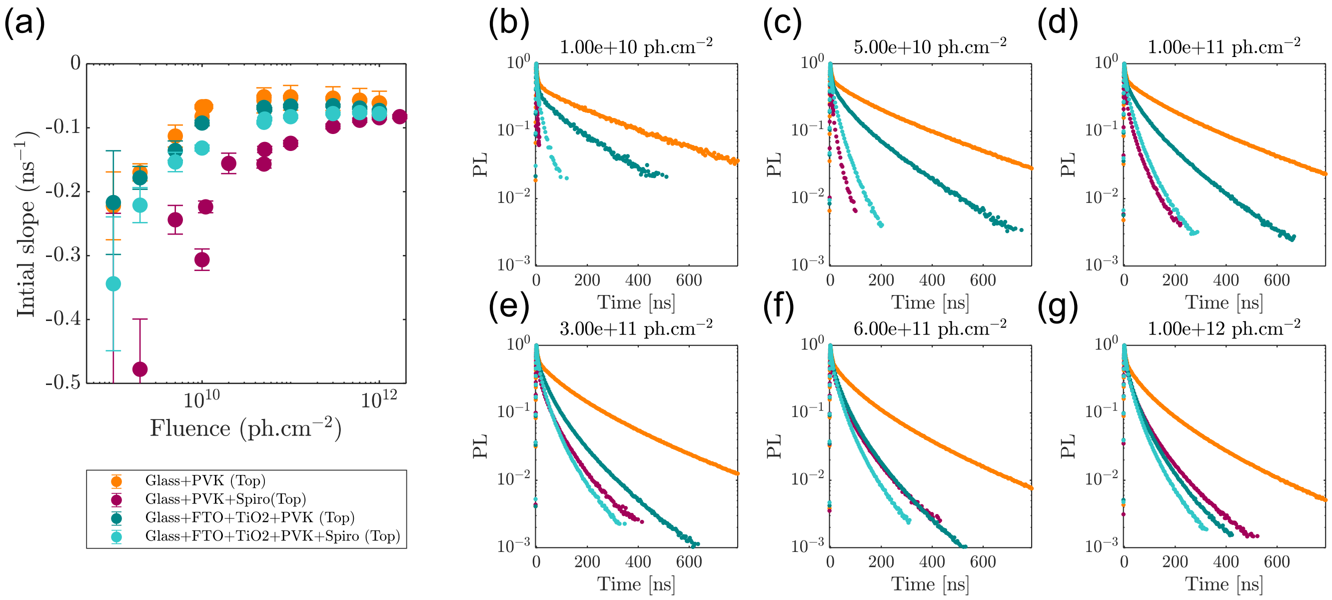

Figure 6.3: *Normalized decays at different fluences and initial derivative of different stack of layers.*

as a function of fluence in the low fluence regime; (ii) this increase is also observed for the layer **without** transport layers —which implies that this behavior is not a signature of the presence of charge transport layers; (iii) Nevertheless, the initial decay is always faster on the CTL side.

We study the IPVF perovskite baseline stack (see Appendix C.1) by decomposing it: we observe a sample with only triple cation perovskite on glass (a) in Figure 6.2, we observe the two half cells: one with Spiro-OMeTAD ($C_{81}H_{68}N_4O_8$) as HTL deposited on top of the perovskite (b), and one with perovskite on top of TiO_2 (ETL) deposited on FTO (c). Finally, we also study the full stack (d) with only gold missing to form the complete and working solar cell.

We perform TR-FLIM experiments in Nitrogen atmosphere and vary the laser fluence between $2 \times 10^{9}\,\mathrm{ph/cm^2}$ and $1 \times 10^{12}\,\mathrm{ph/cm^2}$, while the laser repetition rate is set to 40 kHz. Both a super-resolved short-time and a longer time acquisition are performed and merged. For the low fluences ($n_\gamma \leq 1 \times 10^{10}\,\mathrm{ph/cm^2}$), as the signal quickly became too weak to be measured, only the short time acquisition is performed.

We present the spatially averaged PL decays in Figure 6.3 (b-g) while we show the initial derivative as a function of the fluence for the four sample in (a). For the decays, we cropped the data to where the signal is higher than 30 counts above the noise level (which equals approximately 880 counts for the lowest fluence). We do that cropping because we deem that the signal is not high enough to be considered under this threshold.

We first comment qualitatively the decays. The lowest fluence (b) presents four very different decays. The decay of perovskite on glass (orange) is above all the others. The half cell with HTL (red) present a very fast initial decay (barely visible —but all the curves are normalized so it can be deduced visually). The half cell with TiO_2 (dark blue) presents a rather similar behavior, even though the initial decay is shorter. Then the TiO_2 curve shows a slower decay. Finally, the full cell (light blue) has the more noticeable initial drop.

At a higher fluence, in (c), the decays of the half devices and full device seem to "slow down" because the fast initial decay is less pronounced. The difference between the full cell and the Spiro half cell is also reduced. When the fluence is increased even more, (e-f-g) the three samples with extraction layers see their decays becoming very similar. The perovskite layer on glass still having a slower decay than the half cells and full cell.

To evidence the slowing of the initial decay with increasing laser fluence, we plot in (a) the initial normalized derivative of the decay as a function of laser fluence. We compute it as the fit of a convoluted mono exponential decay between -3 and 10ns. We observe that the Spiro half cell has a steeply increasing behavior. It is less pronounced for the full cell and even less for the TiO_2 half cell. For the bare layer on glass we also find a faster decay for the lowest fluences even if it is less pronounced. However, we see the start of the "regular" decreasing behavior for high fluences as evidenced in Chapter 4.

Therefore with this experimental dataset we evidence the following:

Result 6.1.1. For all samples, including thin film on glass, at low fluence a fast decay is observed. This fast decay is amplified in the case of the full cell, or each of the half cells. At higher fluences, all the devices with extraction layers seem to behave similarly. They all present a decay that is however faster than that of the reference layer on glass.

We will discuss the obtained results and give a model to explain the increase of the initial slope as a function of fluence for thin films on glass.

Neat film as a function of fluence: an explanation via defects

We observed fast decays at low fluence for the thin film on glass, see Figure 6.3. In the literature, this behavior has been attributed to asymmetric defect recombination (see papers by Maiberg). We will show that our measurements are compatible with this interpretation.

The first noticeable correlation is that **we see the increase of the slope only when the scaling of $I_{\mathbf{PL}}(t = 0ns)$ is of order 1, ie when we can consider that the perovskite layer is "doped"**, see Figure 6.7 (c-i) and (d-i) with the dashed line as a guide for the eye. In this range of fluences the perovskite is artificially doped, presumably by its charged vacancy. If we assume (arbitrarily) that the perovskite is p-doped with a density of electron vacancy $N_{\text{vac,e}}$ we have:

$$I_{\text{PL}} \propto \Delta n_e \times (N_{\text{vac,e}} + \Delta n_h) \tag{6.1}$$

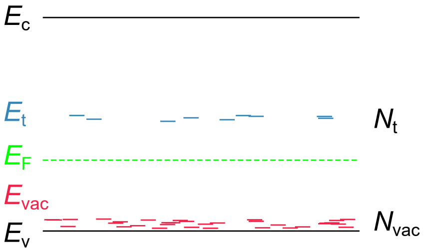

Figure 6.4: *Assumed band diagram in the dark with vacancies that dope the perovskite and recombining traps in the middle of the bandgap.*

How would that change the defect action? By changing the filling of the defects. Indeed, let us consider some defect level at energy E_t, see Figure 6.4, that is not necessarily shallow, but that is above the Fermi level in the dark of the perovskite. In the dark, its electron occupation factor will be:

$$f_e^{\text{dark}} = \frac{1}{1 + \exp\left(\frac{E_t - E_F}{kT}\right)} \approx \exp\left(-\frac{E_t - E_F}{kT}\right) \tag{6.2}$$

If the defect energy is more than a few kT above the Fermi level, in the dark, it is mostly unoccupied by electrons. Now when we photo-generate carriers below the background (assumed p-)doping density $N_{\text{vac,e}}$, only the electron density will vary substantially from the dark situation and equal the photo-generated carrier density $n_\gamma \alpha$. In this case (see Statement 2.1.4), in a few 100ps, the defect will be populated by electrons and the electron occupation factor of the defect will converge approximately to the value (neglecting thermal escape):

$$f_e \approx \frac{1}{1 + C\frac{N_{\text{vac,e}} + n_\gamma \alpha}{n_\gamma \alpha}} \tag{6.3}$$

with the initial electron density equal to $n_e^0 = n_\gamma \alpha$, $n_h^0 = n_\gamma \alpha + N_{\text{vac,e}}$ and $C = \sigma_h v_h / \sigma_e v_e$ the ratio of products of capture cross section and thermal velocities. The occupation factor will then follow the electron and hole densities such that at all times $df_e/dt = 0$. Equation (6.3) is where the "asymmetry" becomes apparent at $t = 0ns$: one carrier density is set by the Fermi level, the other by the photo-generation. The **defect quickly reaches an equilibrium that depends on**

the incoming fluence. This equation does state that at very low fluence, the defects are full of holes (that are the majority carriers here) and as the fluence increases they are more and more populated by electrons. The more they are populated by electrons, the less they are recombining.

$$\frac{d\Delta n_e}{dt} = -\sigma_e v_e N_t(1-f_e)\Delta n_e = -\frac{\sigma_e v_e N_t}{1+\frac{1}{C}\frac{\Delta n_e}{\Delta n_h+N_{\text{vac,e}}}}\Delta n_e \tag{6.4}$$

And in the general case for holes:

$$\frac{d\Delta n_h}{dt} = -\sigma_h v_h N_t(f_e)\Delta n_h = -\frac{\sigma_h v_h N_t}{1+C\frac{\Delta n_h+N_{\text{vac,e}}}{\Delta n_e}}\Delta n_h \tag{6.5}$$

From there, we use the definition of I_{PL} given in Equation (6.1), differentiate it and compute the value at $t = 0ns$. Then we normalize it by:

$$I_{\text{PL}}(t = 0ns) \propto n_\gamma\alpha \times (N_{\text{vac,e}} + n_\gamma\alpha) \tag{6.6}$$

which yields for all fluences (even above doping) to:

$$\left.\frac{1}{I_{\text{PL}}}\frac{dI_{\text{PL}}}{dt}\right|_{t=0ns} = -\frac{\sigma_e v_e N_t}{1+\frac{\sigma_e v_e}{\sigma_h v_h}\frac{n_\gamma\alpha}{N_{\text{vac,e}}+n_\gamma\alpha}} - \left(\frac{n_\gamma\alpha}{N_{\text{vac,e}}+n_\gamma\alpha}\right)\frac{\sigma_h v_h N_t}{1+\frac{\sigma_h v_h}{\sigma_e v_e}\frac{N_{\text{vac,e}}+n_\gamma\alpha}{n_\gamma\alpha}} \tag{6.7}$$

We use this model to fit the experimental data of the top thin film on glass, see Figure 6.5. The model fitted is the following:

$$y = -a\frac{1}{1+\frac{a}{b}\frac{n_\gamma}{N+n_\gamma}} - b\frac{n_\gamma}{N+n_\gamma}\frac{1}{1+\frac{b}{a}\frac{N+n_\gamma}{n_\gamma}} \tag{6.8}$$

The fitting algorithm yields $a = (0.32 \pm 0.03)$ ns^{-1}, $b = (0.031 \pm 0.002)$ns^{-1} and $N = (2.1 \pm 0.3) \times 10^{10}$ cm^{-2}.

First let us state that the fit is very closely representing the data, even if the underlying model is simple which gives us confidence in its output result. Then, the value of $N = N_{\text{vac,e}}/\alpha$ should equal approximately the estimated doping density (over α) and we find a very compatible value: the doping density is estimated around 1×10^{15} cm^{-3} because the transition of orders in $I_{\text{PL}}(t = 0ns)$ in Figure 6.7 (d-i) happens around $n_\gamma = 1 \times 10^{10}$ ph/cm^2 with an estimated $\alpha = 1 \times 10^5$ cm^{-1}. Let us just state that here the defects do not *saturate*, what happens is that when a sufficiently high fluence is reached, the ratio of hole/electron density in the defects does not change anymore with the fluence.

The fitting gives us an asymmetry in the capture cross sections and thermal velocities $\frac{\sigma_e v_e}{\sigma_h v_h} \approx 10$. Actually, since

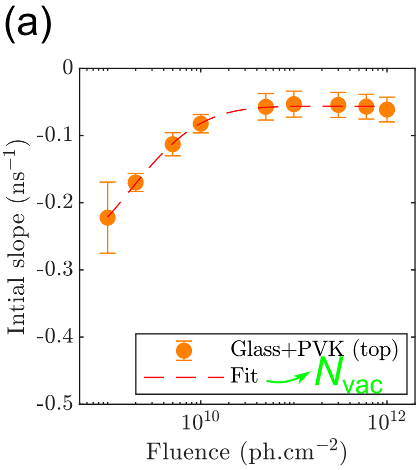

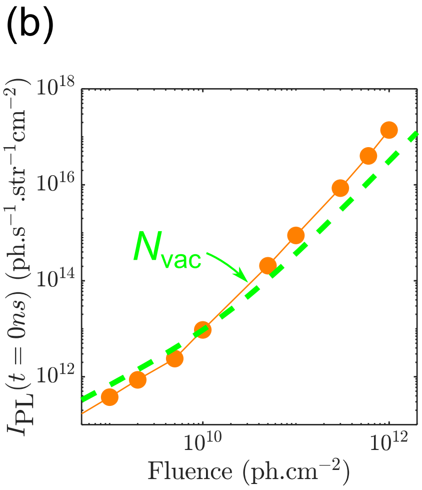

Figure 6.5: *(a) Fitting the defect model to the thin film derivative from the top. Only fluences in the range* $1 \times 10^9 - 1 \times 10^{12}$ ph/cm^2 *are fitted. (b) Application to the scaling of* $I_{PL}(t = 0ns)$. *Curves adjusted with a factor to correspond at the fluence of* $n_\gamma = 1 \times 10^{10}$ ph/cm^2.

we completely arbitrarily assumed that the perovskite was p-doped, we cannot determine if $\frac{\sigma_e v_e}{\sigma_h v_h} \approx 10$ or if $\frac{\sigma_h v_h}{\sigma_e v_e} \approx 10$ (or if the perovskite is n-doped).

Therefore we have:

Result 6.1.2. Our results on the perovskite thin-film on glass suggest a mechanism of a varying defect filling at low fluence, when the photo generated carrier density lies below the background doping density of the perovskite. This results in the surprising increase of the initial decay slope with fluence in the low-fluence regime.

On the interpretation of decays of full cells

However, the TiO_2 and especially the Spiro half cell show a slightly different kind of dynamics: they exhibit increasing initial slope **within** the "intrinsic-like" regime of fluence, see Figure 6.7 (c-ii) and (d-ii).

For the Spiro half cell, the initial slope of the decay is increasing as a function of the carrier fluence, even in the fluence regime where $I_{\mathrm{PL}}(t = 0ns)$ behaves with an order 2, ie in the "intrinsic" regime. To evidence that, we use the previous model and fit the Spiro half cell in Figure 6.6. Then we use the obtained value of N_{vac}/α to obtain the expected scaling of $I_{\mathrm{PL}}(t = 0ns)$ vs. fluence and compare it with the observation. We observe a slight discrepancy. Moreover we think that the model does not explain correctly the increase of the initial derivative, and even of the long decay time behavior with fluence, see Figure 6.8. It is unclear if the following model is enough to explain the behavior of half cells. We think that it is not, considering the discrepancy with $I_{\mathrm{PL}}(t = 0ns)$ but further study is required to conclude on this question.

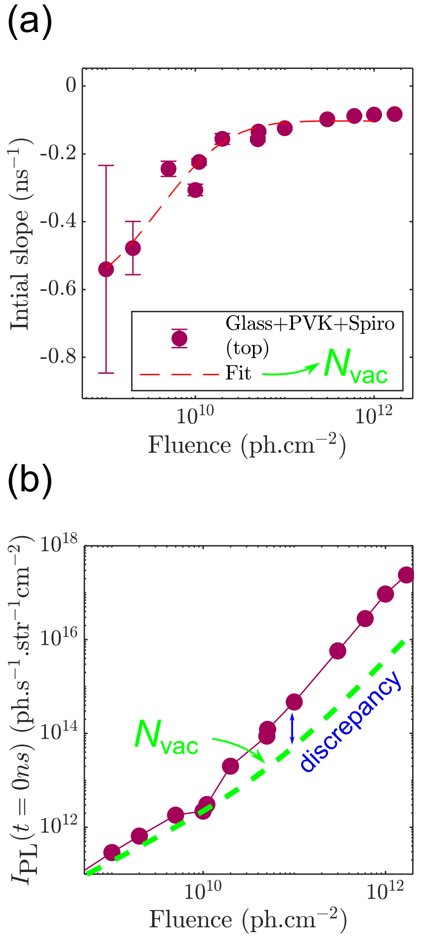

Figure 6.6: *(a) Fitting of the defect model on the Spiro top acquisition, from which we obtain* $N_{vac}/\alpha = (5 \pm 3) \times 10^{10}\mathrm{cm}^{-2}$. *(b) Application to the scaling of* $I_{PL}(t = 0ns)$. *We see a discrepancy for this indicator. Curves adjusted with a factor to correspond at the fluence of* $n_\gamma = 1 \times 10^{10}\,\mathrm{phcm}^{-2}$.

Conclusion

Therefore, in the presence of background doping, there are possibly two characteristic fluences that control how the system behaves:

1. The doping fluence $n_\gamma^{\mathrm{dop.}} = N_{\mathrm{dop}}/\alpha$ the fluence at which the photo-generated carrier density is equal to the background doping density. See chapter 4.3.

2. The electric field screening fluence $n_\gamma^{\mathrm{screen.}}$ that corresponds to the fluence at which the built-in electric field is substantially screened.

Depending on the device, the order and values of these two fluences may change. To this date, we deem that for our devices $n_\gamma^{\text{screen.}} \leq n_\gamma^{\text{dop.}}$. Therefore, the effect of the change of the change of defect occupation factor below $n_\gamma^{\text{dop.}}$ hinders the possibility to observe what the effects of electric fields and extraction is on the decays.

6.1.2 Comparing long and short time decay, as well as top and bottom illumination: towards the evidence of extraction

We showed that the effects of defects and doping changes the low fluence behavior. Nevertheless, our data show that the charge transport layer do have an extra impact on the initial decay, which is still under investigation.

To go further into the analysis, we plot in Figure 6.7 the entire dataset, including the decays acquired on each side of the samples (we remind that our configuration is such that excitation and collection are performed on the same side). In Figure 6.7, row (i) presents the data for the thin film on glass, row (ii) for the Spiro half-cell, row (iii) for the TiO_2 half cell and row (iv) for the full cell. Column (a) are the decays for different fluences acquired from the top (the brighter the color, the higher fluence —as indicated by the green arrows). Column (b) shows decays acquired in the bottom configuration.

Column (c) is the first indicator that we use: the initial derivative of the decay as a function of laser fluence, computed as a convoluted mono exponential fit of the decay in the interval [-2; 10]ns. Column (d) is the second indicator introduced in chapter 4.3: the scaling of the intensity of $I_{\text{PL}}(t = 0ns)$ as a function of fluence. A blue dashed line indicated an order 1 behavior as a guide for the eye, while a red one indicates an order 2 behavior.

Our main observations on this dataset are the following:

1. Looking at column (a) and (b): the neat film on glass and the TiO_2 half cell have long time behavior "as expected", ie the higher the fluence, the lower the decay —see the PL level at $t = 400ns$ for instance.
2. On the contrary, the Spiro half cell shows an opposite behavior, see Figure 6.8, while the full cell on both sides show a rather constant long decay time.
3. Looking at column (c), we observe that the initial derivative increases in a first phase of fluence for all sam-

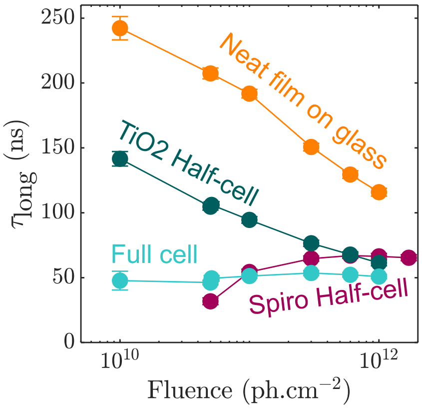

Figure 6.8: *τ_{long} computed between 30ns and 200ns as a function of fluence.*

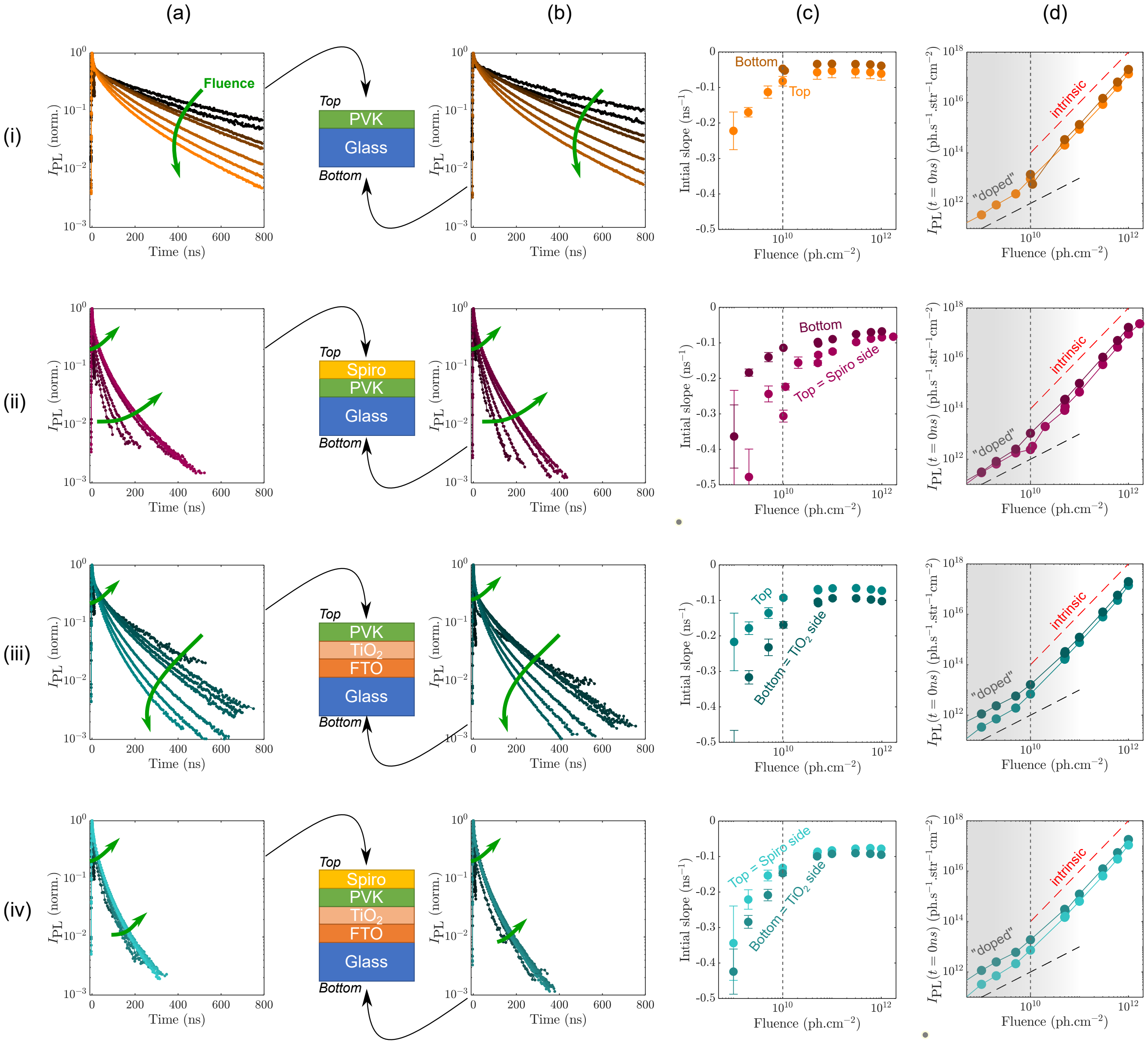

Figure 6.7: *Entire data-set of acquisitions for full cells and half cells. (a) Decays acquired with illumination and collection from the top side. (b) Decays acquired with illumination and collection from the bottom side. (c) Initial derivative observed on the curves as a function of fluence for both sides. (d) Scaling of $I_{PL}(t = 0ns)$ in absolute units as a function of the laser fluence. Rows: (i) Thin film on glass; (ii) Half-cell with SpiroOmetad; (iii) Half cell with TiO_2; (iv) Full stack (missing only the gold contact on top).*

ples and all sides. We see however that for the half cells (c-ii) and (c-iii) the initial derivative is always smaller on the CTL side (top for the Spiro and bottom for the TiO_2). **This observation shows that the presence of the CTL affects the initial derivative at low fluence**. Moreover, still at the relatively high fluence $n_\gamma = 1 \times 10^{12}\,\mathrm{ph/cm^2}$, the initial derivative is smaller on the CTL side meaning that the decay is faster on this side that on the perovskite side.

4. Looking at column (d), we see that all the samples on all the sides show an order 1 scaling of $I_{\mathrm{PL}}(t = 0ns)$ as a function of fluence until $n_\gamma \approx 1 \times 10^{10}\,\mathrm{ph/cm^2}$. After that fluence, the behavior is of order 2. We observe that mainly for the samples with FTO (d-iii) and (d-iv) do we see a noticeable difference in terms of absolute intensity from the bottom and the top side.

Result 6.1.3. On the half cells, the initial decay is always faster when the photo-generation is on the CTL side, suggesting that the charge transport layer does have a signature in the initial decay slope.

We will now propose to the discussion an interpretation tool that allows to compare samples and is applicable to images: the τ_0 vs. τ_{long} plot, see Figure 6.9. This plot follows the following hypothesis: if extraction parameters (that would lead to carrier spatial separation for instance) are expressed in the decay, it is at short time. At longer time, we speculate that the decay is more representative of recombination. In Figure 6.9, we plot the histogram of values obtained over the images on each of the TR-FLIM acquisition at high fluence as an example. Here τ_0 is the initial decay time (0-5ns) and τ_{long} is the decay time at "long" time (30-200ns). We would prefer to compute the decay time in an interval further away from the laser pulse but we are limited by the noise levels of the experimental acquisitions. We would also prefer to apply this reasoning to the low fluence dataset, but it is unfortunately too noisy to be interpreted locally on images.

In Figure 6.9 we see that the thin films on glass show higher τ_{long} than all the other samples, even if all the samples come from the same experimental batch. For the thin film on glass, the data shows a large change in terms of τ_0 between the top and bottom acquisitions which, to this date remains of unknown origin. The half cells show a consistent behavior:

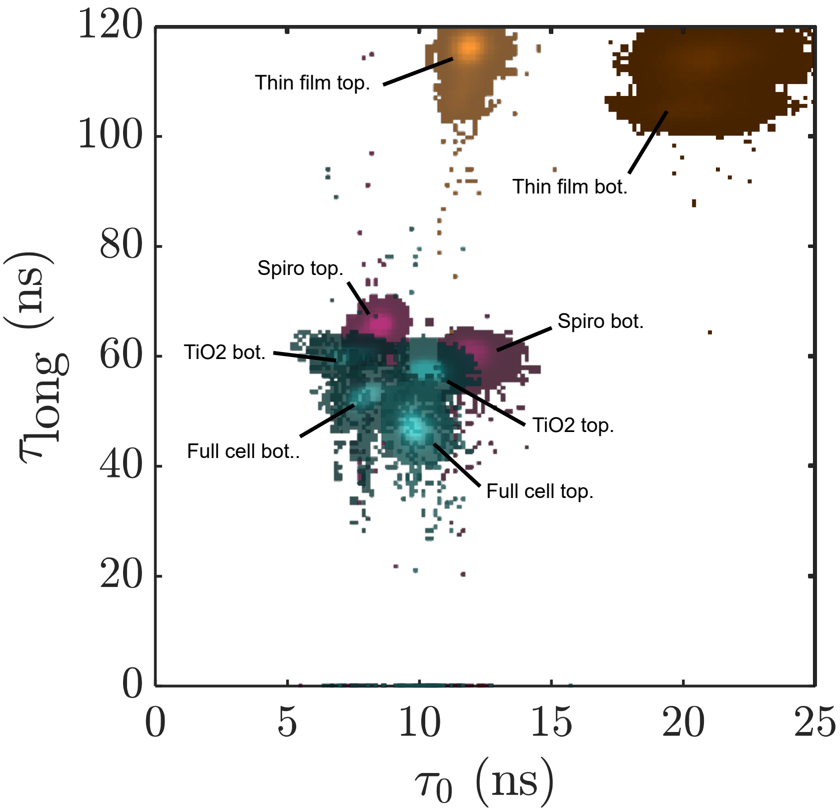

Figure 6.9: *Local correlation on images for the high fluence* $n_\gamma = 1 \times 10^{12}\,\mathrm{ph/cm^2}$. *The blighter spot represent couples of values that are more frequent on each of image.*

when they are illuminated on the CTL side, the values of τ_0 are reduced (top for Spiro, and bottom for TiO_2). The Spiro device shows slightly higher τ_{long}. The full cell shows the smallest τ_{long}. Surprisingly, it shows the inverse behavior in terms of τ_0: the top side (Spiro) should be close to the Spiro half cell top, and the bottom (TiO_2) to the TiO_2 half cell bottom, but the contrary is observed.

Even if all the devices with CTL fall close ones to the other on this plot, we have statistically relevant differences between them because the images allow to obtain an order of 200x200 data points. The same plot could be made at low fluence, however the experimental noise on the data does not allow for the clear distinction of the different regimes. An example is given below.

To sum up, our hypothesis and proposal for interpreting decays on full cells and half-cells with the data currently at hand is the following:

Statement 6.1.1. Proposed qualitative interpretation of decays on full cells and half cells. We propose the following interpretation for the decays:

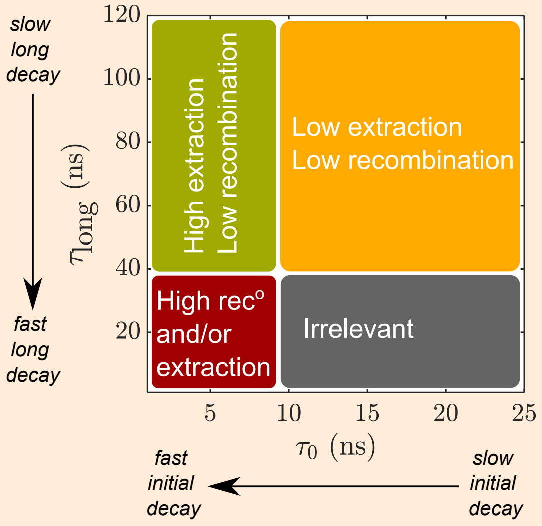

The initial decay bears the mark of the extracting layer while the decay time long after the pulse is more representative of the recombination in the devices. The values given as boundaries are arbitrary.

Interpretation plot as a function of fluence

Here, we discuss the proposed interpretation plot by observing the trajectory followed by the devices on this plot when the fluence is changed. To do so, we use the average decays over the images, as they are presented in Figure 6.7. The trajectories of the devices with CTLs are shown in Figure 6.10. Let us comment on the half cells first. The TiO_2 half-cell shows a decreasing τ_{long} behavior (from top of the plot at low fluence to bottom at high fluence). Both sides show this behavior. We see that the difference in terms of τ_0 between the CTL side and the perovskite side remains rather constant for all fluences. Now if we compare the TiO_2 half-cell with the Spiro half-cell, we see some similarities: one is the CTL to perovskite side τ_0-difference that both half-cells exhibit. The other similarity is that the low τ_0 side is the CTL side, as evidenced above. The major difference between the two half cell is that the Spiro half-cell shows an increasing τ_{long} behavior (from bottom the plot at low fluence to top at high fluence). Interestingly the two CTL curves end up forming only one curve. A similar effect is observed on the perovskite side.

The behavior of the full cell is also represented in Figure 6.10, close to the center of the plot. We note that it displays an increasing behavior, as does the Spiro half-cell.

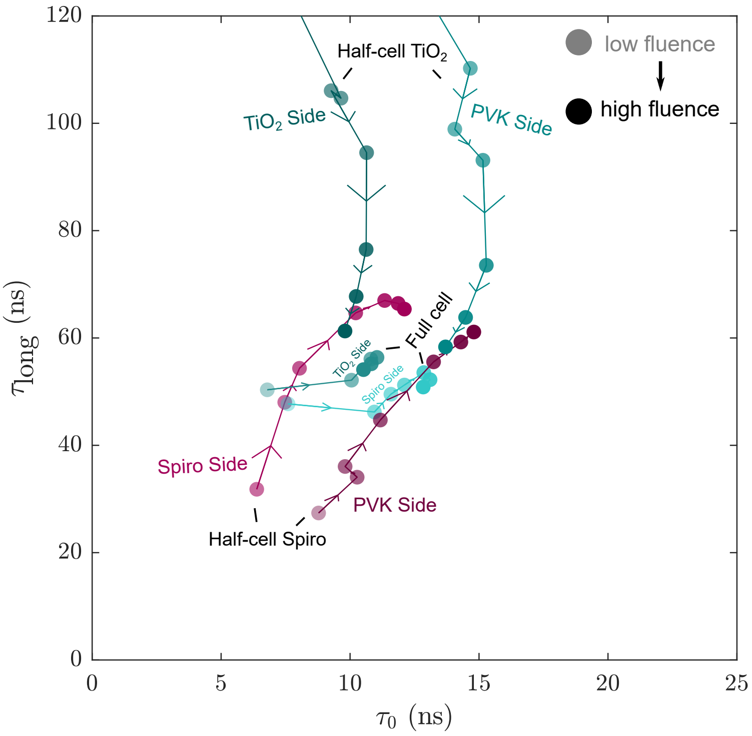

Figure 6.10: *Interpretation plot for the image-average decays of Figure 6.7 for different fluences. The arrows indicate increasing fluence.*

We also note that the lowest fluence points are situated in the low τ_0 (left) side, with the Spiro side point almost exactly situated on a point of the Spiro half cell curve. The TiO_2 side of the full cell converges in an intermediate point.

This plot shows how rich the physics behind our measurement is. We do not have a complete understanding of these trajectories but they do seem to be representative of mechanisms at play in the devices. We note that the higher fluences should yield horizontal trajectories to the left according to the scaling of initial decay slope with fluence discussed in section 4.2.2.

Application to imaging

We apply this reasoning to our imaging dataset by computing the maps of τ_0 and τ_{long} for each of the sub-sample set. In Figure 6.11, we plot the maps for the high fluence acquisition. All the maps share the same colorbar. We grouped the samples by the interface through which we observe the perovskite. On the top left corner the perovskite emission is observed through the Spiro layer, be it in the half cell of full cell. In the top

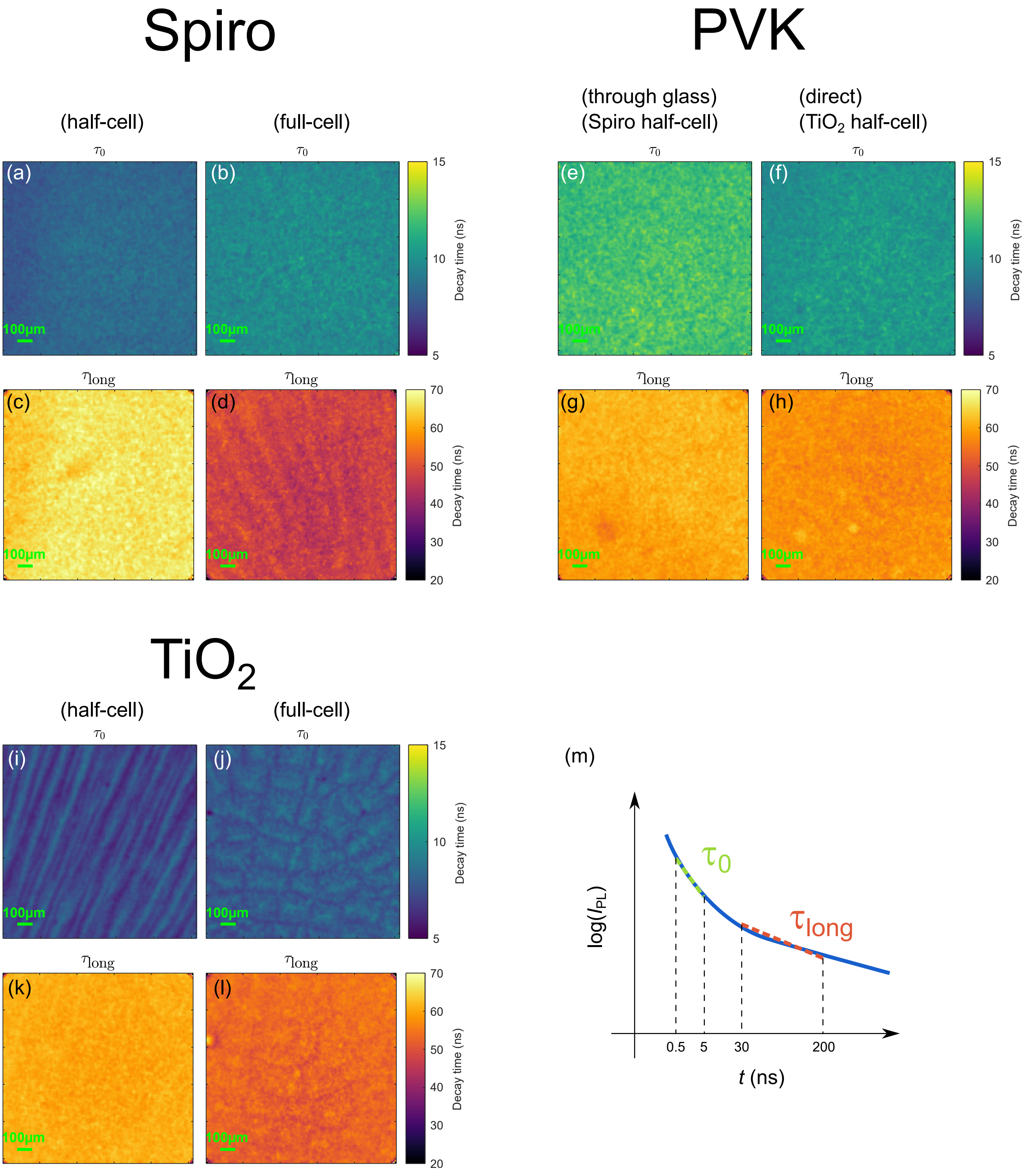

Figure 6.11: *Images of the fitted decay times at high fluence* $n_\gamma = 1 \times 10^{12}\,\text{ph/cm}^2$ *for all the samples of the data set. (a,b,e,f,i,j) maps of* τ_0 *; (c,d,g,h,k,l) maps of* τ_{long}*. (m) Sketch of the fitting intervals used to obtain these maps.*

right the perovskite emission is observed either through glass for the Spiro half cell or directly for the TiO_2 half cell. In the bottom left corner the perovskite is observed through Glass, FTO and TiO_2. Figure 6.11 (m) depicts the fitting intervals used for the computation.

We first observe that the Spiro interface does not show particular inhomogeneity or structure, and this is expected since this layer is not ordered by design in thin films [Shi *et al.* 2016]. By observing the long time behavior, a clear reduction is seen for the full cell which is explained by the image: we see stripes appearing in Figure 6.11 (d) that could correspond to the sprayed TiO_2 structure (visible in (i)). Therefore, if we use our hypothesis we could conclude that the addition of the ETL reduced charge separation compared to the half cell and increased recombination.

For the perovskite through glass or direct in the top right corner of Figure 6.11 we see good compatibility for the two measurements.

The most visible inhomogeneities are seen in Figure 6.11 (i) and (j) which are the τ_0 map of for the TiO_2 interface. We observe that the texture is perfectly visible in the τ_0 maps but nearly erased in the τ_{long} map. We interpret this as to be compatible with our hypothesis: if τ_0 map represented recombination and not carrier extraction/separation its features would also be seen on the τ_{long} map. Yet this is not what is observed for the half cell, and for the full cell only slight features are of the τ_0 map are recognizable on the τ_{long} map. Therefore, we argue that the inhomogeneities in maps (i) and (j) are linked to carrier separation/extraction. The difference in terms of morphology might come from the central/eccentric position we used for the acquisition on the precise samples understudy. The inhomogeneities observed seem to correspond to the texture or height map of the TiO_2 deposited by spray.

Prospective future analysis: observing a transition region with or without TiO_2

To finalize our imaging study, we bring to the discussion data obtained on a transition region on the TiO_2 half cell as a proof of concept of the potential inhomogeneities of extraction that could be observable. The device was introduced in chapter 4.3 and shown in Figure 4.16 (d). It consists in an image where, on the left side, no TiO_2 is present, while it is present on the right side. The approximate scheme is plotted in Figure 6.12 (d1). Laser scribing is used to "open" the FTO layer. This trench of width $100\mu m$ does also create some gradient of the FTO thickness around. TiO_2 is deposited via ALD a posteriori only on the right surface. The exact thickness profile of the TiO_2 is not known in this region and we do not have SEM cross sections. We imaged with TR-FLIM the top and bottom of this region, but we could not exactly place ourselves in the exact same (x,y) position for both.

The results for the high fluence case are given in Figure 6.12 where we plot the maps of τ_0 and τ_{long} along with their correlation histogram for the top and bottom acquisitions. We observe that the values of τ_0 are lower when observing from the TiO_2 side, as is expected with our hypothesis on interpretation. We also observe again that the shapes of TiO_2 are clearly visible in the τ_0 map (a2) but not in the τ_{long} map (b2) —which would coherently attribute τ_0 to extraction properties and not recombination. The τ_{long} is nonetheless precise (see the details around the trench): the fact that we do not see the stripes is not caused by a too low acquisition quality, it is a physical effect.

With the correlation histograms of Figure 6.12 (c1) and (c2), we define regions evidenced by colored rectangle and plot in (e-h) the pixels that fall into these rectangles of correlation. For the top and the bottom acquisition, the red region correspond to the area where no TiO_2 is deposited and perovskite is deposited on FTO: both τ_0 and τ_{long} are low which could be explained by high recombination. The green region is the one that is most similar in terms of $(\tau_0,\tau_{\mathrm{long}})$ to the acquisition "in the middle" of the TiO_2 area presented in Figure 6.11: spatially it also corresponds to this region. The blue area corresponds to pixels with high τ_{long} and rather low τ_0: they would correspond to the region with the highest extraction/separation to recombination ratio. Possibly, this could be an effect of the thickness variation of the perovskite layer. Finally, the gray area corresponding to the rest of the pixels corresponds to the left side of the trench. It is a region with high τ_0 and low τ_{long} which would correspond to low extraction but high recombination.

For the bottom acquisition, we notice that the the blue and red regions have similar τ_{long} as in (c1) but lower τ_0. Again, this is compatible with our hypothesis that τ_0 is linked with the extraction properties. Inside the red region we see that the range of τ_0 has "expanded": we attribute this to the far left side of (a2) : ie the zone where the perovskite is in direct contact with a thick layer of the conducting FTO.

Therefore, we see on this specific area that the interpretation of the decays needs thorough discussion. We would need to improve this analysis with extra measurements to be able to conclude, including measuring the cross section to quantify the thicknesses. However, our results already suggest that rich

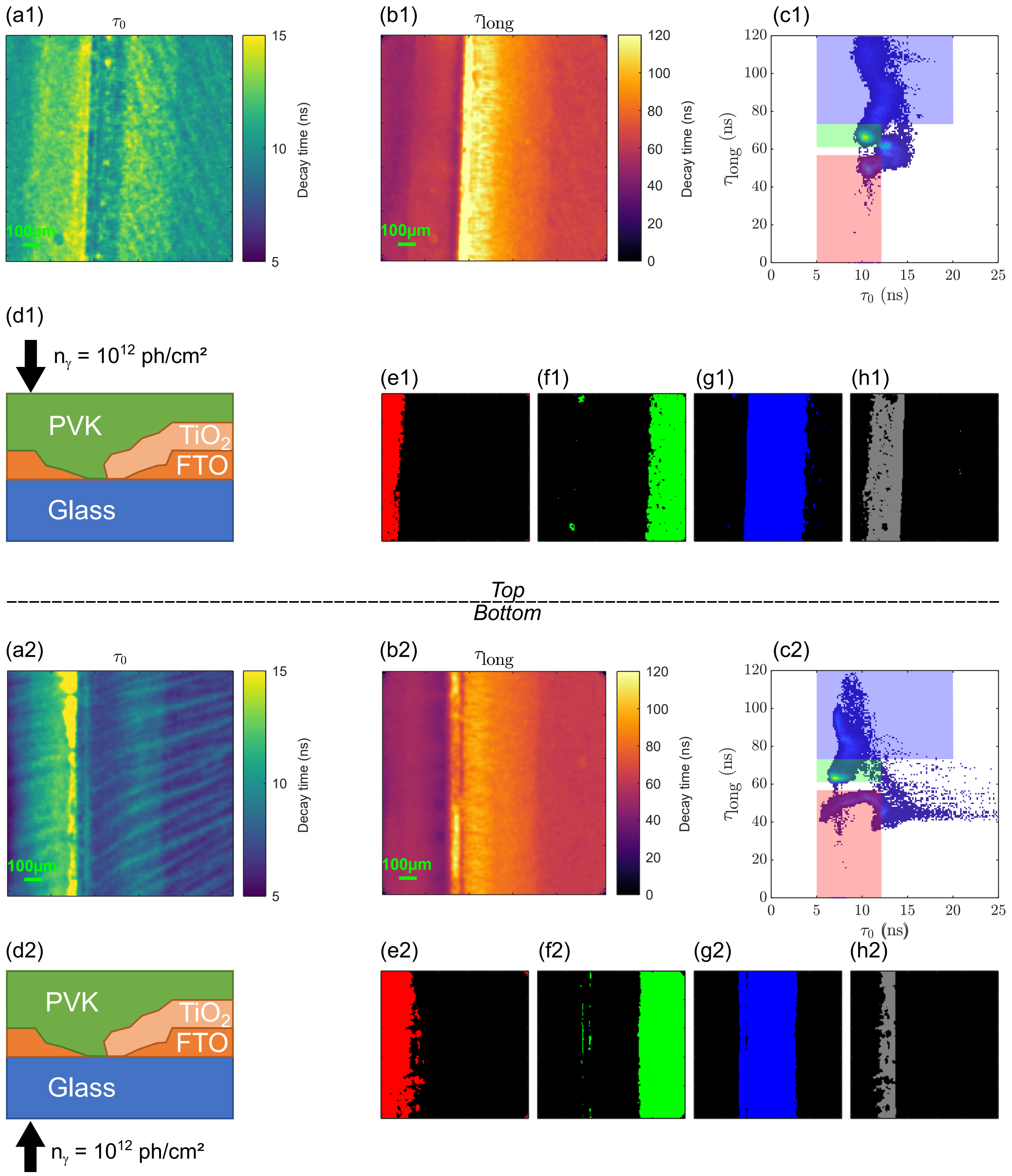

Figure 6.12: *(a) Initial decay time τ_0 computed between 0.5 and 5ns. (b) Longer decay time computed between 30 and 200ns. (c) Pixel-pixel Correlation density map of (a) and (b). Colored rectangles are chosen regions of interest in the correlation plot. (d) Scheme of the sample and of the fluence used. (e-h) Masks corresponding to pixels in the regions of interest defined in the correlation plot (c). Plots labeled with "1" are the top acquisition dataset and those with "2" the bottom acquisition.*

information on extraction/carrier separation and recombination is contained in the correlation plot between τ_0 and τ_{long}.

6.1.3 Conclusion and perspectives

In this subsection we showed a multi-sample analysis of the baseline perovskite solar cell fabricated at IPVF. Our aim was to be able to distinguish and possibly quantify extraction properties from recombination via a fluence study. Today, this goal is not achieved but we showed promising steps towards understanding how to correctly interpret decays obtained on devices with extractors.

First we discussed the low fluence behavior of all the devices —a regime where we expect electric fields to act more visibly. We showed that, unfortunately, this low fluence regime is also the regime where background doping of the perovskite can render the defect's occupation factors fluence dependent. We provided a model that accounts for the fluence dependence of the initial decay slope as a function of fluence.

Second, we observed that devices with extractor generally had lower initial decay slope (ie faster initial decays) than the others and we evidenced a top/bottom comparison that yielded the same observation. Based on that, we discussed an interpretation plot comparing the decay time at the beginning of the decay τ_0 and at longer time τ_{long}. We compared all the samples on this plot. This interpretation is not final and will be the subject of future studies. We applied it to the high fluence images to show how these two characteristic times changed spatially to reveal different regions on the sample.

As perspective, we could try in the future to obtain the best possible images at low fluence to carry an analysis such as that of Figure 6.12. Another possibility would be to test different types of extracting layers to compare their fluence behavior. Finally, we could explore how devices with extracting layers behave under the wavelength-study developed in Chapter 5.

6.2 Using an applied bias to observe the electric field's signature

In order to gain insight on extraction properties on full devices, one idea that comes to mind is to study the effect of an applied bias. The idea is that **by changing the applied bias, one can change the ratio of extraction and recombination**. This was done and theorized in the literature for classical semiconductors, [Rosenwaks *et al.* 1994] on

GaAs, on CIGS [Maiberg *et al.* 2015]. The question one could therefore ask is: what is the effect of an applied bias to the TR-PL decay ? And what extraction properties could we extract from such measurement?

This section will not answer these questions because mixed cations halide perovskite are but a very complex ensemble composed not only of a lattice, its electrons and holes but also of mobile ions. These ions are the ones that compose the very lattice and that were evidenced to move under the effect of electric fields. We refer the reader to the following review that tackles imaging of the effects of ions movement with time resolved microscopy [Chen *et al.* 2021] or to this one on the multiple techniques used in the literature to observe ion migration [Yan *et al.* 2022]. Therefore, when one applies a bias to a perovskite solar cell, electrons and holes will not be the only moving charges. This complicates enormously the answer to the simple question above: not only should one ask what is the decay under such bias? but also: for how much time was the bias applied?

In this section, we show a set of experiments that evidence transients **at the scale of the minute** in the TR-PL signal of perovskite solar cells under bias. To be clear: the bias has an effect on the decays but this effect itself depends on time (presumably due to ions screening the applied field). We were able to monitor precisely how the effect changed when a bias was applied, as a function of the application time of the bias or "lab time", t_{lab}. We think this change can be attributed to the slow (compared to electrons and holes) movement of ions —even if this is just an hypothesis at this hour. We want to stress that this experiment was only possible thanks to the automation software we developed for our camera.

In the rest of this section we describe the experimental procedure, show the slow effect change of bias, propose some observables and conclude on the potential of the technique.

6.2.1 Experimental method

In this experiment, we study baseline perovskite full cell of IPVF composed of triple cation perovskite sandwiched between TiO_2 deposited on FTO and Spiro with gold deposited on top, see Appendix C.1. We place the cell in the cryostat and put it in contact with a Keithley bias generator. We perform TR-FLIM imaging on this sample, see Figure 6.13 (a-2). We work with the decays averaged over the image.

In this experiment, a computer controls both the TR-FLIM acquisition and the Keithley so that we can synchronize the application of bias and the TR-FLIM acquisition. When the Keithley applies its bias, we can also monitor the **current**.

We depict the synchronization in Figure 6.13 (a-1). Every 5 μs, a laser pulse (green triangles) hits the sample with a repetition rate of 200kHz. A PL decay follows (blue line). At some point in the time of the lab, the bias is applied by the software (green region). We define that this time is $t_{\text{lab}} = 0$. This has an effect on the device and on the decays represented by the small arrows. Note that there are virtually two times axes in this experiment: the time of the lab t_{lab} and the time of the decay t_{decay} which is the time that labels all the plots of this thesis.

6.2.2 Results

In Figure 6.13 (b) we show the evolution of decays with an applied bias of $V = 1.05V$. The dark curves correspond to the first acquired decays while the light blue curves correspond to longer times up to approximately 10 minutes of bias application. We observed that the decay "worsens" with time: the curves go down. Of course, obtaining one decay plotted here does not take only 300 ns. Because one acquisition is actually the average of up to 60 000 repetitions of the same experiment. Therefore, here each decay takes approximately 40s to be acquired by the camera. We observed that modifications did happen in this time scale. Therefore the basic experimental method is flawed: while the decay is acquired, it is modified. We will propose in (d) and (e) another observable.

But first let us comment on Figure 6.13 (c) where we plot the measured current in the cell as a function of t_{lab} during the experiment shown in (b). This current is in the range of 0.8 mA, and seems to increase with time. We see that the behavior is not monotonous. We note that this current is not a "continuous" current strictly speaking. Each pulse of light results in a pulse of current (which we did not/can not measure). The Keithley's temporal response is too slow to observe such effects and delivers the (time) average current. The spike in (c) is of unknown origin to us but we observed such spikes for multiple acquisitions. We do not know if these are caveats or real effects. In Figure 6.14 (a) we plot the "IV-curves" obtained with the pulsed laser as the illumination source. We plot the IV-curve before the experiment (b), and after (orange curve). We clearly see a degraded IV curve after the experiment compatible with the ion movement. Then, we let the sample in the dark, at open circuit for 1h. We remeasure the IV curve and obtain the yellow curve, that is very compatible with the IV curve before the experiment. Presumably, the ions are back in place.

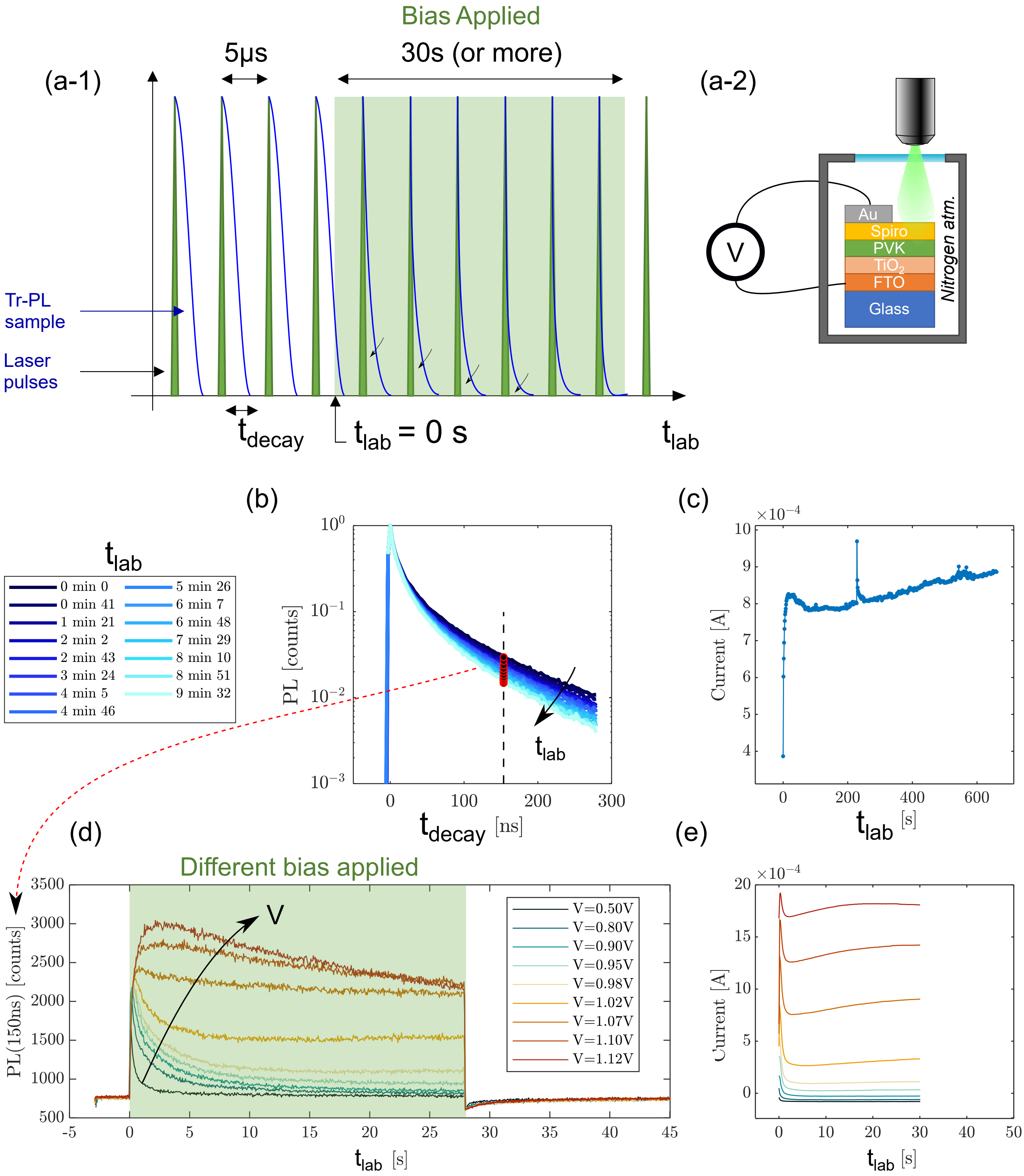

Figure 6.13: *Experiments with applied bias on perovskite full cells. (a-1) Scheme of temporal synchronization. (a-2) Scheme of the setup (b) Decays evolving when a bias of $V = 1.05V$ is applied, the duration of application is displayed on the left. (c) Corresponding current during the experiment. (d) Intensity of PL at $t_{decay} = 150ns$ as a function of t_{lab} after applying different bias. (e) Corresponding currents during the experiments.*

To obtain a finer temporal resolution of the effects observed we slightly changed our experimental procedure: to speed up the FLIM acquisitions **we do not measure the entire decay**. Instead, we measure only one point of the decay: we measure the intensity of PL at $t = 150ns$ in a repetitive manner. One measurement of $I_{\mathrm{PL}}(t = 150ns)$ takes 50ms: therefore we have a 1000 factor in the resolution of this new observable (compared to 1 decay acquired during 40s). Nevertheless, we are limited to observing the effect of bias during less than 50s because the TR-FLIM can only acquire 1000 frames. Therefore, we program a pulse of bias of approximately 30s to be applied and look at the effect of this pulse on $I_{\mathrm{PL}}(t = 150ns)$. This is plotted for different bias in Figure 6.13 (d). We see an effect that could not be observed clearly in Figure 6.13 (b): in the first hundreds of milliseconds after the application, the PL intensity rises and then starts to decrease. This is the case for all applied biases, even the smallest one. In (b), we observe that at the longer time scale of a few minutes, the intensity of PL decreased (see the arrow in (b)). We could in the future devise a way of observing a bias applied for longer than 30s and actually also reconstruct decays by performing experiment (d)

In Figure 6.13 (e), we plot the corresponding current transients measured by the Keithley during the acquisitions of (d). We observe that the behavior of the current follows as well a transient behavior.

In Figure 6.14 (b), we plot the effective IV characteristic obtained with such current transients. We plot two curves: one is the IV curve when we take for the current the values of the maximal observed current in Figure 6.13 (e). The other curve is by taking for the current value the last point of the transient. We also superimpose the IV curve measured with the pulsed laser source as illumination when the bias are applied for a longer time (>1min). We do not yet have a clear interpretation for the IV curve at the maximal intensity but it might hold physical meaning.

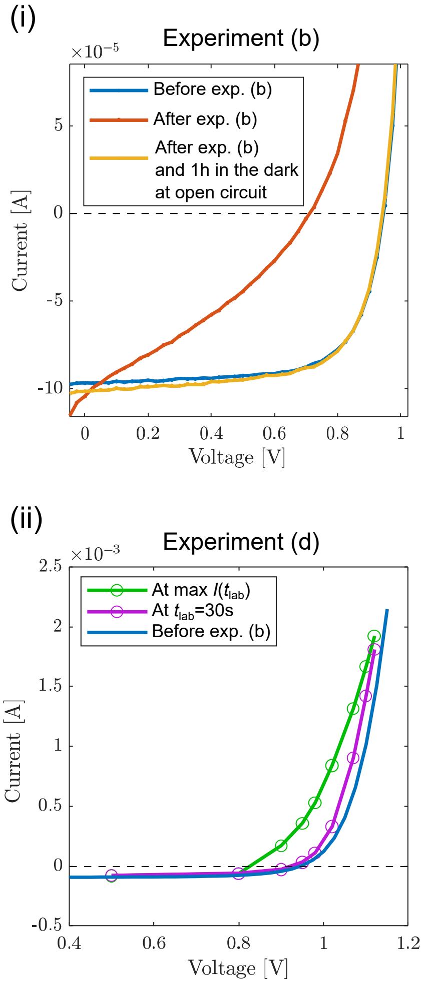

Figure 6.14: *(i) IV curves from the experiment of Figure 6.13(b) (which consists in applying a bias of $V = 1.05V$ for 10 min under laser illumination) ; (ii) IV curves from Figure 6.13(d).*

6.2.3 Discussion

The experiments show that transient the bias effect changes at the scale of the minute when a triple cation perovskite solar cell is placed under bias. Such transient behavior is influenced in amplitude and in duration by the value of the bias.

This rather slow behavior could be caused by the movement of mobile ions in the perovskite solar cell. To obtain a rough estimate of the order of magnitude of the mobility of the species we can estimate that the electric fields amount to 1V over 500nm which gives an electric field of $2 \times 10^4\,\mathrm{V/cm}$. The velocity of the species would be μE. To travel 500nm, it takes approximately say 10s. This would lead to a mobility of $\mu = 2 \times 10^{-10}\,\mathrm{cm^2/Vs}$. This rough estimate is in line with literature where different techniques found mobilities between 1×10^{-10} and $1 \times 10^{-7}\,\mathrm{cm^2/Vs}$ for the ions composing the perovskite [García-Batlle *et al.* 2021, Senocrate *et al.* 2018, Bertoluzzi *et al.* 2018]. Note that the ions might not need to travel the whole thickness of the device to have an effect on the TR-PL decays, hence the mobility could potentially be lower than this estimate. Moreover, the ions might certainly screen the electric field and this effect would require precise modeling. Nonetheless, the observed slow transient behavior could be explained by the movement of ions otherwise evidenced in the literature.

Our results are preliminary and do not yield to precise estimates of the mobility of ions or to images of their motion. However they show hints that such studies could be lead with such experimental procedures.

These results show that **using bias studies to distinguish locally extraction from recombination is not so obvious due to the transient behavior of the decays** at the scale of the minute. This slow transient could be caused by moving ions. One can imaging to observe this slow transient by following its impact on the electron and hole densities as the experimental proof of concept given above.

6.2.4 Using a pulsed applied bias

Then, to distinguish extraction from recombination, one could imagine using pulsed bias, as our team used in the following paper : [Bercegol *et al.* 2020]. The experimental challenge is however increased and other questions arise —like the response time of the perovskite to the applied bias. We studied a planar channel under pulsed bias, see the scheme in Figure 6.15. In this study, we analyzed a symmetric channel composed of two electrodes of Gold+ITO. Pulses of bias were applied: they last 300ns and no bias is applied for more than 5 after each pulse of bias. We evidence an asymmetry of the TR-FLIM decay that we modeled and fitted as an asymmetry of electron and hole mobilities. This allowed us to estimate that the electron mobility would be $\mu_e = 0.22\,\mathrm{cm^2/Vs}$ and the hole mobility $\mu_h = 0.47\,\mathrm{cm^2/Vs}$.

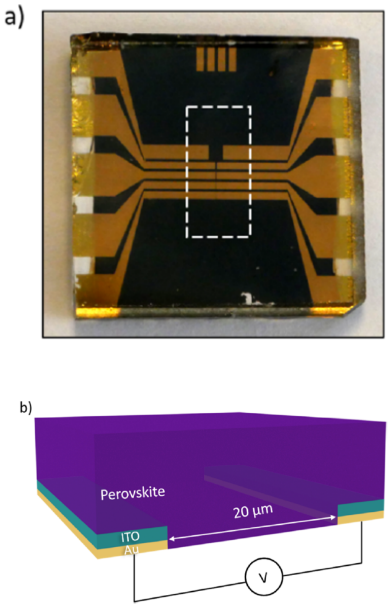

Figure 6.15: *(a) Image of the sample. (b) Scheme of the studied planar channel. Adapted from [Bercegol* et al. *2020]*

An interesting extension of this study would concern asymmetric channels. Such devices are currently being manufactured at IPVF but the work to obtain reproducible devices is still ongoing. Once such device/method is obtained, TR-

FLIM studies could bring new insight into the recombination/extraction interplay.

6.3 Conclusion

Thus, in this last prospective chapter we gave our try at understanding and extracting information from the TR-PL decays of full devices and half cells.

We evidenced that multiple phenomena could alter the decays such as carrier extraction or electric fields. Based on the literature, we discussed the possible experimental observable that could provide information. We introduced experiments on multiple samples and as a function of fluence and illumination side. We obtained hints that the initial decay at low fluence does contain information about extraction/electric fields but the initial decay at low fluence may also hold the signature of defect related fluence effects. Therefore, today the interpretation still needs consolidation but the results presented here are promising.

We also presented another method to play with the ratio of "extraction"/recombination: applying electric fields. This method applied to triple cation perovskite along with our automation of experiments allowed us to evidence that, presumably ions, moved at the scale of the second/minute after the bias is applied. There are two consequences: one is that this movement renders difficult measuring a device in a known configuration (where are the ions when we apply the bias?), the other is that this method could be a way of monitoring the ions motion. We briefly discussed the application of pulses of bias, to avoid ion motion.

Thus, we opened some perspective with this chapter that, hopefully, stimulate research towards imaging extraction parameters from the TR-FLIM signal.

Il faut toujours connaître les limites
du possible. Pas pour s'arrêter,
mais pour tenter l'impossible dans
les meilleures conditions.
*One needs to know the where the
frontiers of what's possible are. Not
to stop there, but to try the
impossible in the best conditions.*

Charge d'âme
Romain Gary, 1977

Chapter 7

General conclusions & perspectives

Here, we summarize our main findings and show how we contributed to the literature. Then, we give a few perspective on next research focus that could follow the work.

7.1 Summary of our findings

Our work has lead to experimental improvements. First, we characterized the TR-FLIM camera in terms of both absolute intensity and noise level. Combined with automation software to control it, it opened us a new range of possibilities to increase the experimental quality of the acquired decay cubes —via repetitions and datacubes from multiple acquisitions. We also pushed the limit of the camera's temporal response further to obtain the super resolved acquisitions, which were then combined with a deconvolution code to retrieve up to now hidden information. Second, we developed a user-friendly program to be able to assess the quality of the experimental data acquired *directly* inside the laser room. This program was of tremendous importance in our experimental work improvement: for instance, we were able to characterize on the spot if light-soaking was happening and if we needed to alter the experimental conditions.

In terms of modeling, we mainly worked with the drift-diffusion model. We brought to the literature a technique based on a scaling law for the initial derivative of the decays as a function of both the fluence and wavelength of the excitation laser. If a power study is performed, the external radiative recombination coefficient may be retrieved. If the wavelength study is performed, the top and bulk defect recombination parameters may be distinguished. This method is applicable on images with very low computation time. We also used the exact solution of the drift-diffusion model to propose another method to distinguish bulk from surface defects, inspired by an already existing method.

Result 7.1.1. Short summary. In this thesis, inhomogeneities of recombination and transport properties of lead-halide perovskite are studied via time resolved photo-luminescence imaging. We developed methods to obtain the corresponding answers:

1. **Question 0:** *How exactly does transport affect the decay compared to recombination?* We provided a new way to plot contributions of the decay, that we name the SIMPLED plot. It is obtained from the drift diffusion model and displays for each instant of time the percentage of the decay rate attributed to diffusion and each type of recombination. Mainly diffusion plays an important role ”at short time” —which for triple cation perovskite is in the range of tens of nanoseconds.

2. **Question 1:** *How many defects are there in a given perovskite layer and how are they distributed on the samples?* We developed a new short-time scaling law technique to answer this question locally on images. Decay time imaging may also be employed. Both result in surface recombination velocities in the order of $S_{\mathrm{top}} = 100\,\mathrm{cm\,s^{-1}}$ and/or bulk lifetime of $\tau_{\mathrm{bulk}} = 500\,\mathrm{ns}$.

3. **Question 2:** *How are the defects distributed in the thickness of the perovskite layer?* To answer this question, we extended our short time scaling to study images acquired at different laser wavelengths. It allowed us to distinguish locally S_{top} and τ_{bulk} —which had never been done on images for perovskite layers in the literature. We applied the method to study perovskite samples exposed to X-Rays. We determined that X-Rays caused mainly bulk defects rather than surface ones.

4. **Question 3:** *How doped are the perovskite layers and how are the dopant distributed on the samples?* We applied an already existing scaling for the intensity at times $t = 0ns$ as a function of fluence. What is new to the literature is its use locally on images to determine the doping density of perovskite layers. We showed that this doping is around $1 \times 10^{15}\,\mathrm{cm^{-3}}$ and obtained *images* of its spatial distribution for $\mathrm{FAPbI_3}$ and triple cation lead halide perovskite.

5. **Question 4:** *Is charge extraction homogeneous on a full device sample?* This question is still under study. Our idea was to observe the impact of built-in electric fields on the decays. To do so, the first method we employed was to place ourselves at low fluence in order to prevent screening of the field. Doing so, we discovered that this regime actually corresponds to a regime where the doping density of the perovskite layer has an impact on the defect occupation factor. Another method was to apply biases and observe their impact on the decays, but we evidenced that presumably ions moved at the scale of the second/minute to screen the applied field —proposing then a possible way to image ion motion.

Therefore we focused our research on imaging the inhomogeneity of recombination and transport of perovskite. We proposed new imaging and interpretation techniques, and applied them to study state of the art samples that lead to publications in the literature, see Appendix A.

7.2 Perspective: what could be studied next (or more)?

In this subsection, we suggest a few directions for the continuation of this work. The techniques we developed during this work could be used as "standard" techniques on new objects of interest. We discuss a few examples. We also give some elements to go further and exploit at maximum the imaging power at our disposal.

7.2.1 Applying the developed techniques to new studies

Even more perovskite samples

We observed a variety of perovskite samples and compositions. We have recently started observing high bandgap perovskite such as fully inorganic $CsPbBr_3$. There is an experimental challenge (because the laser we have to image them is not very intense) that we have partially overcome when we tried to distinguish surface from bulk recombination. The first examples are shown in Figure 7.1: they show many inhomogeneities that could perfectly further our research subject.

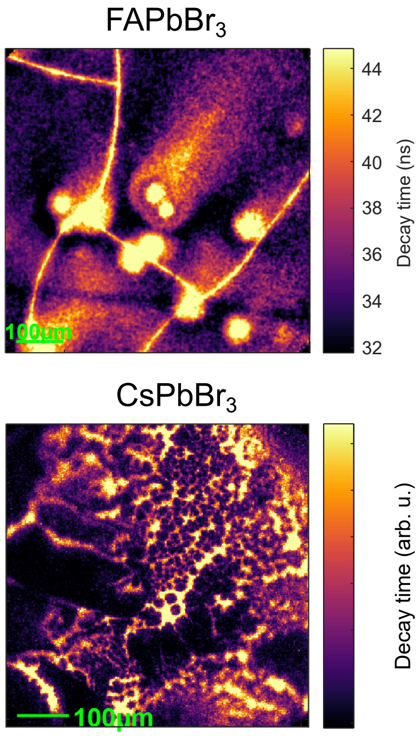

Figure 7.1: *Decay time images of two other perovskite compositions.*

Defects & Doping

The method proposed to determine the doping density locally for perovskite samples needs to be conducted on a wider range of samples. A comparison to other techniques like Urbach energy determination via Hyperspectral measurement or high dynamic range EQE could offer interesting insight: do the three techniques find the same density of defects/dopants? If so, then the $I_{\mathrm{PL}}(t = 0ns)$ technique could reveal the microscopic distribution of such defects/dopants via imaging small regions in high magnification conditions.

Ion movement

The movement of ions suggested by the experiment presented in chapter 6.2 could be continued. With such technique applied in precise imaging conditions, one could potentially obtain maps of velocity for the ions. Lateral heterogeneity could be observed. A comparison of different perovskite compositions would hold great interest as different ions are expected to have different velocities.

Extraction/Recombination

The question of extraction vs. recombination is still understudy and could be improved. Mainly simulation work are undergoing to better represent with TCAD softwares the behavior of the cells. Another set of experiments might also yield better signal to noise ratio for the low fluence acquisitions by benefiting from all the improvements that this work lead to. In terms of experimental plan, it would be of high interest to compare different extraction layer for holes and for electrons as well as their combination into devices. A correlation between the cell's electrical performances (especially their short circuit current) to the photo-luminescence result would be a tremendous proof of the possibility to image extraction.

Improvements in data treatment

One issue we have with decay time imaging is that it needs to be performed at low fluence, as discussed in Chapter 3. It results in low SNR signal. Therefore we need strategies to reduce the noise on the obtained decay times maps. This is the subject of a collaboration started with INRIA and Jean-Christophe Pesquet's group. Etienne Soret, an intern in this collaboration, worked in with Gabriele Scrivanti, a PhD student of INRIA, to include *regularization* functions when fitting decay time maps (or more generally linear models). Regularization uses the fact that the map of fitted decay times is expected to not show too high gradients for instance —thus helping rule out which pixels are subject to noise and which are not. We showed early results of the collaboration at the end of Chapter 3. This collaboration will be continued and the results will be presented shortly.

We highlighted in this thesis how rich the TR-FLIM datacubes were. But we also noted that the amount of available data is often difficult to treat. To treat it, one way would be to simplify the datacube by finding say two "eigendecays" that could represent approximately the whole cube. Each pixel would be a sum of two positive coefficients times the two eigendecays. For instance imagine a sample composed of two species that each have their specific decay (or spectra). This is what "Non-negative matrix factorization" (NNMF) algorithms do. Algorithm for NNMF exist in the literature but we would want to adapt them to Physics. Indeed, in the existing algorithms there are no constraints on the eigendecays or spectra: they could be any mathematical function (including ones with negative values for instance). But our problem is simpler: we know that decays should respect the drift-diffusion equation and we know that spectra should respect the generalized Planck's law. So can we obtain a NNMF algorithm to simplify the cubes by projecting them as sums of eigendecays that respect the drift-diffusion model? We developed a proof of concept for such algorithm and it could very well be improved, for instance via the collaboration with INRIA.

7.2.2 New developments

Adapt the proposed method to other imaging techniques

Some work could be dedicated to generalize what we developed and found to scanning imaging techniques, that are more spread out in research teams around the world. This could lead to the improvement of such techniques.

Static Urbach energy

We used excitation fluence, excitation wavelength, applied bias as stressors to observe their impact on decays. Another stressor that we could use is the device's **temperature**.

Particularly it would be interesting to tackle the question of Urbach energy as a function of temperature (and space via imaging!). The Hyperspectral imager (HI) is very well suited for that purpose. We could select a zone and compare the density of "dopants" obtained via the time resolved measurement (see chapter 4.3) to the Urbach energy maps obtained via HI. Both experiments could be performed on same exact region and for similar temperature. Thus, many correlations could be drawn: are the "dopants" observed in FLIM exactly the defect tail observed with the Urbach energy? Is it true for the whole range of temperatures? How does the correlation $\Delta\mu/\tau$ evolve with temperature (see Figure 3.4)? Does it follow the models discussed in Equation (3.16)?

In the literature, models exist to decompose Urbach energy into two components: the static Urbach energy and the temperature dependent one, see [Ledinsky *et al.* 2019, Kaiser *et al.* 2021]. Can we obtain an image of the static Urbach energy as fitted by such models, and how does it compare to say the decay time image or to the dopants image?

7.3 Final words

With all these new and exciting questions, it is now time to end this manuscript. The next chapters are appendices that contain extra-information.

Appendix A

Publications

This work was partially published in different publications.

A.1 Papers

I had the chance to participate in multiple publications, as first author or not, see Figure A.1.

(a) Mapping Transport Properties of Halide Perovskites via Short-Time-Dynamics Scaling Laws and Subnanosecond-Time-Resolution Imaging, ***Guillaume Vidon***, *Stefania Cacovich, Marie Legrand, Armelle Yaiche, Daniel Ory, Daniel Suchet, Jean-Baptiste Puel, and Jean-François Guillemoles*, Phys. Rev. Applied 16, 044058 – Published 29 October 2021 [Vidon *et al.* 2021]

(b) Mapping surface recombination velocity and bulk lifetime of lead halide perovskites via multi excitation wavelength time resolved photoluminescence imaging, ***Guillaume Vidon*** *et al.*, to be submitted.

(c) Imaging Electron, Hole, and Ion Transport in Halide Perovskite, *Adrien Bercegol, Stefania Cacovich Stefania Cacovich,* ***Guillaume Vidon****, Salim Mejaouri, Armelle Yaiche, Jean-Baptiste Puel, Christophe Longeaud, Jean-François Guillemoles, Sebastien Jutteau, Jean Rousset, Daniel Ory, and Laurent Lombez*, J. Phys. Chem. C 2020, 124, 22, 11741–11748

(d) In-Depth Chemical and Optoelectronic Analysis of Triple-Cation Perovskite Thin Films by Combining XPS Profiling and PL Imaging, *Stefania Cacovich, Pia Dally,* ***Guillaume Vidon****, Marie Legrand, Stéphanie Gbegnon, Jean Rousset, Jean-Baptiste Puel, Jean-François Guillemoles, Philip Schulz, Muriel Bouttemy, and Arnaud Etcheberry*, ACS Appl. Mater. Interfaces 2022, [Cacovich *et al.* 2022a]

(e) Imaging and quantifying non-radiative losses at 23% efficient inverted perovskite solar cells interfaces, *Stefania Cacovich,* ***Guillaume Vidon****, Matteo Degani, Marie Legrand, Laxman Gouda, Jean-Baptiste Puel, Yana Vaynzof, Jean-François Guillemoles, Daniel Ory Giulia Grancini* [Cacovich *et al.* 2022b]

(f) Thermally Controlled Growth of Photoactive $FAPbI_3$ Films for Highly Stable Perovskite Solar Cells, *Sandy Sánchez, Stefania Cacovich,* ***Guillaume Vidon****, Jean François Guillemoles, Felix Thomas Eickemeyer, Shaik Mohammed Zakeeruddin, Juergen Schawe, Jörg F. Löffler, Cyril Cayron, Pascal Schouwink and Michael Grätzel* , Energy Environ. Sci., 2022, [Sánchez *et al.* 2022]

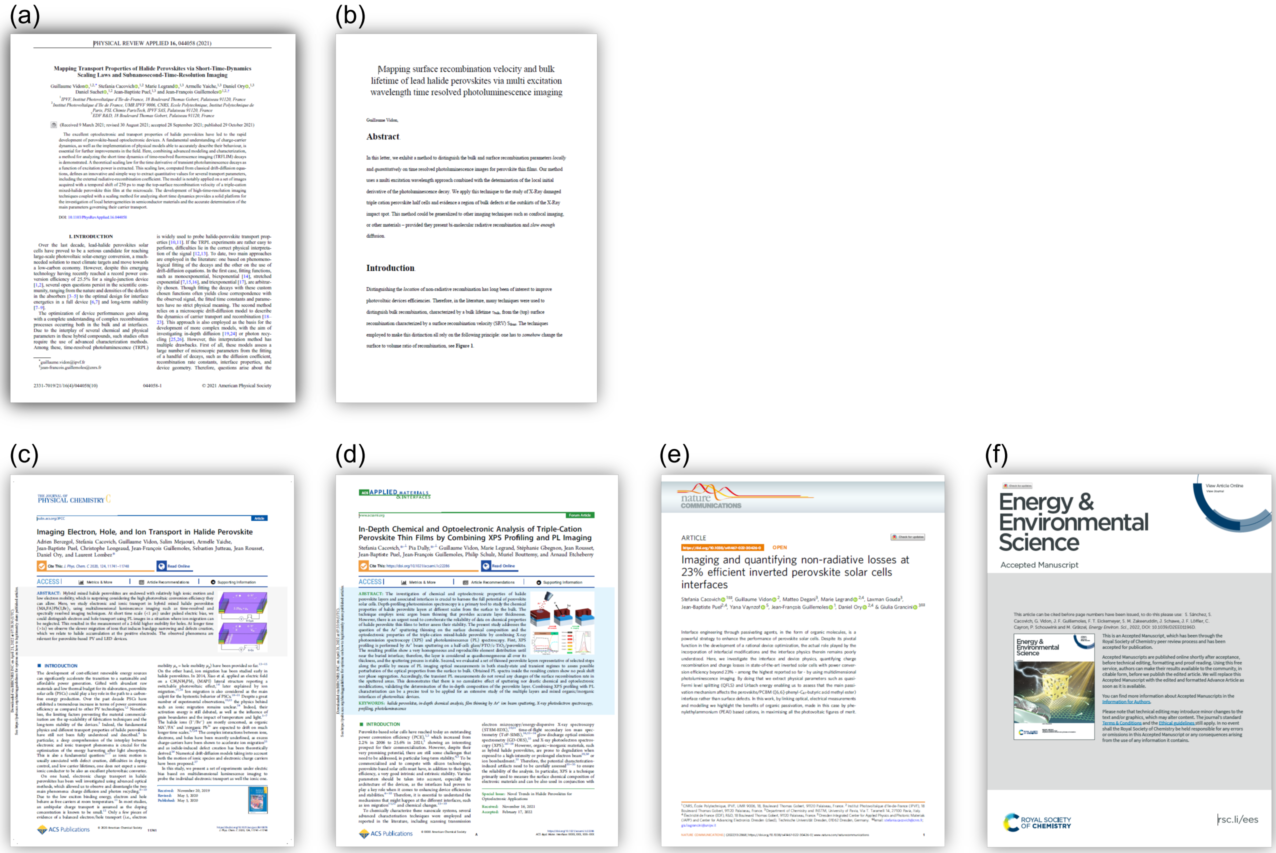

PHYSICAL REVIEW APPLIED **16,** 044058 (2021)

Mapping Transport Properties of Halide Perovskites via Short-Time-Dynamics Scaling Laws and Subnanosecond-Time-Resolution Imaging

Guillaume Vidon,[1,2,*] Stefania Cacovich,[1,2] Marie Legrand,[1,3] Armelle Yaiche,[1,3] Daniel Ory,[1,3] Daniel Suchet,[1,2] Jean-Baptiste Puel,[1,3] and Jean-François Guillemoles[1,2,†]

[1] IPVF, Institut Photovoltaïque d'Ile-de-France, 18 Boulevard Thomas Gobert, Palaiseau 91120, France
[2] Institut Photovoltaïque d'Ile de France, UMR IPVF 9006, CNRS, Ecole Polytechnique, Institut Polytechnique de Paris, PSL Chimie ParisTech, IPVF SAS, Palaiseau 91120, France
[3] EDF R&D, 18 Boulevard Thomas Gobert, Palaiseau 91120, France

(Received 9 March 2021; revised 30 August 2021; accepted 28 September 2021; published 29 October 2021)

The excellent optoelectronic and transport properties of halide perovskites have led to the rapid development of perovskite-based optoelectronic devices. A fundamental understanding of charge-carrier dynamics, as well as the implementation of physical models able to accurately describe their behaviour, is essential for further improvements in the field. Here, combining advanced modeling and characterization, a method for analyzing the short time dynamics of time-resolved fluorescence imaging (TRFLIM) decays is demonstrated. A theoretical scaling law for the time derivative of transient photoluminescence decays as a function of excitation power is extracted. This scaling law, computed from classical drift-diffusion equations, defines an innovative and simple way to extract quantitative values for several transport parameters, including the external radiative-recombination coefficient. The model is notably applied on a set of images acquired with a temporal shift of 250 ps to map the top-surface recombination velocity of a triple-cation mixed-halide perovskite thin film at the microscale. The development of high-time-resolution imaging techniques coupled with a scaling method for analyzing short time dynamics provides a solid platform for the investigation of local heterogeneities in semiconductor materials and the accurate determination of the main parameters governing their carrier transport.

DOI: 10.1103/PhysRevApplied.16.044058

I. INTRODUCTION

Over the last decade, lead-halide perovskites solar cells have proved to be a serious candidate for reaching large-scale photovoltaic solar-energy conversion, a much-needed solution to meet climate targets and move towards a low-carbon economy. However, despite this emerging technology having recently reached a record power conversion efficiency of 25.5% for a single-junction device [1,2], several open questions persist in the scientific community, ranging from the nature and densities of the defects in the absorbers [3–5] to the optimal design for interface energetics in a full device [6,7] and long-term stability [7–9].

The optimization of device performances goes along with a complete understanding of complex recombination processes occurring both in the bulk and at interfaces. Due to the interplay of several chemical and physical parameters in these hybrid compounds, such studies often require the use of advanced characterization methods. Among these, time-resolved photoluminescence (TRPL) is widely used to probe halide-perovskite transport properties [10,11]. If the TRPL experiments are rather easy to perform, difficulties lie in the correct physical interpretation of the signal [12,13]. To date, two main approaches are employed in the literature: one based on phenomenological fitting of the decays and the other on the use of drift-diffusion equations. In the first case, fitting functions, such as monoexponential, biexponential [14], stretched exponential [7,15,16], and triexponential [17], are arbitrarily chosen. Though fitting the decays with these custom chosen functions often yields close correspondence with the observed signal, the fitted time constants and parameters have no strict physical meaning. The second method relies on a microscopic drift-diffusion model to describe the dynamics of carrier transport and recombination [18–23]. This approach is also employed as the basis for the development of more complex models, with the aim of investigating in-depth diffusion [19,24] or photon recycling [25,26]. However, this interpretation method has multiple drawbacks. First of all, these models assess a large number of microscopic parameters from the fitting of a handful of decays, such as the diffusion coefficient, recombination rate constants, interface properties, and device geometry. Therefore, questions arise about the

---

[*] guillaume.vidon@ipvf.fr
[†] jean-francois.guillemoles@cnrs.fr

2331-7019/21/16(4)/044058(10) 044058-1 © 2021 American Physical Society

---

Mapping surface recombination velocity and bulk lifetime of lead halide perovskites via multi excitation wavelength time resolved photoluminescence imaging

Guillaume Vidon,

Abstract

In this letter, we exhibit a method to distinguish the bulk and surface recombination parameters *locally* and *quantitatively* on time resolved photoluminescence images for perovskite thin films. Our method uses a multi excitation wavelength approach combined with the determination of the local initial derivative of the photoluminescence decay. We apply this technique to the study of X-Ray damaged triple cation perovskite half cells and evidence a region of bulk defects at the outskirts of the X-Ray impact spot. This method could be generalized to other imaging techniques such as confocal imaging, or other materials – provided they present bi-molecular radiative recombination and *slow enough* diffusion.

Introduction

Distinguishing the *location* of non-radiative recombination has long been of interest to improve photovoltaic devices efficiencies. Therefore, in the literature, many techniques were used to distinguish bulk recombination, characterized by a bulk lifetime τ_{bulk}, from the (top) surface recombination characterized by a surface recombination velocity (SRV) S_{front}. The techniques employed to make this distinction all rely on the following principle: one has to *somehow* change the surface to volume ratio of recombination, see **Figure 1**.

THE JOURNAL OF PHYSICAL CHEMISTRY C

pubs.acs.org/JPCC Article

Imaging Electron, Hole, and Ion Transport in Halide Perovskite

Adrien Bercegol, Stefania Cacovich, Guillaume Vidon, Salim Mejaouri, Armelle Yaiche, Jean-Baptiste Puel, Christophe Longeaud, Jean-François Guillemoles, Sebastien Jutteau, Jean Rousset, Daniel Ory, and Laurent Lombez*

Cite This: *J. Phys. Chem. C* 2020, 124, 11741−11748 Read Online

ACCESS | Metrics & More | Article Recommendations | Supporting Information

ABSTRACT: Hybrid mixed halide perovskites are endowed with relatively high ionic motion and low electron mobility, which is surprising considering the high photovoltaic conversion efficiency they can allow. Here, we study electronic and ionic transport in hybrid mixed halide perovskites $(MA,FA)Pb(I,Br)_3$ using multidimensional luminescence imaging such as time-resolved and spectrally resolved imaging techniques. At short time scale (<1 μs) under pulsed electric bias, we could distinguish electron and hole transport using PL images in a situation where ion migration can be neglected. This resulted in the measurement of a 2-fold higher mobility for holes. At longer time (>1s) we observe the slower migration of ions that induces bandgap narrowing and defects creation, which we relate to halide accumulation at the positive electrode. The observed phenomena are relevant for perovskite-based PV and LED devices.

INTRODUCTION

The development of cost-efficient renewable energy sources can significantly accelerate the transition to a sustainable and affordable power generation. Gifted with abundant raw materials and low thermal budget for its elaboration, perovskite solar cells (PSCs) could play a key role in the path to a carbon-free energy production. Over the past decade PSCs have exhibited a tremendous increase in terms of power conversion efficiency as compared to other PV technologies.[1,2] Nonetheless, the limiting factors preventing the material commercialization are the up-scalability of fabrication techniques and the long-term stability of the devices.[3] Indeed, the fundamental physics and different transport properties of halide perovskites have still not been fully understood and described.[4] In particular, a deep comprehension of the interplay between electronic and ionic transport phenomena is crucial for the optimization of the energy harvesting after light absorption. This is also a fundamental question:[5−7] as ionic motion is usually associated with defect creation, difficulties in doping control, and low carrier lifetimes, one does not expect a semi-ionic conductor to be also an excellent photovoltaic converter.

On one hand, electronic charge transport in halide perovskites has been well investigated using advanced optical methods, which allowed us to observe and disentangle the two main phenomena: charge diffusion and photon recycling.[8−10] Due to the low exciton binding energy, electron and hole behave as free carriers at room temperature.[11] In most studies, an ambipolar charge transport is assumed as the doping concentration is known to be small.[12] Only a few pieces of evidence of a balanced electron/hole transport (i.e., electron mobility μ_n = hole mobility μ_p) have been provided so far.[13−15] On the other hand, ion migration has been studied early in halide perovskites. In 2014, Xiao et al. applied an electric field on a $CH_3NH_3PbI_3$ (MAPI) lateral structure reporting a switchable photovoltaic effect,[16] later explained by ion migration.[17,18] Ion migration is also considered as the main culprit for the hysteretic behavior of PSCs.[18−21] Despite a great number of experimental observations,[22,23] the physics behind such an ionic migration remains unclear.[24] Indeed, their activation energy is still debated, as well as the influence of grain boundaries and the impact of temperature and light.[5−7] The halide ions (I^-/Br^-) are mostly concerned, as organic MA^+/FA^+ and inorganic Pb^{2+} are expected to drift on much longer time scales.[5,7,24] The complex interactions between ions, electrons, and holes have been recently underlined, as excess charge-carriers have been shown to accelerate ion migration[25] and as iodide-induced defect creation has been theoretically derived.[26] Numerical drift-diffusion models taking into account both the motion of ionic species and electronic charge carriers have been proposed.[27]

In this study, we present a set of experiments under electric bias based on multidimensional luminescence imaging to probe the individual electronic transport as well the ionic one.

Received: November 20, 2019
Revised: May 5, 2020
Published: May 5, 2020

ACS Publications © 2020 American Chemical Society 11741 https://dx.doi.org/10.1021/acs.jpcc.9b10876 J. Phys. Chem. C 2020, 124, 11741−11748

ACS APPLIED MATERIALS & INTERFACES

www.acsami.org Forum Article

In-Depth Chemical and Optoelectronic Analysis of Triple-Cation Perovskite Thin Films by Combining XPS Profiling and PL Imaging

Stefania Cacovich,[*,⊥] Pia Dally,[*,⊥] Guillaume Vidon, Marie Legrand, Stéphanie Gbegnon, Jean Rousset, Jean-Baptiste Puel, Jean-François Guillemoles, Philip Schulz, Muriel Bouttemy, and Arnaud Etcheberry

Cite This: https://doi.org/10.1021/acsami.1c22286 Read Online

ACCESS | Metrics & More | Article Recommendations | Supporting Information

ABSTRACT: The investigation of chemical and optoelectronic properties of halide perovskite layers and associated interfaces is crucial to harness the full potential of perovskite solar cells. Depth-profiling photoemission spectroscopy is a primary tool to study the chemical properties of halide perovskite layers at different scales from the surface to the bulk. The technique employs ionic argon beam thinning that provides accurate layer thicknesses. However, there is an urgent need to corroborate the reliability of data on chemical properties of halide perovskite thin films to better assess their stability. The present study addresses the question of the Ar^+ sputtering thinning on the surface chemical composition and the optoelectronic properties of the triple-cation mixed-halide perovskite by combining X-ray photoemission spectroscopy (XPS) and photoluminescence (PL) spectroscopy. First, XPS profiling is performed by Ar^+ beam sputtering on a half-cell: glass/FTO/c-TiO_2/perovskite. The resulting profiles show a very homogeneous and reproducible element distribution until near the buried interface; therefore, the layer is considered as quasihomogeneous all over its thickness, and the sputtering process is stable. Second, we evaluated a set of thinned perovskite layers representative of selected steps along the profile by means of PL imaging optical measurements in both steady-state and transient regimes to assess possible perturbation of the optical properties from the surface to bulk. Obtained PL spectra inside the resulting craters show no peak shift nor phase segregation. Accordingly, the transient PL measurements do not reveal any changes of the surface recombination rate in the sputtered areas. This demonstrates that there is no cumulative effect of sputtering nor drastic chemical and optoelectronic modifications, validating the determination of the in-depth composition of the perovskite layer. Combining XPS profiling with PL characterization can be a precise tool to be applied for an extensive study of the multiple layers and mixed organic/inorganic interfaces of photovoltaic devices.

KEYWORDS: *halide perovskites, in-depth chemical analysis, film thinning by Ar^+ ion beam sputtering, X-ray photoelectron spectroscopy, profiling, photoluminescence*

INTRODUCTION

Perovskite-based solar cells have reached today an outstanding power conversion efficiency (PCE),[1,2] which increased from 2.2% in 2006 to 25.6% in 2021,[3] showing an interesting prospect for their commercialization. However, despite their very promising potential, there are still some challenges that need to be addressed, in particular long-term stability.[4,5] To be commercialized and to compete with silicon technologies, perovskite-based solar cells must have, in addition to their high efficiency, a very good intrinsic and extrinsic stability. Various parameters should be taken into account, especially the architecture of the devices, as the interfaces had proven to play a key role when it comes to enhancing device efficiencies and stabilities.[6−10] Therefore, it is essential to understand the mechanisms that might happen at the different interfaces, such as ion migration[11,12] and chemical changes.[13−19]

To chemically characterize these nanoscale systems, several advanced characterization techniques were employed and reported in the literature, including scanning transmission electron microscopy/energy-dispersive X-ray spectroscopy (STEM-EDX),[20,21] time-of-flight secondary ion mass spectrometry (ToF-SIMS),[16,22−24] glow discharge optical emission spectrometry (GD-OES),[25] and X-ray photoelectron spectroscopy (XPS).[26−28] However, organic−inorganic materials, such as hybrid halide perovskites, are prone to degradation when exposed to a high-intensity or prolonged electron beam[29,30] or ion bombardment.[31] Therefore, the potential characterization-induced artifacts need to be carefully assessed[32−35] to ensure the reliability of the analysis. In particular, XPS is a technique primarily used to measure the surface chemical composition of electronic materials and can be also used in conjunction with

Special Issue: Novel Trends in Halide Perovskites for Optoelectronic Applications

Received: November 16, 2021
Accepted: February 17, 2022

ACS Publications © XXXX American Chemical Society A https://doi.org/10.1021/acsami.1c22286 ACS Appl. Mater. Interfaces XXXX, XXX, XXX−XXX

---

nature COMMUNICATIONS

ARTICLE

https://doi.org/10.1038/s41467-022-30426-0 OPEN

Check for updates

Imaging and quantifying non-radiative losses at 23% efficient inverted perovskite solar cells interfaces

Stefania Cacovich[1✉], Guillaume Vidon[2], Matteo Degani[3], Marie Legrand[2,4], Laxman Gouda[3], Jean-Baptiste Puel[2,4], Yana Vaynzof[5], Jean-François Guillemoles[1], Daniel Ory[2,4] & Giulia Grancini[3✉]

Interface engineering through passivating agents, in the form of organic molecules, is a powerful strategy to enhance the performance of perovskite solar cells. Despite its pivotal function in the development of a rational device optimization, the actual role played by the incorporation of interfacial modifications and the interface physics therein remains poorly understood. Here, we investigate the interface and device physics, quantifying charge recombination and charge losses in state-of-the-art inverted solar cells with power conversion efficiency beyond 23% - among the highest reported so far - by using multidimensional photoluminescence imaging. By doing that we extract physical parameters such as quasi-Fermi level splitting (QFLS) and Urbach energy enabling us to assess that the main passivation mechanism affects the perovskite/PCBM ([6,6]-phenyl-C_{61}-butyric acid methyl ester) interface rather than surface defects. In this work, by linking optical, electrical measurements and modelling we highlight the benefits of organic passivation, made in this case by phenylethylammonium (PEAI) based cations, in maximising all the photovoltaic figures of merit.

[1] CNRS, École Polytechnique, IPVF, UMR 9006, 18, Boulevard Thomas Gobert, 91120 Palaiseau, France. [2] Institut Photovoltaïque d'Ile-de-France (IPVF), 18 Boulevard Thomas Gobert, 91120 Palaiseau, France. [3] Department of Chemistry and INSTM, University of Pavia, Via T. Taramelli 14, 27100 Pavia, Italy. [4] Électricité de France (EDF), R&D, 18 Boulevard Thomas Gobert, 91120 Palaiseau, France. [5] Dresden Integrated Center for Applied Physics and Photonic Materials (IAPP) and Center for Advancing Electronics Dresden (cfaed), Technische Universität Dresden, 01062 Dresden, Germany. ✉email: stefania.cacovich@cnrs.fr; giulia.grancini@unipv.it

NATURE COMMUNICATIONS | (2022)13:2868 | https://doi.org/10.1038/s41467-022-30426-0 | www.nature.com/naturecommunications 1

Check for updates

View Article Online
View Journal

Energy & Environmental Science

Accepted Manuscript

This article can be cited before page numbers have been issued, to do this please use: S. Sánchez, S. Cacovich, G. Vidon, J. F. Guillemoles, F. T. Eickemeyer, S. M. Zakeeruddin, J. Schawe, J. F. Löffler, C. Cayron, P. Schouwink and M. Grätzel, *Energy Environ. Sci.*, 2022, DOI: 10.1039/D2EE01196D.

This is an Accepted Manuscript, which has been through the Royal Society of Chemistry peer review process and has been accepted for publication.

Accepted Manuscripts are published online shortly after acceptance, before technical editing, formatting and proof reading. Using this free service, authors can make their results available to the community, in citable form, before we publish the edited article. We will replace this Accepted Manuscript with the edited and formatted Advance Article as soon as it is available.

You can find more information about Accepted Manuscripts in the Information for Authors.

Please note that technical editing may introduce minor changes to the text and/or graphics, which may alter content. The journal's standard Terms & Conditions and the Ethical guidelines still apply. In no event shall the Royal Society of Chemistry be held responsible for any errors or omissions in this Accepted Manuscript or any consequences arising from the use of any information it contains.

ROYAL SOCIETY OF CHEMISTRY

rsc.li/ees

Figure A.1: *Front pages of the publications which I co-authored. (a) and (b) are first author papers. (b) is not published to this date and submission is pending.*

A.2 Conferences

I particpitated in international and national conferences as a speaking first author:

1. JNPV, January 2021. (online, live): *Understanding the short-time dynamics of transient photoluminescence experiments*
2. SPIE 2021 Photonics West, March 2021. (online, pre-recorded) *Disentangling processes in transient photoluminescence experiments (TR-PL and TR-FLIM) on lead halide perovskite absorbers thanks to novel analysis of short time dynamics*
3. IEEE PVSC, 2021, (online,pre-recorded) *Analysis of short time dynamics of time resolved photoluminescence applied on perovskite absorbers*
4. JNPV 2022, (onsite, live). **Invited speaker.** *A scaling law for the time derivative of TR-PL allows for a quantitative assessment of radiative and non-radiative recombination parameters of perovskite materials*
5. SPIE Photonics Europe 2022, (onsite, live). **Invited speaker.** *A scaling law for the time derivative of TR-PL/TR-FLIM allows for a quantitative assessment of radiative and non-radiative recombination parameters of perovskite materials.*

I was also co-author of the following contributions:

1. IEEE PVSC 2020, *Imaging Electrons, Holes and Ions Transport in Halide Perovskite*, S Cacovich et al.
2. SPIE Photonics Europe 2022, *Opto-electronic properties of inverted perovskites solar cells with organic cations interfacial passivation*, D Ory et al.
3. SPIE Photonics Europe 2022, *Mapping absorption coefficient of photovoltaic absorbers through photoluminescence imaging*, M Legrand et al.

Miscellaneous:

1. Presentation to a general audience: Fête de la science, October 2020. *Comprendre les matériaux photovoltaïques grace à la lumière qu'ils émettent*
2. Participation in the group that published online "Le solaire photovoltaïque en France : réalité, potentiel et défis". `https://solairepv.fr/`
3. Class given to M1 students at École polytechnique, September 2021, "PHY530: Refresher Course in Physics"
4. Organization and participation of a Würfel Klub at IPVF: a club to discuss theory with PhD Students and anyone willing!

Appendix B

Résumé en français

B.1 Résumé

Les pérovskites forment une famille de matériaux de structure ABX_3 dont les propriétés optiques sont reconnues et utilisés depuis plusieurs décennies. Récemment, elles ont suscité un intérêt pour leur application en tant que couche absorbante de lumière pour le photovoltaïque. Les matériaux à base de pérovskite sont l'objet d'intenses études car ils sont à la fois très faciles à déposer (et à industrialiser) et très performants pour la conversion de la lumière solaire en électricité, avec un record d'efficacité de conversion à 25.7%. Les propriétés radiatives des pérovskites sont excellentes mais la nature et la densité des défauts qu'elles contiennent sont encore sujets à débat, tout comme leurs propriétés de transport. La composition des films les plus performants est un mélange où les sites A, B et X sont occupés par différents atomes ou molécules dans différentes stœchiométries. À l'IPVF (Institut Photovoltaïque d'Ile de France), la composition nominale est A= 5%Cs, 16%MA, 79%FA ; B = Pb ; X = 83%I, 17%Br. Ainsi au sein d'un unique échantillon peut-on s'attendre à observer des inhomogénéités de transport, de recombinaison voire de composition.

Le but de cette thèse est de caractériser et d'imager les inhomogénéités de transport et de recombinaison des pérovskites à l'échelle de la centaine de microns. Pour ce faire, une technique d'imagerie de photoluminescence résolue en temps est utilisée. Cette thèse propose et applique une série de nouvelles méthodes pour l'analyse des déclins de photoluminescence applicables à l'imagerie. Ce travail a nécessité le développement de techniques expérimentales dédiées (super résolution temporelle, calibration absolue), d'outils d'analyse numérique (déconvolution) ainsi que de modèles physiques adaptés aux contraintes imposées par le volume des données à traiter.

Ces méthodes sont présentées dans la première partie de ce manuscrit. Dans une seconde partie, cette thèse aborde l'étude phénoménologique des déclins. Bien qu'applicable facilement aux images, il est notamment montré que les approches phénoménologiques ne suffisent pas toujours à attribuer les inhomogénéités de temps de vie observées à des différences locales de recombinaisons non radiatives. Dans un troisième temps, cette thèse discute l'imagerie des recombinaisons non radiatives. Une méthode liée à la pente initiale des déclins de luminescence en fonction de la fluence du laser d'excitation est proposée. Elle aboutit à la mesure d'une cartographie de recombinaisons non radiative ainsi qu'à l'estimation du coefficient de recombinaisons radiatives. Par ailleurs cette méthode pousse à s'intéresser à la loi d'échelle reliant l'intensité de photoluminescence au début du déclin en fonction de la fluence du laser. Un modèle est proposé et permet d'imager le niveau de dopage effectif dans les couches de pérovskite. Des inhomogénéités de dopage sont mises en évidences dans des échantillons de $(CH(CH_2)_2)PbI_3$. Dans un quatrième temps, la question de la localisation en profondeur des défauts est abordée. Pour y répondre, deux méthodes sont proposées : l'une basée sur la pente initiale des déclins en fonction de la longueur d'onde du laser d'excitation, et l'autre sur la comparaison entre temps courts et temps long. Les deux méthodes sont appliquées sur une série d'échantillons de pérovskite à base de plomb sur dioxyde de titane ayant subi une exposition prolongée aux rayons X. Les méthodes concordent à prouver que les défauts créés par les rayons X sont situés en profondeur dans le matériau plutôt qu'en surface. Enfin, l'impact des couches d'extraction sur l'imagerie de déclins de photoluminescence est abordé. Une méthode d'analyse des échantillons couche par couche conduit à de premiers résultats prometteurs mais ceux-ci restent à consolider. L'impact des ions mobiles est aussi mis en évidence comme ouverture des travaux présentés.

B.2 Deux exemples de resultats

Un des sujets de recherche de l'institut a été d'obtenir des cartographies de temps de vie telles que montrées en Figure B.1 (a). Le matériau étudié est ici une pérovskite $FAPbI_3$ issue d'une collaboration avec l'EPFL qui développe un procédé innovant de fabrication des pérovskites. Le matériau présente de fortes inhomogénéités de temps de vie comme le montre la carte. On observe des domaines séparés par des frontières. L'image a pu être obtenue avec une très grande qualité grâce au développement de nouvelles techniques expérimentales. Cette cartographie de temps de vie ne peut pourtant pas directement être interprétée en termes de densité locale de défauts. En effet, l'épaisseur du matériau n'est pas constante sur cette cartographie comme en témoigne la Figure B.1 (b) obtenue par microscopie optique. Le changement d'épaisseur locale a pour effet de changer le rapport surface sur volume ce qui, toutes choses égales par ailleurs, a pour effet de changer le temps de vie. Des modèles quantitatifs sont alors nécessaires pour discuter l'impact de ces artefacts sur les mesures et remonter aux densités de défauts, ils ont été développés à l'IPVF à l'occasion de ces travaux. Ils permettent une analyse plus fine qui suggère que les zones frontières sont bien également des zones où les défauts sont plus importants.

Un autre sujet de recherche du laboratoire est de corréler les mesures résolues en temps (comme la cartographie de temps de vie) aux conditions réelles d'utilisation des cellules solaires où la lumière est continue dans le temps (au moins à l'échelle de la seconde). Pour ce faire une étude a été menée sur des pérovskites fabriquée à l'IPVF qui ont été irradiées par des rayons X à des fins d'analyses.

Une cartographie de temps de vie est obtenue, montrée en Figure B.2 (a). Une zone de faible temps de vie correspondant au point d'impact du faisceau de rayons X est observée (en bleu foncé sur l'image). Afin d'obtenir un point de comparaison, l'expérience de photoluminescence en continu est réalisée au même endroit. Une cartographie de séparation des quasi niveaux de Fermi est obtenue (c'est-à-dire en termes plus simples, une bonne approximation de la tension de circuit ouvert générée localement dans le matériau). Celle-ci est présentée en Figure B.2 (b).

L'analyse d'images nous permet de tracer en Figure B.2 (c) la corrélation locale entre ces deux quantités physiques en échelle bleu à jaune. Une variation croissante est observée. En rouge, letrait plein présente un modèle simple qui devrait permettre de relier les deux quantités. Il est observé que ce modèle simple rend compte des variations observées sur les deux cartographies. Cela est très remarquable compte tenu des différences majeures entre les deux expériences et semble confirmer que les modèles de semiconducteurs usuels s'appliquent tout à fait aux matériaux pérovskites – ce qui est encore débattu dans la littérature.

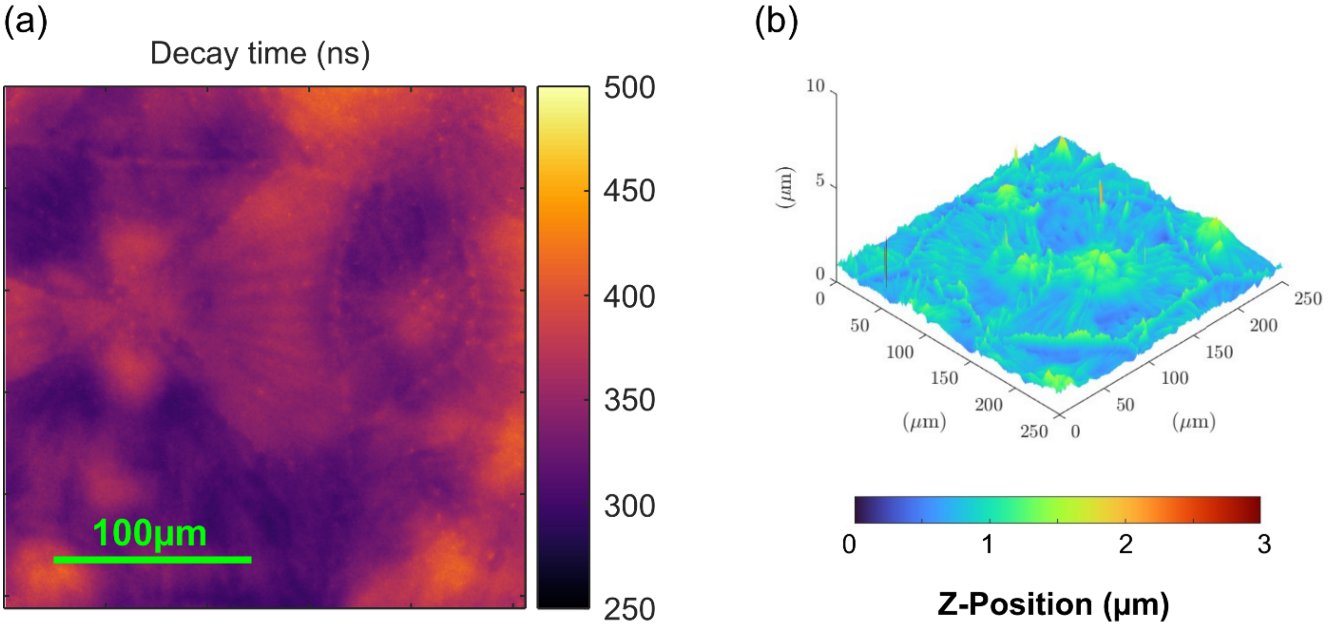

Figure B.1: *(a) Carte de temps de vie obtenue par l'expérience résolue en temps. (b) Carte d'épaisseur de la couche observée (à un autre endroit). On voit que les zones de variations de temps de vie interviennent dans des zones où l'épaisseur des films n'est pas constante ce qui empêche d'attribuer directement les changements de temps de vie à des changement de densité de défauts. Des modèles permettent cependant de discuter l'impact des deux effets.*

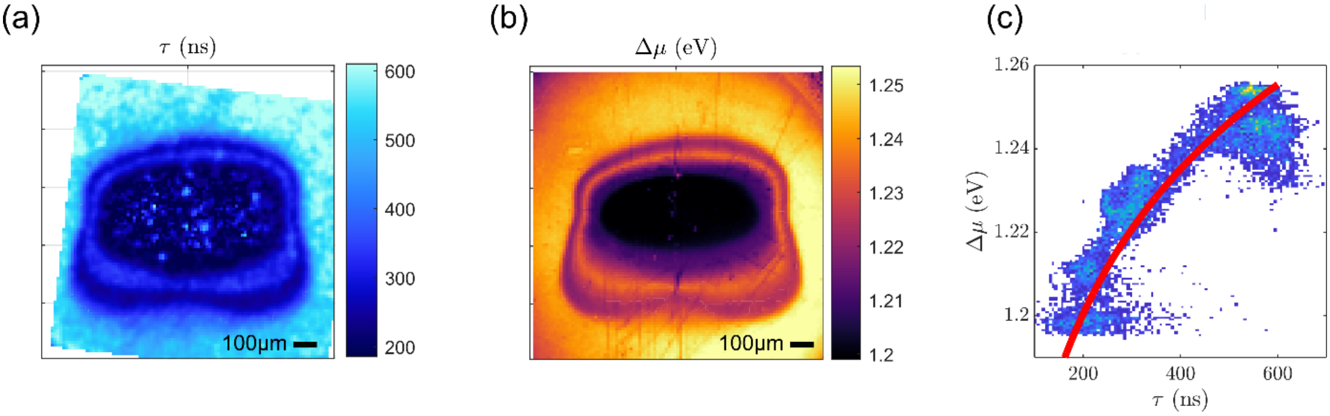

Figure B.2: *(a) Carte de temps de vie obtenue par l'expérience résolue en temps. (b) Carte de séparation des quasi niveaux de Fermi obtenue par l'expérience continue pour le même échantillon au même endroit. (c) Corrélation pixel à pixel des deux cartes (a) et (b). On observe en rouge le fit d'un modèle simple qui permet de rendre compte des variations locales de ces deux quantités.*

Appendix C

Sample preparation

C.1 Samples from IPVF

Fluorine-doped tin oxide (FTO) covered glass substrates (Solems) were cleaned by etching with Zn powder and HCl (4M). The substrates were sonicated for 1 hour in an RBS detergent solution (2 vol %), rinsed with deionized water and ethanol, ultrasonicated in ethanol and dried. A TiO_2 electron blocking layer was prepared by Atomic layer deposition. The substrates were UV–ozone cleaned for 20 min and transferred into a nitrogen-filled glovebox for the perovskite film deposition. A double cation perovskite solution, $(MA_{0.14}FA_{0.86})Pb(I_{0.84}\ Br_{0.16})_3$ was prepared by dissolving 1.10 M PbI_2 (TCI Chemicals), 0.20 M $PbBr_2$ (Alfa Aesar), 1.00 M formamidinium iodide (FAI, Dyesol) and 0.20 M methylammonium bromide (MABr, Dyesol) in a mixture of DMSO:DMF (4:1 in v/v) as solvent. In order to obtain the triple cations perovskite, i.e. $Cs_x(MA_{0.14}FA_{0.86})_{1-x}Pb(I_{0.84}Br_{0.16})_3$, the required quantity of Cs^+ was additionally injected from a precursor solution of CsI (Sigma Aldrich) 1.50 M in DMSO solvent. The solution, after 2 hours of stirring in a magnetic mixer, was spin-coated onto the TiO_2 layer by following a double plateau. First, 35µL of the perovskite solution were spincoated at the rotation of 2000 rpm for 10 seconds at an acceleration of 1000 rpm/sec. Then, 100 µL of chlorobenzene were spin-coated at the speed of 6000 rpm for 30 seconds. After deposition, the perovskite films were submitted to an annealing treatment at the temperature of 100 °C for 30 min in a nitrogen glovebox. The thickness of the perovskite thin films is approximately 400 nm.

C.2 Samples from Pavia and Dresden University

Unless otherwise stated, all materials were purchased from Sigma-Aldrich or Alfa Aesar and used as received. Perovskite films and devices were fabricated using PbI_2 and $PbBr_2$ (99.99% purity) purchased from TCI, organic halide salts purchased from GreatCell Solar and Cesium Iodide (99.99% purity) purchased from Alfa Aesar. The poly(triaryl amine) (PTAA) was purchased from Sigma-Aldrich. The $PC_{61}BM$ was purchase from Solenne. The bathocuproine (BCP; sublimed grade, 99.99% purity). All the anhydrous solvents were purchased from Acros Organics.

C.2.1 Perovskite film preparation and device fabrication

Pre-patterned ITO/glass substrates were sequentially cleaned with acetone and isopropanol by ultrasonication for 15 minutes. The ITO/glass substrates were then dried with N_{24} and treated with oxygen plasma at 100 mW for 10 min. The HTL and the perovskite films were fabricated in a drybox (relative humidity < 2 %), while the ETL and the contacts were deposited inside a glovebox filled with inert atmosphere N2. For reference devices, a hole transport layer of 10 nm thickness made of PTAA with a concentration of 1.5 $\mathrm{mg.ml^{-1}}$ dissolved in toluene was spin-coated at a speed of 2000 rpm for 40 s and then annealed at 100 °C for 10 min. After the annealing step, the samples were washed by DMF by spin-coating it on the prepared PTAA films at 4000 rpm for 30 s. The perovskite precursor solution (1.2 M) composed of mixed cations (Pb, Cs, FA and MA) and halides (I and Br) was dissolved in mixed solvent (DMF/DMSO=4/1) according to a formula of $Cs_{0.05}(FA_{5/6}MA_{1/6})_{0.95}Pb(I_{0.9}Br_{0.1})_3$ with an excess of PbI_2 of 1%. The piperidinium salt $[BMP]^+[BF_4]^-$ was dissolve in the perovskite solution obtained with the molar ratio 0.25 mol %. The perovskite is deposited via a two-step spin-coating procedure with 1000 r.p.m. for 12 s and 5,000 r.p.m. for 27 s was adopted for the preparation of perovskite films. A mixture of antisolvents (CB/IPA=9/1, 150 l) was dripped on the spinning substrate during the 21 s of the second spin-coating step. Subsequently, the sample was annealed at 100 °C for 30 min. The electron transport layers were dynamically deposited from a $PC_{61}BM$ solution (20 mg/mL in CB) and spin-coated onto the perovskite layer at the speed of 2000 rpm for 30 s (with a ramping speed of 1000 rpm/s) and annealed for 10 minutes at 100°C. Next, thin layers of BCP

(0.5 mg/mL in IPA) were spin-coated at 4000 rpm for 30 s (with a ramping rate of 1000 rpm/s) as hole blocking layers. The devices with an area of 4.5 mm^2 were completed by thermally evaporating of Ag (80nm). The devices with modified interfaces were prepared by dissolving a small amount of the A-cations in DMF (20mM) used for washing the PTAA and in the mixture CB/IPA (0.5mM) used in the antisolvent step.

C.3 Samples from EPFL

C.3.1 Substrate preparation

Photovoltaic devices were fabricated on FTO coated glass (Pilkington NSG TEC™). The substrates were cleaned with Hellmanex soap, followed by 30min sonication in a Hellmanex 2% water solution, 15min sonication in IPA, and 5min of oxygen plasma etching. Then, 30nm thick TiO2 compact layers were deposited onto the FTO by spray pyrolysis at 450°C from a precursor solution of titanium diisopropoxide bis (acetylacetonate) in anhydrous ethanol and acetylacetone. After spraying, the FTO substrates were left at 450°C for 5min before cooling to room temperature. A mesoporous TiO_2 layer was deposited by spin-coating for 10s at 4000rpm with a ramp of 2000rpms1, using a 30-nm particle size TiO_2 paste (Dyesol 30 NR-D) diluted in ethanol to 75mg/ml, to produce 150–200nm thick mesoporous layers. After spin-coating, the FTO substrates were dried at 100°C for 10min, and the films were annealed on a programmable hotplate (2000W, Harry Gestigkeit GmbH) to crystallize TiO_2 at 450°C for 30min under dry air flow. The mixed A-cation hybrid perovskite precursor solution was deposited from a precursor solution containing FAI (1.2M), PbI_2 (1.4M), and CsI (0.21M) in anhydrous DMF:DMSO (from Merck) 3:1 (v:v). All the organic salts were acquired from Greatcell Solar, while TCI provided the lead halides and Merck the DMSO and DMF solvents

C.3.2 Perovskite solution preparation

The hybrid perovskite precursor solutions were deposited from a precursor solution containing FAI, and PbI_2 (1.5 M), in anhydrous DMF/DMSO 3:1 (v/v).

C.3.3 FIRA method for perovskite thin-film sintering

The films made by the FIRA method include the spin-coating of the perovskite solution in a single step at 4000 rpm for

10 s. The substrates were then IR irradiated with a 640ms pulse in the FIRA oven, pulling them out immediately after the heating. The films were then placed onto a hotplate at 100°C for 15 min to complete solvent removal. FIRA processing was carried out in a glovebox filled with N_2 atmosphere. The FIRA engineering setup is reported elsewhere. [Sánchez *et al.* 2020a]

Appendix D

Dynamic SRH recombination

This annex presents results obtained with the dynamic SRH model.

1.1.1 SRH Recombination

1.1.1.1 Mathematical description

Let us describe the case of SRH recombination only. Therefore, no space dimension is considered. We consider that a defect level exists within the gap at energy $E_V < E_t < E_C$. This defect may be:

- Negatively charged when occupied by an electron (ie neutral for hole)
- Neutral when occupied by an electron (ie positive for hole)

If we don't consider space, there can be no electric field, therefore the charge of the defect is somewhat irrelevant to the dynamics.

We define n_e and n_h as the electron density in the CB and the hole density in the VB. For the traps, $n_{et} = f_e N_t$ will describe the density of electrons in the traps, $f_e \in [0,1]$ being the occupation factor for electrons in the traps (time dependent) and N_t the density of traps (time independent).

The probability (rate) for an electron in the conduction band to fall into the trap will be proportional to the number of available states for electrons in the traps, ie to $N_t(1-f_e)$. We write:

$$\Gamma_{CB\to t} \propto R_{CB\to t} \times N_t(1-f_e)$$

For electrons in the traps, getting promoted to the CB is difficult. It will still be proportional to the number of available states in the CB. This could be written $N_C \times (1-f_{e,CB})$ (effective density of states in the CB). However we expect that the Fermi Dirac coefficient: $f_{e,CB} = \frac{1}{e^{\frac{E_C-\mu_e}{kT}}+1} \approx e^{\frac{\mu_e - E_c}{kT}} \ll 1$, unless we're in the case of a strongly doped semiconductor. Therefore, there are a lot of available states in the CB, and we can make the first, rough, approximation $\left(1-f_{e,CB}\right) \approx 1$.

$$\Gamma_{t\to CB} \propto R_{t\to CB} \times N_c$$

The law of detailed balance states that for the equilibrium distribution of carriers n_e^{EQ} and f_e^{EQ}, one must have:

$$\Gamma_{CB\to t} n_e^{EQ} = \Gamma_{t\to CB} N_t f_e^{EQ}$$

To go further we use the knowledge of this equilibrium distribution. In the framework of grand canonical ensemble for Fermions, at thermodynamic equilibrium with a reservoir of chemical potential μ and temperature T, one expects that each energy level at energy E will be populated according to Fermi-Dirac statistics, meaning:

$$n_e^{EQ} = N_c \times \frac{1}{e^{\frac{E_c-\mu}{kT}}+1}$$

And:

$$f_e^{EQ} = \frac{1}{e^{\frac{E_t-\mu}{kT}}+1}$$

If we then use the condition of detailed balance together with these formulae, one obtains:

$$N_c \times \frac{1}{e^{\frac{E_c-\mu}{kT}}+1} \times R_{CB\to t} \times N_t \left(1 - \frac{1}{e^{\frac{E_t-\mu}{kT}}+1}\right) = R_{t\to CB} \times N_c \times N_t \times \frac{1}{e^{\frac{E_t-\mu}{kT}}+1}$$

Ie:

$$\frac{R_{t\to CB}}{R_{CB\to t}} = \frac{e^{\frac{E_t-\mu}{kT}}}{e^{\frac{E_c-\mu}{kT}}+1} \approx e^{-\frac{E_c-E_t}{kT}}$$

This states that the electrons going from the trap to the conduction band obey the Arrhenius law, with a barrier of height $E_c - E_t$. This is in the case of "low doping" or in the limit $E_c - \mu \gg kT$. Now the dimension of $R_{CB\to t}$ is in

cm^3s^{-1} and is usually interpreted as the product of a capture cross section for the electrons σ_e and a velocity v_{th} corresponding to the thermal velocity of the electrons, much higher than any other induced velocities (diffusion or drift). Therefore, one can now write the SRH model of capture of electrons from a trap:

$$\Gamma_{CB\to t} \propto \sigma_e v_{th} \times N_t(1-f_e)$$

$$\Gamma_{t\to CB} \propto \sigma_e v_{th}\, e^{-\frac{E_c-E_t}{kT}} \times N_c$$

Therefore, the number of charges per unit time choosing to immigrate from one level to the next can be obtained by multiplying the densities by the densities:

$$j_{CB\to t} = \sigma_e v_{th} \times N_t(1-f_e) \times n_e$$

$$j_{t\to CB} = \sigma_e v_{th}\, e^{-\frac{E_c-E_t}{kT}} \times N_c \times N_t f_e$$

When reaching equilibrium, one needs that these two fluxes compensate. In the limit of $E_c - \mu \gg kT$:

$$j_{CB\to t} = \sigma_e v_{th}^{CB} \times N_t \left(\frac{e^{\frac{E_t-\mu}{kT}}}{e^{\frac{E_t-\mu}{kT}}+1} \right) \times N_c e^{-\frac{E_c-\mu}{kT}}$$

$$j_{t\to CB} = \sigma_e v_{th}^{CB}\, e^{-\frac{E_c-E_t}{kT}} \times N_c \times N_t \frac{1}{e^{\frac{E_t-\mu}{kT}}+1}$$

Which are equal upon inserting $+\mu-\mu$ in the first exponential of line 2.

Now, one has to consider also the second fall to the valence band. This is somewhat similar. For the electrons to fall back to the valence band is easier than for electrons from the valance band to get promoted to the level state. To be coherent with many textbooks we will use the notion of holes to describe this. This allows us to simply reuse our formulae with some modifications:

- The capture cross sections and velocities are now the one of holes getting captured by the level.
- The energy difference $E_c - E_t$ is converted to $E_t - E_v$ (holes see the energy in the *wrong*[1] sense)
- The currents are currents of **holes**

$$j_{t\to VB} = \sigma_h v_{th}^h \times N_t(1-f_e) \times N_v \times e^{-\frac{E_t-E_v}{kT}}$$

$$j_{VB\to t} = \sigma_h v_{th}^h \times n_h \times N_t f_e$$

The system of equations to solve to find the kinetics is therefore:

$$\frac{dn_e}{dt} = j_{t\to CB} - j_{CB\to t}$$

$$N_t \frac{df_e}{dt} = (j_{CB\to t} - j_{t\to CB}) - (j_{VB\to t} - j_{t\to VB})$$

$$\frac{dn_h}{dt} = j_{t\to VB} - j_{VB\to t}$$

The red minus comes from the fact that the currents from and to the VB are hole currents but f_e is the occupation factor for electrons in the traps. For the trap, **at all times**, we have $f_h = 1 - f_e$. This is not the case in the bands out of equilibrium: in general, we have $f_h^{VB} \neq 1 - f_e^{CB}$.This is the same as saying that the Fermi levels for electrons and holes are distinct.

---

[1] Yes, it is the wrong sense.

1.1.1.2 Is it just an exponential?

Once coded with a software, all this mathematical description often gives rise to a mono-exponential behavior. Why is that? When does it not?

To understand the exponential behavior let us rewrite the equation for holes:

$$\frac{dn_e}{dt} = \sigma_e v_{th}\, e^{-\frac{E_c - E_t}{kT}} \times N_c \times N_t f_e - \sigma_e v_{th} \times N_t (1 - f_e) \times n_e$$

$$\frac{dn_e}{dt} = \sigma_e v_{th} N_t \left[N_c f_e\, e^{-\frac{E_c - E_t}{kT}} - (1 - f_e) \times n_e \right]$$

We can state that a sufficient condition for the mono-exponential behavior is that f_e be constant with time. When is the time derivative of $\frac{df_e}{dt}$ "small" with respect to 1? It is when:

$$-\sigma_e v_{th} N_t \left[N_c f_e\, e^{-\frac{E_c - E_t}{kT}} - (1 - f_e) \times n_e \right] - \sigma_h v_{th}^h N_t \left[n_h f_e - (1 - f_e) \times N_v \times e^{-\frac{E_t - E_v}{kT}} \right] \ll N_t$$

In the case of a deep defect, the exponential terms render negligible the terms they are attached to in comparison to the others. The condition is fulfilled in this case as long as:

$$\frac{n_e}{n_h} = \frac{f_e}{1 - f_e} \times \frac{\sigma_h v_{th}^h}{\sigma_e v_{th}^e}$$

This equation also sets the constant f_e level that we except from a symmetric generation (in the intrinsic case) $\frac{n_e}{n_h} \approx 1$ at short time:

$$f_e = \frac{1}{1 + \frac{\sigma_h v_{th}^h}{\sigma_e v_{th}^e} \times \frac{n_h}{n_e}} \tag{1}$$

To test this hypothesis, we consider the following case:

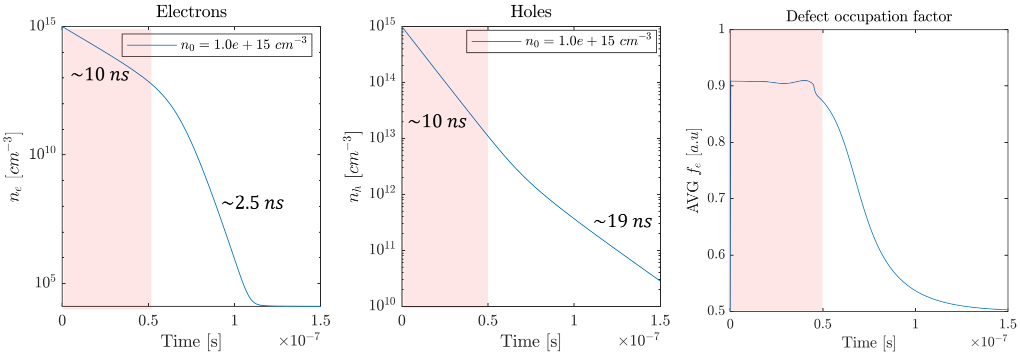

Figure 6: Simulation of the model mentioned before. The capture cross section for electrons is set to 10 times the one for holes ($\sigma_e v_{th}^e = 10^{-4} cm^3/s$ for electrons and $\sigma_h v_{th}^h = 10^{-5} cm^3/s$. $N_t = 10^{13} cm^{-3}$. The defect is mid gap. We can observe that during the red zone highlighted both densities are exponential, and the occupation factor is rather constant during this time. After that, we enter a regime that is completely different. Time indicated are the effective time in the case of mono exponential fit in the region concerned.

In terms of PL decay this would correspond to the following:

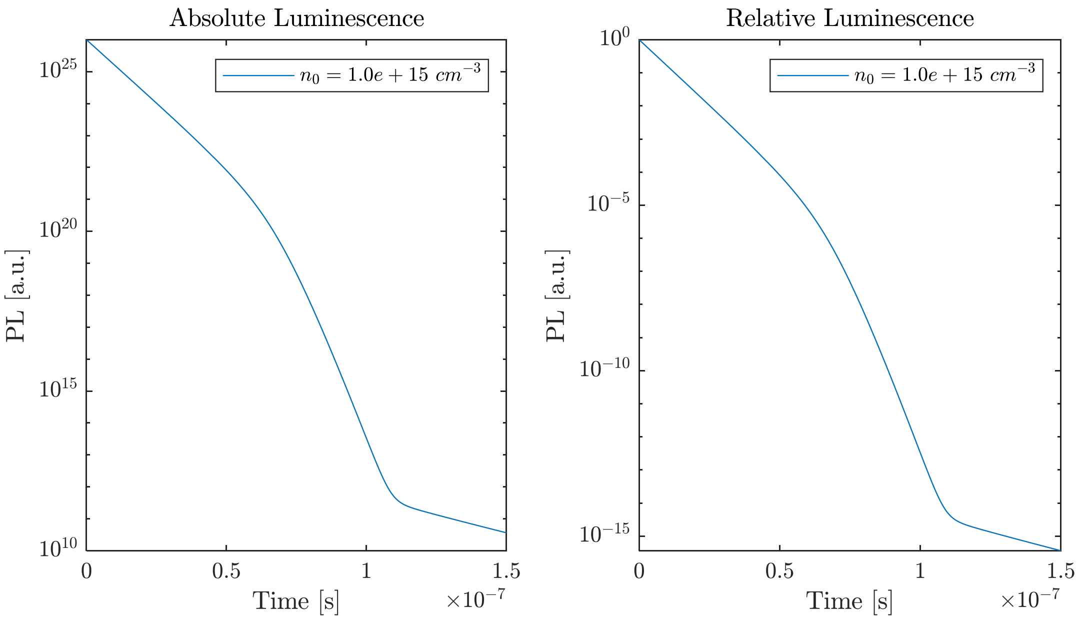

Figure 7: PL decay corresponding to the data of Figure 6.

Note that to observe such behavior, one has to observe luminescence on a lot of orders of magnitude.

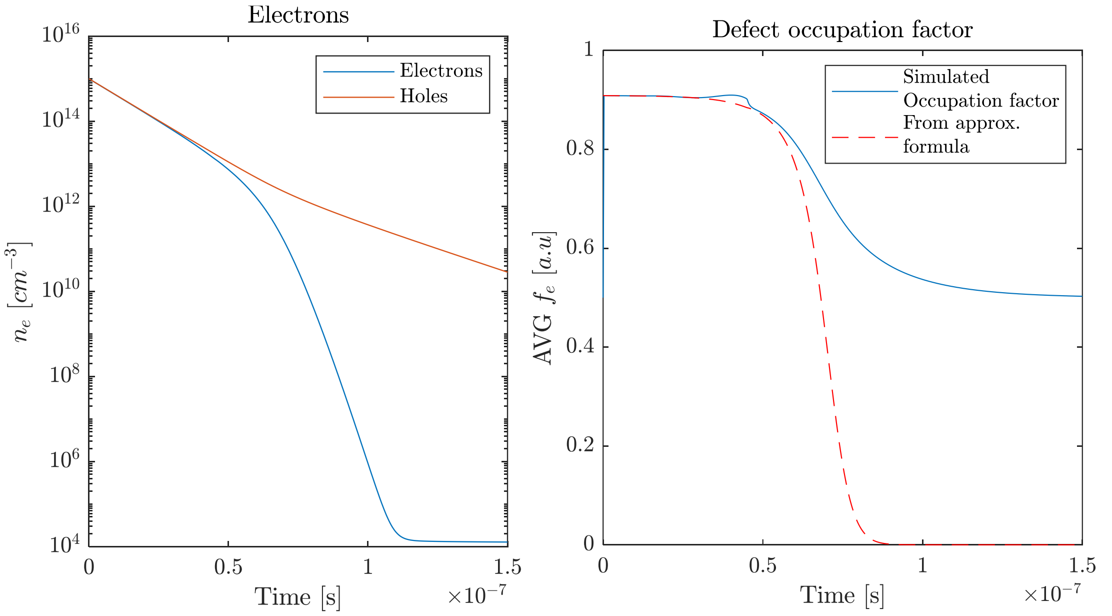

Figure 8: (a) Densities of e and h overlaid. (b) Comparison between the simulated occupation factor and the approximat formula (1)

One question remains: how is this time of change of behavior defined from the parameters. How does it scale?

1.1.1.3 First Regime: populating the traps

We study the first few picoseconds of the dynamics just after light absorption, where one goes from an initial trap occupation factor f_e^i to the expected approximate $f_e^a = \frac{1}{1+\frac{\sigma_h v_{th}^h}{\sigma_e v_{th}^e}\times\frac{n_h}{n_e}}$. There are two questions that arise:

- How much time does it take? (it will be very fast ~30ps)
- What is the resulting asymmetry in the densities that result from it?

An example of such fast population is given in the following figure.

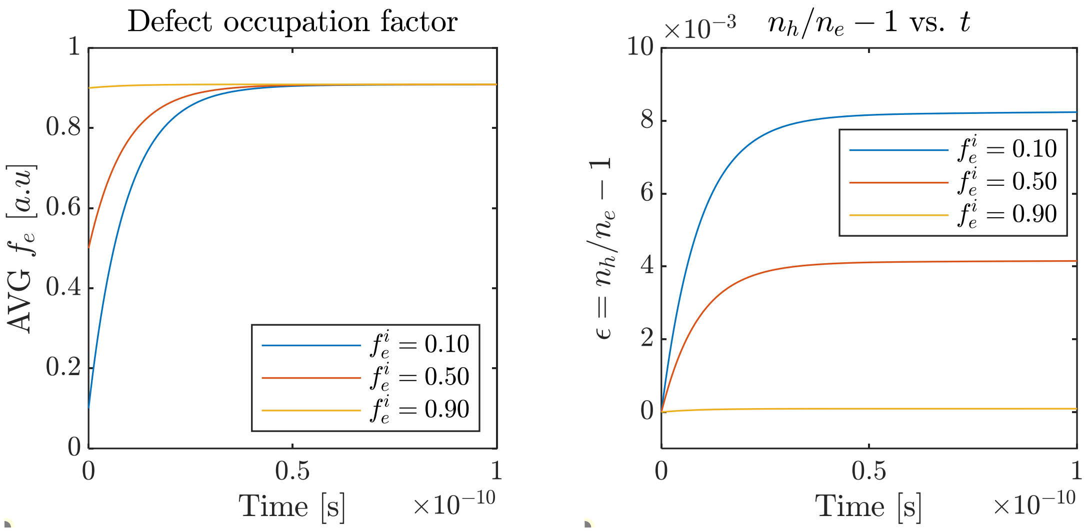

Figure 9: (a) Defect occupation factor as a function of time. The initial occupation factor is set arbitrarily at $f_e^i = 0.1\,;0.5\,;0.9$. Other parameters are similar as before, mainly $\sigma_e = 10\times\sigma_h$. (b) In the same simulation, visualization of the evolution of density of holes vs. density of electrons with the quantity $\epsilon = \frac{n_h}{n_e} - 1$. We see that a plateau is reached that depends on the initial defect density. N.B. This is not a plateau actually, see the following discussion.

For the trap occupation factor we observe a transient behavior converging fastly to the expected:

$$f_e^a \approx \frac{1}{1+\frac{\sigma_h v_{th}^h}{\sigma_e v_{th}^e}}$$

We can observe that this limiting occupation factor is somewhat independent on the initial trap occupation factor, whereas the quantity ϵ is not. We defined:

$$\epsilon \equiv \frac{n_h}{n_e} - 1$$

Photogeneration in an intrinsic absorber will result in $\epsilon(t=0)=0$. We observe here that ϵ undergoes a transient behavior in the 30ps timescale before reaching a plateau. The exact behavior of ϵ on the larger time scale will be dealt with later. In the following we will derive the value of the plateau ϵ_p that is reached, and the time it takes to reach it τ_p. Note that we define τ_p as the time required to go from f_e^i to f_e^a.

We will first derive a relationship between ϵ_p and the decrease of charge densities in the approximation that this decrease is small compared to the initial carrier density n_0. This is verified in our examples with $\Delta n_e(\tau_p) \approx 0.5\%\, n_0$:

$$\epsilon_p \approx \frac{n_h(\tau_p)}{n_e(\tau_p)} - 1 = \frac{n_0 - \Delta n_h(\tau_p)}{n_0 - \Delta n_e(\tau_p)} - 1 = \frac{\Delta n_e(\tau_p) - \Delta n_h(\tau_p)}{n_0 - \Delta n_e(\tau_p)} \approx \frac{1}{n_0}\left(\Delta n_e(\tau_p) - \Delta n_h(\tau_p)\right)$$

Using the system of differential equations, we can say that the trap occupation factor obeys:

$$N_t \frac{df_e}{dt} = \frac{dn_h}{dt} - \frac{dn_e}{dt}$$

Integrating from $t = 0$ to t will give us that:

$$f_e(t) = \frac{1}{N_t}\big(n_h(t) - n_e(t) - (n_h(0) - n_e(0))\big) + f_e^i$$

Now using the previous equations, we can say that ($n_h(\tau_p) = n_0 - \Delta n_h(\tau_p)$):

$$\big(n_h(t) - n_e(t)\big) = \Big(\Delta n_e(\tau_p) - \Delta n_h(\tau_p)\Big) = n_0 \epsilon_p$$

Therefore, we find the value of the plateau to obey:

$$\boxed{\epsilon_p = \frac{N_t}{n_0}\left(f_e^a - f_e^i\right)}$$

This gives a linear relationship between the initial condition f_e^i of the trap occupation factor and the relative change of n_h vs. n_e. As expected, the further from the “correct” trap occupation factor, the more asymmetric the situation becomes after this fast regime is finished. How fast?

One uses:

$$\Delta n_e(\tau_p) = \int_0^{\tau_p} dt \frac{dn_e}{dt} = \sigma_e v_e N_t \int_0^{\tau_p} dt[1 - f_e]n_e$$

We can approximate very roughly this integral by stating that $n_e(t) \approx n_0$ over the interval, which is exactly contradicted by the equation above, but which is reasonable if one considers that the relative change in n_e should be of less than a percent of n_0, compared to the change in $1 - f_e$ which is of order 1. Therefore:

$$\int_0^{\tau_p} dt[1 - f_e]n_e \approx n_0 \times \frac{\tau_p}{2} \times \left[f_e^i - f_e^a\right]$$

Doing a similar approach for $\Delta n_h(\tau_p)$ one can get:

$$n_0 \epsilon_p = \Big(\Delta n_e(\tau_p) - \Delta n_h(\tau_p)\Big) = \frac{n_0 N_t \tau_p}{2}\left(f_e^i - f_e^a\right)[\sigma_e v_e + \sigma_h v_h]$$

Now using our newfound formula for ϵ_p we get:

$$\boxed{\tau_p \approx \frac{2}{n_0[\sigma_e v_e + \sigma_h v_h]}}$$

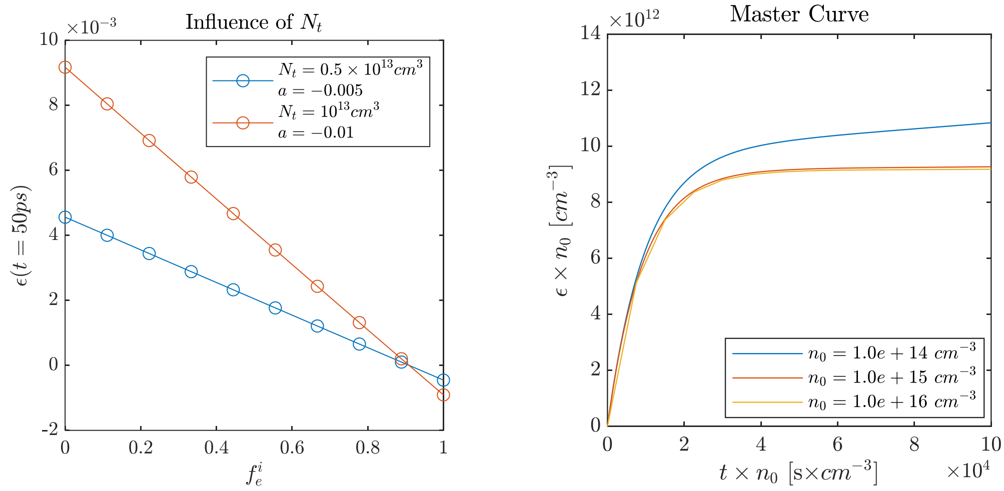

Figure 10: (a) $\epsilon(t = 50ps)$ as a function of the initial condition for two different trap densities illustrating formula (N). The observed slope (fitted) is equal to $-N_t/n_0$. In the case taken here $\tau_p = 18ps$. Qualitatively this is a bit short. (b) $\epsilon(t) \times n_0$ as a function of $n_0 \times t$ giving the master curve underlying this fast process. Here $2/[\sigma_e v_e + \sigma_h v_h]$=1.8e4 s.cm^-3. $N_t = 10^{13} cm^{-3}$.

On this figure one can observe in (b) that the expected formulae work better under high illumination which is understandable given the frequent $\epsilon \ll 1$ approximation we made. This is less and less true as n_0 approaches N_t.

1.1.1.4 Second Regime: Constant defect occupation factor

After the first regime, the system enters a regime where the defect occupation factor is almost time independent and equals:

$$f_e(t) = f_e^a \approx \frac{1}{1 + \frac{\sigma_h v_{th}^h}{\sigma_e v_{th}^e} \times \frac{n_h(t)}{n_e(t)}}$$

This is the case as long as $n_h(t) \approx n_e(t)$. In the following we will find the variations of the quantity $\epsilon(t)$ defined as:

$$\epsilon(t) = \frac{n_h}{n_e} - 1$$

This allows for the simplification of the system of equations.

$$\frac{dn_e}{dt} = -\sigma_e v_e N_t (1 - f_e) n_e = -\frac{N_t \sigma_h v_h}{\frac{n_e}{n_h} + \frac{\sigma_h v_h}{\sigma_e v_e}} \times n_e$$

$$\frac{dn_h}{dt} = -\sigma_h v_h N_t f_e n_h = -\frac{N_t \sigma_h v_h}{1 + \frac{\sigma_h v_h}{\sigma_e v_e} \times \frac{n_h}{n_e}} \times n_h$$

We see in these expressions that the order 0 in n_h/n_e would give a mono exponential decay with the same time constant:

$$\tau_{mono} = \frac{1}{N_t \sigma_h v_h}\left(1 + \frac{\sigma_h v_h}{\sigma_e v_e}\right) = \frac{1}{N_t \sigma_h v_h} + \frac{1}{N_t \sigma_e v_e}$$

This is what is somewhat observed in Figure 8. In order to derive the time that corresponds to the end of this regime we will derive a differential equation on $\epsilon = \frac{n_h}{n_e} - 1$ with the differential equations on n_e and n_h. We have:

$$\frac{d\epsilon}{dt} = \frac{1}{n_e^2}\left(\frac{dn_h}{dt} n_e - \frac{dn_e}{dt} n_h\right)$$

Using the equations above one gets:

$$\frac{d\epsilon}{dt} = \sigma_h v_h N_t \times \frac{\epsilon(\epsilon+1)}{1+\frac{\sigma_h v_h}{\sigma_e v_e}(\epsilon+1)}$$

This is a separable equation that can be solved analytically. A problem arises with the initial condition $\epsilon(t=0)=0$ which would lead to $\forall t,\ \epsilon(t)=0$. This “problem” was not seen in my simulations as an effective initial condition was appearing. Now with the previous paragraph we know that initial condition, it is ϵ_p, and in general is not 0 (unless $f_e^i = f_e^a$). The solution of the equation, if correctly defined is:

$$\frac{\left|\epsilon(t)^{\frac{\sigma_h v_h}{\sigma_e v_e}+1}\right|}{\epsilon(t)+1} = \frac{\left|\epsilon_p^{\frac{\sigma_h v_h}{\sigma_e v_e}+1}\right|}{\epsilon_p+1} e^{\sigma_h v_h N_t t}$$

This means that at short time, when $\epsilon \ll 1$, ϵ is an exponential in time, see Figure 11. In this plot the initial condition and ϵ_p appear as the offset at the origin. Thanks to that knowledge one can define the time when the regime ends to be approximately when $\epsilon(t)=1$ ie $n_h = 2n_e$.

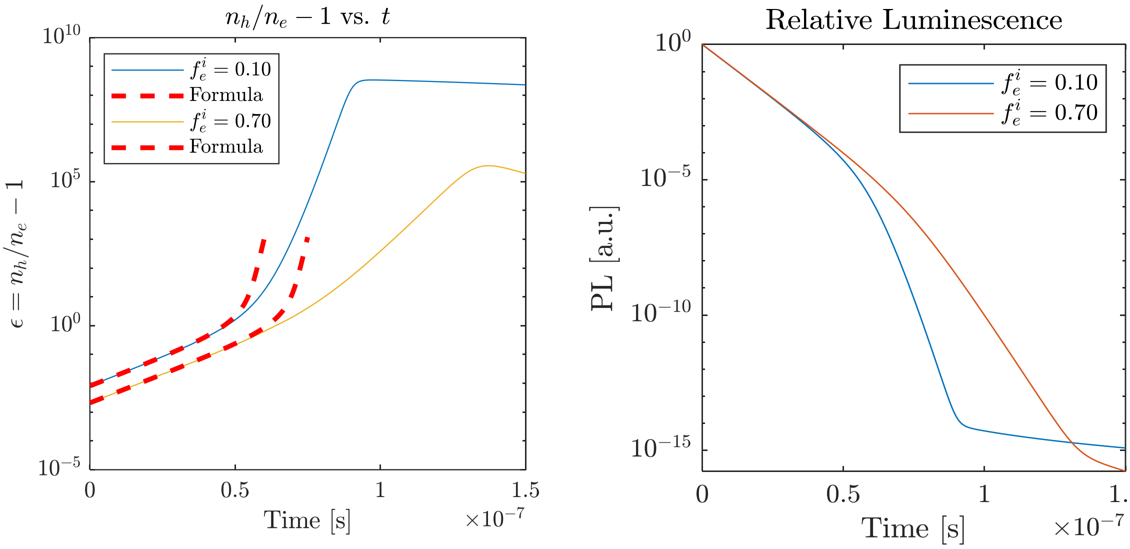

Figure 11: (a) $\epsilon(t)$ simulated and computed from the numerical solving of the formula above. Parameters similar to Figure 6. (b) Corresponding luminescence curves. One an observe the impact of the initial condition in the end of the decay. This is understandable because of the log scale employed.

$$\tau_{end} = \frac{1}{\sigma_h v_h N_t}\ln\left(\frac{(\epsilon_p+1)}{2\left|\epsilon_p^{\frac{\sigma_h v_h}{\sigma_e v_e}+1}\right|}\right) = \frac{1}{\sigma_h v_h N_t}\ln\left(\frac{\left(\frac{N_t}{n_0}\left(f_e^a - f_e^i\right)+1\right)}{2\left[\frac{N_t}{n_0}\left(f_e^a - f_e^i\right)\right]^{\frac{\sigma_h v_h}{\sigma_e v_e}+1}}\right)$$

This horrible formula is valid in the case $\sigma_e v_e < \sigma_h v_h$. In the contrary case, τ_{end} is given when $\epsilon(\tau_{end}) = -1/2$. Therefore, the formula changes slightly with 2 becoming $2^{\frac{\sigma_h v_h}{\sigma_e v_e}}$. The rest is unchanged. The formula seems asymmetric when exchanging holes and electrons. This is in fact not the case, see the following figure.

Care should be taken for the resolution in ϵ: when starting with an initial condition ϵ_p then ϵ keeps its sign for all t. This means that, although the formula for τ_{end} exists for those times, it has no physical meaning.

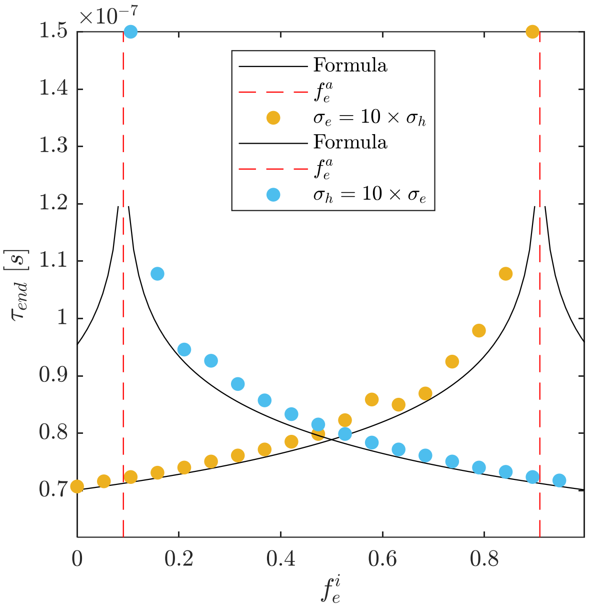

Figure 12: Time of the end of the regime as a function of the initial condition trap density for two cases $\frac{\sigma_h}{\sigma_e} = 10$ and 1/10 resp. The circles are the closest time points in the simulation to $\epsilon = -1/2$ and 1 resp. Black lines correspond to the formula given for τ_{end} above. The last time point of the simulation is 1.5e-7s.

We can note that τ_{end} diverges at $f_e^i = f_e^a$ which is natural: in this case no asymmetry is created in the first time period and therefore one expects $n_e = n_h$ at all times. We see that the formula fits well with the simulated data even if we are applying it in a time region where we cannot say anymore that f_e is almost constant. The theoretical formula is above the real curve as can be seen in Figure 11 (a), where the red curves reach $\epsilon = 1$ before the real ones. The two theoretical curves meet at $f_e^i = 0.5$ and are symmetric as expected physically.

Let us note that the dominant term in the definition of τ_{end} is perfectly understandable and simple: it corresponds to the time required to reach the condition $n_e \approx n_h \approx N_t$ and is given by:

$$\tau_{end}^0 = -\left[\frac{1}{\sigma_h v_h N_t} + \frac{1}{\sigma_e v_e N_t}\right] \ln\left(\frac{N_t}{n_0}\right)$$

Therefore, τ_{end} is the time required to reach a carrier density equal to the trap density modulated by the initial condition of the filling of the traps.

Finally one can observe this time on the PL plots:

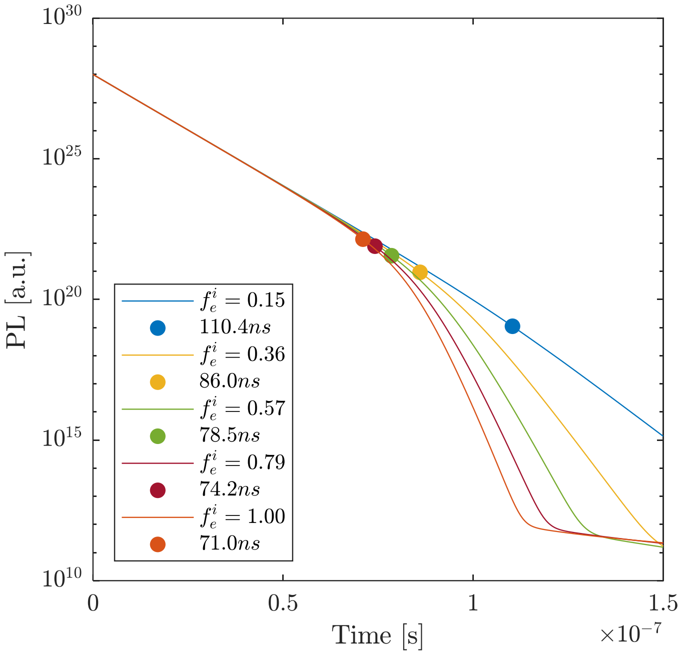

Figure 13: PL signal vs. time for different trap initial conditions, with a dot representing the position of τ_{end} for each curve. The situation corresponds here to the points of Figure 12 blue points, ie $\sigma_h = 10\sigma_e$. The closest one gets to $f_e^a \approx 0.1$ the less pronounced is the change of slope of the PL and the longer the time to reach it becomes.

1.1.1.5 What happens in the case of a Fermi Level initial condition?

In reality, one does not exactly choose the initial condition, it is set at thermal equilibrium by the Fermi Dirac distribution:

$$f_e^i = \frac{1}{\exp\left(\frac{E_t - E_F}{kT}\right) + 1}$$

In particular, under ambient conditions, the level is very likely to be almost completely empty (if $E_t > E_f + 3kT$) or full, (if otherwise).

Moreover, the use of Fermi Energy also induces an asymmetry in the densities of holes and electrons at time 0, it will also affect $\epsilon(t = 0) = \frac{n_h}{n_e} - 1$. Let us note that up until now we were a bit sloppy concerning the starting thermal equilibrium. We will now start with an equilibrium situation where:

$$f_e^i = \frac{1}{\exp\left(\frac{E_t - E_F}{kT}\right) + 1}$$

$$n_e(t = 0) = N_c e^{-(E_c - E_F)/kT} \equiv n_e^0$$

$$n_h(t = 0) = N_v e^{(E_v - E_F)/kT} \equiv n_h^0$$

What will change in the equations given above?

First the +expected occupation factor for electrons in the traps will change slightly:

$$f_e^a \approx \frac{1}{1 + \frac{\sigma_h v_{th}^h}{\sigma_e v_{th}^e} \times \frac{n_0 + n_h^0}{n_0 + n_e^0}}$$

This will not change much though.

In the short time dynamics, one must include the

$$\epsilon_p = \frac{1}{n_0 - \Delta n_e(\tau_p) + n_e^0}\left(\Delta n_e(\tau_p) - \Delta n_h(\tau_p) + n_h^0 - n_e^0\right)$$

But It also appears in the equation

$$f_e(t) = \frac{1}{N_t}\left(n_h(t) - n_e(t) - \left(n_h^0 - n_e^0\right)\right) + f_e^i$$

Which results in (almost) the same equation

$$\boxed{\epsilon_p = \frac{N_t}{n_0 + n_e^0}\left(f_e^a - f_e^i\right)}$$

The $+n_e^0$ will often be negligible for an intrinsic SC in high illumination condition.

To conclude : the short time dynamics are not that affected

To make things clearer, we will now consider the quantity:

$$\gamma \equiv \frac{n_h - n_e}{n_h + n_e}$$

This time, contrary to ϵ our definition is anti-symetric in the exchange e<->h. For instance, if holes are consumed faster than electrons, we can reach the point where $n_e = 2n_h$ in which case $\gamma = -1/3$. On the contrary for $n_h = 2n_e$ we would have $\gamma = 1/3$. Note that we have at all times $-1 < \gamma < 1$. By using the regime previously described of fast adaptation of the traps, where $f_e(t) = f_e^a(t)$ one can obtain a differential equation on $\gamma(t)$:

$$\boxed{\frac{d\gamma}{dt} = \frac{\gamma(1+\gamma)(1-\gamma)}{\frac{1}{\sigma_h v_h N_t}(1+\gamma) + \frac{1}{\sigma_e v_e N_t}(1-\gamma)}}$$

This equation is very nice because it is also invariant when exchanging $e \leftrightarrow h$ (and therefore $\gamma \leftrightarrow -\gamma$). This equation may be solved analytically from $t = \tau_p$ and $\gamma = \gamma_p$ to $\gamma(t)$ and t. In the case $\gamma_p = 0$, the solution is $\gamma(t) = 0$. In the case $\gamma_p \neq 0$, γ will retain the sign of γ_p and will be solution of the following equation:

$$\left(\frac{|\gamma|}{1-\gamma}\right)^{\frac{1}{\sigma_h v_h N_t}}\left(\frac{|\gamma|}{1+\gamma}\right)^{\frac{1}{\sigma_e v_e N_t}} = \left(\frac{|\gamma_p|}{1-\gamma_p}\right)^{\frac{1}{\sigma_h v_h N_t}}\left(\frac{|\gamma_p|}{1+\gamma_p}\right)^{\frac{1}{\sigma_e v_e N_t}} \times \exp(t - \tau_p) \tag{2}$$

In the limit of short time where $|\gamma| \ll 1$, one can obtain the approximate solution:

$$\gamma(t) = sign(\gamma_p) \times cte \times \exp\left(\frac{(t-\tau_p)}{\tau_{mono}}\right)$$

With $\tau_{mono} = \frac{1}{\sigma_h v_h N_t} + \frac{1}{\sigma_e v_e N_t}$. Thus the behavior of γ can be of three types:

"Initial" condition	$\gamma_p < 0$	$\gamma_p = 0$	$\gamma_p > 0$
Limit when $t \to \infty$	$\gamma \to -1$	$\gamma \to 0$	$\gamma \to 1$

Sketch of time behavior	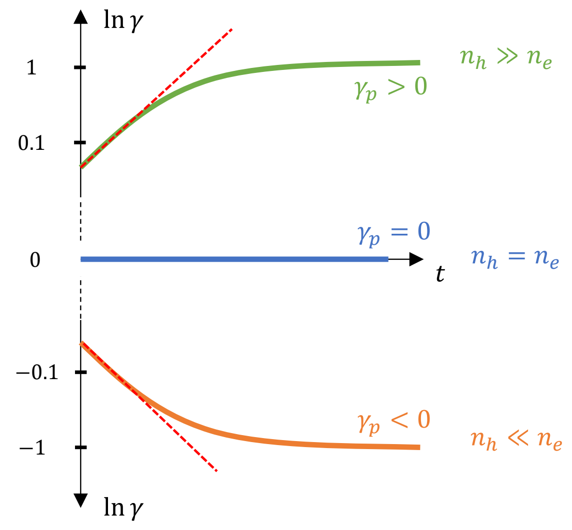

Remark: We see that the initial condition γ_p is of tremendous importance for the rest of the decay, the asymmetry being amplified with time. Note that this condition does not depend on the capture cross sections, except through the value of γ_p. This means that the system is not able to break the asymmetry present in its initial condition, rather it amplifies it.

Now to find the time t_{end} after which we cannot approximate $n_e \approx n_h$ can be defined by the time necessary to obtain that one of them is equal to twice the other, in both cases $|\gamma| = \frac{1}{3}$.

What is γ_p? We use the very short time scale behavior to determine it. We will now start with an equilibrium situation where just before the pulse (that will add $+n_0$ to holes and electrons):

$$f_e^i = \frac{1}{\exp\left(\frac{E_t - E_F}{kT}\right) + 1}$$

$$n_e(t = 0^-) = N_c e^{-(E_c - E_F)/kT} \equiv n_e^0$$

$$n_h(t = 0^-) = N_v e^{(E_v - E_F)/kT} \equiv n_h^0$$

We can compute $\gamma_0 = \frac{n_h^0 - n_e^0}{n_h^0 + n_e^0 + 2n_0}$. During this small-time scale behavior, f_e goes from its initial value f_e^i to f_e^a. We can start from a situation where f_e^i is above, equal or less than f_e^a. The three cases exist.

Using the system of differential equations, we can say that the trap occupation factor obeys:

$$N_t \frac{df_e}{dt} = \frac{dn_h}{dt} - \frac{dn_e}{dt}$$

Integrating from $t = 0$ to t will give us that:

$$f_e(t) = \frac{1}{N_t}\left(n_h(t) - n_e(t) - \left(n_h^0 - n_e^0\right)\right) + f_e^i$$

We compute:

$$\left(n_h(t) - n_e(t)\right) = \left(n_e(t) + n_h(t)\right)\gamma(t)$$

We can see that:

$$\left(n_h(t) - n_e(t) - \left(n_h^0 - n_e^0\right)\right) = \left(n_e(t) + n_h(t)\right)\gamma(t) - \left(n_e(t=0) + n_h(t=0)\right)\gamma(t=0)$$

Of course $n_e(t)$ and $n_h(t)$ will depend on $\gamma(t)$, to first order in $\gamma(t)$ though, one can approximate:

$$n_e(t) + n_h(t) = n_e^0 + n_h^0 + 2n_0 - \Delta n_e(t) - \Delta n_h(t) \approx n_e^0 + n_h^0 + 2n_0$$

Therefore, the equation simplifies to

$$\left(n_h(t) - n_e(t) - \left(n_h^0 - n_e^0\right)\right) \approx \left(n_e^0 + n_h^0 + 2n_0\right)\left(\gamma(t) - \gamma_0\right)$$

We can then find for $t = \tau_p$ for which $f_e(\tau_p) = f_e^a$ and $\gamma(\tau_p) \equiv \gamma_p$:

$$\boxed{\gamma_p = \gamma_0 + \frac{N_t}{2n_0 + n_e^0 + n_h^0}\left(f_e^a - f_e^i\right)}$$

Again $\left(f_e^a - f_e^i\right)$ can be negative in which case under the right conditions the small time behavior may change the appearing asymmetry; it can also be positive or equal to zero. Note: $n_{e,h}^0$ may be negligible compared to n_0 but can also be comparable in the doped case. As:

$$\gamma_0 = \frac{n_h^0 - n_e^0}{2n_0 + n_e^0 + n_h^0}$$

$$\boxed{\gamma_p = \frac{1}{2n_0 + n_e^0 + n_h^0}\left[\left(n_h^0 - n_e^0\right) + N_t\left(f_e^a - f_e^i\right)\right]}$$

Note that only rarely is $\left(n_h^0 - n_e^0\right)$ (~$10^6\ cm^{-3}$)of the same order of magnitude as $N_t\left(f_e^a - f_e^i\right)$ (~$10^{13}\ cm^{-3}$), so that γ_p sign is often determined by the sign of $\left(f_e^a - f_e^i\right)$: it is negative when the Fermi Level has populated the level higher than what the capture cross sections would expect, and it is positive when the level is not populated enough in this regard.

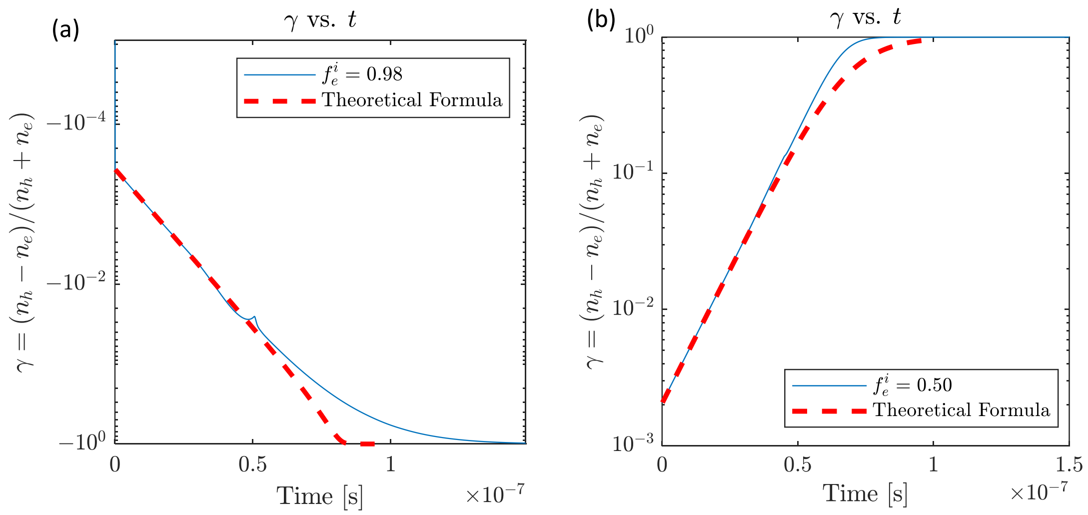

Figure 14: Observed value of $\gamma(t)$ (blue line) for two simulation identical except for the initial condition Fermi Level. Red dots are the theoretical formula (2). (a) Fermi level at $E_f = 0.9\ eV$ (midgap+0.1eV) (b) $E_f = 0.8\ eV$ (midgap). The defect in both cases is midgap.

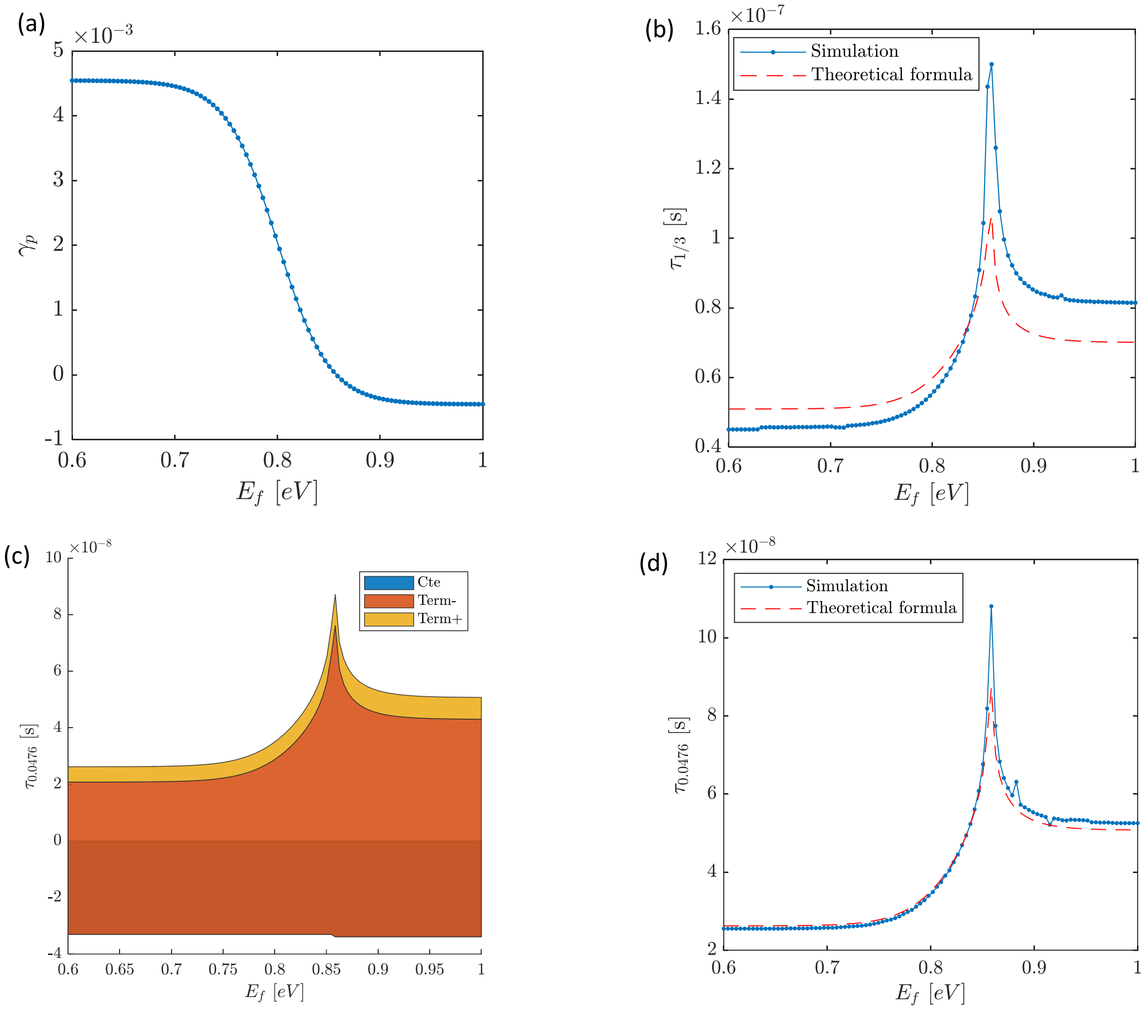

Figure 15: (a) γ_p as a function of the Fermi Level. Note that it can be negative and positive. It is close to zero when the Fermi level is such that the occupation factor for the trap is equal to the dynamic one f_e^a. (b) $\tau_{1/3}$ as described in the text vs. Fermi level, compared to the formula. The agreement is not that good, but the variations and orders of magnitude are well represented. (d) $\tau_{0.0476}$ corresponding to one of the carriers being in 10% excess as a function of Ef compared with the formula. The agreement is very good. (c) Repartition of the terms that are used in the formula for $\tau_{1/3}$: Cte = ln (C), term- corresponds to the -ln(/-) and term+ to the last term. Their sum is the red dot curve of (d).

The time necessary to obtain the doubling of one type of carrier into two is two can be named $\tau_{1/3}$ because it will correspond to $|\gamma| = 1/3$. It is given by

$$\tau_{1/3} - \tau_p = \ln C_{\pm} - \frac{1}{\sigma_h v_h N_t} \ln\left(\frac{|\gamma_p|}{1-\gamma_p}\right) - \frac{1}{\sigma_e v_e N_t} \ln\left(\frac{|\gamma_p|}{1+\gamma_p}\right)$$

Where $C_{\pm}$ is a constant that is defined as:

$$C_+ = 2^{-\frac{1}{\sigma_h v_h N_t}} \times 4^{-\frac{1}{\sigma_e v_e N_t}}$$

$$C_- = 4^{-\frac{1}{\sigma_h v_h N_t}} \times 2^{-\frac{1}{\sigma_e v_e N_t}}$$

If $\gamma_p > 0$, then C_+ should be used, and if $\gamma_p < 0$, then C_- should be used. τ_p is of the order of tens of picoseconds and can often be neglected.

The difference between the regime $\gamma_p > 0$ and $\gamma_p < 0$ is highlighted in the figure below.

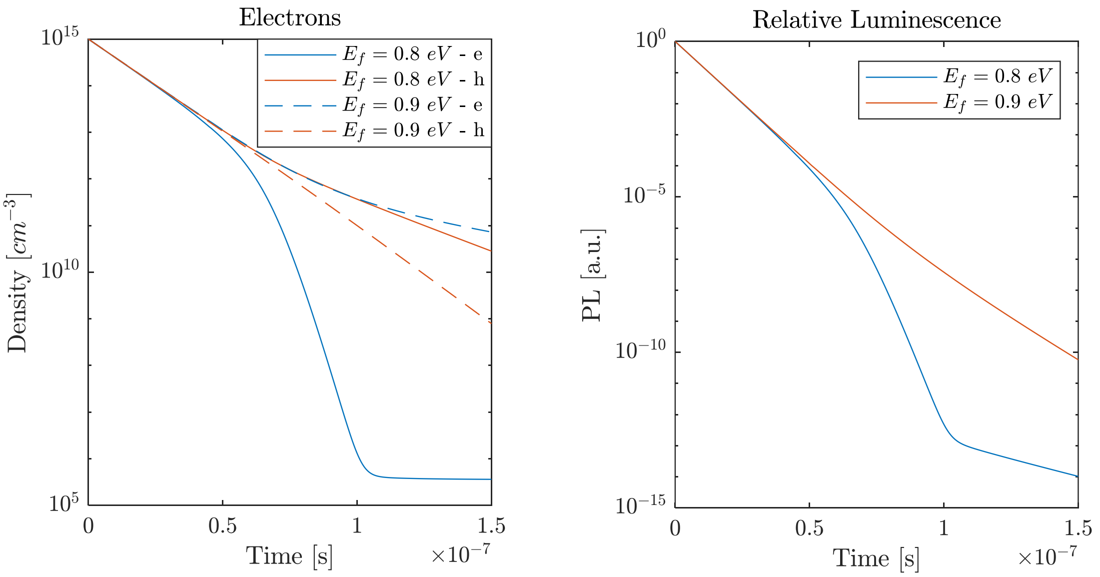

Figure 16: Influence of the initial Fermi level on the dynamics. The capture cross sections are asymmetric for both cases with $\sigma_e = 10\sigma_h$. The ony thing that changes here is the initial Fermi Level. (a) Carrier densities as a function of time. Each color is a type of carrier. Note that in the situation $E_f = 0.8eV$, the electrons are decreasing faster than holes. On the other hand, when $E_f = 0.9eV$, electrons are decreasing slower than holes. (b) PL signal as a function of the Fermi Level. (b) Corresponding PL curves. One is slightly bent upwards, the other more visibly downwards from the simple exponential decay.

Now what information can we hope to obtain from the measurement of say the blue PL curve of Figure 16 (b)? From Figure 15 (c) we observe that the time at which such change exists is mostly determined by one term plus the constant.

$$\tau_{1/3} \approx \ln C - \frac{1}{\sigma_h v_h N_t} \ln\left(\frac{n_h^0 + n_e^0 + N_t\left(f_e^a - f_e^i\right)}{2(n_0 + n_e^0) - N_t\left(f_e^a - f_e^i\right)}\right) \approx \ln C - \frac{1}{\sigma_h v_h N_t} \ln\left(\frac{N_t}{n_0}\left(f_e^a - f_e^i\right)\right)$$

Now: can we hope to see a change under photodoping conditions?

Appendix E

More details on the TR-FLIM characterization

E.1 Transmission of filters used for the absolute calibration

See Figure E.1.

E.2 Statistical model of the TR-FLIM: Uncertainty on the signal and the question of *noise*

In this section, we give elements of answer to the following question: what is the error bar we should put on our experimental signal from the TR-FLIM ?

To do so, we characterized the histograms of the count values. When thinking about making a collection of results to plot an histogram there are two natural ideas: one to make one histogram over the pixels of one image, two to make one histogram from the value of one pixel over many repetitions. Such histograms are presented in Figure E.2. The so called ergodicity hypothesis on the ensemble of pixels states that the two process should give similar results if we are to consider that the pixels of one image are all *similar* one to the other. We can see on the Figure that this is more or less the case, where the blue curve is the histograms of pixel located in (10,10) on the 1024x1024 array over multiple repetitions, while the orange histograms are from the distribution of values in one image. We consider that the ergodicity hypothesis is verified.

Now we wanted to understand the peculiar shape of these

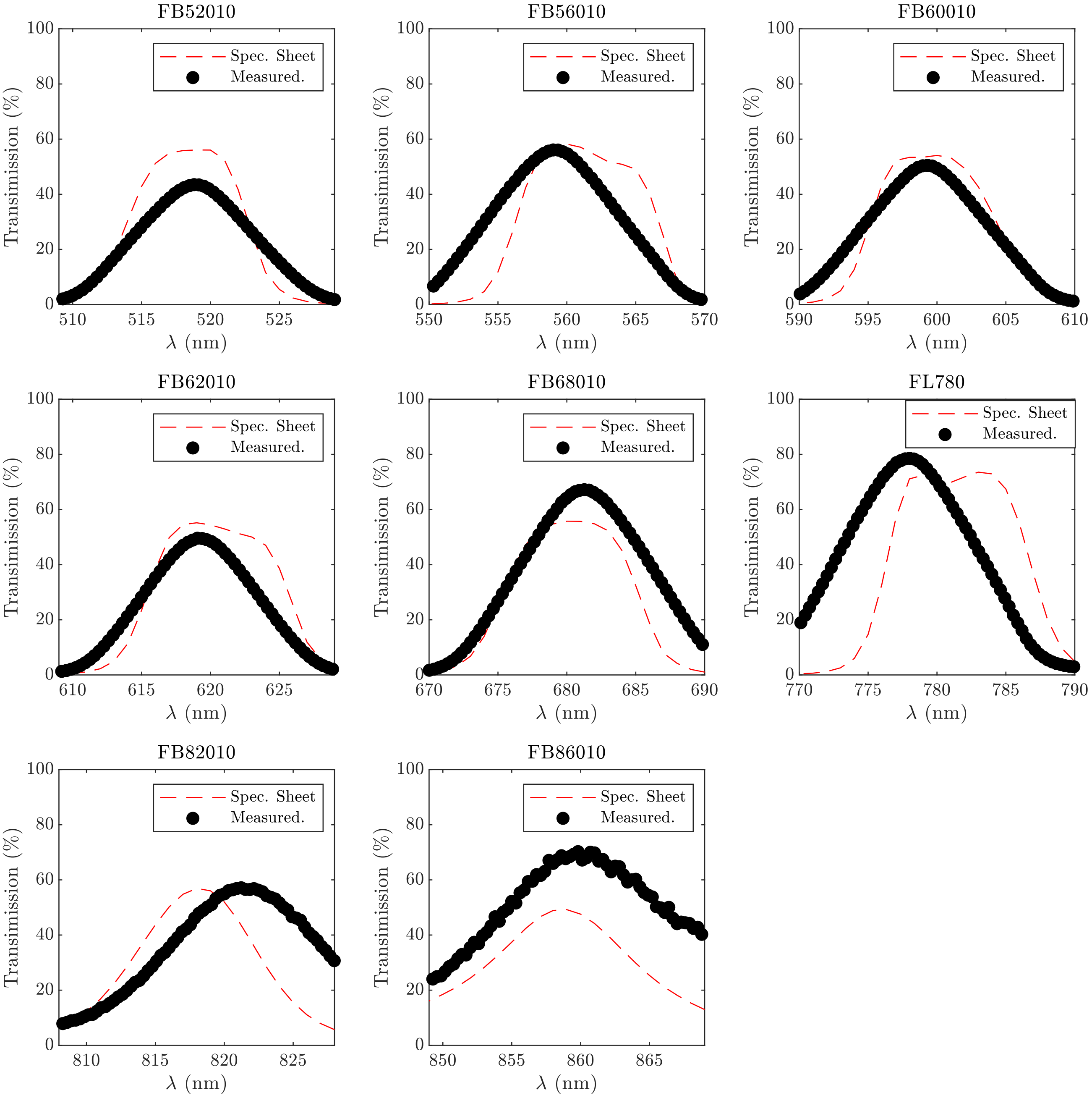

Figure E.1: *Measured transmission of filters (black dots), compared to the specification sheet of each of the filters. Differences of up to 33% between the integrated transmissions were found. All plots are* 40 nm *wide.*

histogram, namely why we obtain results far from the typical Gaussian that everybody expects in any experiments. To do so, we used existing statistical models in the literature and verified their application to our experimental case [Hirsch *et al.* 2013, Avella *et al.* 2016]. With these models, we were able to reproduce quantitatively the histograms and this gave us:

1. An estimate on the real multiplication factor applied to the signal. Indeed, we found out that the parameter I_{emicdd} of the camera is not the direct multiplication factor applied to the signal, rather the real multiplication factor is $\approx 15\%$ of the value of I_{emicdd}. To verify this finding we also used a second method, namely the Photon Transfer Technique [Janesick *et al.* 1985]. This second result was in line with the first.
2. An estimate of the noise levels, as well as offset values by the manufacturer.

These statistical model turned out to be quite compatible with our previous discussion on the Responsivity of the camera, $R(\lambda, I_{\text{emiccd}})$, see Statement 2.2.6. Namely, we were able to obtain an estimate of the quantum efficiency of the photo-cathode by combining both descriptions that matches well with the specification sheet.

With this statistical description, we were able to define a reasonable uncertainty bar on our experimental signal. But this statistical model could also very well be useful for more advanced denoising techniques, such as regularization via total variation algorithms (TVA), [Marnissi *et al.* 2017], as are developed with the collaboration with INRIA. Indeed, these techniques need a precise description of the noise affecting the observable, which this section provides.

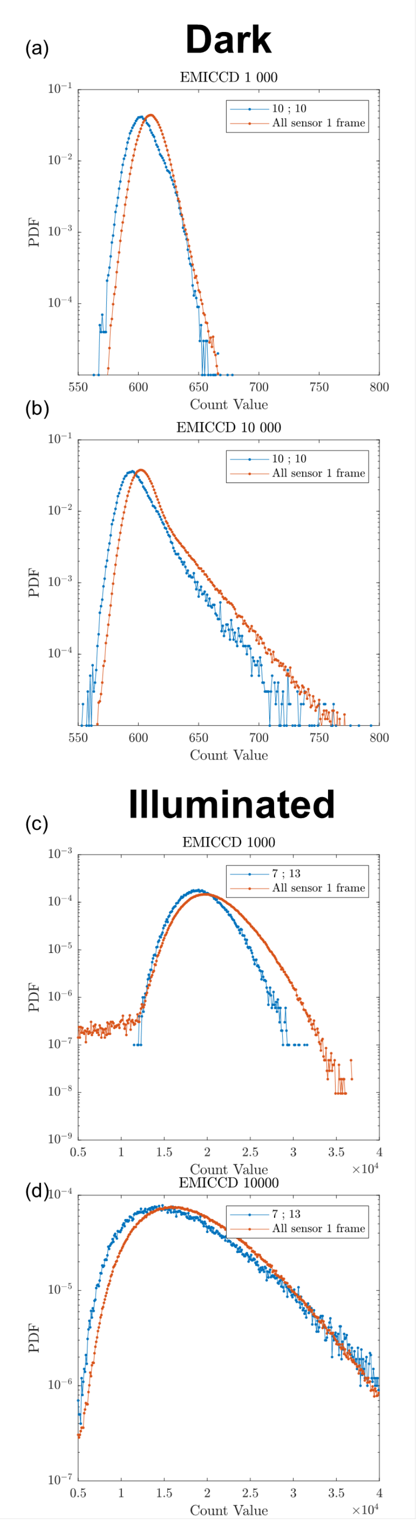

Figure E.2: *Histograms for one pixel over many repetitions compared to the average over all pixels for four cases: dark/light and high/low intensification parameter.*

E.2.1 The statistical model and its hypothesis

We will use the following convention: **bold symbols are used for the statistical variables.** Our model greatly simplifies the reality of how photons are converted to counts, see Figure 2.8. The main hypothesis are the following:

Statement E.2.1. Main hypothesis of the statistical model.

1. The camera has two intensification (multiplication) steps in reality. We will model them as only one.

2. The photocathode will be considered as the only source of wavelength dependant characteristics
3. The dark current may have multiple origins in reality, as spurious charges at the begining of one of the two intensification stages, or as a thermal signal in the pixels of the camera. We will model only one dark current and consider that is comes from spurious charges.

Let us now describe the physical path of signal along the camera's hardware, and give explanation on how we model it statistically. This description follows what is sketched in Figure 2.8. A number of incoming photons $\boldsymbol{N}_{\text{ph.}}$ reaches the photocathode. We consider fixed the integration time, and that the photons have a well defined wavelength λ. The photocathode has a quantum efficiency noted $Q(\lambda)$ in [e/ph]. We consider that the spurious charges (of number $\boldsymbol{N}_{\text{sp.}}$) are similar to a background illumination of photons. Therefore, the number of input electrons for the multiplication process is:

$$\boldsymbol{N_{ie}} = Q(\lambda)\boldsymbol{N}_{\text{ph.}} + \boldsymbol{N}_{\text{sp.}}$$

We will simply model them both statistically as a Poisson process, of parameter $f = Q(\lambda)f_{\text{ph}} + f_{\text{sp}}$. Now statistically, there are qualitatively two cases: low number of photoelectrons ie $N_{ie} < 1000$ and of accumulations, where one needs to describe precisely the accumulation process as a sum of independent Poisson variables, and the case where $N_{ie} > 1000$ where the Poisson process can be approximated by a Normal distribution $\mathcal{N}$ of mean and variance N_{ie}. This second case is easier to implement but does not represent experiments performed in the dark for instance. In both cases we will note the probability distribution function $f_{\text{lum}}(N_{\text{ie}})$:

$$\boldsymbol{N}_{\text{ie}} \sim \text{Pois}\underbrace{\left(Q(\lambda)f_{\text{ph}} + f_{\text{sp}}\right)}_{f} \overset{f\to\infty}{\sim} \mathcal{N}(\mu = f, \sigma^2 = f) \tag{E.1}$$

Then these electrons will be multiplied. The multiplication process will be modeled by a modified gamma law as proposed by Hirsch et al [Hirsch *et al.* 2013, Avella *et al.* 2016], so we can write the probability of obtaining a number of multiplied output electrons $\mathbf{N}_{\text{em}}$ given the number of input electrons:

$$P\left(\boldsymbol{N}_{\text{em}}|N_{\text{ie}}\right) = \begin{cases} \frac{n_{\text{em}}^{N_{\text{ie}}-1}}{\Gamma(N_{\text{ie}})g^{N_{\text{ie}}}}e^{-N_{\text{em}}/g} & \text{If } N_{\text{ie}} > 0 \\ \delta(N_{\text{em}}) & \text{Otherwise} \end{cases}$$

With Γ being the Euler gamma function, and g the multiplication parameter. The mean of such law would be

$$\langle \mathbf{N}_{\text{em}} | N_{\text{ie}} \rangle = g \times N_{\text{ie}} \tag{E.2}$$

Thus this is modeling a multiplication process. Measuring this multiplication parameter and its influence on the signal will be the subject of the next section. But we can already state that g is a function of the camera parameter I_{emiccd}, ie : $g(I_{\text{emiccd}})$.

Then electrons that come from the multiplication stages are added to random read noise that we assume is Gaussian distributed $\mathbf{N}_{\text{RN}}$ of mean 0 and standard deviation σ_{RN}. To obtain our signal in ADU (Analog Digital Unit), the camera gain F in $[\frac{e}{\text{ADU}}]$ is used as a multiplication constant. The signal is offset by the constructor to avoid negative values for the pixels by a number of counts noted N_{off}. Therefore, the random variable of the number of counts read on our pixel $\mathbf{N}_{\text{ADU}}$ is :

$$\mathbf{N}_{\text{ADU}} = N_{\text{off}} + \frac{1}{F} \left(\mathbf{N}_{\text{rn}} + \mathbf{N}_{\text{em}} \right)$$

Considering that the random variables for the noises are independent from one another, one can use the convolution rule to determine the distribution of the sum of random variables. We can then compute the whole distribution as described by the full scale equation, where $f_{\text{lum}}\left(N_{\text{ie}}\right)$ is the PDF of the illumination and dark signal.

Statement E.2.2. The distribution of number of counts N_{ADU} is:

$$f_{\mathrm{ct}}\left(N_{\mathrm{ADU}}\right) = \int_{-\infty}^{+\infty} \mathrm{dN} \frac{1}{\sigma_{\mathrm{rn}}\sqrt{2\pi}} e^{-\frac{\left(N_{\mathrm{ADU}}-N-N_{\mathrm{off}}\right)^2}{2\sigma_{\mathrm{rn}}^2}} \int_{0}^{+\infty} dN_{\mathrm{ie}} \frac{\left(NF - N_{\mathrm{off}}F\right)^{N_{\mathrm{ie}}-1}}{\Gamma\left(N_{\mathrm{ie}}\right) g^{N_{\mathrm{ie}}}} e^{-\frac{\left(NF-N_{\mathrm{off}}F\right)}{g}} f_{\mathrm{lum}}(N_{\mathrm{ie}}) \tag{E.3}$$

Where $f_{\mathrm{lum}}\left(N_{\mathrm{ie}}\right)$ is the PDF of the illumination and of the spurious (dark) signal, see Equation (E.1). In terms of average this gives:

$$\langle \mathbf{N}_{\mathrm{ADU}} \rangle = \underbrace{N_{\mathrm{off}}}_{\text{Offset.}} + \underbrace{\frac{g(I_{\mathrm{emiccd}})}{F} \langle \mathbf{N}_{\mathrm{sp.}} \rangle}_{\text{Dark.}} + \underbrace{\underbrace{\frac{g(I_{\mathrm{emiccd}})Q(\lambda)}{F}}_{\text{Responsivity } R(\lambda, I_{\mathrm{emiccd}})} \langle \mathbf{N}_{\mathrm{ph.}} \rangle}_{\text{Signal.}} \tag{E.4}$$

We observe the link to the responsivity of the camera introduced in Statement 2.2.6. By assuming:

- statistical independence of the spurious charges and photonic signals
- Assumption that they are Poisson-like processes
- Using the law of total variance
- Using the formulae for the variance of the Gamma process

we obtain:

$$\mathrm{Var}\left(\mathbf{N}_{\mathrm{ADU}}\right) = \left(\frac{g(I_{\mathrm{emiccd}})}{F}\right)^2 \left[2\langle \mathbf{N}_{\mathrm{sp.}} \rangle + Q(\lambda)\left(1 + Q(\lambda)\right) \langle \mathbf{N}_{\mathrm{ph.}} \rangle\right] \tag{E.5}$$

E.2.2 Validation of the statistical model by histogram fitting

We applied the previous model and tested its validity with experimental data. The experiment consisted in a time-constant light source lighting a Spectralon diffuser imaged by the camera. The camera parameters were varied, namely the number of accumulations and the multiplication gain parameter I_{EMICDD}. The gate width was kept constant at 5ns. The accumulations were varied between 10 and 65 000 while EMICCD were varied from 10 to 10 000. Each acquisition is composed of a 200x250 pixels region of interest and contains 50 frames.

For each couple of parameters – N_{acc} and I_{EMICDD} –, we can compute a space-time histogram over the 2,5 million values observed. We make the hypothesis that the light source is constant both spatially and temporally. This hypothesis is validated by the good agreement between fit and observations, visible in Figure E.3. For each histogram four parameters are

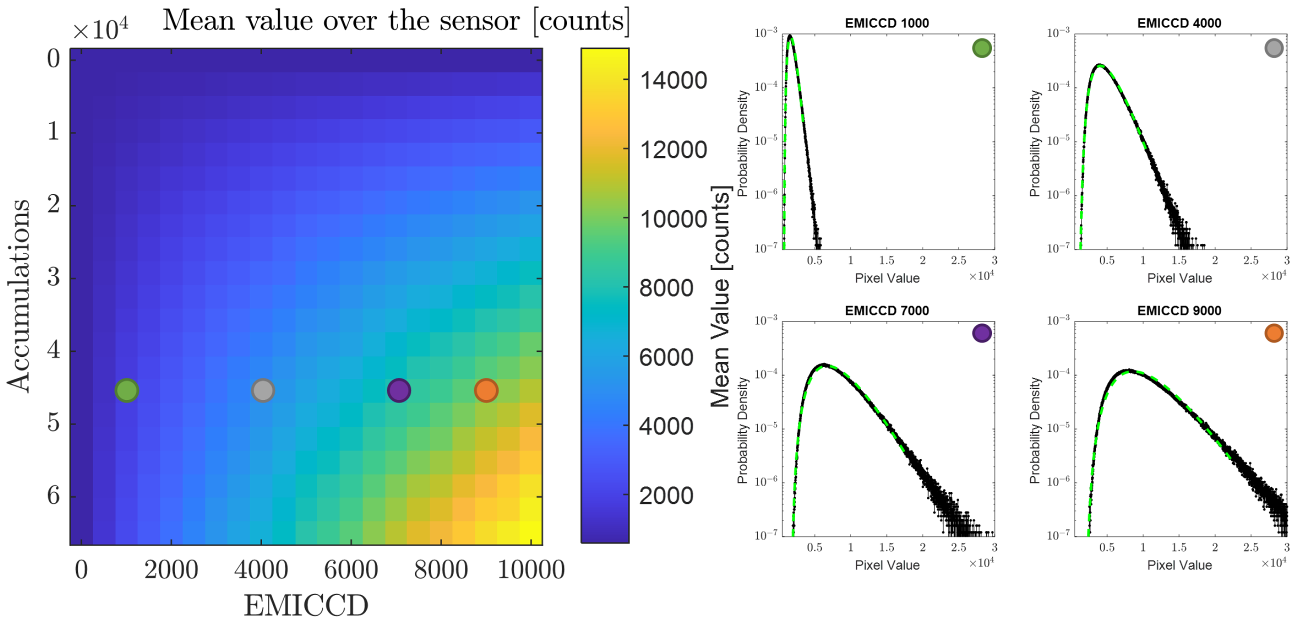

Figure E.3: *Fitting of histograms obtained experimentally with a constant light source. Black points: experimental histogram, green dots: fit according to Equation (E.3). Two camera parameters are varied, the number of accumulations and the intensification parameter.*

fitted: the offset number of counts N_{off}, the Read-Noise standard deviation σ_{RN}, the multiplication gain over the CCD gain g/F and the mean "electron" illumination $\times f$. the spurious charges intensity is set to $f_{\mathrm{SP}} = 10^{-2}$photons. Why did we not fit individual parameters like F and g separately? We used correlation of fitting parameters (see section 2.3.2) to evidence that our model was only sensible to g/F and not to g and F separately. Similar correlation was evidenced for Q and f_{ph}.

The fit quality is good over all accumulations and EMICCD ranges, see Figure E.3 for four examples of fitted histograms. From the fit we can extract the fitted value for the number of photo-electrons Qf_{ph} and for the multiplication gain g/F. They are plotted in Figure E.4 where error bars correspond to standard deviation over the not shown dimension. Values are compatible with the linearity of the camera, evidenced earlier, see Figure 2.16. After this fit on the statistical model, we can state the following. First, our simple description can precisely capture the statistics of the array of pixels. That means that they are sufficiently similar one to the other to be considered as one pixel. Moreover, **our doubly intensified camera can be modeled as simply**

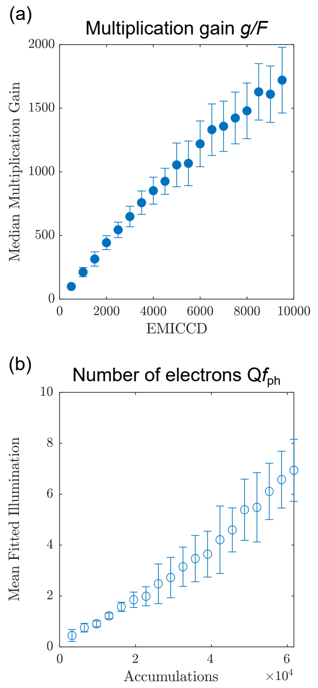

Figure E.4: *Fitting results. (a) Fitted value of the multiplication gain and (b) of the fitted illumination.*

containing one effective intensification stage. This was not obvious given the complexity of the real system. In a more practical point of view, we are able to effectively understand our count signal.

E.2.3 The determined multiplication gain and comparison with the photon transfer technique

The fitting of the histograms under illumination gave us, see Figure E.4(a):

$$\frac{g(I_{\text{emiccd}})}{F} = (0.20 \pm 0.01) \times I_{\text{emiccd}} \tag{E.6}$$

To estimate how relevant this formula is, we implemented another technique than histogram fitting to determine this ratio of g/F: the photon transfer technique, firstly introduced by [Janesick *et al.* 1985]. The photon transfer technique uses the means and variances of the statistical description to determine the parameters. The hypotheses are similar to our model, mainly that the emission follows a Poisson distribution and that we have independence of the different noise sources and electronic signals.

Figure E.5 shows the multiplication gain g/F for the two techniques as a function of the camera parameter I_{emiccd}. We observe a simlar linear trend for the two. The slope is slightly different as we have:

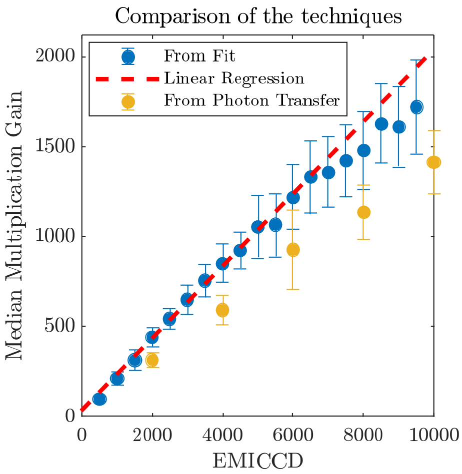

Figure E.5: *Comparison on the obtained multiplication gains by the two techniques as a function of the camera parameter I_{emiccd}.*

$$\frac{g(I_{\text{emiccd}})}{F} = \begin{cases} (0.20 \pm 0.01) \times I_{\text{emiccd}} & \text{from hist. fitting} \\ (0.15 \pm 0.01) \times I_{\text{emiccd}} & \text{from photon transfer} \end{cases} \tag{E.7}$$

Therefore we used the average of the two slopes which is 0.17 ± 0.01. The other parameters relevant to the camera operation were determined from both techniques to be :

$$N_{\text{off}} = 575.3 \pm 0.7 (\text{counts}) \tag{E.8}$$

The read noise was evaluated to range from 8 to 17 ADU from both techniques..

To verify the compatibility of our description, we computed the photocathode quantum efficiency $Q(\lambda)$ from our measurement of $R(\lambda, I_{emiccd} = 5000)$. Indeed, as shown above:

$$Q(\lambda) = \frac{F}{g(I_{emiccd})} \times R(\lambda, I_{emiccd}) \tag{E.9}$$

We used this equation and our measurement of $R(\lambda, I_{emiccd} = 5000)$ to plot Figure E.6. We see that we obtain the good

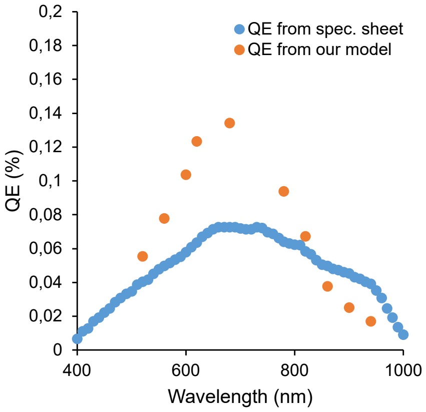

Figure E.6: *Quantum efficiency of the photo-cathode as a function of wavelength. In blue from the specification sheet and in orange from our measurements and models. Note that the manufacturer did not provide specification sheets specific to our precise photo-cathode.*

order of magnitude for the quantum efficency of the photo-cathode which is quite validating our approach. The exact values are not retrieved, but the values of the specification sheet are not the precise measurement of our photo-cathode but rather a generic reference.

Finally we can obtain:

Statement E.2.3. Obtained camera parameters. We have determined that:

$$N_{\text{off}} = 575.3 \pm 0.7(\text{counts}) \tag{E.10}$$

and :

$$\frac{g(I_{\text{emiccd}})}{F} = (0.17 \pm 0.01) \times I_{\text{emiccd}} \tag{E.11}$$

and that:

$$\frac{g(I_{\text{emiccd}})Q(\lambda)}{F} = \frac{I_{\text{emiccd}}}{5000} \underbrace{R(\lambda, I_{\text{emiccd}} = 5000)}_{\substack{\text{Exp. determined in} \\ \text{Figure 2.19}}} \tag{E.12}$$

With these experimental values, numerical applications of Statement E.2.2 may be conducted.

E.2.4 The uncertainty

A first uncertainty may be defined from the image. When taking a spatial average, that is the mean decay over a specific region, two options may be considered to define the error. The first is to first take the average and then use the formula given above. The second would be to apply the formula to each pixel and then take the average under the hypothesis of having independent pixels. In both cases the mean value will be the same, but the error will be slightly different. The difference will arise from the difference there is between the square root of the mean and the mean of the square root of a random variable. Because the square root is convex down the square root of the mean will always exceed the mean of the square root. This means that to overestimate the error one can decide that the correct procedure consists in averaging first and then compute the error.

A second uncertainty comes from the statistical model. With Statement E.2.2 we can devise the following procedure to determine the uncertainty:

Statement E.2.4. Uncertainty on the number of counts. The procedure is the following:

1. Measure a given number of counts N_{ADU}
2. Measure the dark level and measure $N_{\text{ADU}}^{\text{dark}}$. From this value compute:

$$\langle \mathbf{N}_{\text{sp.}} \rangle = \frac{F}{g(I_{\text{emiccd.}})} \left(N_{\text{ADU}}^{\text{dark}} - N_{\text{off}} \right) \tag{E.13}$$

3. Compute $\langle \mathbf{N}_{\text{ph.}} \rangle$ by using the responsivity and formula Equation (E.4).
4. From all of the determined values, compute the uncertainty on the counts number $\Delta N_{\text{ADU}} = \sqrt{\text{Var}(\boldsymbol{N}_{\text{ADU}})}$:

$$\Delta N_{\text{ADU}} = \left(\frac{g(I_{\text{emiccd}})}{F} \right) \sqrt{2\langle \mathbf{N}_{\text{sp.}} \rangle + Q(\lambda)\left(1 + Q(\lambda)\right)\langle \mathbf{N}_{\text{ph.}} \rangle} \tag{E.14}$$

We test our model by comparing two methods to estimate the SNR, see Figure E.7. We use the EPFL samples, that emit at 810nm, we have an acquisition of 35 repetitions. We can compute the Signal over noise ratio (SNR) in a first manner by using the observed mean and standard deviation over the 35 repetitions as described in Figure E.7 (a). But with our procedure described above, we can estimate the SNR with only one measurement (plus a dark measurement), as shown in Figure E.7 (b). In (c) we plot the image of the average number of counts. In (d) the same map but expressed in term of number of photons. Finally in (e) we plot the ratio of the SNR maps. We see that the SNR of our model is under-evaluated at 65% of what is experimentally found. This is a good result: we think we are less precise that we actually are, we do not over-estimate the quality of our signal. Our method (b) has the advantage of being able to estimate the SNR much faster than in method (a) where 35 repetitions were needed.

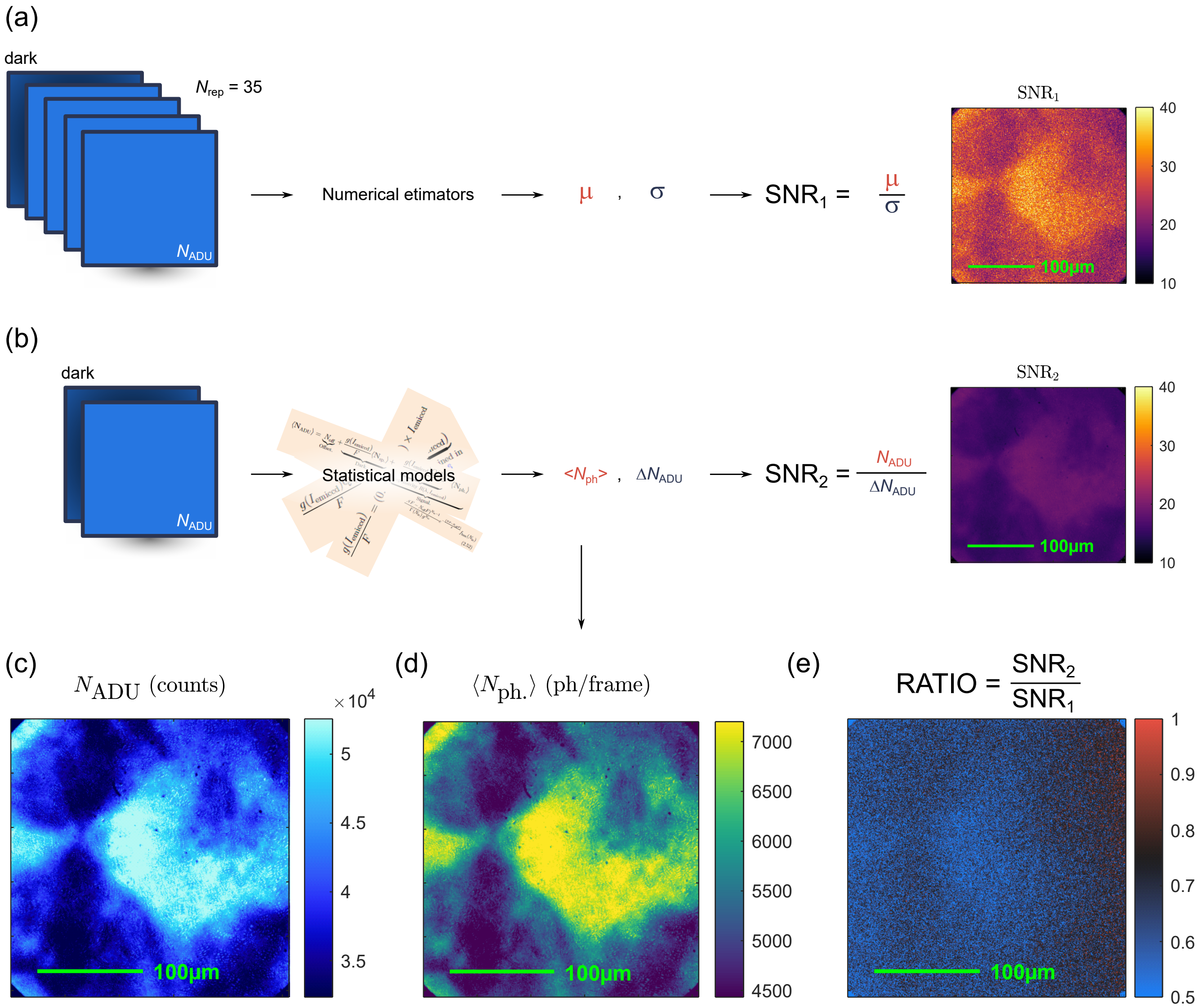

Figure E.7: *Comparison of the SNR implied by our statistical model and the SNR computed from a series of repetition of the images. The ratio is SNR_2 over SNR_1. Our statistical model does slightly overestimate the error with an average ratio of 65 %.*

Appendix F

Short-time scaling additional details

F.1 Additional details

F.1.1 Taking Auger Recombination into account

In Result 4.2.1, Auger recombination are not considered. However, the model can be generalized to include them. We consider the added term $k_3(\Delta n)^3$ in the recombination term, with k_3 the Auger coefficient, so that the recombination term becomes:

$$R = k_1 \frac{(\Delta n)^2}{\Delta n + N_{bulk}} + k_2(\Delta n)^2 + k_3(\Delta n)^3 \tag{F.1}$$

To further simplify, we take the approximation that $\frac{N_{bulk}}{n_\gamma \alpha} \ll 1$. The scaling law can be computed with the added Auger term, following the same demonstration as exposed above. One finds:

$$\left.\frac{dI_{\mathrm{PL}}^{norm}}{dt}\right|_{t=0} = -2\left[k_1 + 2\alpha S_{top} + \alpha^2 D\right] - \frac{4}{3}k_2\alpha n_\gamma - k_3\alpha^2 n_\gamma^2 \tag{F.2}$$

When taking Auger recombination into account, one finds an order 2 polynomial in the laser fluence n_γ. Experimentally, we did not observe this behavior, which justifies the fact that we neglected Auger recombination.

F.1.2 Low absorption regime

We report here the generalized case of the Scaling Law Equation (4.22) for laser wavelengths where the approximation $e^{-\alpha(\lambda)L} \ll 1$ cannot be made. We place ourselves in the case where the defect related densities can be neglected meaning, specifically in the case where N_{bulk},N_{top},$N_{bot} \ll n_\gamma \alpha e^{-\alpha L}$. In this case, the generalized scaling we obtain is the following:

$$\left.\frac{dI_{\mathrm{PL}}^{norm}}{dt}\right|_{t=0} = -2k_1 - 2\alpha^2 D - \frac{4\alpha}{1-e^{-2\alpha L}}\left(S_{top} + S_{bot}e^{-2\alpha L}\right) - \frac{4}{3}k_2\alpha\left(\frac{1-e^{-3\alpha L}}{1-e^{-2\alpha L}}\right)n_\gamma \tag{F.3}$$

In this case, the bottom surface recombination appears, even if it is scaled by a factor $e^{-2\alpha L}$ compared to the top surface recombination coefficient. In the high absorption case considered in this study, we have $e^{-\alpha L} \approx e^{-3.25} \approx 0.039$. This gives the following numerical results for the coefficients:

$$\left.\frac{dI_{\mathrm{PL}}^{norm}}{dt}\right|_{t=0} = -2k_1 - 2\alpha^2 D - 4\alpha\underbrace{\frac{1}{1-e^{-2\alpha L}}}_{\approx 1.0015}\left(S_{top} + S_{bot}\underbrace{e^{-2\alpha L}}_{\approx 0.0015}\right) - \frac{4}{3}k_2\alpha\underbrace{\left(\frac{1-e^{-3\alpha L}}{1-e^{-2\alpha L}}\right)}_{\approx 1.0014}n_\gamma \tag{F.4}$$

This computation justifies our assumption of high absorption that gives Equation (4.22). However, in the case of a laser light closer to the gap of the material under study, the condition $e^{-\alpha L} \ll 1$ may be false and the correct formula for the scaling is given by Equation (F.3).

F.1.3 Computation of the integral I

This subsection described the computation of I, introduced in section 4.2.2, and given by:

$$I = \int_0^L dz \frac{\Delta n^3}{\Delta n + N_{bulk}} \tag{F.5}$$

when the density is equal at short time to $\Delta n(z, t = 0) = n_\gamma \alpha e^{-\alpha z}$. This yields us:

$$I = (n_\gamma \alpha)^2 \int_0^L dz \frac{e^{-3\alpha z}}{e^{-\alpha z} + \frac{N_{bulk}}{n_\gamma \alpha}} \tag{F.6}$$

A change of variables $x = \exp(-\alpha z)$ with $dx = -\alpha x dz$ yields:

$$I = n_\gamma^2 \alpha \int_{e^{-\alpha L}}^1 dx \frac{x^2}{x + \frac{N_{bulk}}{n_\gamma \alpha}} \tag{F.7}$$

A primitive of $\frac{x^2}{x+a}$ is $a^2 \ln(a + x) + \frac{1}{2}x(x - 2a)$. This formula gives us the result:

$$I = n_\gamma^2 \alpha \left[\left(\frac{N_{bulk}}{n_\gamma \alpha}\right)^2 \ln\left(\frac{\frac{N_{bulk}}{n_\gamma \alpha} + 1}{\frac{N_{bulk}}{n_\gamma \alpha} + e^{-\alpha L}}\right) + \frac{1}{2} - \frac{N_{bulk}}{n_\gamma \alpha} - \frac{1}{2}e^{-\alpha L}\left(e^{-\alpha L} - 2\frac{N_{bulk}}{n_\gamma \alpha}\right)\right] \tag{F.8}$$

This formula can be recast in the following way:

$$I = \frac{n_\gamma^2 \alpha}{2} \times C\left(\frac{N_{bulk}}{n_\gamma \alpha}, e^{-\alpha L}\right) \tag{F.9}$$

With C a function described by:

$$C\left(\frac{N_{bulk}}{n_\gamma \alpha}, e^{-\alpha L}\right) = 2\left[\left(\frac{N_{bulk}}{n_\gamma \alpha}\right)^2 \ln\left(\frac{\frac{N_{bulk}}{n_\gamma \alpha}+1}{\frac{N_{bulk}}{n_\gamma \alpha}+e^{-\alpha L}}\right) + \frac{1}{2} - \frac{N_{bulk}}{n_\gamma \alpha} - \frac{1}{2}e^{-\alpha L}\left(e^{-\alpha L} - 2\frac{N_{bulk}}{n_\gamma \alpha}\right)\right] \tag{F.10}$$

We will show that in a wide range of parameters one can make the approximation that $C\left(\frac{N_{bulk}}{n_\gamma \alpha}, e^{-\alpha L}\right) \approx 1$. In our study, $e^{-\alpha L} \approx e^{-3.25} \approx 0.039$, and in Figure F.1 we plot C as a function of $\frac{N_{bulk}}{n_\gamma \alpha}$ and $e^{-\alpha L}$ and report the expected range of our study by a red polygon. To draw this polygon, we allow α to vary $\pm 10\%$ around the value $\alpha = 6.5 \times 10^4\ cm^{-1}$. We see that the value of C depends weekly on both variable (a change of approximately 20% of C for a change of almost 2 orders of magnitude of $\frac{N_{bulk}}{n_\gamma \alpha}$). As long as both $e^{-\alpha L} \ll 1$ and $\frac{N_{bulk}}{n_\gamma \alpha} \ll 1$, the value of C can be considered constant to a first approximation: $C = 1 \pm 0.25$.

Therefore, for our parameter set, we can approximate that:

$$I = \frac{n_\gamma^2 \alpha}{2} \tag{F.11}$$

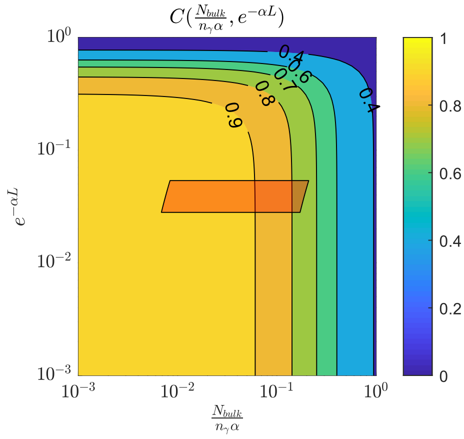

Figure F.1: *Plotting the map of C as a function of $e^{-\alpha L}$ and $\frac{N_{bulk}}{n_\gamma \alpha}$. The red rectangle corresponds to our case of interest, with $L = 500nm$ and $\alpha = 6.5 \times 10^4\ cm^{-1}$ varied from $\pm 10\%$, and $n_\gamma \in [4, 100] \times 10^{11}\ ph.cm^{-2}$ and $N_{bulk} = 4.9 \times 10^{15}\ cm^{-3}$ (as found by our fitting method, see the corresponding section below). In that region, the value of C is close to 1 at 25%.*

F.2 The role of photon recycling and outcoupling

In this subsection we discuss the impact that photon recycling and photon outcoupling could have on Equation (4.22). We use a model found in the literature [Ansari-Rad and Bisquert 2018] to evaluate their impact.

F.2.1 Description of the model

We implement the model of Ansari-Rad and Bisquert [Ansari-Rad and Bisquert 2018]. This model couples the density of photons, noted Γ, and the density of carriers, Δn, via two drift diffusion equations. A coupling parameter β between them is introduced in [Ansari-Rad and Bisquert 2018]. The couple of equations in the present case can be written as:

$$\frac{\partial \Delta n}{\partial t}(z,t) = D\frac{\partial^2 \Delta n}{\partial z^2}(z,t) - k_1\frac{(\Delta n)^2}{\Delta n + N_{bulk}} - k_2(\Delta n)^2 + \beta\Gamma \tag{F.12}$$

$$\frac{\partial \Gamma}{\partial t}(z,t) = D_{\Gamma}\frac{\partial^2 \Gamma}{\partial z^2}(z,t) + k_2(\Delta n)^2 - \beta \Gamma \tag{F.13}$$

with D_{Γ} the effective diffusion coefficient for photons, β the coupling parameter. These equations are accompanied with boundary conditions. For the equation of carriers on Δn, they are given above. For the photon density Γ they are as follows:

$$D_{\Gamma}\frac{\partial \Gamma}{\partial z}(z=0,t) = S_{top-\Gamma}\Gamma(z=0,t) \tag{F.14}$$

$$D_{\Gamma}\frac{\partial \Gamma}{\partial z}(z=L,t) = -S_{bot-\Gamma}\Gamma(z=L,t) \tag{F.15}$$

The initial condition for Γ is set at $\Gamma(z, t = 0) = 0$.

In this framework, one can define the output $I_{\mathrm{PL}}(t)$ to be proportional to $\Gamma(z = 0, t)$, i.e. to the output flow of photons via the top surface.

We used this framework to estimate the impact of photon recycling. To do so, we simulated the decays using these formulae and measured numerically the scaling law on the obtained decays. Our main parameter is the re-absorption coefficient α_{reabs}. In [Ansari-Rad and Bisquert 2018], formulae are given to link the effective diffusion coefficient for photons D_{Γ}, the coupling parameter β and the outcoupling parameters $S_{top-\Gamma}$ and $S_{bot-\Gamma}$ to the re-absorption coefficient α_{reabs}, the speed of light in vacuum c and n_r the refractive index of the perovskite layer.

$$D_{\Gamma} = \frac{c}{n_r \alpha_{reabs}} \tag{F.16}$$

$$\beta = \frac{\alpha_{reabs} c}{n_r} \tag{F.17}$$

$$S_{top-\Gamma} = S_{bot-\Gamma} = \frac{c}{2n_r} \tag{F.18}$$

F.2.2 Parameters of the model

For the recombination and charge carrier parameters, we used the parameters given in Table 4.3. For the photon parameters, we used a value of $n_r = 2.5$ and varied α_{reabs} in the range 10^2 to 10^4 cm^{-1}.

F.2.3 Results of the model

The results are presented in Figure F.2. In (a) two decays obtained at the highest fluence (10^{13} ph.cm^{-2}) are presented for the case without photon recycling and the case with photon recycling with a reabsorption coefficient of $\alpha_{reabs} = 10^2 cm^{-1}$. We observe no notable difference. In (b) we plot the scaling

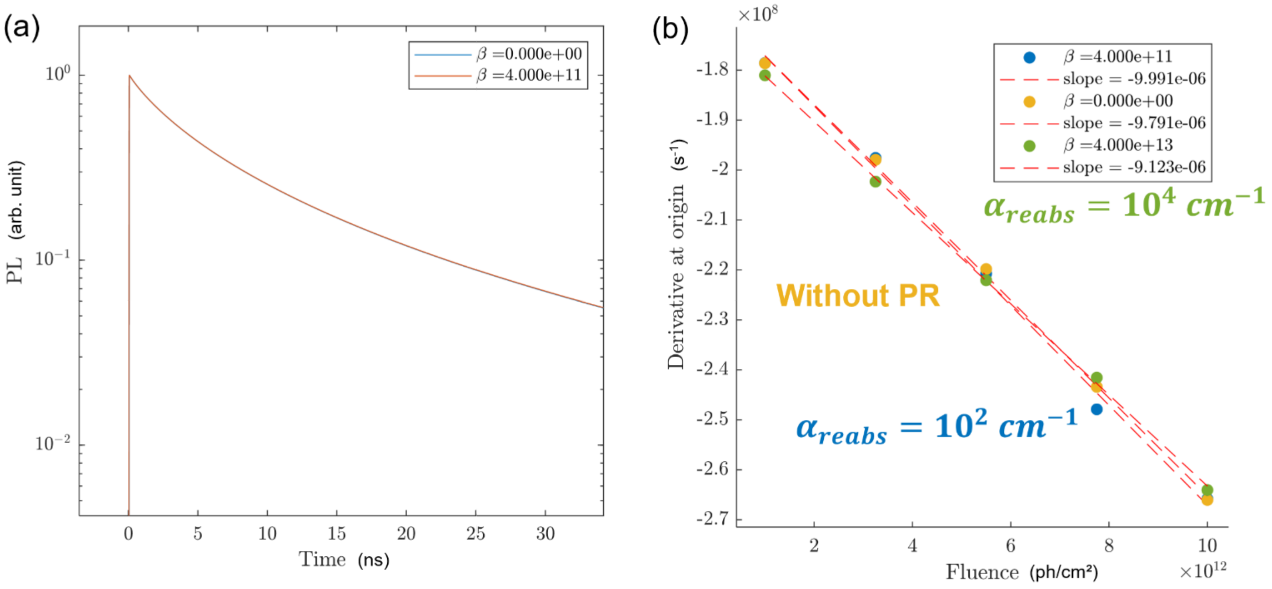

Figure F.2: *Impact of photon recycling. (a) TR-PL decay at high fluence (1e13 ph/cm²) simulated with (blue) and without (orange) photon recycling taken into account. The reabsorption coefficient was set to* $10^2\ cm^{-1}$*. (b) Scaling law at short time as a function of fluence for the case with (blue and green) and without (yellow) photon recycling.*

law obtained for three distinct scenarii: (i) with no photon recycling, (ii) with photon recycling $\alpha_{reabs} = 10^2 cm^{-1}$, (iii) with photon recycling $\alpha_{reabs} = 10^4 cm^{-1}$. All scalings show very similar slopes and intercept. We found an impact of the photon recycling only for $\alpha_{reabs} = 2 \times 10^4 cm^{-1}$ which is a very high value for the absorption coefficient around the emission peak. Therefore, we observe no impact of photon recycling on the scaling for sensible values of reabsorption coefficient. We conclude that in our case, the internal value of the radiative recombination coefficient is close to the external one.

F.2.4 Impact of photon-outcoupling at the surfaces

The impact of the photon outcoupling parameter at the surface is studied here. We start from using the value suggested by Ansari-Rad and Bisquert and modify it with an increase and reduction of one order of magnitude. Two cases are considered: one with low reabsorption ($\alpha_{reabs} = 10^2$ cm^{-1}) and one with high reabsorption ($\alpha_{reabs} = 10^4$ cm^{-1}). Result are shown in Figure F.3 (a) and (b). In the low reabsorption coefficient case, no impact is observed of the outcoupling parameter on the scaling. In the high reabsorption case, an impact is shown on the scaling. We have two observations.

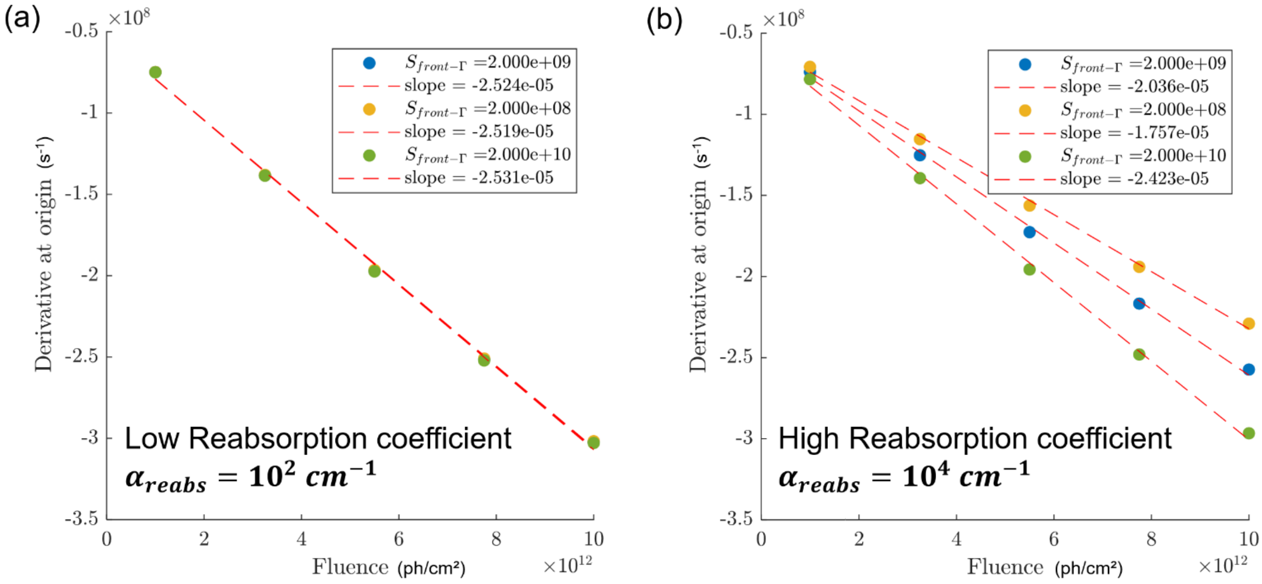

Figure F.3: *Impact of the outcoupling surface parameter on the derived scaling law. (a) Case of low reabsorption ($\alpha_{reabs} = 10^2\ cm^{-1}$) – we see no impact of the surface outcoupling parameter (all the curves are superimposed). (b) Case of high reabsorption ($\alpha_{reabs} = 10^4\ cm^{-1}$), for three different outcoupling parameters: reference value from Ansari-Rad and Bisquert, one order of magnitude less, one order of magnitude more. The impact on slope of the scaling remains in the ± 20% range.*

One, the impact on the slope is limited to ±20% even though we changed the outcoupling parameter by one order of magnitude. This would be below our measurement sensibility. Two, all scalings show a similar intercept. This means that the outcoupling parameter does not affect the intercept of the scaling. We conclude that in the low reabsorption present case, the outcoupling parameter has but low impact on the observed external radiative recombination coefficient. **In a more general case, the observed slope of the scaling would be modified by light outcoupling parameters**: the value of k_2 extracted in this case is what we define as the **external radiative recombination coefficient**.

F.3 The role of deconvolution

This section introduces different deconvolution algortihms and discusses their impact on the obtained result. To correctly evaluate the deconvolution, we measured our apparatus response function as shown in the Methods section (see Figure 2.11) and used Fast Fourier Transform algorithms to recover the original signal. A parameter, noted K is needed for Wiener filter deconvolution, and taken to be $K = 0.1$ for

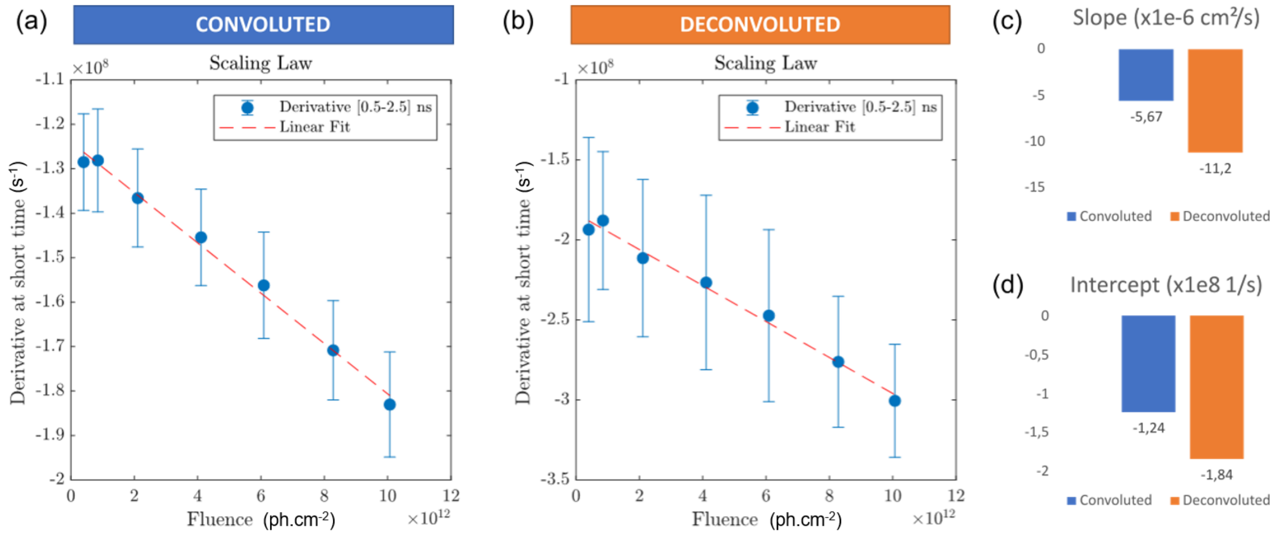

Figure F.4: *(a) Scaling computed on original decays. (b) Scaling computed on deconvoluted decays. The parameter $K = 0.1$. (c) Comparison of the obtain fitted slope (d) Comparison of the obtained fitted intercept.*

the previously given results. Its influence is discussed below. We also tested a third method of deconvolution, via an effective fit of a convolved bi-exponential with results close to the Wiener deconvolution.

F.3.1 Wiener Filter

A deconvolution algorithm via Fourier transform is used. The temporal shape of the gate was acquired and fitted with a model using complementary error-functions, see Figure F.5 (h). The model for the gate temporal shape is:

$$h(t) = \frac{1}{2}\left[\operatorname{erfc}\left(\frac{t-t_1}{\Delta t_1}\right) - \operatorname{erfc}\left(\frac{t-t_2}{\Delta t_2}\right)\right] \tag{F.19}$$

The fitted parameters for our gate are : $t_1 = -(1.361 \pm 0.017)ns$, $\Delta t_1 = (0.719 \pm 0.033)ns$, $t_2 = (1.592 \pm 0.016)ns$, $\Delta t_2 = (0.619 \pm 0.030)ns$. A noise constant of 600 counts was added.

To deconvolve the signal, a Wiener fielter is used. If $S = F(s)$ and $H = F(h)$ are the Fourier transform of the signal and of our temporal gate, then we apply the following to obtain our deconvolved signal s_d:

$$s_d = F^{-1}\left(\frac{S}{H}\frac{|H|^2}{|H|^2 + K}\right) \tag{F.20}$$

with K a chosen coefficient. The computation are performed using Fast Fourier Transform algorithms, and the resulting

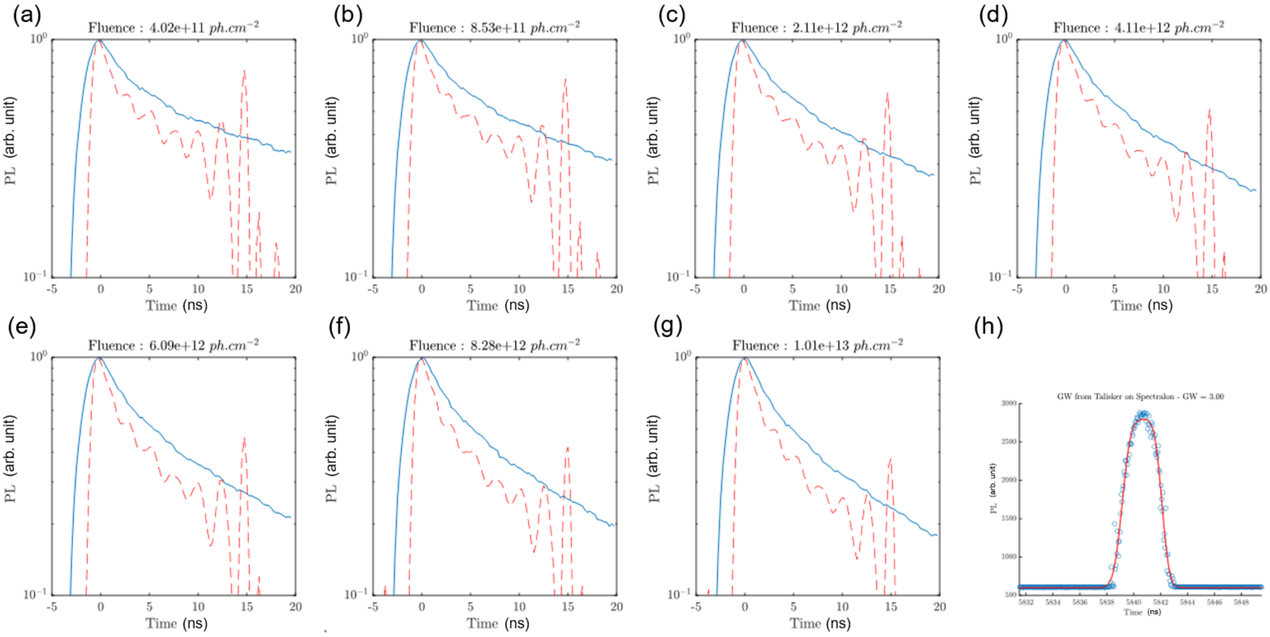

Figure F.5: *(a-g) Deconvolution of the seven highly-resolved decays with Wiener filter. (Blue solid line) Original decays (red dotted line) Deconvoluted decays. For this deconvolution the parameter $K = 0.1$. All curves are normalized to their maximal value. We can observe oscillations after 3ns approximately after the maximum value is reached. (h) Temporal shape of the 3ns-long gate of the camera. (Blue points) Experimental data ; (Red line) Phenomenological fit.*

decay with $K = 0.1$ are shown in Figure F.5 (a-g). The deconvolution works well only for the short time and high signal-to-noise-ratio temporal region, which is the one of interest for us.

The scaling law may be computed for the convoluted and for the deconvoluted cases. Figure F.4 shows the two cases. We observe that temporal convolution has an impact on both the intercept and the slope. The convoluted slope is approximately 50% of the deconvoluted one, which is compatible with our simulations of the impact of deconvolution. The intercept is slightly improved by the deconvolution algorithm.

The influence of the parameter K on the obtained decays and scaling laws is shown in Figure F.6. In (a) and (b) the impact on the the deconvoluted decays is shown. Higher noise is observed when lowering K towards the end of the decay, but sharper results are obtained at the beginning, (a). One can see that the oscillations in the less intense part of the signal become comparable to the maximal value observed. In (b), we see that increasing K gives a smoother result but closer to the original convoluted one. The impact of K on the scaling is shown in (c). The slope is mainly not affected by K with a 10% change when K varies from 0.05 to 0.2. The intercept

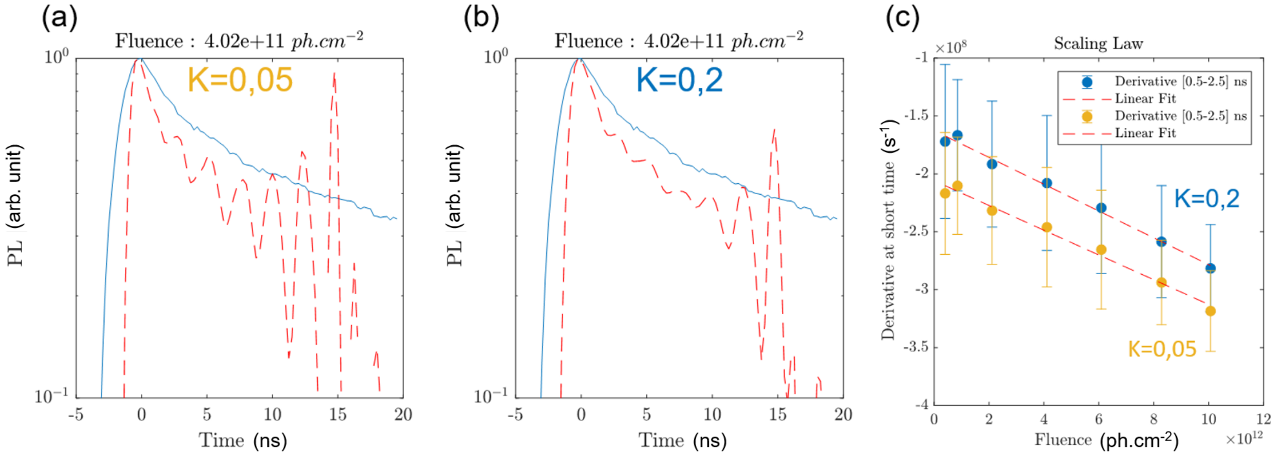

Figure F.6: *Influence of the parameter K. (a-b) Similar decay deconvoluted with (a) $K = 0.05$ and $K = 0.2$. (c). Comparisons of the scaling laws computed on deconvoluted decays with $K = 0.05$ (yellow) and $K = 0.2$ (blue). A linear fit is performed for both. For the blue points with $K = 0.2$, Slope : $-1.16e - 05 \pm 1.28e - 06\ cm^2 s^{-1}$ Intercept: $-1.63e + 08 \pm 7.32e + 06\ s^{-1}$. For the yellow points with $K = 0.05$, Slope : $-1.07e - 05 \pm 1.52e - 06\ cm^2 s^{-1}$ Intercept: $-2.06e + 08 \pm 8.71e + 06\ s^{-1}$.*

is more sensible to a change of K with a 25% change in the intercept when K is divided by 4. The results still are compatible when considering the error-bars. We conclude that K does not affect the slope, hence does not affect the extracted value of αk_2 . We chose $K = 0.1$ as an intermediate solution, with K small enough to have an effect of deconvolution but K high enough to ensure that noise on the deconvoluted decays is less than the maximum of the curves.

F.3.2 Fitting of a convoluted exponential

We implemented a second method of deconvolution. It consists in fitting a bi-exponential decay convoluted by the instrument response function on the experimental decay. From the parameters of the fitted bi-exponential, the derivative at the origin is computed. If the bi-exponential is written:

$$E(t) = a_1 e^{b_1 t} + a_2 e^{b_2 t}$$

Then the derivative at short time is computed as $a_1 b_1 + a_2 b_2$. Only three parameters are fitted as we have the normalization condition $a_1 + a_2 = 1$.

The results are shown in Figure F.7. The Wiener deconvolution is also added for comparison. The fitted convoluted exponential are quite close to the experimental observations. We note that the deconvoluted bi-exponential is very close to the Wiener deconvolution result. The corresponding scaling

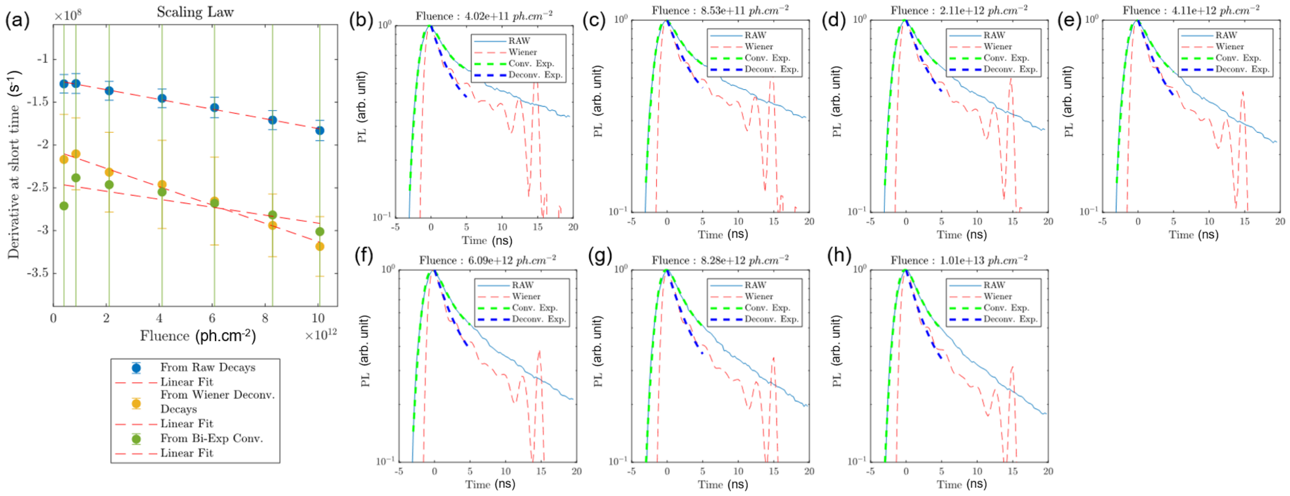

Figure F.7: *Comparison of the deconvolution methods. (a) Scaling law for the three ways to compute the initial slope: from the raw decays (blue), from the Wiener deconvoluted decays (yellow) and from the parameters fitted from a bi-exponential convoluted with the instrument response function (green). (b-h) Decays and the deconvolution results. The original decay (blue line) is super-imposed with the Wiener deconvolution results (dashed red). The fitting result of a convoluted bi-exponential is presented in (dashed green), while the resulting "raw" bi-exponential is in (dashed blue).*

is observed in (a). While the order of magnitude is similar for the Wiener and bi-exp method, the bi-exp method is subject to higher uncertainty. The uncertainty comes from the fitting algorithm and as the derivative is computed with three fitting parameters, all coming with an uncertainty, the total uncertainty is high, of the order of 100%. This makes us conclude that the Wiener Filter is a better method to use.

Appendix G

Theoretical considerations

G.1 The drift diffusion model exact solutions

G.1.1 Approximate analytical solution in the case of top surface recombination only

Here we study the simpler case where $S_{\text{bot.}} = 0$. In this case, one can show that we have the approximate forms in the case where $S_{\text{top}}L/D \ll 1$:

$$\beta_1 \approx \sqrt{\frac{S_{\text{top}}}{LD}} \tag{G.1}$$

And for all $k \geq 2$,

$$\beta_k \approx (k-1)\frac{\pi}{L} + \frac{S_{\text{top}}}{D}\frac{1}{(k-1)\pi + \frac{S_{\text{top}}L}{D}\frac{1}{(k-1)\pi}} \tag{G.2}$$

The lifetime corresponding to each eigenvalue therefore scales for $k \geq 2$,

$$\tau_k \approx \frac{L^2}{D\pi^2(k-1)^2} \tag{G.3}$$

And the amplitude of the given eigenfunction in case of initial condition $\Delta n_0(z) = \alpha n_\gamma e^{-\alpha z}$ is approximately:

$$A_k \approx \frac{2n_\gamma}{L} \times \frac{1 + \frac{S_{\text{top}}}{D\alpha}}{1 + \frac{\beta_k^2}{\alpha^2}} \tag{G.4}$$

G.1.2 The ratio surfaces vs. bulk

One can use the exact resolution to define the bulk vs. surface ratio of recombination. Let us consider a simplified case without radiative recombination $S_{\text{bot.}} = 0\,\text{cm}\,\text{s}^{-1}$. In this case one can define the following recombination currents:

$$j_{\text{top}} = S_{\text{top}} \Delta n(z=0,t) \tag{G.5}$$

$$j_{\text{bulk}} = k_1 \int_0^L \Delta n(z,t)\,dz \approx k_1 L \left\langle \Delta n \right\rangle (t) \tag{G.6}$$

With these quantities defined, we can also define the ratio of top recombination over bulk recombination at time t, $\eta^{\text{tb}}(t)$, as:

$$\underbrace{\eta^{\text{tb}}(t)}_{\substack{\text{Ratio of top}\\ \text{vs bulk rec.}}} \equiv \frac{j_{\text{top}}}{j_{\text{bulk}}} \approx \underbrace{\frac{S_{\text{top}}}{k_1 L}}_{\equiv \eta_0^{\text{tb}}} \times \underbrace{\frac{\Delta n(z=0,t)}{\left\langle \Delta n \right\rangle (t)}}_{\substack{\text{Ratio of top}\\ \text{vs bulk densities}}} \tag{G.7}$$

This ratio can therefore be decomposed into the product of two ratios : one that would occur due to the recombination parameters η_0^{tb} and that can play the role of a proxy of η^{tb} if no other information is known ; the other ratio is a ratio between the density of carriers at the top and the average density of carriers in the bulk. Due to top surface recombination, this ratio is expected to be lower than 1 in the long time. At very long time, we can argue that the ratio of top vs bulk densities is time independent. Indeed, at long time, one can simplify the decomposition of Equation (5.7) by only considering the first term of the sum, and to a certain extent we can compute this ratio as:

$$\frac{\Delta n(z=0,t)}{\left\langle \Delta n \right\rangle (t)} \approx \frac{\Delta n(z=0,t)}{\Delta n(z=L,t)} \underset{t\longrightarrow\infty}{\approx} \frac{U_1(0)}{U_1(L)} \tag{G.8}$$

Where the U_1 spatial function is defined in Equation (5.9). This ratio may actually be computed exactly as a function of $\beta_1 L$:

$$\frac{U_1(0)}{U_1(L)} = \frac{1}{\cos(\beta_1 L)\,(1+\beta_1^2 L^2)} \tag{G.9}$$

In the present case, we have this definition for $\beta_1 L$:

$$(\beta_1 L)\tan(\beta_1 L) = \frac{S_{\text{top}} L}{D} \tag{G.10}$$

In the cases where $\frac{S_{\text{top}} L}{D}$ is small compared to 1, the value of $\beta_1 L$ is simply the square root of this quantity.

Therefore we can say:

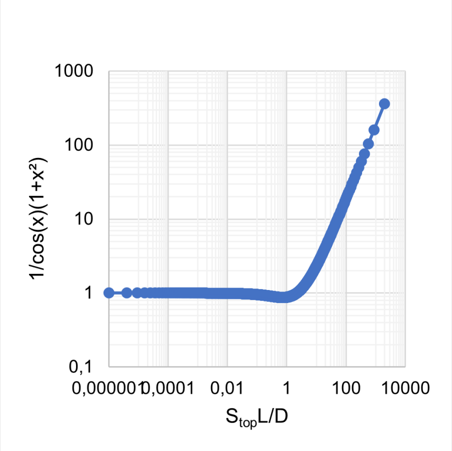

Figure G.1: *Right ratio of Equation (G.11) as a function of* $\frac{S_{top} L}{D}$.

Statement G.1.1. Definition of the ratio top-bulk. In the case of negligible bottom surface recombination, one can obtain the ratio of top recombination over bulk recombination *at long time* via:

$$\eta_{\infty}^{\mathrm{tb}} \approx \underbrace{\frac{S_{\mathrm{top}}}{k_1 L}}_{\equiv \eta_0^{\mathrm{tb}}} \times \frac{1}{\cos(x)\,(1+x^2)} \tag{G.11}$$

Where x is the solution of:

$$x \tan(x) = \frac{S_{\mathrm{top}} L}{D} \tag{G.12}$$

In cases where one has $\frac{S_{\mathrm{top}} L}{D} \ll 1$, one can approximate: $x \approx \sqrt{\frac{S_{\mathrm{top}} L}{D}}$. In the absence of other non radiative recombination, one can compute the share of non radiative recombination as:

$$\%_{\mathrm{top}}^{\text{non rad. rec.}} = \frac{\eta_{\infty}^{\mathrm{tb}}}{1+\eta_{\infty}^{\mathrm{tb}}} \tag{G.13}$$

$$\%_{\mathrm{bulk}}^{\text{non rad. rec.}} = \frac{1}{1+\eta_{\infty}^{\mathrm{tb}}} \tag{G.14}$$

Bibliography

[Adeleye *et al.* 2021] D. Adeleye, A. Lomuscio, M. Sood and S. Siebentritt. 'Lifetime, quasi-Fermi level splitting and doping concentration of Cu-rich CuInS2 absorbers'. *Materials Research Express*, **vol. 8**, no. 2, p. 025905 (2021) (cited page 77)

[Ahrenkiel 1992] R. K. Ahrenkiel. 'Measurement of minority-carrier lifetime by time-resolved photoluminescence'. *Solid State Electronics*, **vol. 35**, no. 3, pp. 239–250 (1992) (cited pages 27, 165)

[Ahrenkiel and Dashdorj 2015] R. K. Ahrenkiel and J. Dashdorj. 'Interface recombination velocity measurement by a contactless microwave technique Interface recombination velocity measurement by a contactless microwave technique'. **vol. 2063**, no. 2004 (2015) (cited page 165)

[Ahrenkiel and Lundstrom 1993] R. K. Ahrenkiel and M. Lundstrom. *Minority Carriers in III-V Semiconductors: Physics and Applications*. Semiconductors and semimetals. Academic Press, Incorporated (1993). ISBN 9780127521398 (cited pages 28, 131, 132)

[Al-Ashouri *et al.* 2020] A. Al-Ashouri, E. Köhnen, B. Li, A. Magomedov, H. Hempel, P. Caprioglio, J. A. Márquez, A. B. M. Vilches, E. Kasparavicius, J. A. Smith, N. Phung, D. Menzel, M. Grischek, L. Kegelmann, D. Skroblin, C. Gollwitzer, T. Malinauskas, M. Jošt, G. Matič, B. Rech, R. Schlatmann, M. Topič, L. Korte, A. Abate, B. Stannowski, D. Neher, M. Stolterfoht, T. Unold, V. Getautis and S. Albrecht. 'Monolithic perovskite/silicon tandem solar cell with ¿29% efficiency by enhanced hole extraction'. *Science*, **vol. 370**, no. 6522, pp. 1300–1309 (2020) (cited page 23)

[Ansari-Rad and Bisquert 2018] M. Ansari-Rad and J. Bisquert. 'Insight into Photon Recycling in Perovskite Semiconductors from the Concept of Photon Diffusion'. *Physical Review Applied*, **vol. 10**, no. 3, p. 034062 (2018) (cited pages 48, 267, 268)

[Avella *et al.* 2016] A. Avella, I. Ruo-Berchera, I. P. Degiovanni, G. Brida and M. Genovese. 'Absolute calibration of an EMCCD camera by quantum correlation, linking photon counting to the analog regime'. *Optics Letters*, **vol. 41**, no. 8, p. 1841 (2016) (cited pages 255, 256)

[Baloch *et al.* 2018] A. A. Baloch, F. H. Alharbi, G. Grancini, M. I. Hossain, M. K. Nazeeruddin and N. Tabet. 'Analysis of Photocarrier Dynamics at Interfaces in Perovskite Solar Cells by Time-Resolved Photoluminescence'. *Journal of Physical Chemistry C*, **vol. 122**, no. 47, pp. 26805–26815 (2018) (cited pages 28, 131)

[Becquerel 1867] E. Becquerel. *La lumiere, ses causes et ses effets*, vol. 1. Paris (1867) (cited page 77)

[Bercegol *et al.* 2018] A. Bercegol, F. J. Ramos, A. Rebai, T. Guillemot, D. Ory, J. Rousset and L. Lombez. 'Slow Diffusion and Long Lifetime in Metal Halide Perovskites for Photovoltaics'. *The Journal of Physical Chemistry C*, **vol. 122**, no. 43, pp. 24570–24577 (2018) (cited pages 23, 28, 118, 119, 122, 134, 136, 138)

[Bercegol *et al.* 2019] A. Bercegol, D. Ory, D. Suchet, S. Cacovich, O. Fournier, J. Rousset and L. Lombez. 'Quantitative optical assessment of photonic and electronic properties in halide perovskite'. *Nature Communications* (2019) (cited pages 23, 28)

[Bercegol *et al.* 2020] A. Bercegol, S. Cacovich, G. Vidon, S. Mejaouri, A. Yaiche, J. B. Puel, C. Longeaud, J. F. Guillemoles, S. Jutteau, J. Rousset, D. Ory and L. Lombez. 'Imaging Electron, Hole, and Ion Transport in Halide Perovskite'. *Journal of Physical Chemistry C*, **vol. 124**, no. 22, pp. 11741–11748 (2020) (cited pages 28, 123, 131, 217)

[Bertoluzzi *et al.* 2018] L. Bertoluzzi, R. A. Belisle, K. A. Bush, R. Cheacharoen, M. D. McGehee and B. C. O'Regan. 'In Situ Measurement of Electric-Field Screening in Hysteresis-Free PTAA/FA0.83Cs0.17Pb(I0.83Br0.17)3/C60 Perovskite Solar Cells Gives an Ion Mobility of 3 × 10-7 cm2/(V s), 2 Orders of Magnitude Faster than Reported for Metal-Oxide-Contacted Perovskite Cells with Hysteresis'. *Journal of the American Chemical Society*, **vol. 140**, no. 40, pp. 12775–12784 (2018) (cited pages 24, 217)

[Bidaud 2021] T. Bidaud. *Characterization of nanomaterials by cathodoluminescence for photovoltaic applications.* Ph.D. thesis, Université Paris-Saclay (2021) (cited page 27)

[Brenes *et al.* 2019] R. Brenes, M. Laitz, J. Jean, D. W. deQuilettes and V. Bulovi\ifmmode \acutec\else ć\fi. 'Benefit from Photon Recycling at the Maximum-Power Point of State-of-the-Art Perovskite Solar Cells'. *Phys. Rev. Applied*, **vol. 12**, no. 1, p. 14017 (2019) (cited pages 48, 138, 142, 143)

[Buczkowski *et al.* 1991] A. Buczkowski, Z. J. Radzimski, G. A. Rozgonyi and F. Shimura. 'Bulk and surface components of recombination lifetime based on a two-laser microwave reflection technique'. *Journal of Applied Physics*, **vol. 69**, no. 9, pp. 6495–6499 (1991) (cited page 165)

[Burgelman *et al.* 2000] M. Burgelman, P. Nollet and S. Degrave. 'Modelling polycrystalline semiconductor solar cells'. *Thin Solid Films*, **vol. 361**, pp. 527–532 (2000) (cited page 95)

[Burgelman *et al.* 2013] M. Burgelman, K. Decock, S. Khelifi and A. Abass. 'Advanced electrical simulation of thin film solar cells'. *Thin Solid Films*, **vol. 535**, no. 1, pp. 296–301 (2013) (cited page 71)

[Cacovich *et al.* 2020] S. Cacovich, D. Messou, A. Bercegol, S. Béchu, A. Yaiche, H. Shafique, J. Rousset, P. Schulz, M. Bouttemy and L. Lombez. 'Light-induced passivation in triple cation mixed halide perovskites: Interplay between transport properties and surface chemistry'. *ACS Applied Materials and Interfaces*, **vol. 12**, no. 31, pp. 34784–34794 (2020) (cited pages 24, 48, 52)

[Cacovich *et al.* 2022a] S. Cacovich, P. Dally, G. Vidon, M. Legrand, S. Gbegnon, J. Rousset, J.-B. Puel, J.-F. Guillemoles, P. Schulz, M. Bouttemy and A. Etcheberry. 'In-Depth Chemical and Optoelectronic Analysis of Triple-Cation Perovskite Thin Films by Combining XPS Profiling and PL Imaging'. *ACS Applied Materials & Interfaces*, p. acsami.1c22286 (2022) (cited pages 87, 98, 124, 127, 181, 184, 225)

[Cacovich *et al.* 2022b] S. Cacovich, G. Vidon, M. Degani, M. Legrand, L. Gouda, J.-B. Puel, Y. Vaynzof, J.-F. Guillemoles, D. Ory and G. Grancini. 'Imaging and quantifying non-radiative losses at 23% efficient inverted perovskite solar cells interfaces'. *Nature Communications 2022 13:1*, **vol. 13**, no. 1, pp. 1–9 (2022) (cited pages 24, 25, 98, 101, 102, 225)

[Ceratti *et al.* 2018] D. R. Ceratti, Y. Rakita, L. Cremonesi, R. Tenne, V. Kalchenko, M. Elbaum, D. Oron, M. A. C. Potenza, G. Hodes and D. Cahen. 'Self-Healing Inside APbBr3 Halide Perovskite Crystals'. *Advanced Materials*, **vol. 30**, no. 10, p. 1706273 (2018) (cited page 24)

[Chen *et al.* 2021] W. Chen, Z. Gan, M. A. Green, B. Jia and X. Wen. 'Revealing Dynamic Effects of Mobile Ions in Halide Perovskite Solar Cells Using Time-Resolved Microspectroscopy'. *Small Methods*, **vol. 5**, no. 1, p. 2000731 (2021) (cited page 213)

[Crothers *et al.* 2017] T. W. Crothers, R. L. Milot, J. B. Patel, E. S. Parrott, J. Schlipf, P. Müller-Buschbaum, M. B. Johnston and L. M. Herz. 'Photon Reabsorption Masks Intrinsic Bimolecular Charge-Carrier Recombination in CH3NH3PbI3 Perovskite'. *Nano Letters*, **vol. 17**, no. 9, pp. 5782–5789 (2017) (cited page 48)

[Dashdorj *et al.* 2004] J. Dashdorj, R. Ahrenkiel and W. Metzger. 'Modeling of recombination lifetimes in charge-separation device structures'. *MRS Online Proceedings Library 2004 799:1*, **vol. 799**, no. 1, pp. 141–145 (2004) (cited page 193)

[Delamarre 2013] A. Delamarre. *Developpement de nouvelles methodes de caracterisation opto-electroniques des cellules solaires*. Ph.D. thesis (2013) (cited page 86)

[DeQuilettes *et al.* 2015] D. W. DeQuilettes, S. M. Vorpahl, S. D. Stranks, H. Nagaoka, G. E. Eperon, M. E. Ziffer, H. J. Snaith and D. S. Ginger. 'Impact of microstructure on local carrier lifetime in perovskite solar cells'. *Science*, **vol. 348**, no. 6235, pp. 683–686 (2015) (cited pages 27, 77, 131)

[Dequilettes *et al.* 2019] D. W. Dequilettes, K. Frohna, D. Emin, T. Kirchartz, V. Bulovic, D. S. Ginger and S. D. Stranks. 'Charge-Carrier Recombination in Halide Perovskites' (2019) (cited page 131)

[Draguta *et al.* 2018] S. Draguta, J. A. Christians, Y. V. Morozov, A. Mucunzi, J. S. Manser, P. V. Kamat, J. M. Luther and M. Kuno. 'A quantitative and spatially resolved analysis of the performance-bottleneck in high efficiency, planar hybrid perovskite solar cells'. *Energy and Environmental Science*, **vol. 11**, no. 4, pp. 960–969 (2018) (cited page 148)

[El-Hajje *et al.* 2016] G. El-Hajje, C. Momblona, L. Gil-Escrig, J. Ávila, T. Guillemot, J. F. Guillemoles, M. Sessolo, H. J. Bolink and L. Lombez. 'Quantification of spatial inhomogeneity in perovskite solar cells by hyperspectral luminescence imaging'. *Energy and Environmental Science*, **vol. 9**, no. 7, pp. 2286–2294 (2016) (cited page 87)

[Eränen and Blomberg 1984] S. Eränen and M. Blomberg. 'Simultaneous measurement of recombination lifetime and surface recombination velocity'. *Journal of Applied Physics*, **vol. 56**, no. 8, pp. 2372–2374 (1984) (cited page 165)

[Feldmann *et al.* 2019] S. Feldmann, S. Macpherson, S. P. Senanayak, M. Abdi-Jalebi, J. P. H. Rivett, G. Nan, G. D. Tainter, T. A. S. Doherty, K. Frohna, E. Ringe, R. H. Friend, H. Sirringhaus, M. Saliba, D. Beljonne, S. D. Stranks and F. Deschler. 'Photodoping through local charge carrier accumulation in alloyed hybrid perovskites for highly efficient luminescence'. *Nature Photonics 2019 14:2*, **vol. 14**, no. 2, pp. 123–128 (2019) (cited page 148)

[García-Batlle *et al.* 2021] M. García-Batlle, S. Deumel, J. E. Huerdler, S. F. Tedde, A. Guerrero, O. Almora and G. Garcia-Belmonte. 'Mobile Ion-Driven Modulation of Electronic Conductivity Explains Long-Timescale Electrical Response in Lead Iodide Perovskite Thick Pellets'. *ACS Applied Materials and Interfaces*, **vol. 13**, no. 30, pp. 35617–35624 (2021) (cited pages 24, 217)

[Gaubas and Vanhellemont 1996] E. Gaubas and J. Vanhellemont. 'A simple technique for the separation of bulk and surface recombination parameters in silicon'. *Journal of Applied Physics*, **vol. 80**, no. 11, pp. 6293–6297 (1996) (cited pages 165, 166, 169, 183, 189)

[Gaubas *et al.* 2018] E. Gaubas, T. Čeponis, D. Dobrovolskas, J. Mickevičius, J. Pavlov, V. Rumbauskas, J. V. Vaitkus, N. Alimov and S. Otajonov. 'Study of polycrystalline CdTe films by contact and contactless pulsed photo-ionization spectroscopy'. *Thin Solid Films*, **vol. 660**, no. February, pp. 231–235 (2018) (cited page 165)

[Giesecke *et al.* 2010] J. A. Giesecke, M. Kasemann, M. C. Schubert, P. Würfel and W. Warta. 'Separation of local bulk and surface recombination in crystalline silicon from luminescence reabsorption'. *Progress in Photovoltaics: Research and Applications*, **vol. 18**, no. 1, pp. 10–19 (2010) (cited pages 92, 166)

[Głowienka *et al.* 2020] D. Głowienka, D. Zhang, F. Di Giacomo, M. Najafi, S. Veenstra, J. Szmytkowski and Y. Galagan. 'Role of surface recombination in perovskite solar cells at the interface of HTL/CH3NH3PbI3'. *Nano Energy*, **vol. 67**, p. 104186 (2020) (cited page 47)

[Goetz *et al.* 2020] K. P. Goetz, A. D. Taylor, F. Paulus, Y. Vaynzof, K. P. Goetz, A. D. Taylor, F. Paulus and Y. Vaynzof. 'Shining Light on the Photoluminescence Properties of Metal Halide Perovskites'. *Advanced Functional Materials*, **vol. 30**, no. 23, p. 1910004 (2020) (cited page 99)

[Guillemoles *et al.* 2019] J. F. Guillemoles, T. Kirchartz, D. Cahen and U. Rau. 'Guide for the perplexed to the Shockley–Queisser model for solar cells' (2019) (cited pages 20, 37)

[Haddad *et al.* 2020] J. Haddad, B. Krogmeier, B. Klingebiel, L. Krückemeier, S. Melhem, Z. Liu, J. Hüpkes, S. Mathur and T. Kirchartz. 'Analyzing Interface Recombination in Lead-Halide Perovskite Solar Cells with Organic and Inorganic Hole-Transport Layers'. *Advanced Materials Interfaces*, **vol. 7**, no. 16, p. 2000366 (2020) (cited page 47)

[Hall 1952] R. N. Hall. 'Electron-hole recombination in germanium [21]' (1952) (cited page 42)

[Handa *et al.* 2017] T. Handa, D. M. Tex, A. Shimazaki, A. Wakamiya and Y. Kanemitsu. 'Charge Injection Mechanism at Heterointerfaces in CH3NH3PbI3 Perovskite Solar Cells Revealed by Simultaneous Time-Resolved Photoluminescence and Photocurrent Measurements'. *Journal of Physical Chemistry Letters*, **vol. 8**, no. 5, pp. 954–960 (2017) (cited page 45)

[He *et al.* 2022] X. He, M. Xia, H. Wu, X. Du, Z. Song, S. Zhao, X. Chen, G. Niu and J. Tang. 'Quasi-2D Perovskite Thick Film for X-Ray Detection with Low Detection Limit'. *Advanced Functional Materials*, **vol. 32**, no. 7, p. 2109458 (2022) (cited page 187)

[Heinz *et al.* 2017] F. D. Heinz, W. Warta and M. C. Schubert. 'Separation of the surface and bulk recombination in silicon by means of transient photoluminescence'. *Applied Physics Letters*, **vol. 110**, no. 4 (2017) (cited page 165)

[Henri Bergson 1889] Henri Bergson. *Essai sur les données immédiates de la conscience*. Paris, puf ed. (1889). ISBN 978-2-13-056273-3, 1–322 pp. (cited page 30)

[Herz 2017] L. M. Herz. 'Charge-Carrier Mobilities in Metal Halide Perovskites: Fundamental Mechanisms and Limits'. *ACS Energy Letters*, **vol. 2**, no. 7, pp. 1539–1548 (2017) (cited page 23)

[Hirsch *et al.* 2013] M. Hirsch, R. J. Wareham, M. L. Martin-Fernandez, M. P. Hobson and D. J. Rolfe. 'A Stochastic Model for Electron Multiplication Charge-Coupled Devices - From Theory to Practice'. *PLoS ONE*, **vol. 8**, no. 1 (2013) (cited pages 255, 256)

[Hoke *et al.* 2014] E. T. Hoke, D. J. Slotcavage, E. R. Dohner, A. R. Bowring, H. I. Karunadasa and M. D. McGehee. 'Reversible photo-induced trap formation in mixed-halide hybrid perovskites for photovoltaics'. *Chemical Science*, **vol. 6**, no. 1, pp. 613–617 (2014) (cited page 22)

[Holovský *et al.* 2017] J. Holovský, S. De Wolf, J. Werner, Z. Remeš, M. Müller, N. Neykova, M. Ledinský, L. Černá, P. Hrzina, P. Löper, B. Niesen and C. Ballif. 'Photocurrent Spectroscopy of Perovskite Layers and Solar Cells: A Sensitive Probe of Material Degradation'. *Journal of Physical Chemistry Letters*, **vol. 8**, no. 4, pp. 838–843 (2017) (cited page 135)

[Hutter *et al.* 2020] E. M. Hutter, T. Kirchartz, B. Ehrler, D. Cahen and E. v. Hauff. 'Pitfalls and prospects of optical spectroscopy to characterize perovskite-transport layer interfaces'. *Applied Physics Letters*, **vol. 116**, no. 10, p. 100501 (2020) (cited page 131)

[IPCC 2022] IPCC. 'Climate Change 2022: Mitigation of Climate Change. Contribution of Working Group III to the Sixth Assessment Report of the Intergovernmental Panel on Climate Change'. Tech. rep. (2022) (cited pages 16, 17)

[Janesick *et al.* 1985] J. Janesick, K. Klaasen and T. Elliott. 'CCD Charge Collection Efficiency And The Photon Transfer Technique'. *https://doi.org/10.1117/12.950297*, **vol. 0570**, pp. 7–19 (1985) (cited pages 255, 260)

[Jariwala *et al.* 2021] S. Jariwala, S. Burke, S. Dunfield, R. C. Shallcross, M. Taddei, J. Wang, G. E. Eperon, N. R. Armstrong, J. J. Berry and D. S. Ginger. 'Reducing surface recombination velocity of methylammonium-free mixed-cation mixed-halide perovskites via surface passivation'. *Chemistry of Materials*, **vol. 33**, no. 13, pp. 5035–5044 (2021) (cited page 48)

[Jeong *et al.* 2021] J. Jeong, M. Kim, J. Seo, H. Lu, P. Ahlawat, A. Mishra, Y. Yang, M. A. Hope, F. T. Eickemeyer, M. Kim, Y. J. Yoon, I. W. Choi, B. P. Darwich, S. J. Choi, Y. Jo, J. H. Lee, B. Walker, S. M. Zakeeruddin, L. Emsley, U. Rothlisberger, A. Hagfeldt, D. S. Kim, M. Grätzel and J. Y. Kim. 'Pseudo-halide anion engineering for α-FAPbI3 perovskite solar cells'. *Nature 2021 592:7854*, **vol. 592**, no. 7854, pp. 381–385 (2021) (cited page 21)

[Jin *et al.* 2020] H. Jin, E. Debroye, M. Keshavarz, I. G. Scheblykin, M. B. Roeffaers, J. Hofkens and J. A. Steele. 'It's a trap! on the nature of localised states and charge trapping in lead halide perovskites'. *Materials Horizons*, **vol. 7**, no. 2, pp. 397–410 (2020) (cited page 23)

[Kaienburg *et al.* 2020] P. Kaienburg, L. Krückemeier, D. Lübke, J. Nelson, U. Rau and T. Kirchartz. 'How solar cell efficiency is governed by the $\alpha\mu\tau$ product'. *Physical Review Research*, **vol. 2**, no. 2, p. 23109 (2020) (cited page 20)

[Kaiser *et al.* 2021] C. Kaiser, O. J. Sandberg, N. Zarrabi, W. Li, P. Meredith and A. Armin. 'A universal Urbach rule for disordered organic semiconductors'. *Nature Communications 2021 12:1*, **vol. 12**, no. 1, pp. 1–9 (2021) (cited pages 23, 223)

[Kanevce *et al.* 2014] A. Kanevce, D. H. Levi and D. Kuciauskas. 'The role of drift, diffusion, and recombination in time-resolved photoluminescence of CdTe solar cells determined through numerical simulation'. *Progress in Photovoltaics: Research and Applications*, **vol. 22**, no. 11, pp. 1138–1146 (2014) (cited page 132)

[Kiligaridis *et al.* 2021] A. Kiligaridis, P. A. Frantsuzov, A. Yangui, S. Seth, J. Li, Q. An, Y. Vaynzof and I. G. Scheblykin. 'Are Shockley-Read-Hall and ABC models valid for lead halide perovskites?' *Nature Communications*, **vol. 12**, no. 1, pp. 1–19 (2021) (cited page 23)

[Kim *et al.* 2021] E. B. Kim, M. S. Akhtar, H. S. Shin, S. Ameen and M. K. Nazeeruddin. 'A review on two-dimensional (2D) and 2D-3D multidimensional perovskite solar cells: Perovskites structures, stability, and photovoltaic performances'. *Journal of Photochemistry and Photobiology C: Photochemistry Reviews*, **vol. 48**, p. 100405 (2021) (cited page 99)

[Kirchartz and Rau 2018] T. Kirchartz and U. Rau. 'What Makes a Good Solar Cell?' *Advanced Energy Materials*, **vol. 8**, no. 28, p. 1703385 (2018) (cited page 20)

[Kirchartz *et al.* 2020] T. Kirchartz, J. A. Márquez, M. Stolterfoht and T. Unold. 'Photoluminescence-Based Characterization of Halide Perovskites for Photovoltaics'. *Advanced Energy Materials*, p. 1904134 (2020) (cited pages 28, 83, 99, 131, 136)

[Kojima *et al.* 2009] A. Kojima, K. Teshima, Y. Shirai and T. Miyasaka. 'Organometal halide perovskites as visible-light sensitizers for photovoltaic cells'. *Journal of the American Chemical Society*, **vol. 131**, no. 17, pp. 6050–6051 (2009) (cited page 21)

[Kousik *et al.* 2003] G. S. Kousik, Z. G. Ling and P. K. Ajmera. 'Nondestructive technique to measure bulk lifetime and surface recombination velocities at the two surfaces by infrared absorption due to pulsed optical excitation'. **vol. 141**, no. 1992 (2003) (cited page 165)

[Krogmeier *et al.* 2018] B. Krogmeier, F. Staub, D. Grabowski, U. Rau and T. Kirchartz. 'Quantitative analysis of the transient photoluminescence of CH 3 NH 3 PbI 3 /PC 61 BM heterojunctions by numerical simulations'. *Sustainable Energy and Fuels*, **vol. 2**, no. 5, pp. 1027–1034 (2018) (cited pages 132, 136)

[Krückemeier *et al.* 2021a] L. Krückemeier, B. Krogmeier, Z. Liu, U. Rau and T. Kirchartz. 'Understanding Transient Photoluminescence in Halide Perovskite Layer Stacks and Solar Cells'. *Advanced Energy Materials*, **vol. 11**, no. 19, p. 2003489 (2021) (cited pages 99, 193)

[Krückemeier *et al.* 2021b] L. Krückemeier, Z. Liu, B. Krogmeier, U. Rau, T. Kirchartz, L. Krückemeier, Z. Liu, B. Krogmeier, U. Rau and T. Kirchartz. 'Consistent Interpretation of Electrical and Optical Transients in Halide Perovskite Layers and Solar Cells'. *Advanced Energy Materials*, **vol. 11**, no. 46, p. 2102290 (2021) (cited page 193)

[Kumar *et al.* 2020] S. Kumar, G. Hodes and D. Cahen. ‘Defects in halide perovskites: The lattice as a boojum?’ *MRS Bulletin*, **vol. 45**, no. 6, pp. 478–484 (2020) (cited pages 23, 166)

[Ledinsky *et al.* 2019] M. Ledinsky, T. Schönfeldová, J. Holovský, E. Aydin, Z. Hájková, L. Landová, N. Neyková, A. Fejfar and S. De Wolf. ‘Temperature Dependence of the Urbach Energy in Lead Iodide Perovskites’. *Journal of Physical Chemistry Letters*, **vol. 10**, no. 6, pp. 1368–1373 (2019) (cited pages 23, 223)

[Ledinsky *et al.* 2020] M. Ledinsky, A. Vlk, T. Schonfeldova, J. Holovsky, E. Aydin, H. X. Dang, Z. Hajkova, L. Landova, J. Valenta, A. Fejfar and S. de Wolf. ‘Impact of cation multiplicity on halide perovskite defect densities and solar cell voltages’. *Journal of Physical Chemistry C*, **vol. 124**, no. 50, pp. 27333–27339 (2020) (cited page 23)

[Levine *et al.* 2018] I. Levine, S. Gupta, A. Bera, D. Ceratti, G. Hodes, D. Cahen, D. Guo, T. J. Savenije, J. Ávila, H. J. Bolink, O. Millo, D. Azulay and I. Balberg. ‘Can we use time-resolved measurements to get steady-state transport data for halide perovskites?’ *Journal of Applied Physics*, **vol. 124**, no. 10, p. 103103 (2018) (cited pages 85, 148)

[Lin *et al.* 2020] H. J. Lin, S. Cacovich, A. Rebai, J. Rousset and C. Longeaud. ‘Influence of Environment and Light-Stress on the Optoelectronic Properties of Triple-Cation Perovskite Thin Films’. *ACS Applied Materials and Interfaces*, **vol. 12**, no. 17, pp. 19495–19503 (2020) (cited page 135)

[Ling and Ajmera 1991] Z. G. Ling and P. K. Ajmera. ‘Measurement of bulk lifetime and surface recombination velocity by infrared absorption due to pulsed optical excitation’. *Journal of Applied Physics*, **vol. 69**, no. 1, pp. 519–521 (1991) (cited page 165)

[Ling *et al.* 1998] Z. G. Ling, P. K. Ajmera, G. S. Kousik, Z. G. Ling, P. K. Ajmera and G. S. Kousik. ‘Simultaneous extraction of bulk lifetime and surface recombination velocities from free carrier absorption transients Simultaneous extraction of bulk lifetime and surface recombination velocities from free carrier absorption transients’. **vol. 2718**, no. 1994, pp. 1–4 (1998) (cited page 165)

[Look and Leach 2016] D. C. Look and J. H. Leach. ‘On the accurate determination of absorption coefficient from reflectanceand transmittance measurements: Application to Fe-doped GaN’. *Journal of Vacuum Science & Technology B, Nanotechnology and Microelectronics: Materials, Processing, Measurement, and Phenomena*, **vol. 34**, no. 4, p. 04J105 (2016) (cited page 182)

[Löper *et al.* 2015] P. Löper, M. Stuckelberger, B. Niesen, J. Werner, M. Filipič, S. J. Moon, J. H. Yum, M. Topič, S. De Wolf and C. Ballif. ‘Complex refractive index spectra of CH3NH3PbI3 perovskite thin films determined by spectroscopic ellipsometry and spectrophotometry’. *Journal of Physical Chemistry Letters*, **vol. 6**, no. 1, pp. 66–71 (2015) (cited page 135)

[Luke and Cheng 1987] K. L. Luke and L. J. Cheng. ‘Analysis of the interaction of a laser pulse with a silicon wafer: Determination of bulk lifetime and surface recombination velocity’. *Journal of Applied Physics*, **vol. 61**, no. 6, pp. 2282–2293 (1987) (cited page 165)

[Mahmud *et al.* 2020] M. A. Mahmud, T. Duong, Y. Yin, H. T. Pham, D. Walter, J. Peng, Y. Wu, L. Li, H. Shen, N. Wu, N. Mozaffari, G. Andersson, K. R. Catchpole, K. J. Weber and T. P.

White. ‘Double-Sided Surface Passivation of 3D Perovskite Film for High-Efficiency Mixed-Dimensional Perovskite Solar Cells’. *Advanced Functional Materials*, **vol. 30**, no. 7, p. 1907962 (2020) (cited page 99)

[Maiberg and Scheer 2014] M. Maiberg and R. Scheer. ‘Theoretical study of time-resolved luminescence in semiconductors. II. Pulsed excitation’. *Journal of Applied Physics*, **vol. 116**, no. 12, p. 123711 (2014) (cited pages 28, 46, 90, 131, 132, 133)

[Maiberg *et al.* 2015] M. Maiberg, C. Spindler, E. Jarzembowski and R. Scheer. ‘Electrical characterization of Cu(In,Ga)Se2-solar cells by voltage dependent time-resolved photoluminescence’. *Thin Solid Films*, **vol. 582**, pp. 379–382 (2015) (cited pages 193, 213)

[Marnissi *et al.* 2017] Y. Marnissi, Y. Zheng, E. Chouzenoux and J.-C. Pesquet. ‘A Variational Bayesian Approach for Image Restoration—Application to Image Deblurring With Poisson–Gaussian Noise’. *IEEE Transactions on Computational Imaging*, **vol. 3**, no. 4, pp. 722–737 (2017) (cited pages 31, 255)

[McKelvey 1982] J. P. McKelvey. *Solid state and semiconductor physics.* Krieger Pub. Co, New York, harper and row ed. (1982). ISBN 9780898743968, 512 pp. (cited page 165)

[McMeekin *et al.* 2016] D. P. McMeekin, G. Sadoughi, W. Rehman, G. E. Eperon, M. Saliba, M. T. Hörantner, A. Haghighirad, N. Sakai, L. Korte, B. Rech, M. B. Johnston, L. M. Herz and H. J. Snaith. ‘A mixed-cation lead mixed-halide perovskite absorber for tandem solar cells’. *Science*, **vol. 351**, no. 6269, pp. 151–155 (2016) (cited page 22)

[Michl *et al.* 2012] B. Michl, J. A. Giesecke, W. Warta and M. C. Schubert. ‘Separation of front and backside surface recombination by photoluminescence imaging on both wafer sides’. *IEEE Journal of Photovoltaics*, **vol. 2**, no. 3, pp. 348–351 (2012) (cited pages 92, 166)

[Miyata *et al.* 2015] A. Miyata, A. Mitioglu, P. Plochocka, O. Portugall, J. T. W. Wang, S. D. Stranks, H. J. Snaith and R. J. Nicholas. ‘Direct measurement of the exciton binding energy and effective masses for charge carriers in organic–inorganic tri-halide perovskites’. *Nature Physics 2014 11:7*, **vol. 11**, no. 7, pp. 582–587 (2015) (cited page 37)

[Motti *et al.* 2019] S. G. Motti, T. Crothers, R. Yang, Y. Cao, R. Li, M. B. Johnston, J. Wang and L. M. Herz. ‘Heterogeneous Photon Recycling and Charge Diffusion Enhance Charge Transport in Quasi-2D Lead-Halide Perovskite Films’. *Nano Lett*, **vol. 19**, p. 11 (2019) (cited page 23)

[Musiienko *et al.* 2021] A. Musiienko, D. R. Ceratti, J. Pipek, M. Brynza, H. Elhadidy, E. Belas, M. Betušiak, G. Delport and P. Praus. ‘Defects in Hybrid Perovskites: The Secret of Efficient Charge Transport’. *Advanced Functional Materials*, p. 2104467 (2021) (cited page 23)

[Nayak *et al.* 2018] P. K. Nayak, M. Sendner, B. Wenger, Z. Wang, K. Sharma, A. J. Ramadan, R. Lovrinčić, A. Pucci, P. K. Madhu and H. J. Snaith. ‘Impact of Bi3+ Heterovalent Doping in Organic-Inorganic Metal Halide Perovskite Crystals’. *Journal of the American Chemical Society*, **vol. 140**, no. 2, pp. 574–577 (2018) (cited page 23)

[NREL] NREL. ‘Best Research-Cell Efficiency Chart — Photovoltaic Research — NREL’ (cited page 21)

[Ogita 2013] Y. Ogita. 'Bulk lifetime and surface recombination velocity measurement method in semiconductor wafers Bulk lifetime and surface recombination velocity measurement method in semiconductor wafers'. **vol. 6954**, no. 1996 (2013) (cited page 165)

[Ory *et al.* 2021] D. Ory, N. Paul and L. Lombez. 'Extended quantitative characterization of solar cell from calibrated voltage-dependent electroluminescence imaging'. *Journal of Applied Physics*, **vol. 129**, no. 4, p. 043106 (2021) (cited page 27)

[Palais and Arcari 2004] O. Palais and A. Arcari. 'Contactless measurement of bulk lifetime and surface recombination velocity in silicon wafers'. **vol. 4686**, no. 2003, pp. 1–6 (2004) (cited page 165)

[Pazos-Outón *et al.* 2016] L. M. Pazos-Outón, M. Szumilo, R. Lamboll, J. M. Richter, M. Crespo-Quesada, M. Abdi-Jalebi, H. J. Beeson, M. Vrućinić, M. Alsari, H. J. Snaith, B. Ehrler, R. H. Friend and F. Deschler. 'Photon recycling in lead iodide perovskite solar cells'. *Science*, **vol. 351**, no. 6280, pp. 1430–1433 (2016) (cited page 48)

[Péan *et al.* 2019] E. V. Péan, C. S. De Castro and M. L. Davies. 'Shining a light on the photoluminescence behaviour of methylammonium lead iodide perovskite: investigating the competing photobrightening and photodarkening processes'. *Materials Letters*, **vol. 243**, pp. 191–194 (2019) (cited page 121)

[Rahmany and Etgar 2021] S. Rahmany and L. Etgar. 'Two-dimensional or passivation treatment: the effect of hexylammonium post deposition treatment on 3D halide perovskite-based solar cells'. *Materials Advances*, **vol. 2**, no. 8, pp. 2617–2625 (2021) (cited page 99)

[Rakita *et al.* 2015] Y. Rakita, S. R. Cohen, N. K. Kedem, G. Hodes and D. Cahen. 'Mechanical properties of APbX3 (A = Cs or CH3NH3; X= I or Br) perovskite single crystals'. *MRS Communications 2015 5:4*, **vol. 5**, no. 4, pp. 623–629 (2015) (cited page 24)

[Rau and Kirchartz 2019] U. Rau and T. Kirchartz. 'Charge Carrier Collection and Contact Selectivity in Solar Cells'. *Advanced Materials Interfaces*, **vol. 6**, no. 20, p. 1900252 (2019) (cited page 23)

[Richter *et al.* 2016] J. M. Richter, M. Abdi-Jalebi, A. Sadhanala, M. Tabachnyk, J. P. Rivett, L. M. Pazos-Outón, K. C. Gödel, M. Price, F. Deschler and R. H. Friend. 'Enhancing photoluminescence yields in lead halide perovskites by photon recycling and light out-coupling'. *Nature Communications*, **vol. 7** (2016) (cited page 48)

[Roldán-Carmona *et al.* 2015] C. Roldán-Carmona, P. Gratia, I. Zimmermann, G. Grancini, P. Gao, M. Graetzel and M. K. Nazeeruddin. 'High efficiency methylammonium lead triiodide perovskite solar cells: the relevance of non-stoichiometric precursors'. *Energy & Environmental Science*, **vol. 8**, no. 12, pp. 3550–3556 (2015) (cited page 191)

[Rong *et al.* 2018] Y. Rong, Y. Ming, W. Ji, D. Li, A. Mei, Y. Hu and H. Han. 'Toward Industrial-Scale Production of Perovskite Solar Cells: Screen Printing, Slot-Die Coating, and Emerging Techniques'. *Journal of Physical Chemistry Letters*, **vol. 9**, no. 10, pp. 2707–2713 (2018) (cited page 22)

[Rosenwaks *et al.* 1994] Y. Rosenwaks, B. R. Thacker, R. K. Ahrenkiel, A. J. Nozik and I. Yavneh. 'Photogenerated carrier dynamics under the influence of electric fields in III-V semiconductors'. *Physical Review B*, **vol. 50**, no. 3, pp. 1746–1754 (1994) (cited pages 193, 212)

[Saba *et al.* 2014] M. Saba, M. Cadelano, D. Marongiu, F. Chen, V. Sarritzu, N. Sestu, C. Figus, M. Aresti, R. Piras, A. Geddo Lehmann, C. Cannas, A. Musinu, F. Quochi, A. Mura and G. Bongiovanni. 'Correlated electron-hole plasma in organometal perovskites'. *Nature Communications*, **vol. 5**, no. 1, pp. 1–10 (2014) (cited pages 132, 148)

[Sanchez *et al.* 2018] S. Sanchez, X. Hua, N. Phung, U. Steiner and A. Abate. 'Flash Infrared Annealing for Antisolvent-Free Highly Efficient Perovskite Solar Cells'. *Advanced Energy Materials*, **vol. 8**, no. 12, p. 1702915 (2018) (cited page 104)

[Sánchez *et al.* 2019] S. Sánchez, M. Vallés-Pelarda, J. A. Alberola-Borràs, R. Vidal, J. J. Jerónimo-Rendón, M. Saliba, P. P. Boix and I. Mora-Seró. 'Flash infrared annealing as a cost-effective and low environmental impact processing method for planar perovskite solar cells'. *Materials Today*, **vol. 31**, pp. 39–46 (2019) (cited page 104)

[Sánchez *et al.* 2020a] S. Sánchez, X. Hua, A. Günzler, E. Bermúdez-Ureña, D. Septiadi, M. Saliba and U. Steiner. 'Flash Infrared Pulse Time Control of Perovskite Crystal Nucleation and Growth from Solution'. *Crystal Growth and Design*, **vol. 20**, no. 2, pp. 670–679 (2020) (cited pages 104, 236)

[Sánchez *et al.* 2020b] S. Sánchez, J. Jerónimo-Rendon, M. Saliba and A. Hagfeldt. 'Highly efficient and rapid manufactured perovskite solar cells via Flash InfraRed Annealing'. *Materials Today*, **vol. 35**, pp. 9–15 (2020) (cited page 104)

[Sánchez *et al.* 2021] S. Sánchez, B. Carlsen, V. Škorjanc, N. Flores, P. Serafini, I. Mora-Seró, P. Schouwink, S. M. Zakeeruddin, M. Graetzel and A. Hagfeldt. 'Thermodynamic stability screening of IR-photonic processed multication halide perovskite thin films'. *Journal of Materials Chemistry A*, **vol. 9**, no. 47, pp. 26885–26895 (2021) (cited page 104)

[Sánchez *et al.* 2022] S. Sánchez, S. Cacovich, G. Vidon, J. F. Guillemoles, F. T. Eickemeyer, S. M. Zakeeruddin, J. Schawe, J. F. Löffler, C. Cayron, P. Schouwink and M. Grätzel. 'Thermally Controlled Growth of Photoactive FAPbI3 Films for Highly Stable Perovskite Solar Cells'. *Energy & Environmental Science* (2022) (cited pages 26, 104, 225)

[Sarritzu *et al.* 2017] V. Sarritzu, N. Sestu, D. Marongiu, X. Chang, S. Masi, A. Rizzo, S. Colella, F. Quochi, M. Saba, A. Mura and G. Bongiovanni. 'Optical determination of Shockley-Read-Hall and interface recombination currents in hybrid perovskites'. *Scientific Reports*, **vol. 7**, no. February, pp. 1–10 (2017) (cited page 99)

[Sarritzu *et al.* 2018] V. Sarritzu, N. Sestu, D. Marongiu, X. Chang, Q. Wang, S. Masi, S. Colella, A. Rizzo, A. Gocalinska, E. Pelucchi, M. L. Mercuri, F. Quochi, M. Saba, A. Mura and G. Bongiovanni. 'Direct or Indirect Bandgap in Hybrid Lead Halide Perovskites?' *Advanced Optical Materials*, **vol. 6**, no. 10 (2018) (cited page 23)

[Schulz *et al.* 2015] P. Schulz, L. L. Whittaker-Brooks, B. A. MacLeod, D. C. Olson, Y.-L. Loo and A. Kahn. 'Electronic Level Alignment in Inverted Organometal Perovskite Solar Cells'. *Advanced Materials Interfaces*, **vol. 2**, no. 7, p. 1400532 (2015) (cited page 24)

[Schulz *et al.* 2019] P. Schulz, D. Cahen and A. Kahn. 'Halide Perovskites: Is It All about the Interfaces?' *Chemical Reviews*, **vol. 119**, no. 5, pp. 3349–3417 (2019) (cited page 24)

[Senocrate *et al.* 2018] A. Senocrate, I. Moudrakovski, T. Acartürk, R. Merkle, G. Y. Kim, U. Starke, M. Grätzel and J. Maier. 'Slow CH3NH3+ Diffusion in CH3NH3PbI3 under Light Measured by Solid-State NMR and Tracer Diffusion'. *Journal of Physical Chemistry C*, **vol. 122**, no. 38, pp. 21803–21806 (2018) (cited pages 24, 217)

[Shi *et al.* 2016] D. Shi, X. Qin, Y. Li, Y. He, C. Zhong, J. Pan, H. Dong, W. Xu, T. Li, W. Hu, J. L. Brédas and O. M. Bakr. 'Spiro-OMeTAD single crystals: Remarkably enhanced charge-carrier transport via mesoscale ordering'. *Science Advances*, **vol. 2**, no. 4 (2016) (cited page 209)

[Shockley and Queisser 1961] W. Shockley and H. J. Queisser. 'Detailed balance limit of efficiency of p-n junction solar cells'. *Journal of Applied Physics*, **vol. 32**, no. 3, pp. 510–519 (1961) (cited pages 20, 25)

[Shockley and Read 1952] W. Shockley and W. T. Read. 'Statistics of the recombinations of holes and electrons'. *Physical Review*, **vol. 87**, no. 5, pp. 835–842 (1952) (cited page 42)

[Sinton and Trupke 2012] R. A. Sinton and T. Trupke. 'Limitations on dynamic excess carrier lifetime calibration methods'. *Progress in Photovoltaics: Research and Applications*, **vol. 20**, no. 2, pp. 246–249 (2012) (cited pages 84, 92)

[Son *et al.* 2016] D. Y. Son, J. W. Lee, Y. J. Choi, I. H. Jang, S. Lee, P. J. Yoo, H. Shin, N. Ahn, M. Choi, D. Kim and N. G. Park. 'Self-formed grain boundary healing layer for highly efficient CH3 NH3 PbI3 perovskite solar cells'. *Nature Energy*, **vol. 1**, no. 7, pp. 1–8 (2016) (cited pages 27, 131)

[Sproul 1994] A. B. Sproul. 'Dimensionless solution of the equation describing the effect of surface recombination on carrier decay in semiconductors'. *Journal of Applied Physics*, **vol. 76**, no. 5, pp. 2851–2854 (1994) (cited page 91)

[Sridharan *et al.* 2021] A. Sridharan, N. K. Noel, B. P. Rand and S. Kéna-Cohen. 'Role of Photon Recycling and Band Filling in Halide Perovskite Photoluminescence under Focussed Excitation Conditions'. *The Journal of Physical Chemistry C*, **vol. 125**, pp. 2240–2249 (2021) (cited page 28)

[Staub *et al.* 2016] F. Staub, H. Hempel, J.-C. Hebig, J. Mock, U. W. Paetzold, U. Rau, T. Unold and T. Kirchartz. 'Beyond Bulk Lifetimes: Insights into Lead Halide Perovskite Films from Time-Resolved Photoluminescence'. *Physical Review Applied*, **vol. 6**, no. 4, p. 044017 (2016) (cited page 48)

[Stolterfoht *et al.* 2018] M. Stolterfoht, C. M. Wolff, J. A. Márquez, S. Zhang, C. J. Hages, D. Rothhardt, S. Albrecht, P. L. Burn, P. Meredith, T. Unold and D. Neher. 'Visualization and suppression of interfacial recombination for high-efficiency large-area pin perovskite solar cells'. *Nature Energy 2018 3:10*, **vol. 3**, no. 10, pp. 847–854 (2018) (cited page 99)

[Sutanto *et al.* 2020] A. A. Sutanto, N. Drigo, V. I. Queloz, I. Garcia-Benito, A. R. Kirmani, L. J. Richter, P. A. Schouwink, K. T. Cho, S. Paek, M. K. Nazeeruddin and G. Grancini. 'Dynamical evolution of the 2D/3D interface: a hidden driver behind perovskite solar cell instability'. *Journal of Materials Chemistry A*, **vol. 8**, no. 5, pp. 2343–2348 (2020) (cited page 99)

[Sutanto *et al.* 2021] A. A. Sutanto, P. Caprioglio, N. Drigo, Y. J. Hofstetter, I. Garcia-Benito, V. I. Queloz, D. Neher, M. K. Nazeeruddin, M. Stolterfoht, Y. Vaynzof and G. Grancini. '2D/3D perovskite engineering eliminates interfacial recombination losses in hybrid perovskite solar cells'. *Chem*, **vol. 7**, no. 7, pp. 1903–1916 (2021) (cited page 99)

[Taheri *et al.* 2021] M. M. Taheri, T. M. Truong, S. Li, W. N. Shafarman, B. E. McCandless and J. B. Baxter. 'Distinguishing bulk and surface recombination in CdTe thin films and solar cells using time-resolved terahertz and photoluminescence spectroscopies'. *Journal of Applied Physics*, **vol. 130**, no. 16, p. 163104 (2021) (cited pages 48, 165)

[Tennyson *et al.* 2019] E. M. Tennyson, T. A. Doherty and S. D. Stranks. 'Heterogeneity at multiple length scales in halide perovskite semiconductors'. *Nature Reviews Materials*, **vol. 4**, no. 9, pp. 573–587 (2019) (cited page 22)

[Trimpl *et al.* 2020] M. J. Trimpl, A. D. Wright, K. Schutt, L. R. V. Buizza, Z. Wang, M. B. Johnston, H. J. Snaith, P. Müller-Buschbaum and L. M. Herz. 'Charge-Carrier Trapping and Radiative Recombination in Metal Halide Perovskite Semiconductors'. *Advanced Functional Materials*, **vol. 30**, no. 42, p. 2004312 (2020) (cited pages 28, 131, 136)

[Valeur and Berberan-Santos 2011] B. Valeur and M. N. Berberan-Santos. 'A brief history of fluorescence and phosphorescence before the emergence of quantum theory'. *Journal of Chemical Education*, **vol. 88**, no. 6, pp. 731–738 (2011) (cited page 77)

[Vidon *et al.* 2021] G. Vidon, S. Cacovich, M. Legrand, A. Yaiche, D. Ory, D. Suchet, J.-B. Puel and J.-F. Guillemoles. 'Mapping Transport Properties of Halide Perovskites via Short-Time-Dynamics Scaling Laws and Subnanosecond-Time-Resolution Imaging'. *Physical Review Applied*, **vol. 16**, no. 4, p. 044058 (2021) (cited pages 48, 119, 121, 131, 137, 141, 165, 225)

[Wang and Kampwerth 2014] K. Wang and H. Kampwerth. 'Separation algorithm for bulk lifetime and surface recombination velocity of thick silicon wafers and bricks via time-resolved photoluminescence decay'. *Journal of Applied Physics*, **vol. 115**, no. 17 (2014) (cited page 166)

[Wang *et al.* 2019a] J. Wang, W. Fu, S. Jariwala, I. Sinha, A. K. Jen and D. S. Ginger. 'Reducing Surface Recombination Velocities at the Electrical Contacts Will Improve Perovskite Photovoltaics'. *ACS Energy Letters*, **vol. 4**, no. 1, pp. 222–227 (2019) (cited pages 24, 27, 131)

[Wang *et al.* 2019b] Q. Wang, E. Mosconi, C. Wolff, J. Li, D. Neher, F. De Angelis, G. P. Suranna, R. Grisorio and A. Abate. 'Rationalizing the Molecular Design of Hole-Selective Contacts to Improve Charge Extraction in Perovskite Solar Cells'. *Advanced Energy Materials*, **vol. 9**, no. 28, p. 1900990 (2019) (cited page 191)

[Wang *et al.* 2019c] R. Wang, M. Mujahid, Y. Duan, Z. Wang, J. Xue and Y. Yang. 'A Review of Perovskites Solar Cell Stability'. *Advanced Functional Materials*, **vol. 29**, no. 47, p. 1808843 (2019) (cited page 24)

[Warby *et al.* 2022] J. Warby, F. Zu, S. Zeiske, E. Gutierrez-Partida, L. Frohloff, S. Kahmann, K. Frohna, E. Mosconi, E. Radicchi, F. Lang, S. Shah, F. Peña-Camargo, H. Hempel, T. Unold, N. Koch, A. Armin, F. De Angelis, S. D. Stranks, D. Neher and M. Stolterfoht. ' Understanding Performance Limiting Interfacial Recombination in pin Perovskite Solar Cells '. *Advanced Energy Materials*, **vol. 2103567**, p. 2103567 (2022) (cited page 165)

[Weiss *et al.* 2019] T. P. Weiss, B. Bissig, T. Feurer, R. Carron, S. Buecheler and A. N. Tiwari. ‘Bulk and surface recombination properties in thin film semiconductors with different surface treatments from time-resolved photoluminescence measurements’. *Scientific Reports*, **vol. 9**, no. 1, p. 5385 (2019) (cited pages 90, 119, 167)

[Wolff *et al.* 2021] C. M. Wolff, S. A. Bourelle, L. Q. Phuong, J. Kurpiers, S. Feldmann, P. Caprioglio, J. A. Marquez, J. Wolansky, T. Unold, M. Stolterfoht, S. Shoaee, F. Deschler and D. Neher. ‘Orders of Recombination in Complete Perovskite Solar Cells – Linking Time-Resolved and Steady-State Measurements’. *Advanced Energy Materials*, p. 2101823 (2021) (cited page 148)

[Würfel *et al.* 1995] P. Würfel, S. Finkbeiner and E. Daub. ‘Generalized Planck’s radiation law for luminescence via indirect transitions’. *Applied Physics A Materials Science & Processing*, **vol. 60**, no. 1, pp. 67–70 (1995) (cited page 38)

[Wurfel 2005] P. Wurfel. *Physics of solar cells : from principles to new concepts*. Wiley-VCH (2005). ISBN 9783527404285, 186 pp. (cited pages 18, 26, 39, 41, 45, 163)

[Yamada *et al.* 2017] T. Yamada, Y. Yamada, Y. Nakaike, A. Wakamiya and Y. Kanemitsu. ‘Photon Emission and Reabsorption Processes in CH3NH3PbBr3 Single Crystals Revealed by Time-Resolved Two-Photon-Excitation Photoluminescence Microscopy’. *Physical Review Applied*, **vol. 7**, no. 1, p. 014001 (2017) (cited pages 27, 131)

[Yan *et al.* 2022] X. Yan, W. Fan, F. Cheng, H. Sun, C. Xu, L. Wang, Z. Kang and Y. Zhang. ‘Ion migration in hybrid perovskites: Classification, identification, and manipulation’. *Nano Today*, **vol. 44**, p. 101503 (2022) (cited page 213)

[Yang *et al.* 2015] Y. Yang, Y. Yan, M. Yang, S. Choi, K. Zhu, J. M. Luther and M. C. Beard. ‘Low surface recombination velocity in solution-grown CH 3 NH 3 PbBr 3 perovskite single crystal’. *Nature Communications*, **vol. 6** (2015) (cited pages 48, 166)

[Yang *et al.* 2017] Y. Yang, M. Yang, D. T. Moore, Y. Yan, E. M. Miller, K. Zhu and M. C. Beard. ‘Top and bottom surfaces limit carrier lifetime in lead iodide perovskite films’. *Nature Energy*, **vol. 2**, no. 2, pp. 1–7 (2017) (cited pages 48, 166)

[Young 2015] P. Young. *Everything You Wanted to Know About Data Analysis and Fitting but Were Afraid to Ask*. SpringerBriefs in Physics. Springer International Publishing, Cham (2015). ISBN 978-3-319-19050-1 (cited pages 71, 73)

[Zhang *et al.* 2014] M. Zhang, H. Yu, M. Lyu, Q. Wang, J. H. Yun and L. Wang. ‘Composition-dependent photoluminescence intensity and prolonged recombination lifetime of perovskite CH3NH3PbBr3x Clxfilms’. *Chemical Communications*, **vol. 50**, no. 79, pp. 11727–11730 (2014) (cited pages 27, 131)

[Zhang *et al.* 2017] M. Zhang, J. Wang, L. Li, G. Zheng, K. Liu, M. Qin, H. Zhou, X. Zhan, M. Zhang, J. Wang, L. Li, G. Zheng, K. Liu, M. Qin, H. Zhou and X. Zhan. ‘High-Mobility p-Type Organic Semiconducting Interlayer Enhancing Efficiency and Stability of Perovskite Solar Cells’. *Advanced Science*, **vol. 4**, no. 9, p. 1700025 (2017) (cited page 191)

[Zhang *et al.* 2020a] F. Zhang, J. F. Castaneda, S. Chen, W. Wu, M. J. DiNezza, M. Lassise, W. Nie, A. Mohite, Y. Liu, S. Liu, D. Friedman, H. Liu, Q. Chen, Y. H. Zhang, J. Huang and Y. Zhang. ‘Comparative studies of optoelectrical properties of prominent PV materials: Halide perovskite, CdTe, and GaAs'. *Materials Today*, **vol. 36**, no. June, pp. 18–29 (2020) (cited page 150)

[Zhang *et al.* 2020b] S. Zhang, P. E. Shaw, G. Zhang, H. Jin, M. Tai, H. Lin, P. Meredith, P. L. Burn, D. Neher and M. Stolterfoht. 'Defect/Interface Recombination Limited Quasi-Fermi Level Splitting and Open-Circuit Voltage in Mono-and Triple-Cation Perovskite Solar Cells'. *ACS Applied Materials and Interfaces*, **vol. 12**, no. 33, pp. 37647–37656 (2020) (cited page 77)

[Zhao *et al.* 2014] X. H. Zhao, M. J. Dinezza, S. Liu, C. M. Campbell, Y. Zhao and Y. H. Zhang. 'Determination of CdTe bulk carrier lifetime and interface recombination velocity of CdTe/MgCdTe double heterostructures grown by molecular beam epitaxy'. *Applied Physics Letters*, **vol. 105**, no. 25 (2014) (cited pages 48, 165)

ECOLE
DOCTORALE

Titre : Pourquoi les déclins déclinent ? Étude des dynamiques de transport et de recombinaison dans les cellules solaires par imagerie de photoluminescence résolue en temps : application aux pérovskites hybrides.

Mots clés : Luminescence, Photovoltaïque, Transport, Inhomogénéités, Déclin

Résumé : Les pérovskites forment une famille de matériaux qui ont récemment suscité un intérêt pour leur application en tant que couche absorbante de lumière pour le photovoltaïque. Ils sont à la fois très faciles à déposer (et à industrialiser) et très performants pour la conversion de la lumière solaire en électricité. Les propriétés radiatives des pérovskites sont excellentes maisla nature et la densité des défauts qu'elles contiennent sont encore sujets à débat, tout comme leurs propriétés de transport. Au sein d'un unique échantillon on peut s'attendre à observer des inhomogénéités de transport, de recombinaison voire de composition. Le but de cette thèse est de caractériser et d'imager les inhomogénéités de transport et de recombinaison des pérovskites à l'échelle de la centaine de microns. Pour ce faire, une technique d'imagerie de photoluminescence résolue en temps est utilisée. Cette thèse propose et applique une série de nouvelles méthodes pour l'analyse des déclins de photoluminescence applicables à l'imagerie.
Ces méthodes sont présentées dans la première partie de ce manuscrit. Dans une seconde partie, cette thèse aborde l'étude phénoménologique des déclins. Bien qu'applicable facilement aux images, il est notamment montré que les approches phénoménologiques ne suffisent pas toujours à attribuer les inhomogénéités de temps de vie observées à des différences locales de recombinaisons non radiatives. Dans un troisième temps, cette thèse discute l'imagerie des recombinaisons non radiatives. Une méthode liée à la pente initiale des déclins de luminescence en fonction de la fluence du laser d'excitation est proposée. Elle aboutit à la mesure d'une cartographie de recombinaisons non radiative ainsi qu'à l'estimation du coefficient de recombinaisons radiatives. Dans un quatrième temps, la question de la localisation en profondeur des défauts est abordée. Pour y répondre, deux méthodes sont proposées : l'une basée sur la pente initiale des déclins en fonction de la longueur d'onde du laser d'excitation, et l'autre sur la comparaison entre temps courts et temps long. Enfin, l'impact des couches d'extraction sur l'imagerie de déclins de photoluminescence est abordé. Une méthode d'analyse des échantillons couche par couche conduit à de premiers résultats prometteurs mais ceux-ci restent à consolider. L'impact des ions mobiles est aussi mis en évidence comme ouverture des travaux présentés.

Title : Why do decays decay? Transport and recombination dynamics of solar cells revealed via time resolved photoluminescence imaging: application to hybrid perovskites.

Keywords : Luminescence, Photovoltaic, Transport, Inhomogeneities, Decay

Abstract : Perovskites are a family of material that recently gathered interest for their potential application as an absorbing layer for photovoltaics. They are both easily deposited (thus industrialized) and show high performance for solar energy conversion – with a record power conversion efficiency of 25.7%. The radiative properties of perovskite are excellent but the nature and density of their defects are still debated – as are their transport properties. Inhomogeneities of transport, recombination or even composition could be expected even within one sample. The aim of this thesis is to characterize and image transport and recombination inhomogeneities of perovskites at the scale of the hundreds of microns. To do so, a technique of time resolved photoluminescence imaging technique is used. This thesis introduces and applies a series of new image-applicable-methods to analyze photoluminescence decays.
These methods are discussed in the first part of this manuscript. In a second part, this thesis tackles the phenomenological study of decays. Even if the phenomenological approach is well suited for imaging analysis, it is shown that the interpretation does not always succeed in attributing inhomogeneities of decay time to local differences of defect densities. In a third part, this thesis discusses non radiative recombination imaging. A new method is introduced, based on the slope of decays as a function of laser excitation fluence. This technique allows for imaging non radiative recombination as well as the estimation of radiative recombination coefficient for a triple cation perovskite sample. In a forth part, the question of localizing defect in the material's thickness is tackled. Two methods are proposed: one based on the initial slope of the decays observed as a function of laser wavelength, the other on the comparison between long and short time. Finally, the impact of the extracting layers on decays is studied. A method of layer by layer analysis is proposed but needs to be improved. The impact of mobile ion is also evidenced, as a possible perspective of this work.

Institut Polytechnique de Paris
91120 Palaiseau, France